UNIVERSITY OF COPENHAGEN



Københavns Universitet





Glacial Rock Flour

its Characteristics and Enhanced Weathering Potential

Ray Sarkar, Sneha

Publication date:
2023

Document version
Publisher's PDF, also known as Version of record

Citation for published version (APA):
Ray Sarkar, S. (2023). *Glacial Rock Flour: its Characteristics and Enhanced Weathering Potential*. GLOBE Institute, Faculty of Health and Medical Sciences, University of Copenhagen.

Download date: 04. nov.. 2026

PhD thesis

GLACIAL ROCK FLOUR

its Characteristics and Enhanced Weathering Potential



Sneha Ray Sarkar

2021
KØBENHAVNS UNIVERSITET
GLOBE INSTITUTE

GLACIAL ROCK FLOUR

its Characteristics and Enhanced Weathering Potential

Glacial Rock Flour: its characteristics and enhanced weathering potential

Author: Sneha Ray Sarkar

Affiliation: Globe Institute, University of Copenhagen

PhD Supervisor:
Minik Thorleif Rosing
Professor, University of Copenhagen

Assessment committee
External opponents:
Gry Hoffmann Barfod
Assistant Professor,
Department of Geoscience, University of Aarhus

Ole Bennike
Senior Researcher,
Geological Survey of Denmark and Greenland (GEUS)

Internal Chairman:
Kurt Kjær
Professor, University of Copenhagen

Cover image by Minik Thorleif Rosing
© Minik Thorleif Rosing

KØBENHAVNS UNIVERSITET
GLOBE INSTITUTE

GLACIAL ROCK FLOUR

its Characteristics and Enhanced Weathering Potential

PhD Thesis by
SNEHA RAY SARKAR

Academic supervisor
MINIK THORLEIF ROSING

Submitted
09 JULY 2021

Globe Institute
University of Copenhagen

Contents

ACKNOWLEDGEMENTS viii
SUMMARY x
RESUME PÅ DANSK xi

Thesis Introduction 1
1.1. GENERAL 1
1.2. AIM OF THIS STUDY 2
1.3. WHY DO WE NEED TO STUDY GRF? 2
1.4. STRUCTURE OF THIS THESIS 3

A literature survey of Glacial Rock Flour 5
2.1. GENERAL 5
2.2. GRF IN GREENLAND 7
2.3. CONCEPTUAL MODEL OF A GRF DEPOSIT 8
2.4. FIELD TRIALS 10
2.5. WEATHERING REACTIONS 10

Geochemical characteristics of Greenlandic Glacial Rock Flour 14
3.1. INTRODUCTION 15
3.2. STUDY AREAS 16
3.3. SAMPLES AND ANALYTICAL PROCEDURES 20
3.3.1. SAMPLE PREPARATION 20
3.3.2. PARTICLE ANALYSIS 23
3.3.3. MINERAL COMPOSITION ANALYSES 24
3.3.4. GEOCHEMICAL ANALYSES 26
3.4. RESULTS 28
3.4.1. PHYSICAL PROPERTIES OF GRF 28
3.4.2. CHEMICAL PROPERTIES OF GRF 42
3.5. DISCUSSION 61
3.5.1. PROVENANCE 61
3.5.2. SEDIMENT SORTING 63
3.5.3. ENVIRONMENTAL IMPACT OF GRF APPLICATION 65

3.6. CONCLUSIONS 67

Field reports from a Glacial Rock Flour deposit in West Greenland 69

4.1. INTRODUCTION 70

4.2. STUDY AREA 71

4.3. METHODOLOGY 77

4.3.1. FIELD MEASUREMENTS AND SAMPLE COLLECTION 77

4.3.2. ANALYTICAL METHODS 81

4.4. RESULTS 83

4.4.1. COMPOSITION OF THE WATER AT THE DEPOSIT 83

4.4.2. STREAM AND SPRING DISCHARGE 85

4.4.3. ALKALINITY AND pCO_2 90

4.4.4. STABLE ISOTOPIC COMPOSITION 92

4.5. DISCUSSIONS 94

4.5.1. SOURCE OF CATIONS AND ANIONS 94

4.5.2. DISCHARGE RATE AND SOLUTE CONCENTRATION 99

4.5.3. CO_2 CONSUMPTION AND ALKALINITY 99

4.6. CONCLUSIONS 102

Acid and alkaline leach of Glacial Rock Flour and its dissolution reaction in ambient and elevated pCO_2 conditions 103

5.1. INTRODUCTION 104

5.2. BACKGROUND OF REACTION KINETICS 105

5.3. EXPERIMENTAL METHOD 106

5.3.1. STARTING MATERIAL 106

5.3.2. EXPERIMENTAL SETUP 108

5.3.3. CALCULATION OF MINERAL SATURATION INDICES 110

5.3.4. REPRODUCIBILITY 110

5.4. RESULTS 111

5.4.1. GRF DISSOLUTION IN ACIDIC PH 111

5.4.2. GRF DISSOLUTION IN ALKALINE PH 117

5.4.3. GRF DISSOLUTION AT TWO pCO_2 CONDITIONS 117

5.5. DISCUSSIONS 128

5.5.1. ACID AND ALKALINE LEACH 128

5.5.2. ELEMENT-TO-MINERAL ATTRIBUTION 129

5.5.3. DISSOLUTION MECHANISMS CONTROLLING THE APPARENT STEADY STATE RELEASE 134

5.5.4. EFFECT OF GRAIN SIZE AND SURFACE AREA 136

5.6. CONCLUSIONS 137
Conclusions and Perspectives 138
Appendix 141
References 158

ACKNOWLEDGEMENTS

I am deeply indebted to my supervisor Prof. Minik Thorleif Rosing for his guidance and support during the past few years. I am grateful to him for giving me the opportunity to be part of this project of potential global significance. His suggestions, expertise and experience have been immensely valuable for me in completing this work.

I thank Søren Jessen who has been crucial in helping me steer the project. I also thank Astrid Vester-Ebbesen and Nanna Thekla Grønbæk, for their help in carrying out the field and laboratory experiments.

I thank Knud Dideriksen, Nynke Keulen, Tue Hassenkam and Tais Wittchen Dahl, for their support and assistance in various analyses, most of which form part of this thesis, the result interpretations and discussions. Their suggestions helped me shape my project and I'm extremely grateful for that.

I thank Tonci Balic Zunic for performing the XRD analysis, Anne Thoisen for the IC analysis and Christina Rosenberg Lynge for the BET measurements.

I thank Emily Pope for giving me the opportunity to be a teaching assistant in her course at the University of Copenhagen, which equipped me in carrying out this research in many ways.

I am thankful to Mogens Greve for giving me the opportunity to work him at the Institute of Agroecology, University of Aarhus.

I thank Austin Jarl Boyd for providing additional suggestions and perspectives to the thesis.

I'd like to thank Rebekka Johanne Knudsen, not just for her administrative assistance, but also for her immense help in my smooth transition as an international student.

I'd like to thank my colleagues in the Geobiology group: Álvaro del Rey, Aske Sørensen, Christian Rasmussen, Kasper Olesen, Magnus Harding, Nicholas Rose, Rasmus Dyrberg, Salik Rosing, Susanne Arens, Stefan Piasecki, and everyone through my timeline at the University of Copenhagen: Jasmina,

Julius, Quinten and Tom, with whom I've shared this student-cum-employee journey, for being so welcoming and for all the wonderful insights.

I'd like to extend my thanks to Peter Weber and Rene Larsen from University of Aarhus; Alan from Ilisimatusarfik/University of Greenland, and everyone I had the opportunity to work with from the Geogenetics group, the Starplan group at the Globe Institute, and other departments and sections in the University of Copenhagen and the Geological Survey of Denmark and Greenland (GEUS) especially Luisa, Case, Tue, Christiana, Klara, Lars, Andreas, Stanislev, Karina and Anthony.

I thank all the administrative staff at the National History Museum of Denmark and the University of Copenhagen for their many assistances.

I thank Novo Nordisk Foundation for funding my PhD study, which gave me the opportunity to not just conduct this research but also to acquaint with scientific researchers worldwide and widen my perspective.

I thank all my precious friends, especially Abhyuday Chatterjee, Ayusman Dash, Purba Kashyap and Saptarshi Rajan Sarkar, who have been integral to this journey.

I thank my family for their constant moral support and encouragement and for their blessings that helped me reach this feat.

Lastly, I would like to thank the PhD School of University of Copenhagen, Denmark for giving me this great opportunity to learn from some of the finest minds in the world and evolve in a holistic manner. I am eternally grateful for this experience.

|| धन्यवादः ||

SUMMARY

Glacial rock flour is a fine-grained, clay-sized material produced as a result of abrasion of the bedrock surface by the moving ice. In Greenland, gigatons of these freshly eroded mineral particles are being annually produced and deposited along the deltas, as well as are discharged into the North Atlantic and the Arctic Oceans. The suspended sediments are rich in nutrients and support marine biodiversity, especially in the summer, when the discharge is high. They are also reported to promote plant productivity in nutrient deficit soils. In Greenland their abundant deposition along the fjord outlets, however, has led to an increase in delta size and their progradation. This unfortunately demands a frequent relocation of the docks for a smooth functioning of waterways, which is the main means of transport in Greenland.

While copious amounts of glacial rock flour deposition is a cause of distress among the Greenlandic community, it might be a boon for the global tribe. Anthropogenic climate change is currently a human existential concern and understanding the options of CO_2 removal from the atmosphere and their deployment is a matter of urgency. Glacial rock flour consists of primary minerals such as feldspars and mica that consume CO_2 in the presence of water and release base cations that are essential nutrients for plant growth. Their fineness is associated with a high specific surface area, which enables their accelerated weathering capacity. Enhanced silicate weathering also releases bicarbonate ions that might contribute to ocean alkalinity.

This thesis looks into the geochemical characteristics of glacial rock flour in Greenland and its reaction kinetics, as a step towards understanding the material better and perhaps opening doors for further research into its applications.

RESUME PÅ DANSK

Gletsjermel er et fint bjergartsmel, der produceres når gletsjerbevægende is glider bevæger sig over landet og knuser den jorskorpens bjergarterne i den underliggende jordskorpe Det finkornede sediment, som dannes i denne proces, transporteres fra isen med smeltevandsfloder og bliver aflejret i fjorde, langs kyster eller ført ud i havet. Flere gigatons af denne glaciale bjergartsmel produceres årligt i Grønland og ledes ud i det nordlige Atlanterhav og i det Arktiske Hav. Materialet forbliver suspenderet i smeltevandet og forøger den biologiske produktivitet i havet, især om sommeren, hvor afsmeltningen er størst. Grønlandsk gletsjermel findes også i meget store mængder i deltaudløb, hvor det skaber problemer for den grønlandske lokalbefolkning, da den konstante aflejring gør det nødvendigt at flytte kajer og moler. Disse udgør ofte vigtige knudepunkter for transport af folk og gods via havet, som i Grønland er den vigtigste transportvej.

Mens store aflejringer af gletsjermel forårsager problemer for det grønlandske samfund, kan aflejringerne blive en velsignelse for menneskeheden globalt. I øjeblikket er der en stor risiko for at menneskeskabte klimaændringer vil have store konsekvenser for menneskers fremtidige velstand og helbred. Derfor er det vigtigt at forstå hvilke teknologiske muligheder der er for fjernelse af kuldioxid fra atmosfæren og hvad der kræves for at de kan implementeres. Accelereret forvitring af gletjsermel kan potentielt være en af disse teknologiske muligheder.

Gletsjermel består hovedsagelig af feldspat og glimmer, som i kontakt med vand, kan reagere med CO_2 og frigive basiskationer (f.eks. K^+, Na^+, Ca^{2+} eller Mg^{2+}), som er vigtige næringsstoffer for planter. Mineralernes finkornethed giver et højt specifikt overfladeareal, hvilket muliggør deres accelererede forvitring. Denne accelererede forvitring tilføjer også alkanitet til havvand.

Denne afhandling udforsker den geokemiske sammensætning af gletsjermel samt dets reaktionskinetik. Dette gøres for at forstå materialets potentiale for forvitring og dermed dets potentiale som landbrugsgødning og som redskab til at trække CO_2 ud af atmosfæren. Derudover er det et mål at skabe grundlag for yderligere forskning i dets anvendelser.

Chapter 1

Thesis Introduction

1.1. General

Glacial erosion is the most powerful and widespread erosional process in Greenland, contributing ~7-9 % of the global sediment flux to the sea (Overeem et al., 2017). Greenlandic meltwater streams originate from the Greenland Ice Sheet (GRIS) and from local glaciers. The GRIS is more than 3000 m thick, and the pressure at the base is generally very high. The strong pressure gradients in the englacial and subglacial conduit renders meltwater streams violent and turbulent (Drewry, 1986). The flow of ice from the accumulation zones in the interior part of GRIS towards the ablation zones and calving fronts along the margin causes the dense ice to move across its base. The moving ice hauls debris that abrades and scours the bedrock while meltwater moves along the ice/land interface or in localized conduits. Most of the topographic relief along the coast of Greenland is carved by glacial erosion.

The debris from glacial erosion can range from large boulders to silt and clay sized particles. The finest sediments remain in suspension and are transported into the coastal ocean waters. In Greenland, meltwater transports 1.28 ± 0.51 Gt of suspended sediments to the oceans annually (Overeem et al., 2017; Syvitski and Kettner, 2011). Considering the inter-annual variability in weather as well as unpredictability of events such as glacier calving and surge or mudslides, precise determination of this discharge is difficult. Previously, the annual sediment delivery of 0.59 ± 0.45 Gt (Hasholt et al., 2006) and 1.3 ± 0.86 Gt (Hawkings et al., 2017) has been estimated from Greenland to its surrounding seas.

Hasholt et al. (2018) found that when the discharge is low, ~70% of the sedimentary particles was <20 µm, while 98% of the sediments were <63 µm (Hasholt et al., 2013). The fine sediments, therefore, dominate the suspended sediment load before the peak flow season. These fine-grained sediments are referred to as 'glacial rock flour'. These are freshly eroded mineral grains that are carried in suspension by meltwater to the proglacial riparian or

lacustrine environments and eventually to the ocean (Hawkings et al., 2014, 2015, 2016, 2017; Meire et al., 2016). The large surface area to volume ratio of the finer particles renders them with a high surface energy (Kranck, 1973), which are usually negatively charged and therefore, repel each another in a non-turbulent environment (Hunter and Liss, 1979). Particles can aggregate to form larger clusters or flocs following collisions during transport. This tendency may be accentuated by biologic factors such as organic coatings. These large clusters have low settling velocities in freshwater due to low density and it is unlikely for the particles to settle at the bottom due to differential settling in estuarine and coastal environments (Stolzenbach and Elimelich, 1994; Winterwerp, 2002). However, when the meltwater mixes with seawater, the higher ionic strength of the water compresses the electrostatic double layer surrounding a particle, prompting the particles to aggregate (Maggi, 2005). The front cover of this thesis shows an aerial photograph of mud suspensions and glacial meltwater plume from a glaciofluvial delta at the mouth of Carlsberg Fjord in East Greenland. The sharp interface marks the transition of large freshwater flocs into more compact flocs due to high salinity.

1.2. AIM OF THIS STUDY

The research presented in this thesis is aimed at furthering our knowledge of glacial rock flour from Greenland and understanding its interaction with reservoirs in the field and conditions set in the laboratory. The results of this study are expected to show limited chemical weathering of the material in Greenland due to subarctic temperatures. Its primary mineral composition and fine-grained size would render the material highly reactive. The study focusses on how the provenance and the transport of mud suspensions influence the GRF geochemical composition and examines whether the material is generic in nature

1.3. WHY DO WE NEED TO STUDY GRF?

As the glacier advance by sliding on the bedrock, they abrade and pluck the surfaces. The glacial meltwater produced by the melting of the glacier ice facilitates this and in the process transports sediments along with it. Evans et al., (2007) estimate annual sedimentation rates of 0.01 mm for polar glaciers, to 1.0 mm for alpine temperate glaciers, to 10–100 mm for

Alaskan glaciers. The subglacial meltwater particles in Greenland are usually silt-sized as the water film at the contact of the base of the glaciers and the bedrock is ~20 µm allowing only the finer particles to be transported. Sediment transported by meltwater from its source can undergo several processes, which occur successively.

Suspension – The fine sediments are carried in suspension by the meltwater. Due to negligible presence of ions in the freshwater, the sediments are able to remain in a colloidal state rendering the suspension turbid with a milk-like appearance. The suspension of clay- to silt-sized sediments that are cohesive in nature give rise to muddy water (or mud suspension).

Flocculation – Aggregates of fine particles in suspension that gel upon contact during transport (Kranck, 1973; Eisma, 1986).The process depends upon the collision of particles during transport and cohesiveness of the particles on contact. Their size and growth rate depends upon hydrodynamic conditions, sediment properties, residence times, pH and salinity (Mietta et al., 2009). In highly saline seawater, the flocs become larger, denser and increasingly unstable, consequently settling down in the water column.

Deposition – Settling of sediments to the bed due to their settling velocities or an unstable physical state.

Weathering – This involves physical disintegration of a rock and its chemical decomposition

Alteration – This refers to chemical weathering or hydrothermal alteration of a particle such that a mineral particle has undergone changes in chemical composition producing secondary minerals.

1.4. STRUCTURE OF THIS THESIS

The thesis consists of an introductory chapter followed by three individual, albeit interconnected, chapters that provide a cohesive account of the author's work. This chapter discusses the processes that a meltwater sediment can undergo during transport from its source to the sea and a discussion of the incentives for this research. A literature summary on GRF and its applications is presented in Chapter 2. Chapter 3 characterizes these fine-grained sediments from various sites in Greenland based on their physical and chemical properties. Chapter 4 reports field observations on the water chemistry of various water

bodies at a GRF deposits in West Greenland. This describes the chemical interactions between rock flour and its natural environment from one field site in Greenland and provides ground-truth observations as a basis for contextualization of the data presented in Chapter 3. The naturally occurring silicate mineral heterogeneity of GRF complicates the element-to-mineral attribution in our dissolution study. Nevertheless, Chapter 5 attempts at understanding the dissolution of the bulk material, its reactivity and factors affecting its kinetics in a laboratory setting at different pH and pCO_2 conditions. Conclusions and perspectives for further research are presented in Chapter 6.

Chapter 2

A literature survey of Glacial Rock Flour

2.1. General

The United Nations Framework Convention on Climate Change signed the Paris Agreement 2015 aiming to keep the global temperature rise below 2°C by 2100. As the goal becomes increasingly arduous, implementing large-scale mitigation schemes for CO_2 sequestration are becoming more pertinent. Several geo-engineering schemes for carbon dioxide removal (CDR) have been suggested by the Intergovernmental Panel on Climate Change (IPCC 2013) in their fifth Assessment Report. For example, direct air capture (DAC), where air capture plants captures CO_2, which is either geologically stored (Oelkers et al., 2008) or is used for producing CO_2-containing products (Peters et al., 2011; Sanz-Pérez et al., 2016 and references therein). Large-scale implementation of bioenergy with carbon capture and storage (BECCS) is also suggested to potentially attain the negative emission goals. However, BECCS is still in its developmental phase and its technological feasibility with respect to storage and costs (Strefler et al., 2015) are uncertain. Further, the sociopolitical impact of BECCS has led to controversy surrounding its use (Fridahl and Lehtveer, 2018).

In comparison to the technology mentioned above, application of pulverized rocks to nutrient deficient soil is less likely to encounter social or technical impediment. The dissolution of silicate mineral consumes CO_2 and converts it to bicarbonate ions while releasing monovalent and divalent cations. While agricultural practices have led to depletion in soil nutrients in some regions, many soils are intrinsically depleted in mineral nutrients. This is especially true in the tropical regions, where hot humid climatic conditions have led to extensive weathering of the primary basement minerals to great depths. The bicarbonate ions produced during silicate weathering are carried by rivers into the oceans and are a significant source of ocean alkalinity. However, natural silicate weathering operates on a timescale for significant changes in atmospheric composition of ~10^6 year (Colbourn et al., 2015). Accelerating this process by the application of crushed silicate rocks can speed up the process to occur at timescales comparable with those of human activity. This is currently being developed as one

of the geoengineering techniques that can be used to remove atmospheric CO_2, and is gaining more cognizance in the recent studies (Hartmann et al., 2013; Beerling et al., 2020). Application of pulverized Ca/Mg-rich silicate rocks report increase in crop yield in tropical agricultural fields. Temperate and tropical croplands can be most efficient for enhanced weathering with crushed silicate rocks due to warmer temperatures and wet conditions that enhance the mineral weathering rates (Edwards et al., 2017; Beerling et al., 2020).

Enhanced weathering (EW) would increase the chemical weathering rates, sequestering CO_2 from the atmosphere at timescales comparable with those of human activity. Ultramafic rocks, (e.g. dunite), followed by mafic rocks (e.g. basalt) have the highest CO_2 draw down potential during EW due to their low silica and high alkaline earth content. Rocks of these compositions are estimated to potentially drawdown 1.1 t CO_2 and 0.3 tCO_2 per t of the material, respectively (Strefler et al., 2018). However, ultramafic rocks often contain harmful trace elements and are therefore, unlikely to be deployed in agricultural systems at a large scale. Basalt (Strefler et al., 2018) and GRF (this thesis) are better alternatives due to lower concentration of potentially toxic contaminants. The abundance of GRF deposits along the coastlines of Greenland and its natural fine-grained size (Chapter 3) are important parameters that significantly reduce comminution costs for enhanced weathering implementation.

Grain size of a potential EW agent is one of the key parameters that determines the feasibility of its carbon capture. In general, finer grain size is associated with a higher carbon removal rate as larger specific surface areas enhance the weathering rate of a mineral. It is estimated that comminution of ultramafic and mafic rock requires approximately 13-2327 kWh tCO_2^{-1} energy usage (Renforth, 2012). Furthermore, energy required for grinding the material increases exponentially with the fineness of the resultant grain size, thereby, increasing energy costs (Edwards, 2017) and reducing the net carbon capture efficiency. Renforth (2012) estimate that rock comminution can potentially cost 4.45-53.2 US$ t^{-1} material. Meanwhile, gigatons of freshly eroded and bedrock fragments pulverized naturally by the moving glaciers are being deposited along the shorelines of Greenland annually (Overeem et al., 2017; Hawkings et al., 2017). These fragments range from boulders to fine-grained silt particles in size, but the silt to clays size fraction is transported on a scale of ca. 1 Gt a^{-1}. For a silicate rock with a cation dissolution rate of 10^{-14} mol cm^{-2} s^{-1}, Renforth (2012) estimate that a target surface area of 1-10 m^2 g^{-1} will be desirable for the pulverized material to be effective. Glacial

rock flour presents a tremendous benefit in this regard, as the material is glacially milled to the requisite grain size. Therefore, it is apposite to understand the physical and chemical properties of glacial rock flour and its chemical kinetics to explore the applications this naturally pulverized material could present.

2.2. GRF IN GREENLAND

Rock flour is produced during glacial advances and can be found in Greenland, Svalbard, northern Europe, United States and northern Asia. The extent of Last Glacial Maximum (~21 ka) is correlated with high productivity agricultural areas in northern Europe, North America and China (Gornall et al., 2010; Binney et al., 2017). In India, for example, meltwater from mountain glaciers is associated with high productivity of crops such as wheat, rice, cotton, sugarcane etc. along the floodplains of river Ganga (Biemans et al., 2019). In a study, Frederiksen (2018) interestingly notes a difference in the grain size distribution of GRFs from Greenland, Svalbard, Alaska and Argentina and found that GRFs from Greenland are finest among them. She suggests that the thermal regime and the bedrock composition play critical role in determining the GRF grain size. Since the water film under a glacier is around 20 µm, the cold temperature glaciers in Greenland allow subglacial meltwater to carry mostly clay- to silt-sized particles.

Greenland is the largest island on Earth with a total area of 2,166,000 km^2 and about eighty percent of this area is covered with ice. Most of the exposed ice-free part of Greenland is composed of Precambrian crystalline rocks, which formed during a succession of Archean and early Proterozoic orogenic event and stabilized as part of the Laurentian shield ~1.6 Ga (Escher and Watt, 1976). The retreat of the Greenland Ice Sheet (GrIS) since the start of Holocene induced glacial erosion of the bedrock, producing glacial and glacio-fluviatile deposits in massive amounts along the coasts of Greenland. In Tasersuaq Lake, for example, GRF deposition at the rate of 0.5 cm y^{-1}, on average, since deglaciation (~10 ka) has contributed to >50 m of sediments in the lake (Bennike et al., 2019; Medford et al., 2021). These results are based on study of seismic profiles of the area.

The amount of sediments ultimately discharged to the open sea depends upon several factors such as source to coast distance, runoff, basal topography and slope, presence of sediment

sinks (e.g. lakes), and ice dynamics. The GrIS produces 1.28 ± 0.51 Gt suspended sediments annually, which is ~7-9% of the global suspended sediment load (Overeem et al., 2017, Syvitski and Kettner, 2011). Previously Hasholt et al. (2006) had estimated 0.59 ± 0.45 Gt of annual sediment delivery from Greenland to the adjoining oceans while Hawkings et al. (2017) had estimated 1.3 ± 0.86 Gt. The large uncertainty in annual discharge estimates can be attributed to the inter-annual variability in weather, unpredictable events such as glacier calving and surge, mudslides (or jökulhlaups), and difficulty in determining the contributions from ice-rafted debris with precision. Glaciated areas in East Greenland have a higher surface relief and are closer to the sea than on the western coast. As higher surface gradient would be expected to influence the severity of glacial erosion largely, Hasholt (2013) previously predicted a higher sediment transport along the eastern margin. However, in a recent study, Overeem et al. (2017) report that West Greenland is the major contributor of sediments to the ocean instead. They report that Baffin Bay and Davis Strait together receive ~70 % of the total suspended sediment flux from the GrIS, whereas Denmark Strait, Scoresby Sound and Greenland Sea together receive <30 % of the total flux. The annual contribution to the Arctic Ocean in the north is relatively much lower at 0.02 Gt (~2-3 %). As climate warming continues, the extent of ice sheet melting also increases accompanied by an accelerated rate of sediment transport.

2.3. CONCEPTUAL MODEL OF A GRF DEPOSIT

Among the ten GRF deposits across Greenland investigated in Chapter 3 of this thesis, Maalutu GRF has been extensively researched in various studied. Maalutu is a raised marine deposit located a few kilometers north of Nuuk in West Greenland (Chapter 4). Grønbæk (2019) reports low rate of infiltration of the GRF deposit by rainwater and snow melt, such that majority of the meteoric water is collected in the surficial layer and is discharged to the sea via streams. She suggests a conceptual model of the study area based on the physical observation of sediment profile samples as shown in Figure 2.1 and compares the depositional environment to that of outwash plains. The top 5 – 40 cm layer of the study area is characterized by roots of vascular plants and decomposing plant material and has a high organic carbon content due to high biological activity (Vester-Ebbesen, 2020). This developed soil layer is underlain by layers of an unsorted mix of fine- to coarse-grained sand, which

becomes increasingly predominant in sand in the successive layers. They are generally poorer in organic material and have a low organic carbon content (Vester-Ebbesen, 2020). In some areas, partially decayed plant materials were identified in the layers following the top soil and are referred to as peat. The layers of sand and fine gravels is followed by a layer of fine, clay-sized sediments, grayish green in color, which is referred to as glacial rock flour. The organic carbon content of the GRF ranges from 0.9 to 1.3 % (Vester-Ebbesen, 2020).

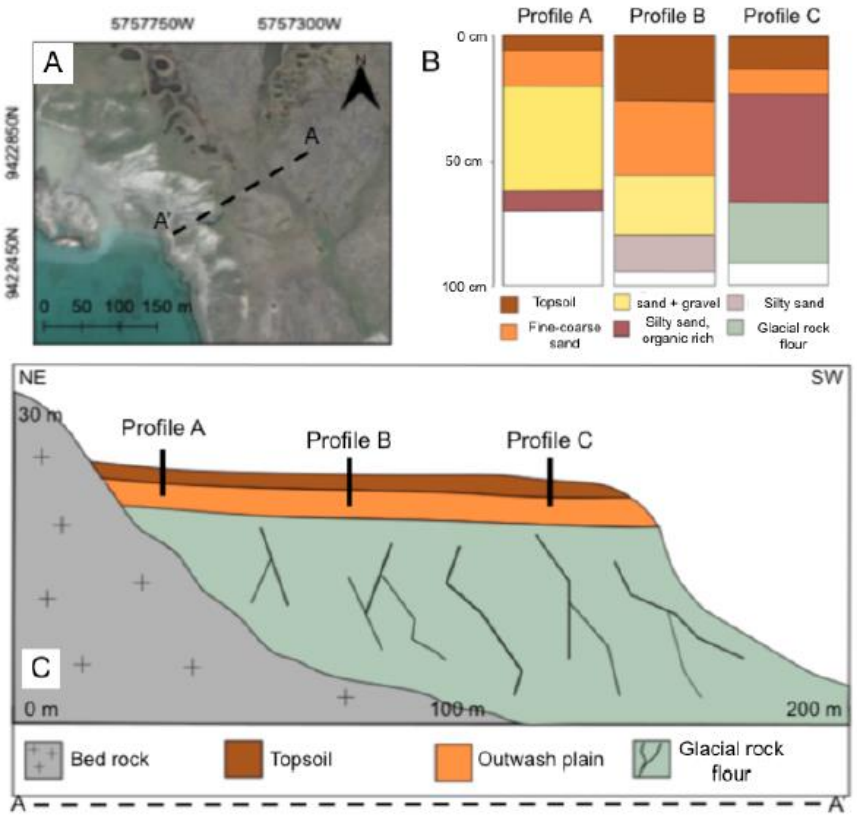


Figure 2.1: Conceptual model of the Maalutu GRF deposit from Grønbæk (2019).

Maalutu GRF is composed of the primary minerals plagioclase (43.5 %), microcline (10.7 %), quartz (23.1 %), biotite (7.8 %), amphiboles (10.4 %), augite (1.8 %) and epidote (2.7 %) (Section 3.3.3). The mineral composition of Maalutu GRF vary with grain size. Phyllosilicate and amphibole is dominant in the clay-sized fraction while the larger size fractions are relatively richer in quartz, while feldspars and epidote are present in all particle size fraction in similar proportions (Steffensen, 2020). Field applications of Maalutu GRF to soil increases plant growth and can be a potential alternative to fertilizers (Gunnarsen et al., 2019).

2.4. FIELD TRIALS

Field trials of a potential soil fertilizer are necessary to affirm the material for large-scale application and estimate the conditions (of soil, weather conditions etc.) which may affect the usage. Several pot trials as well as field trials are reported using Greenlandic GRF, which document the material's response under natural conditions (Frederiksen, 2018; Gunnarsen et al., 2019, 2020; Sukstorf et al., 2020). Gunnarsen et al. (2019) suggest Maalutu GRF as an alternative to K and Mg fertilizers. Their results show that the depletion of K-bearing minerals occurs more slowly than the crop-cycling period, which would allow GRF to provide essential nutrients for more than one growing season. They find that application of GRF to Danish soil increases maize and potato yield by 24 % and 19 %, respectively. For GRF from another Greenlandic site, Ilulialik in Nuuk fjord region, Gunnarsen (2020) report that although crops such as wheat and ryegrass show toxic response to high salinity of Ilulialik GRF, a washing treatment of the GRF yields higher productivity. However, not all studies report positive results for application of Greenlandic GRFs in agricultural productivity. Sukstorf et al. (2020) suggest Tasersuaq GRF as not suitable for agricultural supplement as it did not affect nutrient uptake by plant or an increase in biomass. Since Ilulialik and Tasersuaq form part of the same sedimentary system in the Nuuk fjord region, where glacial meltwater from Saqqap Sermersua discharges to Ilulialik via Lake Tasersuaq, their effectiveness would be expected to be in harmony. The possible reasons for disparity could be due to the experimental setup and method of application. The latter's application is in a southern Greenland agricultural field where the climate is subarctic, and the rate of chemical weathering in low temperature arctic/subarctic environments is low (White and Blum, 1995) and are estimated to be approximately 5 times lower than the tropics (Huh, 2003). The experiment was carried out without addition of N, which might have been a limiting nutrient.

2.5. WEATHERING REACTIONS

Mineral weathering proceeds by the dissolution media attacking structural defects and by a selective dissolution of more soluble components of the mineral (White and Buss, 2014). In general, a mineral dissolution takes the form

$$\mathrm{A}_{\nu_A}\mathrm{B}_{\nu_B(\mathrm{s})} \rightarrow \nu_{\mathrm{A}}\,\mathrm{A}^{q_{\mathrm{A}}}_{(\mathrm{aq})} + \nu_{\mathrm{B}}\,\mathrm{B}^{q_{\mathrm{B}}}_{(\mathrm{aq})} \qquad (2.1)$$

where ν_i is the stoichiometric coefficient of the reaction for species i and q_i is the charge of the aqueous species. Quartz is the most chemically stable of the common rock forming silicate minerals on Earth's surface, while olivine is the most chemically unstable of the common rock forming silicate minerals and is thus the most susceptible to chemical weathering.

Typical mineral reactions

(educts ⇨ ions and silica in solution, secondary minerals ⇨ precipitation reactions in the ocean)

Calcium carbonate (not a silicate)
$CaCO_3 + CO_2 + H_2O \Rightarrow Ca^{2+} + 2HCO_3^- \Rightarrow CaCO_3\downarrow + CO_2\uparrow + H_2O$
(No net-sink of 'consumed' atmospheric CO_2)

Olivine (silicate)
$Mg_2SiO_4 + 4CO_2 + 4H_2O \Rightarrow 2Mg^{2+} + 4HCO_3^- + H_4SiO_4 \Rightarrow 2MgCO_3\downarrow + SiO_2\downarrow + 2CO_2\uparrow + 4H_2O$
(Net-sink for 50% of 'consumed' atmospheric CO_2)

Albite (silicate)
$2NaAlSi_3O_8 + 2CO_2 + 11H_2O \Rightarrow Al_2Si_2O_5(OH)_4 + 2Na^+ + 2HCO_3^- + 4H_4SiO_4 \Rightarrow 2Na^+ + 2HCO_3^- + 4SiO_2\downarrow + 8H_2O$
(Net-sink for 100% of 'consumed' atmospheric CO_2)

Figure 2.2: Typical reaction equations for carbonate and silicate mineral dissolution from Hartmann et al., 2013.

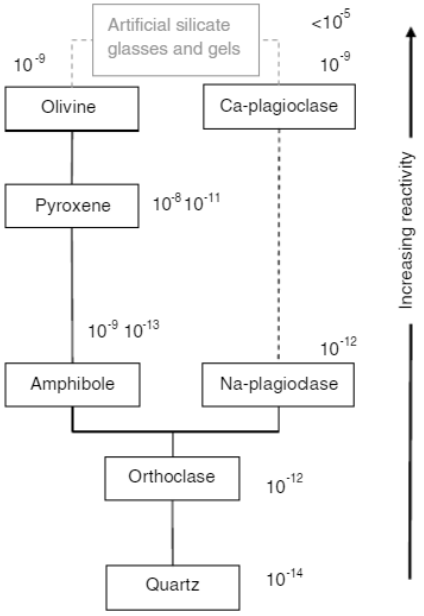


Figure 2.3: Goldich mineral reactivity series (Goldich 1938) showing and the variation in dissolution rates for different minerals (from Hartmann et al. 2013). Chemical weathering rates are from Palindri and Kharaka (2004) at pH = 6, 25 °C in mol m^{-2} s^{-1}.

In general, dissolution of silicate minerals involves consumption of CO_2 and release of cations (Ca^{2+}, Mg^{2+}, Na^{+}, and K^{+}) and bicarbonate ions (HCO_3^-). Figure 2.2 shows typical mineral reactions for simple carbonate and silicate minerals. Over geological time scales, these cations enter the sea. As a fate, they can (i) precipitate as minerals, such as $CaCO_3$, which sequesters carbon in mineral form; (ii) exchange with other elements in submarine basalts; (iii) undergo chemical reactions during the diagenesis and alteration of sedimentary minerals on the seafloor; or (iv) precipitate in the form of evaporites (Hartmann et al., 2013, and references therein). Based on stoichiometry of the above reaction, it follows that the rate of reaction, r, can be expressed as

$$r = -\frac{d\left[\mathrm{A}_{\nu_\mathrm{A}}\mathrm{B}_{\nu_\mathrm{B}}\right]}{dt} = \frac{1}{\nu_\mathrm{A}}\frac{d\left[\mathrm{A}_{\nu_\mathrm{A}}\right]}{dt} = \frac{1}{\nu_\mathrm{B}}\frac{d[\mathrm{B}_{\nu_\mathrm{B}}]}{dt} \tag{2.2}$$

where $[i]$ is the concentration of species i. Mineral dissolution rates are usually normalized to the surface area of the material and are expressed as moles of a given component per unit surface area per unit time (Brantley, 2008). It can be expressed as

$$r = \frac{\mathrm{V_o}}{\nu_\mathrm{B}\, A\, m}\frac{d[\mathrm{B}^{q_\mathrm{B}}]}{dt} \tag{2.3}$$

where $\mathrm{V_o}$ is the volume of solution, A is the specific surface area of the mineral and m is the mass of the mineral. The reaction proceeds via an initial diffusive exchange of protons, and alkalis and alkaline earths between the exposed surface of the mineral and the solution. Therefore, a larger effective surface area of a mineral leads to a greater rate of dissolution.



Carlsberg Fjord, East Greenland
© Minik Thorleif Rosing

Chapter 3

Geochemical characteristics of Greenlandic Glacial Rock Flour

Abstract

Glacial meltwater annually transports gigatons of sediments carrying clay-sized mineral particles to proglacial environments and the polar oceans. The sedimentary grains are pristine, and therefore, highly reactive. Consequently, they supply nutrients to the coastal areas and enhance primary productivity. Here, we characterize fine-grained 'glacial rock flour' (GRF) sourced from ten deposits in Greenland. Several of the deposits are actively accumulating, whereas others are raised 'fossil' marine deposits following isostatic uplift after glacial retreat.

The GRFs showed a median size range of 2-11 µm and a BET surface area range of 5-20 $m^2 g^{-1}$. The material is dominantly composed of primary igneous and high-grade metamorphic minerals: quartz, K-feldspar, oligoclase, anorthite, biotite, muscovite and amphiboles, with proportions varying in different deposits. The REE and trace element compositions are similar to bedrock in the hinterland glacial catchment, suggesting that the material has experienced negligible chemical weathering. Sm-Nd model ages for the GRFs reflect the age of the basement rocks in the region. The fine-grained size provides a high specific surface area, which means, that with the determined mineralogy, the GRF would be expected to be highly reactive when exposed to aqueous environments.

3.1. INTRODUCTION

As climate warming continues, the accelerated net loss of ice from the GrIS causes increased sediment flux from land to the coastal zone (Hawkings et al., 2015; Overeem et al., 2017; Bendixen et al., 2017, 2019). The ice flows from zones of deposition to zones of ablation, traversing the underlying basement. The base of the ice erodes the supporting rock underneath, becoming a mélange of rock fragments, ice and meltwater that upon meeting produces debris particles. The debris can range in size from building-size boulders to nanoparticles. The fine-grained fraction, here referred to as 'glacial rock flour' (GRF), is carried in suspension by meltwater to the proglacial riparian or lacustrine environments and eventually to the ocean.

GRF is a naturally occurring silicate mineral composite that is particularly plentiful along the margins of the GrIS. Due to its fine grained particle size, the material acts as a colloid in non-saline water and has a long settling time leading to the common moniker of 'glacial milk' for this particular type of suspension (Keller and Reesman, 1963). Finer sediments have a relatively larger specific surface area and therefore, a high surface energy (Kranck, 1973). Such surfaces are usually negatively charged, which allows them to repel neighboring particles and hence, remain in suspension in fresh waters (Hunter and Liss, 1979). When meltwater mixes with seawater, the substantial increase in ionic strength leads to compression of the electrostatic double layer surrounding the particles, causing their aggregation (Maggi, 2005). This process is common in estuarine and coastal environments and is likely to have taken place throughout the Pleistocene glaciation of Greenland as well. Since the onset of the Holocene retreat of the GrIS, Greenland has experienced isostatic uplift and shoreline regression exposing marine deposits GRF. Presently, there are many such raised marine deposits in Greenland and new deposits are actively forming in deltas, where meltwater mixes with seawater. Weathering of pristine basement minerals releases plant nutrients that could sustain increased crop yields if applied in agriculture. The potential for using GRF to increase local, regional or global crop yields makes it pertinent to study the geology of GRF deposits, the physical and geochemical characteristics of the GRF material, and reaction pathways and rates in soil fluids.

Here, we present the mineralogy, chemical composition and particle size of ten rock flour deposits from Greenland to understand their weathering potential. We compare the variability of major and trace element compositions, including rare earth elements, within and between the GRF deposits to examine whether the material is generic and to evaluate its impacts in the environment.

3.2. Study Areas

GRF samples for this study were derived from sedimentary sequences from the Proterozoic Nagssugtoqidian province of central West Greenland, the Archean Block of the Nuuk region in southern West Greenland, the Proterozoic Ketilidian Province in South Greenland and finally, from the Late Archean alkaline Skjoldungen igneous province of Southeast Greenland.

The Proterozoic Nagssugtoqidian mobile belt transects and defines the northern boundary of the E-W trending Archean Block in West Greenland. It is characterized by reworked Archean gneisses intercalated with minor juvenile Proterozoic igneous components and is dominated by granulite to amphibolite facies granodioritic to quartz-dioritic felsic gneisses. The belt is divided into three metamorphic zones: southern, central and northern Nagssutoqidian Orogen. The belt was a result of continental collision between two crustal blocks of Archean age based on predominance of Archean gneisses in the southern and the northern zone (Nutman, Kalsbeek and Friend, 2008). The central zone, however, consists of rocks of Archean and Paleoproterozoic age. It consists of the juvenile Paleoproterozoic (~1.92 Ga) Sisimiut charnockite suite of calc-alkaline intrusions, which are seen as evidence for inter-continental collision model (Kalsbeek and Nutman, 1996; Whitehouse et al., 1998; van Gool et al., 2002). A sediment core from a site near the southern margin of this complex, Amerloq (66° 54.167N 53°16.818W) at 536 m water depth, was analyzed in this study. The cores were bulging shortly after recovery from the site and were rich in a flammable gas (Naja Mikkelsen, personal communication). They show episodic units of sandy turbidites and fine-grained partly bioturbated muds. Another GRF sample was obtained from the Kangerlussuaq fjord, which receives meltwater from two major river systems, the Watson River (Akuliarusiarsuup Kuua river) and the Ørkendalen river (Figure 3.1a).

The Nuuk region is part of the extensive North Atlantic craton in southern West Greenland, which has been subjected to recrystallization during multiple events of amphibolite to granulite facies metamorphism (e.g. McGregor 1973; Nutman et al., 2004, 2007). The Nuuk region consists of several terranes of Eo- to Neoarchean age. These contain amphibolite to granulite facies tonalite-trondhjemite-granodiorite gneisses with significant components of granite, metasedimentary rocks, metabasalts and ultramafic lithologies (Friend and Nutman, 2005; Windley and Garde, 2009). The complex is divided into two terranes: the Færingehavn terrane in the central and southern part of the Nuuk region, and the Isukasia terrane in the north. The Færingehavn terrane was subjected to early Archean high-grade metamorphism followed by intrusions of Paleoarchean basic Ameralik dykes (McGregor and Mason, 1977; Griffin et al., 1980; Nutman et al., 1989). It underwent further events of metamorphism in the Meso- and Neoarchean and therefore, is much more deformed than the Isukasia. North of the Nuuk fjord lies the Paleo- to Mesoarchean Akia terrane which consists of a ~3.22 Ga dioritic core and enclaves of 3.03-2.97 Ga tonalitic orthogneiss, leucogabbros and mafic volcanic rocks. The Akia terrane was affected by granulite-facies metamorphism at ~3 Ga (Garde, 1997, 2007). In this study, the Nuuk region is represented by seven samples from Ameralik fjord and samples from four sites in the Nuup Kangerlua fjord, i.e. Maalutu, SON, Tasesuaq and Ilulialik. The Maalutu and SON GRF deposit sites are in the Akia terrane (Figure 3.1b).

To the south of the Archaean block lies the Ketilidian mobile belt consisting juvenile early Proterozoic (2-1.75 Ga) gneisses, granites and supracrustal rocks overlain by sediments and volcanic rocks. The region is described in terms of several zones that progressively become strongly deformed and metamorphosed towards the south (Windley, 1991; Chadwick and Garde, 1996). Chadwick and Garde (1996) explain that the Ketilidian Orogen resulted from an oblique convergence between the North Atlantic craton and an oceanic plate that was subducting from the south. The margin experienced back arc extension and several granitic intrusions and lies adjacent to the Julianehåb batholith, a calc-alkaline complex that was emplaced into the Archean craton around 1.8 Ga. Bredefjord and Igaliku (Figure 3.1c) receive meltwater derived from this suite of granitic and granodioritic rocks. To the inner part of the Igaliku fjord lies the alkaline Gardar igneous province (1.3-1.12 Ga), which has significant components of LILE enriched undersaturated rocks including nepheline syenites, carbonatites

and lamprophyres. Sediment core samples were obtained in Bredefjord (60° 48.465N 46° 46.519W) using a gravity corer as part of the third Galathea expedition (Galathea 3) (Mikkelsen et al., 2006). Bredefjord is dominated by turbidite sedimentation and receives meltwater from the adjacent GrIS margin. The sediment cores have a 2-5 cm bioturbated unit containing calcareous benthic foraminifera at the top, followed by a 10-150 cm fining-upward unit devoid of microfossils (Nørgaard-Pedersen and Mikkelsen, 2009). In this study, a fjord-proximal core Ga3-11 at 650 m water depth was examined. Igaliku is a raised marine deposit like Maalutu and SON and is located in the main agricultural area in South Greenland. Unlike its Nuuk fjord counterparts, Ilulialik has been formerly tilled and cultivated (Weber et al., 2020).

The Skjoldungen province of Southeast Greenland (Figure 3.1d) is underlain by Late Archean (~2.8 Ga) felsic gneiss basement that has been intruded by a large number of syn- to post-tectonic (~2.7 Ga) alkaline intrusions including hornblendites, diorites, monzonites, syenites and nephelinitic rocks and carbonatites (Rosing et al., 1988; Nielsen and Rosing, 1990; Nutman and Rosing, 1994; Blichert-Toft et al., 1995). A sediment core sample was obtained from a lake in the alkaline province. The rocks are characterized by high potassium and phosphate content.

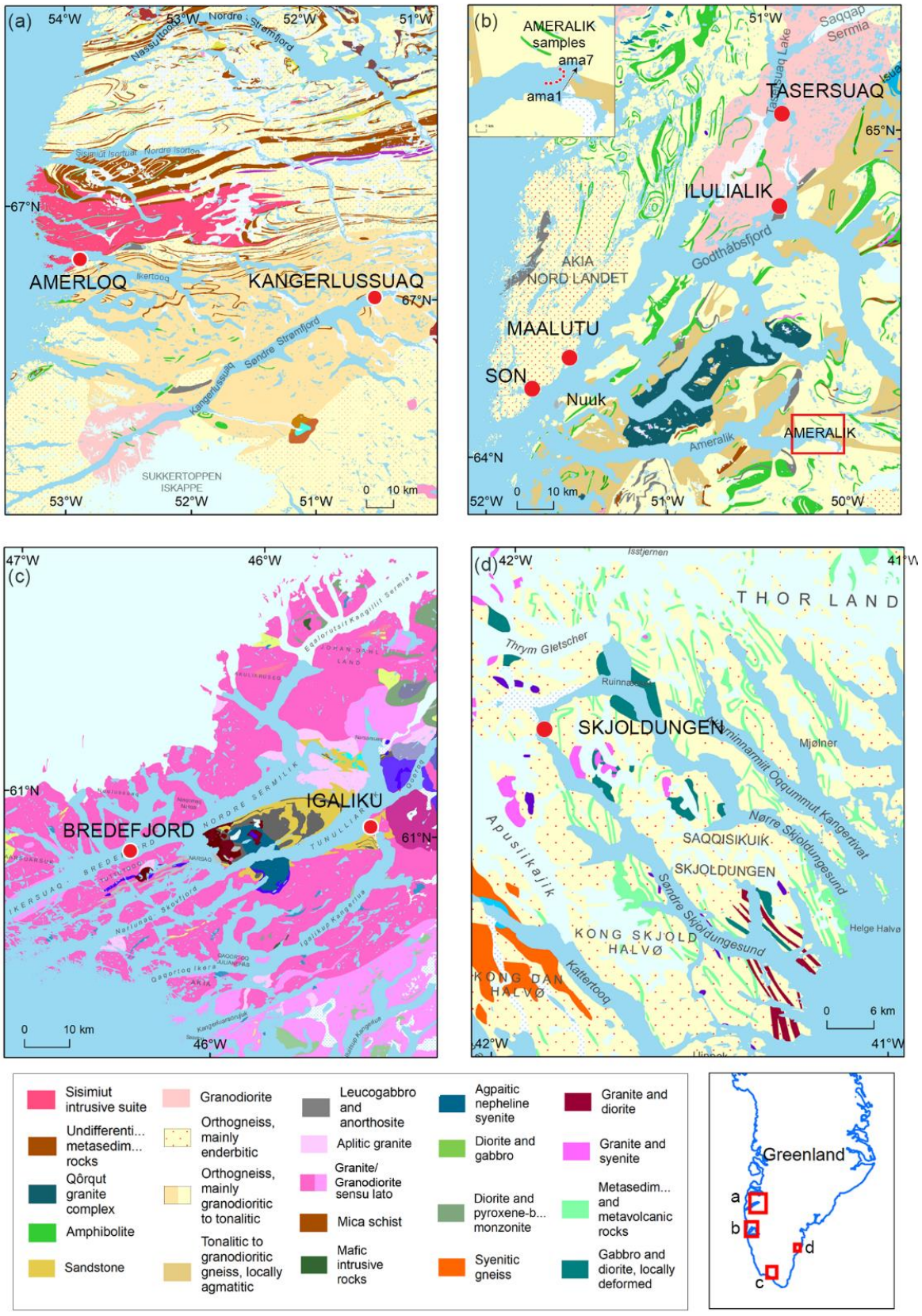


Figure 3.1: Geological Map of Greenland showing sampling locations (red filled circles) and their regional geology: (a) Kangerlussuaq region, (b) Nuuk fjord region and Ameralik fjord (inset map showing Ameralla site), (c) Southern West Greenland, (d) Skjoldungen.

3.3. SAMPLES AND ANALYTICAL PROCEDURES

3.3.1. SAMPLE PREPARATION

All raw GRF samples were dried at 60 °C overnight and were prepared for further analysis. The drying temperature was kept at 60 °C to avoid minerals from losing water of crystallization, if any, upon heating. A washing treatment was done for one marine sample, Ilulialik, to remove soluble salts derived from marine porewater. Both the unwashed (raw) and washed Ilulialik samples were investigated to study the effect of washing on its geochemistry and grain size distribution. No other marine samples were washed and were studied as they were sampled. The detailed procedure for washing of the sample is given in Box 3.1. There was a mass loss of ~10 % during the preparation of washed Ilulialik sample (ILU/W-21 and ILU-B5). The washing cycle was terminated after the third rinse when the electrical conductivity of the supernatant solution was comparable to that of terrestrial, raised marine GRF deposits, such as Maalutu, at the same GRF to DI water ratio.

Box 3.1

Following steps were followed to wash and remove soluble salts for the Ilulialik marine GRF sample:

1. 2 g of GRF was washed in 45 mL deionized (DI) water at 5 °C for 1 hour in 50 mL centrifuge tubes.
2. After washing, these were centrifuged at 8700 rpm for 1 hour.
3. The supernatant was then carefully extracted using pipettes ensuring no disturbance to the settled GRF pellet.
4. After centrifugation, the pellet was re-suspended by hand-shaking and the washing process was repeated 3 times.
5. The electrical conductivity was measured for each supernatant fluid and results from one such batch for Ilulialik GRF are as follows:

   After 1st rinse: 1778.83 ± 25.39 µS cm^{-1}
   After 2nd rinse: 152 ± 7.56 µS cm^{-1}
   After 3rd rinse: 23.44 ± 2.73 µS cm^{-1}
6. The resulting filtrate was then dried in the oven at 60 °C overnight and was labelled as washed Ilulialik GRF sample.

Since the GRF material was in the form of aggregates, it was gently disaggregated using the back of the sieve brush or by hand and was sieved through 2 mm. In case of larger cobble-sized aggregates that were strongly held, hammer was used to obtain smaller and weaker

aggregates. No particles were discarded in the process but visible organic materials, such as shells and twigs, were manually removed from the samples with the help of tweezers. In all cases, with the exception of pre-washed Ilulialik, small amounts of fine-grained organic materials could have remained undetected. GRFs from a total of 10 active and raised marine deposits, and sediment cores were investigated in this study. These samples are subdivided into four groups based on the geological region of their occurrence: Nuuk fjord region, Western Greenland, Ameralik fjord, and Southern and South-Eastern Greenland. GRF samples were selected based on their depositional environment for each analytical measurements to study and compare their physical and chemical properties. Table 3.1 lists all the samples and the analyses corresponding to each sample.

Table 3.1: List of glacial rock flour samples investigated in this study and the analyses corresponding to each sample.

Sample site	PM	LD	BET	XRD	SEM	AQM	Major, trace & REE	Sr-Nd Isotopes
Nuuk fjord region								
MAL-01	●	●	●	●	●	●	●	●
MAL-02	●							
MAL 2-10							●	
MAL 2-11							●	
SON-1	●	●	●	●		●	●	●
SON-190003	●	●	●				●	
SON-190004	●	●	●				●	
SON-190005	●	●					●	
SON-190006	●	●					●	
SON-190007	●	●					●	
ILU 3-1							●	
ILU 3-2							●	
ILU 3-3							●	
ILU/U-01	●		●	●		●	●	●
ILU/U-02	●							
ILU/W-21	●		●	●	●	●	●	
TSQ-01	●	●	●	●		●	●	●
TSQ-02	●							
Ameralik								
AMA-1	●		●				●	
AMA-2	●		●				●	
AMA-3				●			●	
AMA-4							●	
AMA-5	●		●				●	
AMA-6							●	
AMA-7	●		●	●			●	
Kangelussuaq region								
AMQ-1	●						●	
AMQ-2	●	●	●	●		●	●	●
KLS-01	●	●	●	●			●	●
Julienhåb bugt region								
BRED-1	●						●	
BRED-2	●	●	●	●		●	●	●
IGA-1	●						●	
IGA-2	●		●	●			●	●
Skjoldungen								
SKJ-1	●	●	●				●	
SKJ-2	●		●				●	
SKJ-3	●		●	●		●	●	●

For some analytical techniques, only selected samples were analyzed that were roughly representative of each study area. PM = Texture analysis by pipette method; LD = Wet laser diffraction analysis; BET = Brunauer, Emmett and Teller- for specific surface area; SEM= Scanning electron microscopy; AQM = Automated Quantitative Mineralogy using SEM. Details of the analytical procedures are given in Section 3.3.

MAL = Maalutu; SON = South of Nuuk; ILU = Ilulialik; TSQ = Tasersuaq; AMA = Ameralik Fjord; AMQ = Amerloq Fjord; KLS = Kangerlussuaq Fjord; BRED = Bredefjord; IGA = Igaliku; SKJ = Skjoldungen

3.3.2. PARTICLE ANALYSIS

3.3.2.1. Particle size analysis - Pipette method

A representative sample was obtained from each bulk GRF samples by cone and quartering method. Samples were sieved through 2 mm and were sent to Agrolab in Germany for texture analysis. As a first step towards the analysis, the amount of organic substances, such as humus, in a GRF sample was measured by dry combustion of the sample and were removed by oxidation with H_2O_2 (after DIN EN 15936 : 2012-11). The latter was done irrespective of the organic content previously determined. The material texture was determined for the remaining sample by pipette method (DIN ISO 11277 : 2002-08): wet-sieving (for sand fractions) and sedimentation (for <63 µm). Pyrophosphate was used as a dispersant. The finer fraction was suspended in a water bath and was let to stand for several hours to equilibrate. The suspension was then thoroughly stirred using an up and down motion. Using the Stokes' law, the settling times for the silt and clay fractions were calculated from the time stirring was stopped. After the appropriate time interval, the required sample fraction was carefully withdrawn from the water bath using a pipette. The respective fractions were weighed after drying the clay suspension at 105 °C and cooling in a desiccator.

3.3.2.2. Particle size analysis - Laser diffraction

The volume-based particle size distribution (PSD) for GRF samples was analyzed in water suspension by laser diffraction using a Mastersizer 2000 laser diffractometer from Malvern Instruments with a Hydro 2000G dispersant unit. It involves PSD measurement by analyzing the angular intensity of the light scattered as a laser beam interacts with a dilute dispersion of particles. The dry GRF sample was added in small amounts to deionized water as dispersant until the obscuration range was reached. Due to fine size (<50 µm) of the material, a low obscuration range of 5-10% was maintained to avoid multiple scattering. Sodium

hexametaphosphate was added to the DI water to assist dispersion of particles. In addition, the ultrasonic power of the instrument was also turned to 100% to avoid particles from aggregating and settling. In the calculation of size from diffraction data, it is assumed that particles are spherical and that they reflect light with similar efficiency. Since GRF is a heterogeneous mineral composite, these assumptions most likely introduce errors in results. Thus, the data were examined primarily for a qualitative comparison of the different GRFs.

3.3.2.3. Specific surface area

Specific surface areas were determined for the GRFs at the Geological Survey of Denmark and Greenland (GEUS) on a Coulter SA3100 analyzer using nitrogen. The instrument uses the BET (Brunauer, Emmett and Teller) theory, where BET surface area relates to the physical adsorption of a gas on the surface of a solid. The amount of adsorbed gas molecules corresponding to a monomolecular layer on the surface of the particles is used to calculate the specific surface area. Prior to the measurement, the samples were outgassed in dry nitrogen at 80 °C for 1020 minutes to remove any previously adsorbed gases and moisture from the surface of the sample before analysis.

3.3.3. MINERAL COMPOSITION ANALYSES

The chemical composition in mineral grains of GRFs were determined by scanning electron microscopy with energy dispersive spectroscopy (SEM-EDS) as well as automated quantitative mineralogy using SEM (AQM-SEM), and X-ray diffraction (XRD). SEM-EDS and AQM-SEM were performed for selected GRF samples at the University of Copenhagen and GEUS, respectively, to characterize grain morphology with no crushing of the particles.

3.3.3.1. X-Ray Diffraction

Samples for XRD analysis were crushed using mortar and pestle to attain clay-sized consistency for the entire sample. These were then sent to X-ray diffraction laboratory at Department of Geosciences and Nature Resource Management (IGN), University of Copenhagen. XRD measurements for mineral identification and compositional parameters were conducted using a Bruker-AXS D8 Advance diffractometer equipped with a Cu X-ray tube, a primary beam Ge111 monochromator (wavelength 1.54059 Å) and a silicon-strip LynxEye detector with 3.3° opening. The measurements were made in reflection mode, Bragg-Brentano technique, with fixed divergence of the primary beam (0.3°). They were carried out

within the scattering angles (2θ) ranging from 5° to 80° at a step of 0.02° per minute. Quantitative analysis of the powder X-Ray Diffraction data was conducted with Rietveld refinement (Rietveld, 1969; Young, 1993) using the program Topas version VI (Bruker-AXS). In the calculations, the scale factors, unit cell parameters and the preferred orientation parameters (for minerals with expressed cleavage) were refined. The starting crystal structure data for the minerals were taken from the ICSD database (FIZ, 2020).

3.3.3.2. Scanning Electron Microscopy

Regular Scanning Electron Microscopy (SEM) were performed on samples from Maalutu and Ilulialik to determine grain morphology and texture. The material was transferred to carbon tape that had been mounted on Al sample stubs and the samples were coated with approximately 10 nm Au. Secondary electron imaging was performed on a FEI Quanta 3D FEG SEM using an accelerating voltage of 20 keV and, typically, a current of 7.5 or 15 pA. The interaction between the incident electrons with the surface of the sample produce backscattered electrons (BSE), secondary electrons and X-rays that yield information about their topographic features (such as size, shape and texture), crystal structure and composition of the sample.

3.3.3.3. Automated Quantitative Mineralogy (AQM) using SEM

About 0.5-1.0 g dry sample was mounted in epoxy such that the grains were evenly distributed with respect to their grain size and density. The epoxy mounts were polished and coated with 15 nm carbon to minimize charging. The polished mounts were studied with a Zeiss SIGMA 300VP SEM, equipped with two Bruker XFlash 6|30 energy-dispersive spectroscopy detectors (EDX), set to 129 eV energy resolution, and with the Zeiss Mineralogic automated quantitative mineralogy software platform. A detailed description of the software and the analytical method is given in Keulen et al. (2020). The entire sample, or a major part of it, and a high resolution representative section of the sample were selected and imaged to provide a BSE contrast mosaic. In addition, on this region of interest, a quantitative mineralogical analysis (AQM) was carried out using the program Mineralogic to create a mineral map overlying the BSE image.

The acceleration voltage of the primary electron beam was reduced to 10 kV to reduce the interaction volume and therefore to minimize the amount of mixed pixel data, and the 60-µm

aperture providing a 1.8-nA beam current was used. Despite this reduction of primary electron energy to 10 kV, the interaction volume still had a diameter of up to approximately 1 µm for minerals with the lowest average atomic number (Z) and down to 400 nm for a high Z phase topographically on top of a low Z phase (Graham and Keulen, 2019). Despite the size of the interaction volume, a 200-nm EDX pixel size is feasible for analysis, for the following reasons: 1) the Mineralogic software platform provides full access to the EDX data for each pixel in the mineral map. In the Mineralogic mineral library mixed signals could be deconvoluted to provide a reliable quantitative mineralogy and textural assessment. This enabled the creation of highly discriminatory mineral classifications in the mineral library whereby "contamination" of the chemical analysis provided by the mixed signals were able to be identified and factored into the mineral classification (Graham & Keulen, 2019). This capability and deconvolution procedure allowed the creation of true mineral classifications without the risk of creating false mixed signal classifications. 2) Monte Carlo simulations show that at the chosen analytical conditions at least 50 % of the EDX signal comes from the 200 nm central sample surface area (Graham and Keulen, 2019). The mineral classifications can, therefore, be used on particles down to 200 nm, even though the interaction volume of the beam was larger than 200 nm. Thus, the obtained resolution of the analysis is 200 nm, while the applied pixel size for the mineral maps of the detailed sections is 500 nm.

3.3.4. GEOCHEMICAL ANALYSES

3.3.4.1. Major and trace element analyses

Geochemical analysis of the GRFs required the samples to be crushed <80 µm. Since most of the particles were fine-grained, the larger grains were crushed for the entire sample to pass through 50-µm sieve. The analyses was performed at *Centre de Recherches Pétrographique et Géochimiques* (CNRS) in Paris in *Service d'Analyse des Roches et des Minéraux* (SARM).

Powdered samples (300 mg) were fused in Pt crucibles with $LiBO_2$ at 980 °C in an automatic tunnel oven. After cooling to room temperature, they were dissolved in a mixture of HNO_3-H_2O_2-glycerol. While H_2O_2 was added to stabilize elements such as Ti and other HFSEs, glycerol was added to lubricate the sample introduction system and the nebulizer of the ICP-MS system. Major elements, expressed in oxides, were analyzed by emission spectrometry (ICP-OES) using a Thermo Fischer iCap6500. Trace element analyses were done by flow injection

inductively coupled plasma mass spectrometry (FI-ICP-MS) using techniques described in Carignan et al. (2001). A multi-element doped solution of the reference material BR (alkali basalt) was used to calibrate the Sciex Perkin Elmer ELAN 5000a quadrupole mass spectrometer. Rare earth element (REE) contents were measured by an automatic on-line, low pressure liquid chromatography (LC-ICPMS) sample introduction system using a Sciex Perkin Elmer ELAN 6000 instrument.

Degree of weathering

The degree of diagenetic alteration can be described by weathering indices, which rely upon molar concentration of elements that are considered leachable during diagenesis and of elements that are considered immobile, such as Chemical Index of Alteration (CIA; Nesbitt and Young, 1982) and Chemical Index of Weathering (CIW; Harnois, 1988). CIA and CIW were calculated for GRFs in molecular proportions using the following equations:

$$CIW = \frac{Al_2O_3}{Al_2O_3 + CaO^* + Na_2O} \times 100 \quad (3.1)$$

$$CIA = \frac{Al_2O_3}{Al_2O_3 + CaO^* + Na_2O + K_2O} \times 100 \quad (3.2)$$

CaO* was CaO corrected for phosphate using P_2O_5 and if molar CaO* was higher than molar Na_2O, CaO* was assumed equivalent to Na_2O (McLennan, et al., 1993). During weathering, K^+ leached into solution can be retained in the secondary solid phases such as clay minerals that tend to adsorb K, and therefore, CIW excludes K_2O. However, CIA includes K_2O along with CaO and Na_2O as mobile components as it indicates alteration of the primary mineral.

3.3.4.2. Isotope analyses

For analysis of Sr and Nd isotopes, about 100-200 mg of the powdered GRF samples were placed into a 15 mL Savillex beakers and were digested using a mixture of sub-boiled conc. HNO_3 and HF in the ratio of 4:1. The solution was heated at 115 °C for 24-48 h. After acid evaporation, the beakers were re filled with conc. HCl and heated for another 24 h until complete digestion of the samples indicated by a clear solution. For Sr and Nd isolation, the

samples were then diluted with 2 M HNO_3. The protocol followed a chromatographic separation of Sr and Nd, similar to Pin and Zalduegi (1997). An additional step was applied for further isolation of Nd from Sm using Ln spec resin following the chemistry described by Pin and Zalduegi (1997).

The purified Sr samples were analyzed using a TIMS (Triton Plus from Thermo) operated in multicollection mode and Nd isotopes were measured using MC-ICP-MS (Neptune+ from Thermo). $^{86}Sr/^{88}Sr$ and $^{146}Nd/^{144}Nd$ were normalized to 0.1194 and 0.7219, respectively, to correct for instrumental mass bias. To control the method accuracy for Sr measurements, NBS 987 was measured while in case of Nd, JNdi was measured to control the method accuracy. The average concentration of blanks for Sr (~300 pg) and Nd (~100 pg) were always negligible with respect to that of the samples.

3.4. RESULTS

3.4.1. PHYSICAL PROPERTIES OF GRF

3.4.1.1. Particle size distribution

Dry GRF has a talc powder-like floury consistency whereas moist GRF tend to form aggregates while drying. These coarse particle aggregates can be broken by sonication in water, or by gentle mechanical disaggregation by mortar and pestle. The particle size distribution (PSD) of the disaggregated material was determined using two methods: a pipette method (PM) using sedimentation and wet sieving, and wet laser diffraction (LD) using the angular intensity of the scattered light as a laser beam interacts with a dilute dispersion of particles.

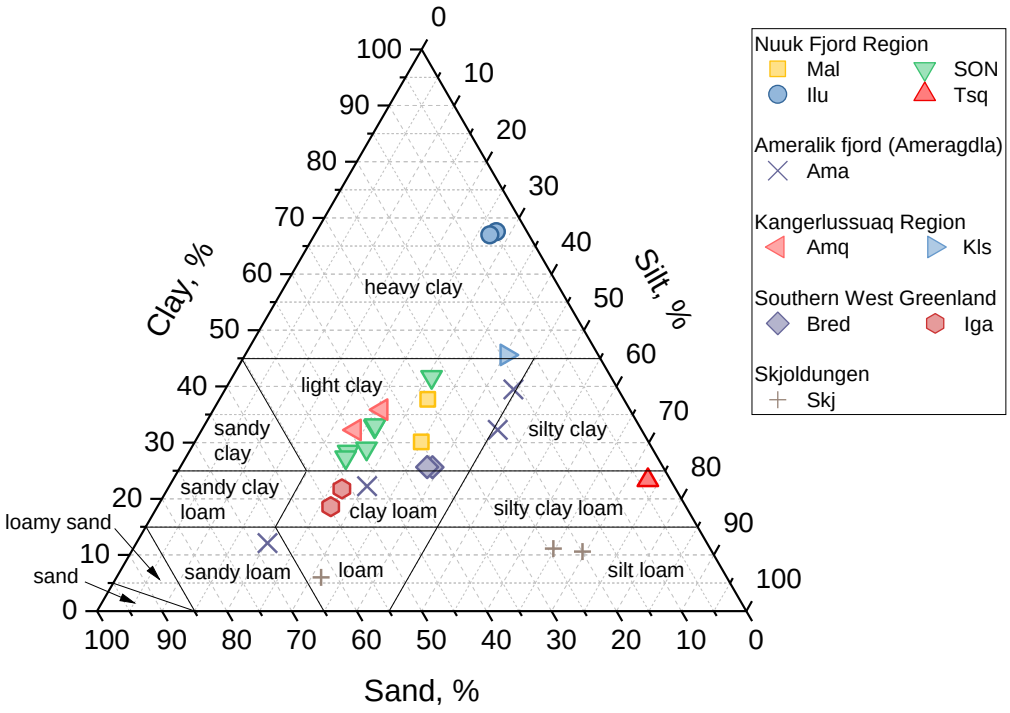


Figure 3.4.12: Distribution of glacial rock flours from Greenland in International Soil Science Society (ISSS) textural classes.

Based on the PM, the GRFs investigated in this study were predominantly silt and clay textured with ~55-75 % of the mass made up of particles <20 µm (Table 3.2). Majority of the GRFs occupied the light clay and clay loam textural classes in International Soil Science Society (ISSS) classification system.

Table 3.2 provides the BET specific surface areas of GRF as well as Portland cement and fly ash for comparison with GRF. It ranged from 3.9 to 19.6 $m^2 g^{-1}$ for the GRFs investigated in this study. Ilulialik GRF exhibited the maximum BET surface area and has the lowest median size based on LD. However, the median size of a GRF material was not proportional to its specific surface area. For example, GRFs from both Lake Tasersuaq and Skjoldungen were unimodal in PSD but they correspond to a much lower value in BET surface area, in comparison to the rest of the GRFs. A repeated BET analysis for Lake Tasersuaq at outgassing temperature of 120 °C returned 4.5 $m^2 g^{-1}$, similar to the value at the outgassing temperature of 100 °C.

Figure 3.3 illustrates the difference in PSD among the GRFs based on LD, categorizing them into two groups: a) Unimodal grain size distribution GRFs, such as Ilulialik, and b) Bimodal

grain size distribution GRFs, such as Maalutu. LD measurements assume that the GRF particles are to be spheres, which is an unlikely case for mineral particles. A platy mica grain, for example, if measured at the longer edge would lead to an overestimation on a higher grain size and vice versa. This limited us from extending the particle size comparison based on LD quantitatively. Nevertheless, LD suggests a median size range of 2.5-17 μm for the GRFs in this study, indicating they were medium to very fine silts (Table 1.2). This is supported by the results derived from PM.

Table 3.2: Particle size distribution and BET-N2 specific surface areas of glacial rock flours from Greenland.

Sample site	Lat.	Long.	Elevation (m)	Depth (cm)	Organic matter / Humus	Clay % (<2 µm)	Silt % (2–20 µm)	Fine sand % (20–200 µm)	Coarse sand % (0.2-2 mm)	BET-N_2 ($m^2 g^{-1}$)	d_{10} (µm)	d_{50} (µm)	d_{90} (µm)	Sample ID
Nuuk Fjord Region														
Maalutu (Mal)	64.28°N	51.72°W			<0.1	30.1	34.9	32.6	2.4	15	0.98	7.86	53.60	MAL-01
Mal	64.28°N	51.72°W			<0.1	37.7	32.1	27.9	2.3	-	-	-	-	MAL-02
South of Nuuk (SON)	64.21°N	51.9°W			<0.1	28.4	24.5	45.7	1.4	11.4	1.09	11.56	72.92	SON-1
SON	64.21°N	51.9°W			<0.1	41.7	30.7	27.4	0.2	-	0.84	4.50	35.23	SON-190003
SON	64.21°N	51.9°W			<0.1	27.4	24.6	46.9	1.1	-	1.26	13.56	95.00	SON-190004
SON	64.21°N	51.9°W			<0.1	29.7	26.8	42.8	0.8	-	1.14	11.47	80.81	SON-190005
SON	64.21°N	51.9°W			<0.1	32.9	26.3	39.6	1.2	-	1.08	9.19	63.75	SON-190006
SON	64.21°N	51.9°W			<0.1	33.1	26.3	39.7	0.9	-	1.04	11.71	70.98	SON-190007
Ilulialik (Ilu) (unwashed)	64.76°N	50.66°W			0.2	67.4	27.7	4.2	0.5	19.6	0.71	2.61	9.37	ILU/U-01
Ilu (unwashed)	64.76°N	50.66°W			0.2	66.9	27.0	5.3	0.7	-	-	-	-	ILU/U-02
Ilu (washed)	64.76°N	50.66°W			0.2	-	-	-	-	-	-	-	-	ILU/W-21
Tasersuaq (Tsq)	65°N	50.8°W			<0.1	23.5	76.5	<0.1	<0.1	5.3	1.27	5.36	15.01	TSQ-01
Tsq	65°N	50.8°W			<0.1	23.3	73.2	3.4	0.1	-	-	-	-	TSQ-02
Mean					<0.1	36.8	35.9	28.7	1.1	-	1.0	8.6	55.2	
Min					<0.1	23.3	24.5	3.4	0.1	-	0.7	2.6	9.4	

Max					0.2	67.4	76.5	46.9	2.4	-	1.3	13.6	95.0	
σ					-	14.5	17.7	16.1	0.7	-	0.2	3.6	27.9	
Ameralik Fjord (Ameragdla)														
Ameralik (Ama)					0.1	12.1	20.2	67.3	0.4	-				AMA-1
Ama					0.2	22.2	30.4	46.3	0.9	-				AMA-2
Ama						-	-	-	-	11	1.07	6.84	30.78	AMA-4
Ama					0.2	32.2	45.5	21.7	0.4	-	-	-	-	AMA-5
Ama					0.2	39.4	44.3	15.7	0.4	-	-	-	-	AMA-7
Mean					0.2	26.5	35.1	37.8	0.5	11	1.07	6.84	30.78	
Min					0.1	12.1	20.2	15.7	0.4	-	-	-	-	
Max					0.2	39.4	45.5	67.3	0.9	-	-	-	-	
σ					0.0	10.3	10.5	20.6	0.2	-	-	-	-	
Kangerlussuaq Region														
Amerloq (Amq)	66.88°N	53.32°W		5	4.6	34.2	24.7	36.2	0.3	-	1.72	10.29	33.35	AMQ-1
Amq	66.88°N	53.32°W		70	5.1	30.6	22.4	41.4	0.5	18.8	2.33	17.07	49.24	AMQ-2
Kangerlussuaq (Kls)	66.96°N	50.95°W			0.4	45.4	40.1	13.0	1.1	14.9	0.90	4.73	21.76	KLS-01
Mean					3.4	36.7	29.1	30.2	0.6	16.9	1.7	10.7	34.8	
Min					0.4	30.6	22.4	13.0	0.3	14.9	0.9	4.7	21.8	
Max					5.1	45.4	40.1	41.4	1.1	18.8	2.3	17.1	49.2	
Σ					2.1	6.3	7.9	12.3	0.3	1.9	0.6	5.0	11.3	
Julianehåb Bugt Region														
Bredefjord (Bred)	60.9°N	46.41°W		5	0.4	25.5	38.7	34.5	0.9	-	-	-	-	BRED-1
Bred	60.9°N	46.41°W		72	0.1	25.6	38	36.1	0.2	11.1	1.24	8.86	42.70	BRED-2
Igaliku (Iga)	61.01°N	45.45°W	0.5		<0.1	18.6	26.7	38.3	16.4	-	1.25	15.53	370.05	IGA-1
Iga	61.01°N	45.45°W	5		<0.1	21.8	26.9	38.3	13.2	-	1.34	11.57	300.95	IGA-2
Mean					0.3	22.9	32.6	36.8	7.7	11.1	1.3	12.0	237.9	
Min					<0.1	18.6	26.7	34.5	0.2	-	1.2	8.9	42.7	

Max				0.4	25.6	38.7	38.3	16.4	-	1.3	15.5	370.1	
σ				-	2.9	5.8	1.6	7.2	-	0.0	2.7	140.9	
Skjoldungen Region													
Skjoldungen (Skj)	63.45°N	41.89°W	10	0.1	10.6	69.4	17.3	2.6	-	1.75	9.57	26.28	SKJ-1
Skj	63.45°N	41.89°W	50	0.2	11.1	64.6	18.6	5.5	-	-	-	-	SKJ-2
Skj	63.45°N	41.89°W	130	0.3	6.0	31.4	60.0	2.3	3.9	-	-	-	SKJ-3
Mean				0.2	9.2	55.1	32.0	3.5	3.9	1.75	9.57	26.28	
Min				0.1	6.0	31.4	17.3	2.3	-	-	-	-	
Max				0.3	11.1	69.4	60.0	5.5	-	-	-	-	
σ				0.1	2.3	16.9	19.8	1.4	-	-	-	-	
Portland cement (hydrated for 7 years)									89[a]				
Fly ash									4-21[b]				

Particles in sand fraction were separated by wet-sieving and those in clay and silt-size range were separated by sedimentation (DIN ISO 11277:2002-08) at Agrolab, Germany. Organic matter/humus was calculated from total organic carbon following DIN EN 15936:2012-11 at Agrolab before size distribution analysis. General physical characteristics of Portland cement and fly ash are given for comparison.

MAL = Maalutu; SON = South of Nuuk; ILU = Ilulialik; TSQ = Tasersuaq; AMA = Ameralik Fjord; AMQ = Amerloq Fjord; KLS = Kangerlussuaq Fjord; BRED = Bredefjord; IGA = Igaliku; SKJ = Skjoldungen

d_{10}, d_{50} and d_{90} indicate value of the particle diameter at 10%, 50% and 90% of the cumulative distribution, respectively. The value at d_{50} is also called the median diameter.

[a] Odler, 2003

[b] Wang et al., 2008

- data not available

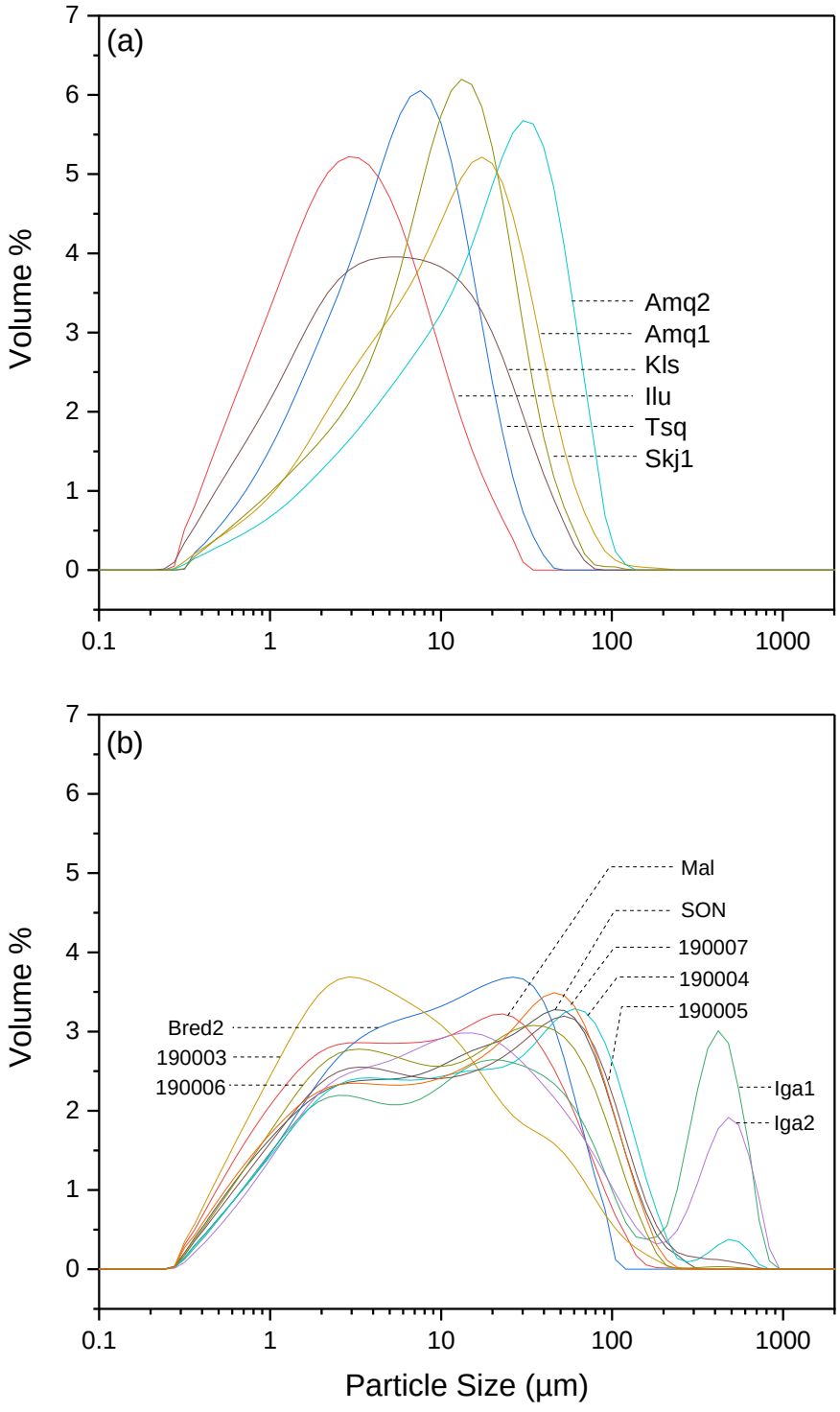


Figure 3.3: Particle size distribution using wet Laser Diffraction (LD-PSD) analysis for GRFs in volume %, showing (a) unimodal and (b) bimodal distribution. The distributions are average of triplicate analysis using Malvern Mastersizer 2000 laser diffractometer.

3.4.1.2. Microscopic features

Microscopic examination was performed for two GRF samples, Maalutu and washed Ilulialik, each representing the bimodal and unimodal LD-PSD, respectively. Both samples reveal the abundance of fine-grained particles in the material (Figure 3.4 and 3.5). The matrix was predominantly composed of platy phyllosilicates that were <1 µm that appeared to have a strong tendency for aggregation. Larger individual grains were blocky and were euhedral to subhedral in shape but often occur covered by the phyllosilicates. The tendency to form aggregates appeared to be lower in the larger particle size of the material. In Maalutu, amorphous materials appear to be more abundant and they blanket the surfaces of the larger feldspars and quartz grains along with phyllosilicates. The Ilulialik GRF was washed to reduce soluble salts of the sample. This step could have removed some of the very fine particles and/or the amorphous material leading to the ~10% mass loss in the material observed after the washing treatment. This might have uncovered the surfaces of larger grains revealing their surface features. Ilulailik grains had sharp edges, whereas Maalutu had softer grain edges. The EDX analyses of some of the larger grains indicate them to be mainly feldspars and quartz. Minerals such as apatite were also identified under SEM as seen in Figure 3.5c.

The abundance of very fine particles can be seen from SEM images of the epoxy mounts of Maalutu and Ilulialik as well. The BSE maps for the two GRFs exhibit a distinct dissimilarity in their PSDs. They demonstrate that while Maalutu has an unsorted mixture of larger and smaller grains, Ilulialik has grains predominantly <5 µm. This suggests a more poorly-sorted grain distribution in Maalutu than in Ilulialik.

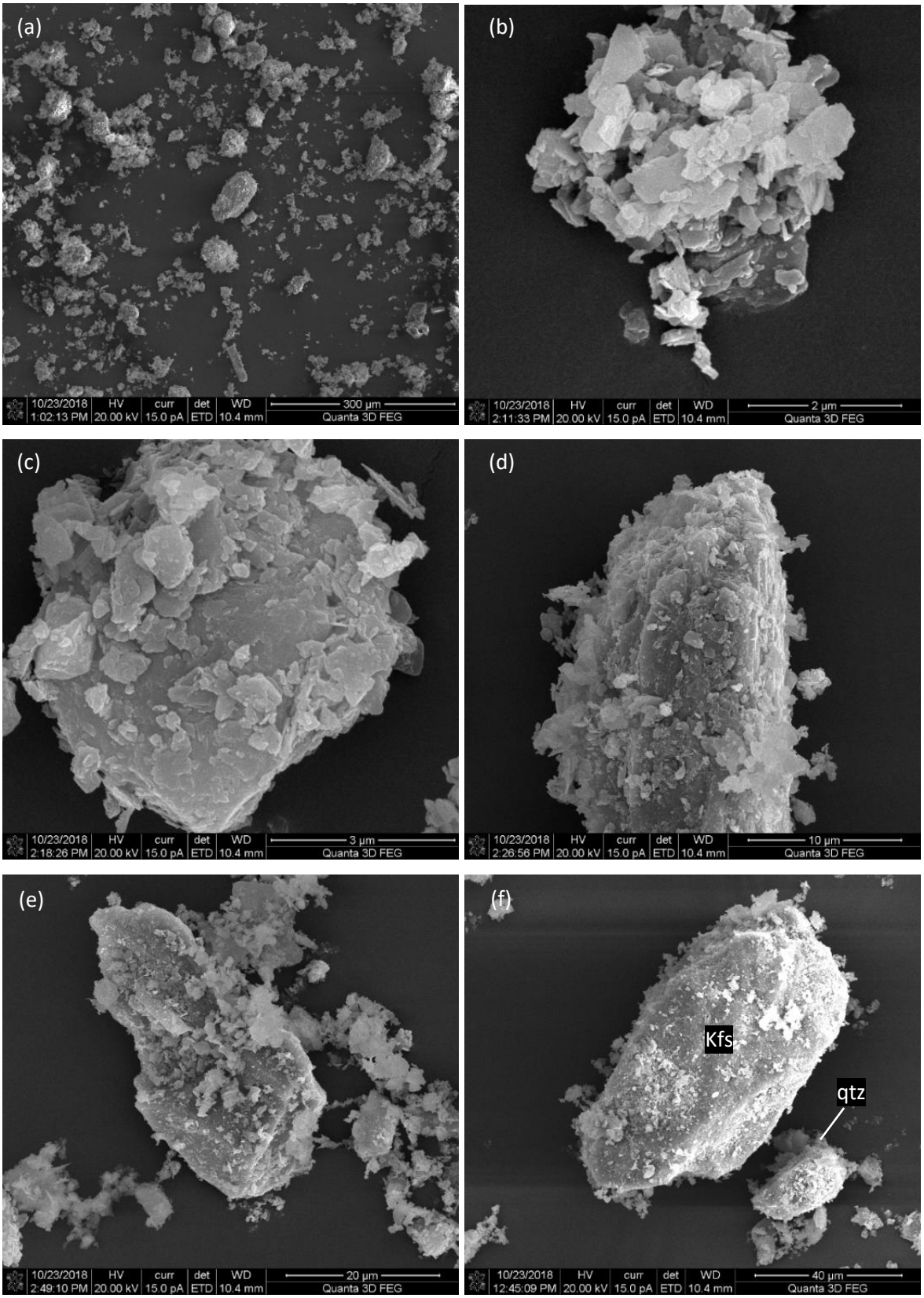


Figure 3.4: SEM images of Maalutu (RF Mal): (a) overall view showing particle size distribution, (b) aggregate of phyllosilicates less than 1 µm, (c, d) mineral aggregates covering the larger mineral grain, (e) finer grains are more aggregated while larger grains occur individually, (f) K-feldspar (larger grain) and quartz (smaller grain)

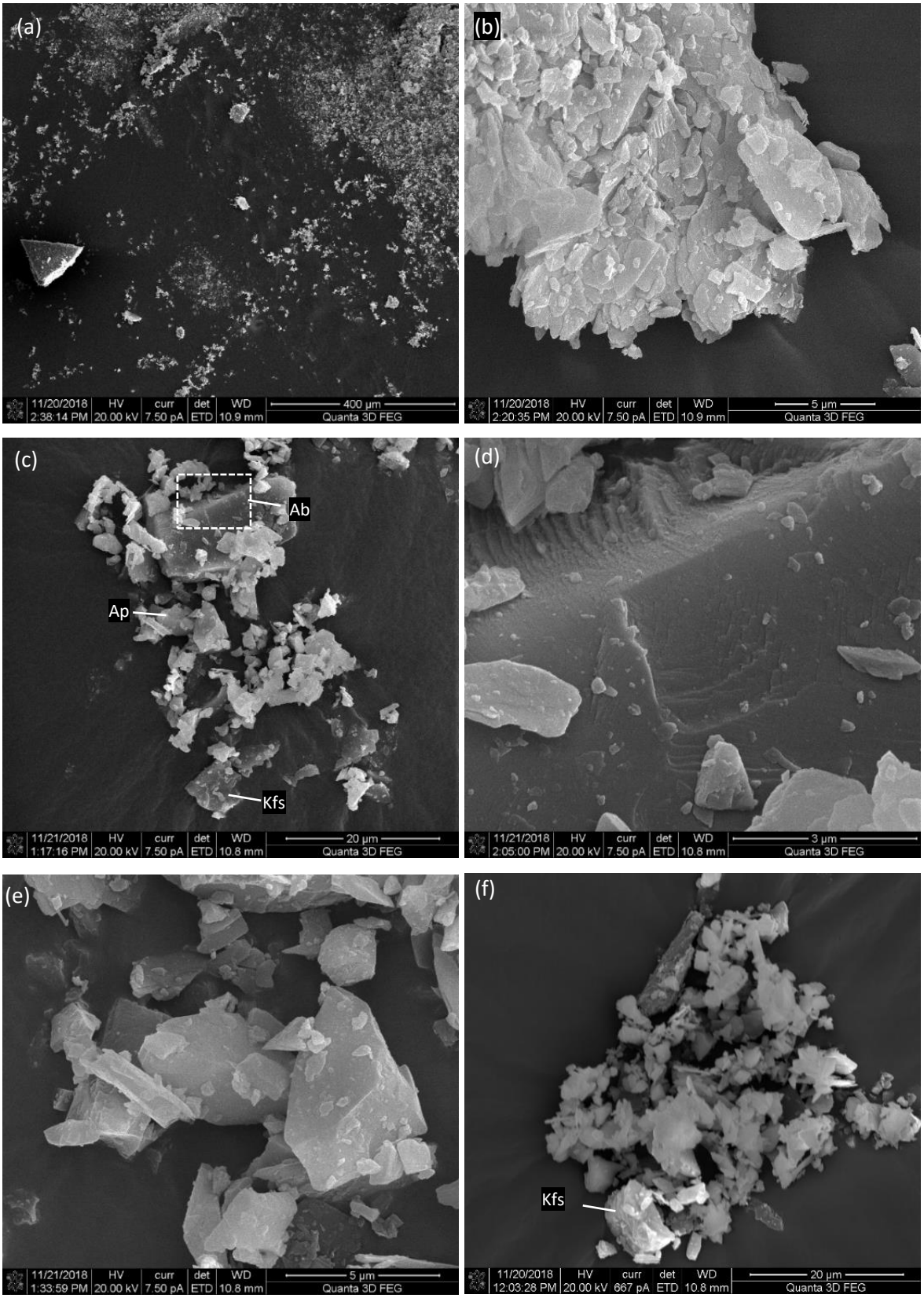


Figure 3.5: SEM images of Ilulialik (Ilu B5): (a) overall view showing grain size distribution, (b) aggregate of fine grained phyllosilicates, (c) mineral aggregates covering a larger albite mineral grain, (d) zoomed view of area from fig. c showing the deformation features on the mineral surface, (e)-(f) aggregates of fine grained and sharp edged mineral grains.

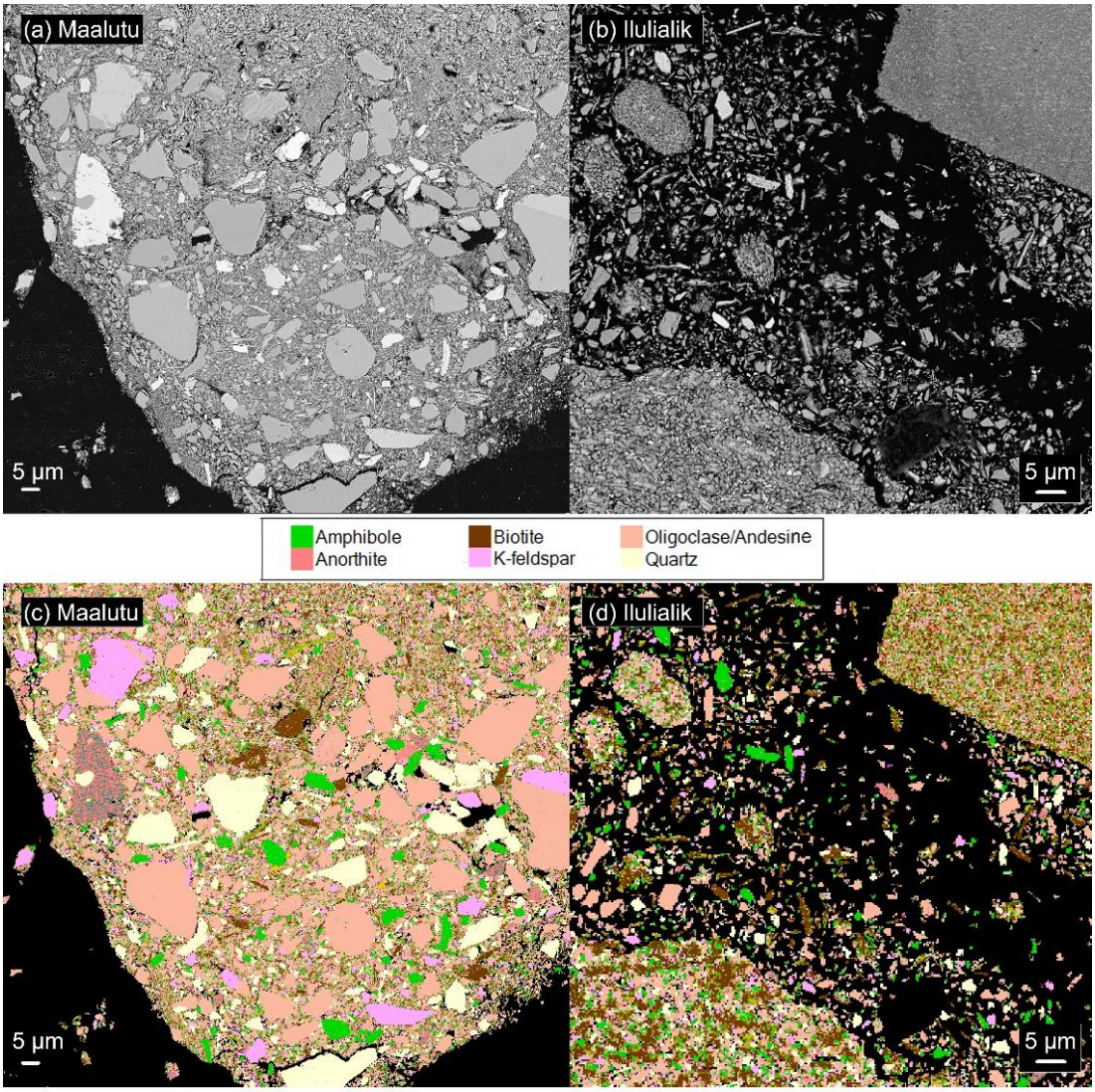


Figure 3.6: Images showing BSE micrograph for (a) Maalutu (RFMal) and (b) Ilulialik (Ilu B5), and mineral maps for (c) Maalutu and (d) Ilulialik. Legend for the mineral map lists only the phases that are present in quantities over 5 %.

3.4.1.3. Mineral composition

Table 3.3 presents the most abundant and some selected minerals in the GRFs in area %. The mineral maps created by the quantitative mineralogical (AQM) analysis were performed on the BSE images of the epoxy mounts of the GRFs. They show that plagioclase feldspars, quartz and biotite occupied the largest area % of the material. The plagioclase in the GRFs was identified as oligoclase/andesine composition. Although anorthite was detected as one of the mineral phases, the assigned composition included elements such as K, Mg and Fe, which is incorrect (Table 3.4). Since the GRFs are very fine-grained materials, the particles <1 µm were rendered as only few pixels in the mineral map. It is possible that the fine nature of the

material gave rise to an incorrect mineral assignment for the very fine particles such as anorthite. Therefore, only dominant mineral phases accounting for ~80 % of the total area were used for comparison in this study. Accessory minerals such as epidote, apatite, titanite, halite etc., which constitute <1 % of the total area of the mineral map section, were determined by AQM analysis. The complete list of minerals identified under AQM for all GRF samples includes 31 minerals altogether and is given in Appendix Table A.1.

Table 3.3: Comparison between most abundant and selected other minerals determined in area % by quantitative mineralogical analysis (AQM) of glacial rock flours from Greenland.

	MAL	SON	ILU	TSQ	BRED	SKJ	Std dev
Quartz	16.65	22.73	9.56	16.21	14.59	13.69	3.95
Anorthite	10.35	8.62	10.74	5.52	6.93	0.99	3.31
K-feldspar	6.84	7.45	2.84	5.94	6.90	21.93	6.13
Oligoclase/Andesine	29.25	29.77	17.65	30.93	23.27	40.82	7.13
Biotite	12.20	8.94	20.14	10.08	7.26	2.60	5.34
Chloritised biotite	2.86	2.03	11.74	2.77	7.79	0.97	3.81
Muscovite	1.53	1.27	1.74	1.68	1.64	1.03	0.25
Amphibole	6.13	5.74	10.50	11.32	7.48	6.79	2.15
Epidote	0.45	0.55	0.13	0.49	0.60	0.19	0.18
Clinochlore	0.19	0.17	1.42	0.74	1.75	0.35	0.61
Apatite	0.05	0.04	0.08	0.13	0.14	0.89	0.30
Calcite	0.02	0.02		0.02	0.21		0.08
Chamosite	0.11	0.08	1.70	0.24	1.49	0.71	0.65
Enstatite	0.03	0.06	0.03	0.04		0.02	0.01
Fe metal	0.01	0.12				0.03	0.05
Fe-Oxide/Hydroxide	0.76	0.67	1.79	1.12	3.06	3.64	1.14

Table 3.4: A representative quantitative mineralogical (AQM) analysis data is presented along with average mineral composition of Maalutu. The composition details of all the minerals determined is given in Appendix Table A.2..

	Area %	Weight %	Grain Size (µm)	Grain Size Std Dev (µm)	Average Composition
Quartz	16.65	18.18	19.98	17.52	Si 52.66; O 39.59; Al 2.7; Fe 2.06; K 0.82; Mg 0.77; Ca 0.73; Na 0.67;
Anorthite	10.35	11.77	15.47	10.13	O 35.77; Si 30.67; Al 12.68; Fe 6.61; Ca 5.51; Mg 3.02; K 2.93; Na 2.8;

K-feldspar	6.84	7.21	15.27	11.56	Si 35.6; O 34.72; K 12.95; Al 11.63; Fe 2.19; Na 1.1; Ca 0.95; Mg 0.86;
Oligoclase/ Andesine	29.25	31.58	26.43	28.63	O 35.86; Si 35.4; Al 13.84; Na 6.2; Ca 3.7; Fe 2.62; K 1.31; Mg 1.07;
Biotite	12.20	15.09	16.90	12.15	Si 33.22; O 32.36; Al 11.86; Fe 10.69; K 6.08; Mg 3.88; Na 1.91;
Chloritised biotite	2.86	3.54	11.33	4.27	O 34.37; Si 29.6; Fe 13.83; Al 11.83; Mg 5.17; K 3; Na 2.2;
Muscovite	1.53	3.05	11.00	4.18	O 38.74; Si 32.72; Al 15.01; K 7.67; Fe 3.4; Mg 2.46;
Amphibole	6.13	7.63	13.79	8.62	O 35.23; Si 29.49; Fe 13.33; Al 8.06; Ca 7.91; Mg 5.99;

The most abundant mineral phases in GRFs determined by XRD were plagioclase, microcline, quartz, biotite, chlorite, amphibole, augite and epidote. Feldspars dominate the mineral composition, constituting >40 % in most of the GRFs, followed by quartz, which ranged from 5.8 % to 36 %. Plagioclase feldspar was found to have approximately 20 % anorthite component, K-feldspar was maximum microcline, biotite had around 25 % annite component. Minor amounts of chlorite, augite and epidote were also detected in the GRFs by XRD. Among all the GRFs, calcite (2.5 %) was detected only in Amerloq GRF by XRD. In general, the mineralogy of the samples determined by XRD were comparable to that by AQM for minerals >1 % by volume. The XRD results reveal roughly an inverse relationship between quartz and biotite area % among the GRFs. Samples from Ilulialik and Ameralik, for example, had a high biotite content but correspond to a low quartz content whereas SON and Skjoldungen show high quartz low biotite content.

GRFs from marine deposits, such as Amerloq, Ilulialik, Ameralik and Bredefjord consisted of halite, reflective of their saline depositional environment. As seen in Table 3.5, the mineral composition of the unwashed and the washed Ilulialik GRF were comparable, except for the loss of halite in the washed GRF.

Table 3.5: Comparison between mineral phases determined by XRD among the glacial rock flours from Greenland.

	MAL	SON	TSQ	ILU (U/W)	ILU	AMA3	AMA7	KLS	AMQ2	BRED2	IGA2	SKJ-3
plagioclase	43.5(4)	45.9(4)	42.0(4)	37.4(4)	38.2(4)			44.2(5)	42.3(4)	43.2(5)	46.2(6)	50.3(5)
microcline	10.7(3)	10.7(2)	7.4(3)	8.4(3)	7.7(3)	48.1(4)	47.8(4)	9.9(3)	8.2(3)	9.7(3)	19.9(4)	18.9(4)
quartz	23.1(2)	28.5(3)	18.4(2)	11.4(2)	12.7(2)	5.8(2)	9.3(3)	16.4(2)	16.7(2)	23.6(3)	17.7(3)	18.1(2)
biotite	7.8(3)	4.0(6)	9.3(6)	23.4(6)	22.5(6)	36.0(3)	22.2(2)	9.4(7)	8.3(6)	3.1(7)	4.0(7)	1.3(5)
chlorite			1.1(1)	1.1(1)	1.2(1)	2.8(5)	7.8(6)	1.3(1)	1.2(1)	4.8(2)	1.6(1)	0.6(1)
amphibole	10.4(3)	8.3(3)	15.8(3)	14.1(3)	13.8(3)		1.8(1)	14.1(3)	10.9(3)	6.3(3)	3.7(3)	6.3(3)
augite	1.8(2)	0.5(2)	2.5(3)	2.2(3)	2.0(3)	5.5(2)	8.7(3)	3.8(3)	2.4(3)	5.6(4)	5.5(4)	2.2(5)
epidote	2.7(3)	2.2(2)	3.5(3)		1.7(3)			1.0(2)		2.8(3)	1.5(4)	1.5(3)
calcite						1.8(3)	1.6(3)		2.5(1)			
gypsum									1.6(2)			
apatite												0.8(2)
halite				2.1(1)					4.8(1)	0.9(1)		
pyrite							0.8(1)		1.3(1)			

XRD analysis were performed using a Bruker-AXS D8 Advance diffractometer equipped with a Cu X-ray tube at Department of Geosciences and Nature Resource Management (IGN), University of Copenhagen. The values in bracket indicates the standard error in measurement.

3.4.2. CHEMICAL PROPERTIES OF GRF

3.4.2.1. Elemental composition

The major, minor and trace element contents of the GRF are reported in Tables 3.6 and 3.8. GRFs were classified for their modal compositions based on their elemental composition. Table 3.6 lists the CIPW normative calculations of GRF after Hutchison (1974). In modal quartz-alkali feldspars-plagioclase (QAP) classification, the GRF samples occupy the granodiorite and quartz monzodiorite fields (Figure 3.7a). The normative anorthite-albite-orthoclase (wt. %) composition suggest that majority of the GRFs could be derived from granodioritic and tonalitic basement rocks. Both the Amerloq GRF samples occupy the trondhjemite field.

The concentrations of major elements were normalized to their anhydrous values for GRF characterization. Their total SiO_2 content ranged from 55 wt. % in Ilulialik to 66 wt. % in Ameralik. In general, all GRF samples had a high total alkali content (K_2O+Na_2O = 5.9-8.4 %) with Na_2O >3.5 %. Majority of the samples plot in the fields of high-K calc-alkaline series on the K_2O vs SiO_2 plot (Figure 3.7b; Peccerillo and Taylor, 1976; Rickwood, 1989). Although the source lithologies for the GRFs investigated in this study are different, majority of them follow a general trend. TiO_2, Fe_2O_3, MnO, MgO, K_2O contents show positive correlation suggesting majority of the oxides are primarily derived from silicates. However, CaO and Na_2O do not systematically vary with Al_2O_3. Negative correlation between Al_2O_3 and SiO_2 is possibly related with quartz content such that SiO_2 is mostly present as quartz and the negative trend suggesting grain sorting effect such that other silicate minerals such as feldspars and mica are predominant in finer grain size (Cullers and Podkovyrov, 2002).

Relationships between some major element oxide ratios such as SiO_2/Al_2O_3, Na_2O/K_2O and Fe_2O_3/K_2O are used to determine the mineralogical maturity and stability of the GRFs (Pettijohn et al., 1972; Herron, 1988). While SiO_2/Al_2O_3 distinguishes chemically mature sediments from immature, Fe_2O_3/K_2O is effective in determining mineral stability. Most of the stable rock-forming minerals such as K-feldspar and mica are rich in K but low in Fe, whereas less stable rock-forming minerals are rich in Fe. They allow distinction between quartz-rich sandstones (high-ratio), wackes and feldspathic and lithic sandstones (intermediate-ratio) and clay-rich shales (low-ratio). Using these parameters, all GRFs were identified as

greywacke after Pettijohn et al. (1972) but after Herron (1988) some GRFs were identified as shale. These classifications suggest that GRFs investigated in this study were chemically immature.

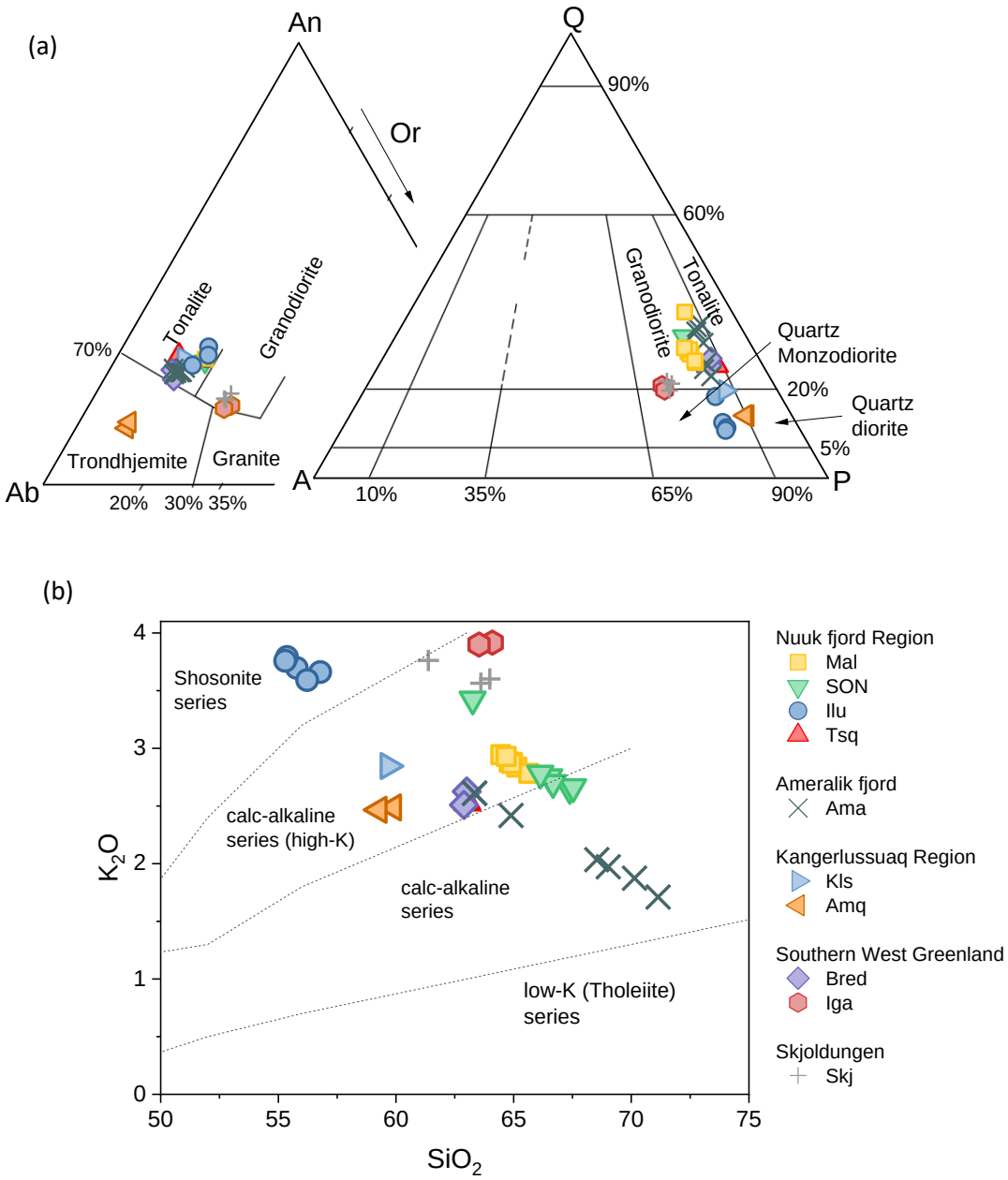


Figure 3.8: (a) Normative compositions of glacial rock flours from Greenland based on An-Ab-Or (after Barker, 1979) and QAP (after Streckeisen, 1974); (b) K_2O vs SiO_2 plot showing high alkali ratio of GRF samples.

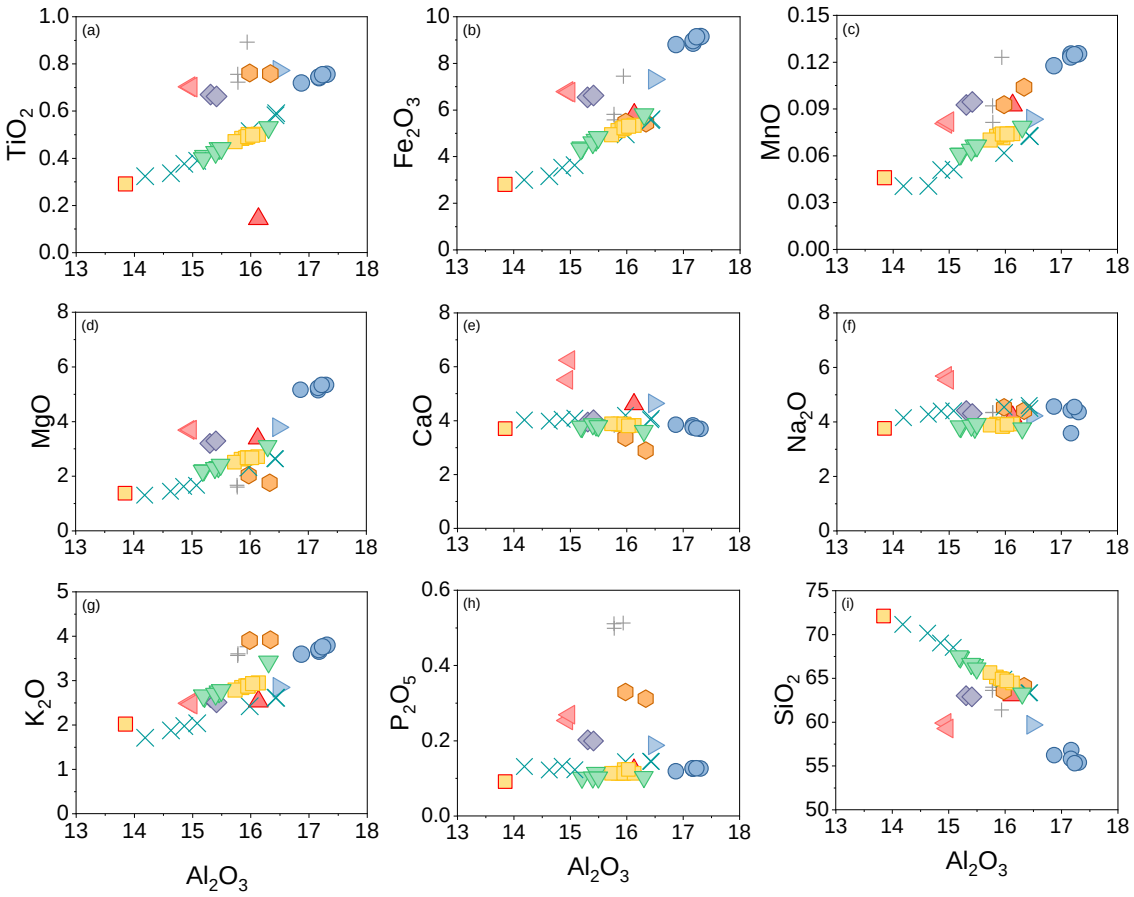


Figure 3.9: Harker diagram of major element oxides versus Al2O3 in wt. % for Greenlandic glacial rock flours.

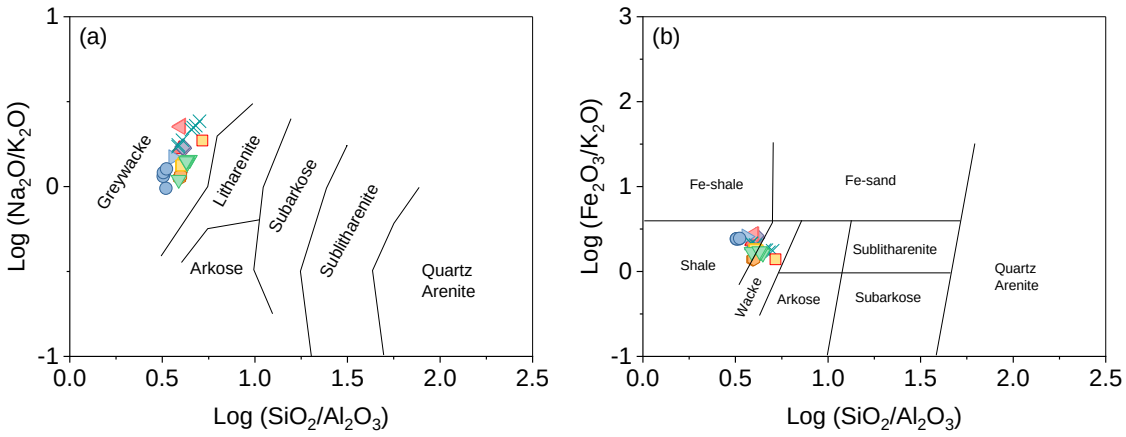


Figure 3.10: Geochemical classification of Greenlandic glacial rock flours after (a) Pettijohn et al. (1972) and (b) Herron (1988).

Aluminum saturation index was calculated from the molecular ratio Al/(Ca-1.67P+Na+K) (A/CNK; Shand, 1943). All GRF samples had an A/CNK <1.1, indicating they were metaluminous to weakly peraluminous in nature (Table 3.6). GRF derived from Amerloq had a considerably low A/CNK value (~0.8) than the average. This could be due to a relatively higher Ca content in Amerloq GRF than rest of the GRFs investigated in this study. The calculated values for the weathering indices CIA and CIW of GRFs are given in Table 3.6. CIA for GRF samples in this study varied from 52.88 to 61.75 and CIW varied from 57.92 to 72.32, which indicates low extent of chemical weathering. Amerloq GRF has the lowest degree of alteration (CIA ≈ 53) and weathering (CIW ≈ 58).

Table 3.6: Major element and modal composition of glacial rock flours from Greenland in wt. %.

	Detection Limit (%)	RF Mal	Mal 2-10	Mal 2-11	Mal P1	Mal P2	Mal P3	Mal P4	Mal P5	Ilu 3-1	Ilu 3-2
SiO_2	0.05	63.47	62.76	63.03	63.41	63.28	63.92	63.18	71.14	52.67	52.40
Al_2O_3	0.04	15.63	15.71	15.62	15.43	15.51	15.32	15.53	13.67	16.47	16.33
Fe_2O_3	0.015	5.17	5.20	5.16	4.98	5.05	4.81	5.09	2.77	8.70	8.65
MnO	0.015	0.07	0.07	0.07	0.07	0.07	0.07	0.07	0.05	0.12	0.12
MgO	0.03	2.62	2.64	2.60	2.55	2.58	2.44	2.60	1.36	5.08	5.05
CaO	0.03	3.78	3.71	3.70	3.77	3.74	3.78	3.77	3.65	3.51	3.51
Na_2O	0.02	3.76	3.81	3.80	3.81	3.80	3.77	3.73	3.71	4.15	4.30
K_2O	0.03	2.82	2.87	2.85	2.76	2.80	2.71	2.79	1.99	3.61	3.56
TiO_2	0.02	0.49	0.49	0.48	0.47	0.48	0.46	0.48	0.29	0.72	0.71
P_2O_5	0.10	0.12	0.11	0.12	0.11	0.11	0.11	0.11	0.09	0.12	0.12
LOI		2.14	2.35	2.21	1.76	1.87	1.95	2.11	1.17	4.26	4.41
Total		100.06	99.72	99.65	99.11	99.30	99.32	99.45	99.87	99.39	99.18
Recalculated to anhydrous values											
SiO_2		64.81	64.46	64.69	65.14	64.95	65.64	64.91	72.08	55.37	55.29
Al_2O_3		15.96	16.13	16.03	15.85	15.92	15.73	15.95	13.85	17.31	17.24
Fe_2O_3		5.28	5.34	5.29	5.11	5.19	4.94	5.23	2.81	9.14	9.13
MnO		0.07	0.07	0.07	0.07	0.07	0.07	0.07	0.05	0.13	0.12
MgO		2.68	2.71	2.67	2.62	2.65	2.51	2.67	1.37	5.33	5.33
CaO		3.86	3.81	3.80	3.87	3.84	3.88	3.87	3.70	3.69	3.70
Na_2O		3.84	3.92	3.90	3.91	3.90	3.87	3.83	3.75	4.36	4.54
K_2O		2.88	2.94	2.93	2.84	2.88	2.78	2.87	2.01	3.79	3.76
TiO_2		0.50	0.50	0.50	0.48	0.49	0.47	0.49	0.29	0.76	0.75
P_2O_5		0.12	0.11	0.12	0.11	0.11	0.11	0.11	0.09	0.13	0.13
Total		100	100	100	100	100	100	100	100	100	100
A/CNK		1.07	1.07	1.07	1.06	1.06	1.06	1.07	1.03	1.03	1.01
Na/K		1.19	1.19	1.19	1.23	1.21	1.24	1.19	1.67	1.03	1.08
CIW		68.64	68.69	68.75	68.16	68.38	68.09	68.54	65.97	69.42	68.78
CIA		61.08	61.04	61.08	60.74	60.86	60.77	61.02	60.19	60.26	59.81
r_{CO2}		0.16	0.16	0.16	0.16	0.16	0.16	0.16	0.12	0.22	0.22
Q		19.67	18.62	19.12	19.90	19.60	21.01	19.85	33.42	0.23	0.00
C		0.00	0.00	0.00	0.00	0.00	0.00	0.00	0.00	0.00	0.00
Or		17.02	17.40	17.31	16.77	17.00	16.45	16.95	11.90	22.41	22.21
Ab		32.49	33.14	33.02	33.10	32.98	32.75	32.38	31.77	36.88	38.41
An		17.81	17.75	17.58	17.30	17.45	17.34	17.88	14.99	16.47	15.55
Di		0.00	0.00	0.00	0.00	0.00	0.00	0.00	1.49	0.00	0.00
Hy		6.67	6.74	6.65	6.53	6.60	6.24	6.64	2.73	13.29	11.32
Ol		0.00	0.00	0.00	0.00	0.00	0.00	0.00	0.00	0.00	1.37
Il		0.15	0.16	0.16	0.16	0.16	0.15	0.16	0.10	0.27	0.27
Hm		5.28	5.34	5.29	5.11	5.19	4.94	5.23	2.81	9.15	9.13
Tn		0.38	0.31	0.31	0.81	0.62	0.82	0.42	0.59	0.70	1.41
Ru		0.27	0.29	0.29	0.07	0.16	0.06	0.24	0.00	0.33	0.04
Ap		0.29	0.27	0.29	0.27	0.27	0.27	0.27	0.22	0.30	0.30
Sum		100.02	100.02	100.02	100.02	100.02	100.02	100.02	100.01	100.02	100.02

Table 3.6: Major element and modal composition of glacial rock flours from Greenland in wt. % (contd.).

	Ilu 3-3	Ilu (w)	Ilu (u/w)	SON	SON-190003	SON-190004	SON-190005	SON-190006	SON-190007
SiO_2	52.83	54.45	52.05	65.89	61.03	65.81	63.76	65.11	64.54
Al_2O_3	16.26	16.47	15.62	14.87	15.73	14.80	14.82	15.04	15.12
Fe_2O_3	8.49	8.49	8.14	4.29	5.60	4.23	4.52	4.49	4.72
MnO	0.12	0.12	0.11	0.06	0.076	0.060	0.064	0.062	0.065
MgO	4.95	4.93	4.78	2.17	3.00	2.15	2.24	2.25	2.36
CaO	3.55	3.66	3.56	3.68	3.49	3.69	3.67	3.78	3.71
Na_2O	4.18	3.43	4.22	3.73	3.63	3.74	3.63	3.77	3.83
K_2O	3.50	3.51	3.32	2.59	3.30	2.60	2.64	2.64	2.71
TiO_2	0.70	0.71	0.67	0.40	0.51	0.39	0.42	0.42	0.43
P_2O_5	0.12	0.12	0.11	0.10	0.10	< L.D.	0.11	0.10	0.10
LOI	4.20	3.15	7.34	1.74	2.77	2.25	3.82	1.47	1.73
Total	98.91	99.04	99.91	99.53	99.24	99.70	99.68	99.13	99.32
Recalculated to anhydrous values									
SiO_2	55.79	56.78	56.23	67.39	63.26	67.53	66.51	66.67	66.13
Al_2O_3	17.17	17.18	16.87	15.21	16.31	15.19	15.46	15.40	15.50
Fe_2O_3	8.97	8.85	8.80	4.39	5.80	4.34	4.71	4.60	4.83
MnO	0.12	0.13	0.12	0.06	0.08	0.06	0.07	0.06	0.07
MgO	5.22	5.14	5.16	2.22	3.11	2.20	2.34	2.30	2.42
CaO	3.74	3.82	3.85	3.76	3.62	3.78	3.83	3.87	3.80
Na_2O	4.42	3.58	4.55	3.81	3.76	3.84	3.79	3.86	3.92
K_2O	3.70	3.66	3.59	2.65	3.42	2.66	2.75	2.70	2.78
TiO_2	0.74	0.74	0.72	0.41	0.53	0.40	0.44	0.43	0.44
P_2O_5	0.13	0.13	0.12	0.10	0.10	0	0.11	0.10	0.10
Total	100	100	100	100	100	100	100	100	100
A/CNK	1.02	1.09	0.98	1.05	1.06	1.01	1.06	1.02	1.00
Na/K	1.07	0.87	1.13	1.29	1.19	1.07	1.19	1.03	1.08
CIW	68.93	71.11	67.82	67.76	69.87	66.59	68.12	67.57	67.73
CIA	60.03	61.75	59.27	60.60	60.93	59.63	60.76	60.41	60.39
r_{CO2}	0.22	0.21	0.22	0.15	0.17	0.15	0.15	0.15	0.15
Q	0.84	6.48	1.12	24.30	16.20	24.17	22.85	22.83	21.58
C	0.00	0.69	0.00	0.00	0.08	0.00	0.00	0.00	0.00
Or	21.85	21.63	21.22	15.65	20.23	15.74	16.25	15.96	16.44
Ab	37.38	30.27	38.54	32.28	31.83	32.46	32.08	32.67	33.21
An	16.11	18.12	14.99	16.55	17.27	16.35	17.04	16.71	16.45
Di	0.00	0.00	0.99	0.21	0.00	0.99	0.00	0.47	0.35
Hy	13.02	12.81	12.40	5.43	7.74	5.03	5.82	5.53	5.87
Ol	0.00	0.00	0.00	0.00	0.00	0.00	0.00	0.00	0.00
Il	0.26	0.27	0.25	0.13	0.17	0.13	0.14	0.14	0.14
Hm	8.97	8.86	8.80	4.39	5.81	4.34	4.71	4.60	4.83
Tn	1.15	0.00	1.44	0.84	0.00	0.81	0.84	0.87	0.90
Ru	0.14	0.60	0.00	0.00	0.44	0.00	0.03	0.00	0.00
Ap	0.30	0.30	0.28	0.24	0.25	0.00	0.27	0.24	0.24
Sum	100.02	100.02	100.02	100.02	100.01	100.01	100.03	100.01	100.02

Table 3.6: Major element and modal composition of glacial rock flours from Greenland in wt. % (contd.).

	Tsq	Kls	Amq1	Amq2	Bred1	Bred2	Iga1	Iga2
SiO_2	61.54	57.24	52.00	50.71	59.27	59.90	61.70	61.74
Al_2O_3	15.75	15.81	12.98	12.82	14.40	14.68	15.73	15.53
Fe_2O_3	5.65	7.01	5.89	5.78	6.15	6.30	5.23	5.32
MnO	0.09	0.08	0.07	0.07	0.09	0.09	0.10	0.09
MgO	3.29	3.63	3.20	3.16	3.01	3.13	1.69	1.98
CaO	4.49	4.45	4.78	5.34	3.71	3.84	2.78	3.27
Na_2O	4.09	4.05	4.93	4.74	4.15	4.10	4.24	4.40
K_2O	2.47	2.73	2.16	2.11	2.47	2.39	3.77	3.79
TiO_2	0.52	0.74	0.61	0.60	0.63	0.63	0.73	0.74
P_2O_5	0.12	0.18	0.22	0.23	0.19	0.19	0.30	0.32
LOI	1.60	3.52	13.24	13.92	5.88	4.33	2.96	2.06
Total	99.59	99.44	100.07	99.47	99.92	99.58	99.22	99.23
Recalculated to anhydrous values								
SiO_2	63.03	59.67	59.88	59.27	63.01	62.89	64.09	63.53
Al_2O_3	16.13	16.48	14.95	14.98	15.31	15.41	16.34	15.98
Fe_2O_3	5.79	7.31	6.78	6.76	6.54	6.61	5.43	5.47
MnO	0.09	0.08	0.08	0.08	0.09	0.09	0.10	0.09
MgO	3.37	3.78	3.68	3.69	3.20	3.29	1.76	2.04
CaO	4.60	4.64	5.50	6.24	3.94	4.03	2.89	3.36
Na_2O	4.19	4.22	5.68	5.54	4.41	4.30	4.40	4.53
K_2O	2.53	2.85	2.49	2.47	2.63	2.51	3.92	3.90
TiO_2	0.14	0.77	0.70	0.70	0.67	0.66	0.76	0.76
P_2O_5	0.12	0.19	0.25	0.27	0.20	0.20	0.31	0.33
Total	100	100	100	100	100	100	100	100
A/CNK	1.02	1.01	0.79	0.76	1.00	1.02	1.04	0.97
Na/K	1.48	1.33	2.04	2.01	1.50	1.53	1.01	1.04
CIW	65.82	66.68	59.12	57.92	66.58	66.77	72.32	70.17
CIA	59.66	59.80	53.82	52.88	59.76	60.22	61.64	59.91
r_{CO2}	0.19	0.20	0.14	0.14	0.11	0.11	0.09	0.10
Q	15.38	10.08	4.59	3.91	15.52	16.01	15.57	13.56
C	0.00	0.00	0.00	0.00	0.00	0.00	0.35	0.00
Or	14.95	16.82	14.70	14.57	15.52	14.83	23.14	23.05
Ab	35.45	35.73	48.04	46.88	37.33	36.42	37.27	38.31
An	17.74	17.62	7.96	8.73	14.21	15.32	12.29	11.76
Di	3.22	1.41	12.12	14.29	1.61	1.12	0.00	0.38
Hy	6.90	8.77	3.56	2.58	7.23	7.67	4.37	4.90
Ol	0.00	0.00	0.00	0.00	0.00	0.00	0.00	0.00
Il	0.20	0.18	0.17	0.18	0.20	0.20	0.22	0.20
Hm	5.79	7.31	6.78	6.76	6.54	6.62	5.43	5.48
Tn	0.10	1.66	1.50	1.50	1.39	1.36	0.00	1.61
Ru	0.00	0.00	0.00	0.00	0.00	0.00	0.64	0.00
Ap	0.29	0.44	0.60	0.64	0.48	0.47	0.74	0.78
Sum	100.02	100.02	100.02	100.02	100.02	100.02	100.03	100.03

Table 3.6: Major element and modal composition of glacial rock flours from Greenland in wt. % (contd.).

	Ama1	Ama2	Ama3	Ama4	Ama5	Ama6	Ama7	Skj1	Skj2	Skj3
SiO_2	68.89	67.87	70.30	60.92	63.06	67.03	61.11	59.87	62.89	62.29
Al_2O_3	14.37	14.61	14.02	15.80	15.53	14.75	15.86	15.55	15.51	15.45
Fe_2O_3	3.10	3.46	2.96	5.35	4.81	3.55	5.40	7.26	5.48	5.69
MnO	0.04	0.05	0.04	0.07	0.06	0.05	0.07	0.12	0.08	0.09
MgO	1.42	1.60	1.29	2.54	2.25	1.63	2.54	1.96	1.57	1.63
CaO	3.91	3.98	3.97	3.88	4.07	4.00	3.94	3.69	3.75	3.80
Na_2O	4.20	4.32	4.10	4.42	4.41	4.31	4.33	4.06	4.27	4.25
K_2O	1.84	1.94	1.69	2.51	2.35	1.99	2.52	3.67	3.54	3.49
TiO_2	0.33	0.37	0.32	0.56	0.50	0.38	0.57	0.87	0.71	0.74
P_2O_5	0.12	0.13	0.13	0.14	0.14	0.12	0.14	0.50	0.49	0.50
LOI	1.65	1.79	0.93	3.35	3.00	1.73	3.11	1.80	0.88	1.02
Total	99.86	100.12	99.76	99.53	100.17	99.53	99.59	99.34	99.16	98.93
Recalculated to anhydrous values										
SiO_2	70.14	69.02	71.14	63.33	64.89	68.53	63.34	61.37	63.98	63.61
Al_2O_3	14.63	14.86	14.19	16.43	15.98	15.08	16.44	15.94	15.78	15.78
Fe_2O_3	3.16	3.52	3.00	5.56	4.95	3.63	5.60	7.44	5.58	5.81
MnO	0.04	0.05	0.04	0.07	0.06	0.05	0.07	0.12	0.08	0.09
MgO	1.45	1.63	1.31	2.64	2.32	1.67	2.63	2.01	1.60	1.66
CaO	3.98	4.05	4.02	4.03	4.19	4.09	4.08	3.78	3.82	3.88
Na_2O	4.28	4.39	4.15	4.60	4.54	4.41	4.49	4.16	4.34	4.34
K_2O	1.87	1.97	1.71	2.61	2.42	2.03	2.61	3.76	3.60	3.56
TiO_2	0.34	0.38	0.32	0.58	0.51	0.39	0.59	0.89	0.72	0.76
P_2O_5	0.12	0.13	0.13	0.15	0.14	0.12	0.15	0.51	0.50	0.51
Total	100	100	100	100	100	100	100	100	100	100
A/CNK	1.03	1.02	1.03	1.04	1.02	1.02	1.05	0.99	0.97	0.97
Na/K	2.04	1.99	2.17	1.57	1.68	1.94	1.54	0.99	1.08	1.09
CIW	65.08	65.00	64.74	66.85	65.96	65.09	67.02	71.88	70.83	70.76
CIA	60.08	59.84	60.05	60.44	59.98	59.84	60.57	61.45	60.97	61.01
r_{CO2}	0.09	0.09	0.08	0.11	0.10	0.09	0.10	0.10	0.10	0.10
Q	28.57	26.11	31.16	15.01	18.04	25.11	15.48	13.49	16.38	16.00
C	0.00	0.00	0.00	0.00	0.00	0.00	0.00	0.00	0.00	0.00
Or	11.07	11.66	10.11	15.42	14.29	12.02	15.44	22.23	21.28	21.06
Ab	36.18	37.18	35.11	38.88	38.40	37.29	37.98	35.22	36.76	36.72
An	15.19	14.99	15.04	16.49	16.09	15.36	16.99	13.70	12.92	13.04
Di	2.14	2.42	2.39	0.65	1.71	2.32	0.42	0.00	0.43	0.47
Hy	2.61	2.93	2.15	6.28	4.98	3.08	6.36	5.01	3.78	3.93
Ol	0.00	0.00	0.00	0.00	0.00	0.00	0.00	0.00	0.00	0.00
Il	0.09	0.11	0.09	0.16	0.13	0.11	0.16	0.26	0.17	0.20
Hm	3.16	3.52	3.00	5.56	4.95	3.63	5.60	7.44	5.58	5.81
Tn	0.71	0.78	0.68	1.23	1.09	0.81	1.25	1.21	1.55	1.60
Ru	0.00	0.00	0.00	0.00	0.00	0.00	0.00	0.26	0.00	0.00
Ap	0.29	0.31	0.31	0.35	0.34	0.29	0.34	1.21	1.18	1.21
Sum	100.02	100.02	100.02	100.02	100.02	100.02	100.02	100.04	100.04	100.04

Major elements were analyzed by emission spectrometry (ICP-OES) and reported as wt%, LOI = loss on ignition at 1000 °C.
A/CNK = Al/(Ca-1.67P+Na+K) in molecular ratio (Shand, 1943)
Chemical Index of Weathering, CIW = Al_2O_3/(Al_2O_3 + CaO* + Na_2O) × 100 (Harnois, 1988)
Chemical Index of Alteration, CIA= Al_2O_3/(Al_2O_3 + CaO* + Na_2O + K_2O) × 100 (Nesbitt and Young, 1982)

CaO* was CaO corrected for phosphate using P_2O_5 and if molar CaO* was higher than molar Na_2O, CaO* was assumed equivalent to Na_2O (McLennan, et al., 1993). CIPW normative calculations done after Hutchison (1974), where Q = quartz, C = corundum, Or = orthoclase, Ab = albite, An = anorthite, Wo = wollastonite, Il = Illite, Hm = hematite, Ap = apatite, Bi = bismuth.

CO_2 capture potential, r_{CO2} = [η × ∑(moles of monovalent cations) + 2η × ∑(moles of divalent cations)] × $\frac{m_{CO_2}}{100}$, where η is the CO_2 capture efficiency. η depends upon ocean salinity and temperature (ref). Here, a capture efficiency of 0.86 per charge was used following Beerling et al. 2020.

The minor and trace elements data normalized to the upper continental crust (UCC) are presented in four groups of study areas based on their depositional environment in Figure 3.11. In general, these contents were comparable to those found in soil (Table 3.7). Some exceptions, however, were biologically toxic elements such as As and Mo in GRF samples from Amerloq. Mo is highly toxic, especially to animals, and its concentration in the samples greatly exceeded its concentration in soil. The Amerloq GRFs also exceeded the UCC concentrations in U content. However, these were within the concentration range found in soil (Bowen 1966) and are potentially not toxic.

Table 3.7: Average minor and trace element concentrations (ppm) of glacial rock flours in Greenland and their range compared with soil.

Element	GRF (This study)[a]	Dry soil[b]
As	0.55-6.19	6 (0.1-40)[b]
Ba	490-1289.2	500 (100-3000)[b]
Be	0.92-3.57	6 (0.1-40) [b]
Bi	0.05-0.12	-
Cd	0.05-0.32	0.06 (0.01-7) [b]
Co	7.76-32.29	8 (1-40) [b]
Cr	27.39-215.89	100 (5-3000) [b]
Cu	13.94-80.96	20 (2-100) [b]
Ga	17.2-25.97	30 (0.4-300) [b]
Mo	0.52-16.33	2 (0.2-5) [b]
Ni	12.58-135.87	40 (10-1000) [b]
Pb	10.3-26	10 (2-200) [b]
Sb	0.28-0.62	0.6-10
Sc	7.67-16.22	7 (10-25) [b]
Sr	249.4-533.68	300 (50-1000)[b]
U	0.22-3.87	20-250
V	43.17-109.07	100 (20-500) [b]
Zn	38.3-135.37	50 (10-300) [b]
Zr	43.16-489.4	300 (60-2000) [b]
La	18.45-87.88	30 (1-5000) [b]
Ce	35.43-196.8	50 [b]

[a]Concentrations were determined by flow injection inductively coupled plasma mass spectrometry (FI-ICP-MS) (Carignan et al., 2001).
[b]Data taken from Bowen (1966) and Allaway (1968) and references therein.

Aside from Igaliku and Skjoldungen, majority of the GRFs show a moderate to strong depletion compared to UCC for most of the Large Ion Lithophile Elements (LILE: Cs, Rb, Ba, Sr, Th, U) and High Field Strength Elements (HFSE: Zr, Hf, Nb, Ta and Ti). While samples from

Kangerlussuaq and the Nuuk region show an enrichment for transition state elements (Cr, Co, Ni, V), samples from Igaliku and Skjoldungen have moderate depletion.

REE abundances of the GRFs are given in Table 3.8 and their chondrite-normalized REE variations are shown in Figure 3.12. All the GRF samples show a smooth fractionated REE pattern with a more enriched LREE. The La_N/Yb_N ratio ranges from 12.4 for Bredefjord to 29.9 for Ilulialik. GRFs exhibit slightly negative Eu anomaly (average Eu/Eu* = 0.8), with Ilulialik exhibiting the maximum negative Eu anomaly (Eu/Eu*= 0.6). The Eu anomaly is either low or absent in Ameralik Fjord samples. The uniformity in HREE patterns for the GRFs, except in case of Skjoldungen and Bredefjord, may imply similarity in REE concentration of the source lithologies. The enriched HREE in Skjoldungen and Bredefjord are likely due to their alkaline setting. The GRFs had a $(La/Gd)_N$ from 6.9 to 10.5 and a $(Tb/Lu)_N$ from 1.4 to 2.2. The variability in LREE enrichment could be related to the grain size. This is more pronounced in Nuuk fjord GRFs, where although Tasersuaq and Ilulialik GRFs are part of the same sedimentary system, Ilulialik is more enriched in LREE due to fine sediments (Figure 3.12a). Nuuk Fjord GRFs were fractionated in their LREE with respect to Eu with Ilulialik being the most fractionated and Tasersuaq being the least. Skjoldungen GRF had higher REE content (mean ∑REE = 392.2 ppm) than the rest of the GRFs, where ∑REE varied from 83.6 ppm to 279.7 ppm.

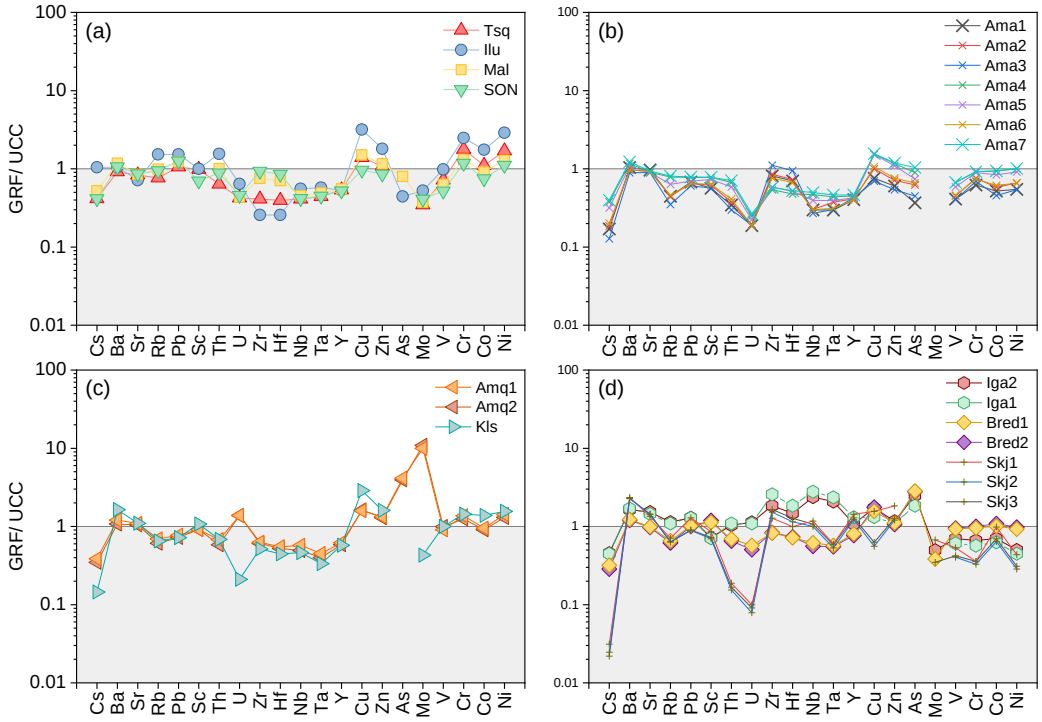


Figure 3.4.211: Trace element variation diagram for Greenlandic Glacial Rock Flour. (a) Nuuk fjord region; (b) Ameralik fjord; (c) Kangerlussuaq region; (d) southern West Greenland. Normalizing values for upper continental crust are from Taylor and McLennan (1985).

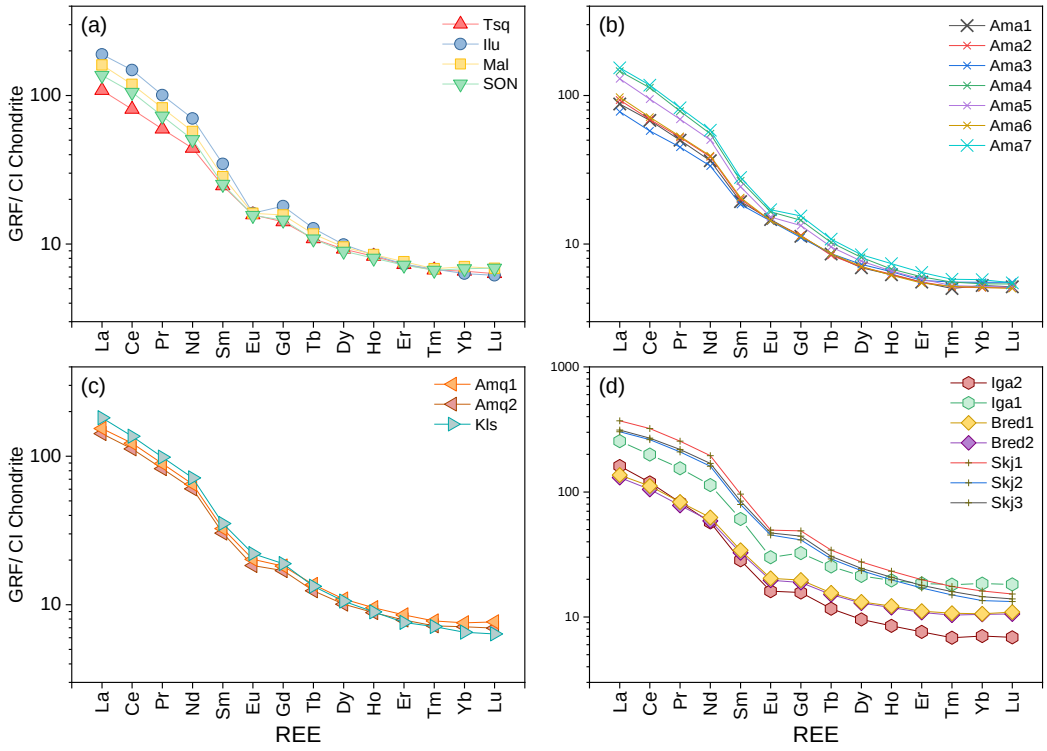


Figure 3.12: Normalized REE pattern for Greenlandic Glacial Rock Flour. (a) Nuuk fjord region; (b) Ameralik; (c) Kangerlussuaq region; (d) southern West Greenland. Normalizing values for primitive mantle are from McDonough and Sun (1995).

Table 3.8: Trace element and REE composition of glacial rock flours from Greenland in ppm (contd).

	Detection Limit	RF Mal	Mal 2-10	Mal 2-11	Mal P1	Mal P2	Mal P3	Mal P4	Mal P5	Ilu 3-1
As	0.50	1.2	0.95	<0.50	633.50	659.11	602.25	641.87	525.36	1.16
Ba	5.5	649.67	651.09	633.50	1.23	1.26	1.34	1.25	1.28	592.20
Be	0.05	1.32	1.35	1.23	0.07	0.07	0.06	0.07	0.05	1.43
Bi	0.045	0.07	0.07	0.07	0.05	0.06	0.06	0.06	0.07	0.09
Cd	0.02	0.07	0.06	0.05	15.03	15.20	14.01	15.13	7.82	0.07
Co	0.08	15.45	15.97	15.03	105.29	109.60	99.98	106.07	68.04	32.29
Cr	0.50	110.15	112.81	105.29	2.33	2.47	2.12	2.40	0.87	215.89
Cs	0.02	2.41	2.50	2.33	29.82	29.08	26.45	30.14	14.65	4.78
Cu	2.0	37.59	30.58	29.82	21.54	22.39	20.99	21.41	17.74	80.96
Ga	0.02	22.03	22.61	21.54	1.09	1.16	1.13	1.16	0.90	25.97
Ge	0.04	1.13	1.21	1.09	4.04	4.07	4.04	3.81	5.05	1.32
Hf	0.03	4.08	3.65	4.04	< L.D.	< L.D.	< L.D.	< L.D.	< L.D.	1.43
In	0.03	< L.D.	0.04	<0.03	0.60	0.97	0.64	0.61	0.99	0.04
Mo	0.50	0.56	0.67	0.60	5.40	5.66	5.13	5.34	3.10	0.83
Nb	0.015	5.43	5.55	5.40	54.50	55.65	49.90	54.60	26.78	6.75
Ni	2.0	56.62	58.36	54.50	20.71	22.15	19.88	21.01	17.93	135.87
Pb	0.45	20.82	21.07	20.71	113.42	118.93	107.71	115.25	63.47	25.94
Rb	0.15	110.65	109.72	113.42	< L.D.	< L.D.	< L.D.	< L.D.	< L.D.	172.81
Sb	0.06	10.72	< L.D.	< L.D.	10.55	10.65	10.55	10.66	8.40	<L.D.
Sc	0.6	10.65	11.10	10.55	1.50	1.51	1.44	1.55	1.28	13.62
Sn	0.30	1.4	1.52	1.50	297.58	299.61	285.72	285.09	303.76	1.66
Sr	0.70	296.34	306.88	297.58	0.49	0.53	0.47	0.48	0.30	249.40
Ta	0.004	0.49	0.49	0.49	10.57	11.53	9.84	10.99	3.76	0.56
Th	0.015	10.73	11.11	10.57	1.36	1.31	1.14	1.15	0.69	17.90
U	0.01	1.21	1.17	1.36	69.87	69.74	66.37	68.44	42.00	2.50
V	0.85	67.8	71.41	69.87	< L.D.	< L.D.	< L.D.	< L.D.	< L.D.	109.07
W	0.80	< L.D.	<0.80	<0.80	11.87	12.26	11.42	11.67	10.07	<0.80
Y	0.02	12.14	12.27	11.87	72.14	74.00	67.76	74.65	35.74	11.70
Zn	7.0	81.87	80.99	72.14	144.96	142.24	144.91	135.60	189.09	135.01
Zr	1.50	142.63	132.90	144.96	36.25	38.42	33.88	37.16	17.01	49.95
La	0.02	38.14	38.94	36.25	72.17	76.77	66.82	74.07	34.05	48.94
Ce	0.03	73	73.48	72.17	7.52	7.94	6.98	7.69	3.73	93.58
Pr	0.004	7.66	7.79	7.52	25.81	27.08	24.06	26.31	13.34	9.80
Nd	0.016	26.13	26.53	25.81	4.23	4.34	3.95	4.29	2.46	33.10
Sm	0.005	4.21	4.23	4.23	0.92	0.96	0.87	0.91	0.71	5.11
Eu	0.002	0.91	0.92	0.92	3.12	3.27	2.94	3.09	2.03	0.89
Gd	0.005	3.13	3.20	3.12	0.42	0.44	0.39	0.42	0.30	3.68
Tb	0.001	0.42	0.42	0.42	2.40	2.52	2.27	2.35	1.79	0.46
Dy	0.004	2.35	2.36	2.40	0.46	0.48	0.44	0.46	0.37	2.43
Ho	0.001	0.46	0.46	0.46	1.23	1.27	1.19	1.22	1.00	0.45
Er	0.002	1.22	1.22	1.23	0.18	0.19	0.17	0.17	0.15	1.13
Tm	0.001	0.17	0.16	0.18	1.14	1.18	1.10	1.12	0.99	0.15
Yb	0.002	1.13	1.13	1.14	0.17	0.18	0.17	0.17	0.16	0.99
Lu	0.001	0.17	0.17	0.17	633.50	659.11	602.25	641.87	525.36	0.15

Table 3.8: Trace element and REE composition of glacial rock flours from Greenland in ppm.

	Ilu 3-2	Ilu 3-3	Ilu B5	ILU/U-01	Son	SON-190003	SON-190004	SON-190005	SON-190006	SON-190007
As	0.95	1.00	0.67	1.44	<0.50	0.72	< L.D.	0.54	0.62	0.67
Ba	585.40	588.74	579	498.94	585	555.62	532.55	524.27	536.07	544.70
Be	1.39	1.40	1.29	1.32	1.39	1.52	1.37	1.38	1.43	1.42
Bi	0.08	0.08	0.09	0.13	0.06	0.06	0.06	0.07	0.06	0.07
Cd	0.07	0.07	0.06	0.07	0.06	0.09	0.06	0.06	0.05	0.08
Co	31.63	31.66	29.8	28.18	12.7	16.41	12.06	13.09	12.88	13.99
Cr	214.13	213.33	206	192.35	98.0	134.92	96.33	100.24	99.93	105.02
Cs	4.46	4.48	4.82	4.02	1.91	2.96	1.86	1.94	1.88	2.13
Cu	76.99	75.74	79.5	70.87	24.1	32.52	23.34	29.34	27.50	28.13
Ga	25.13	25.58	25	23.50	21.2	22.93	20.26	20.43	20.62	21.18
Ge	1.30	1.30	1.29	1.22	1.09	1.17	1.07	1.12	1.08	1.16
Hf	1.29	1.40	1.49	1.47	4.95	3.50	4.18	4.47	3.93	4.00
In	0.04	0.04	0.03	0.03	<0.03	0.03	< L.D.	< L.D.	< L.D.	< L.D.
Mo	0.72	0.78	0.79	0.70	0.61	0.93	0.58	0.57	0.54	< L.D.
Nb	6.57	6.66	6.65	5.96	5.00	6.12	4.37	4.91	4.66	5.02
Ni	132.30	132.67	127	116.15	48.9	67.71	45.78	48.84	48.41	52.46
Pb	24.78	25.07	26	23.85	21.5	24.82	20.26	20.33	20.54	21.23
Rb	164.27	163.43	171	154.27	106	151.92	98.31	102.06	98.63	108.90
Sb	<0.06	<0.06	<0.06	0.10	<0.06	0.06	0.08	0.06	0.07	0.07
Sc	13.72	13.74	13.63	12.74	9.51	10.42	9.35	9.54	9.77	9.97
Sn	1.64	1.64	1.9	1.38	1.46	1.48	1.00	1.38	1.19	1.12
Sr	250.00	254.68	250	231.04	301	267.94	287.37	273.74	279.67	282.69
Ta	0.55	0.55	0.57	0.52	0.45	0.55	0.42	0.46	0.43	0.48
Th	16.92	16.96	16.6	14.99	9.47	14.56	8.74	9.33	9.19	10.20
U	1.93	2.04	1.79	1.77	1.28	1.74	1.11	1.24	1.11	1.32
V	106.47	107.96	105	91.16	55.7	59.80	50.27	54.25	54.42	56.58
W	<0.80	<0.80	<0.80	< L.D.	<0.80	< L.D.	< L.D.	< L.D.	< L.D.	< L.D.
Y	11.49	11.80	11.8	10.90	11.5	12.00	14.30	11.14	11.20	11.50
Zn	135.37	133.11	128	123.43	60.8	92.07	62.42	68.48	66.48	72.79
Zr	43.16	46.98	48.7	49.07	177	125.72	155.54	161.96	148.07	145.82
La	47.37	47.44	44.80	41.10	32.40	45.01	29.32	32.10	32.33	35.03
Ce	90.64	90.66	91.00	82.76	64.60	89.09	55.55	59.31	59.52	64.73
Pr	9.50	9.42	9.36	8.59	6.76	9.19	6.29	6.62	6.68	7.16
Nd	32.14	31.96	32.00	29.60	23.10	30.62	21.40	22.60	22.91	24.66
Sm	5.00	5.03	5.12	4.67	3.74	4.72	3.61	3.71	3.67	3.89
Eu	0.87	0.89	0.91	0.82	0.88	0.90	0.83	0.82	0.84	0.88
Gd	3.56	3.61	3.58	3.32	2.88	3.34	2.82	2.79	2.76	2.94
Tb	0.45	0.46	0.46	0.42	0.39	0.43	0.41	0.38	0.38	0.40
Dy	2.36	2.44	2.44	2.24	2.20	2.37	2.53	2.17	2.16	2.24
Ho	0.44	0.45	0.46	0.42	0.44	0.44	0.52	0.43	0.42	0.44
Er	1.11	1.12	1.17	1.06	1.15	1.15	1.44	1.12	1.12	1.15
Tm	0.15	0.15	0.17	0.15	0.16	0.16	0.22	0.16	0.16	0.17
Yb	0.96	0.99	1.02	0.94	1.10	1.05	1.46	1.05	1.05	1.08
Lu	0.14	0.15	0.15	0.14	0.17	0.16	0.22	0.16	0.16	0.16

Table 3.8: Trace element and REE composition of glacial rock flours from Greenland in ppm (contd) .

	Tsq	Kls	Amq1	Amq2	Bred1	Bred2	Iga1	Iga2
As	<0.50	<0.50	6.19	5.91	4.25	4.17	2.77	3.72
Ba	504.43	901.57	664.08	590.92	674.96	661.16	931.9	904.08
Be	1.39	1.04	1.04	1.02	1.51	1.45	3.57	3.41
Bi	0.06	<0.045	0.05	0.05	0.09	0.08	0.1	0.12
Cd	0.07	0.08	0.24	0.32	0.07	0.08	0.14	0.10
Co	18.81	23.49	16.21	15.37	17.20	18.42	10.65	11.91
Cr	147.43	119.45	113.31	103.69	79.30	82.81	47.08	55.02
Cs	1.91	0.67	1.78	1.60	1.47	1.31	2.06	2.10
Cu	34.86	71.82	39.60	40.47	39.18	44.04	32.93	43.10
Ga	21.22	22.69	20.53	18.17	18.98	19.17	21.28	22.07
Ge	1.10	1.28	1.04	0.97	1.19	1.13	1.4	1.50
Hf	2.29	2.58	3.19	3.03	4.17	4.26	10.68	8.54
In	0.03	0.04	0.04	<0.03	0.04	0.04	0.04	0.05
Mo	0.52	0.64	14.92	16.33	0.58	<0.50	<0.50	0.75
Nb	4.92	5.56	6.87	5.90	7.39	6.68	33.36	28.47
Ni	74.48	68.83	62.59	57.38	40.73	42.92	19.75	21.95
Pb	17.96	12.23	13.13	12.28	17.27	17.01	21.90	22.05
Rb	85.45	72.88	77.28	68.41	73.33	68.92	122.51	127.21
Sb	<0.06	<0.06	0.34	0.39	0.34	0.28	0.4	0.62
Sc	13.41	14.62	12.41	12.45	15.39	16.22	9.63	9.77
Sn	1.17	1.44	1.48	1.43	1.92	1.84	3.48	3.25
Sr	291.70	384.91	382.69	365.33	346.42	339.99	506.97	533.68
Ta	0.44	0.33	0.45	0.40	0.57	0.55	2.36	2.08
Th	6.82	7.33	7.25	6.25	7.39	6.95	11.69	11.14
U	1.19	0.59	3.87	3.86	1.60	1.42	3.07	3.17
V	77.06	107.26	96.88	106.57	99.75	101.74	65.11	74.70
W	<0.80	<0.80	<0.80	<0.80	<0.80	<0.80	0.96	1.15
Y	11.84	12.60	13.64	12.93	17.62	16.88	28.75	23.66
Zn	76.89	114.04	94.61	91.98	78.86	75.61	77.8	82.80
Zr	78.05	97.99	119.03	114.96	156.74	158.42	489.4	350.77
La	25.67	43.11	36.45	33.67	32.38	30.95	60.33	55.30
Ce	49.56	83.66	74.97	68.67	68.34	64.31	121.99	114.59
Pr	5.53	9.14	8.30	7.65	7.70	7.25	14.34	13.12
Nd	20.20	32.65	29.66	27.63	28.58	26.79	51.84	47.39
Sm	3.65	5.22	4.82	4.50	5.06	4.83	8.99	8.11
Eu	0.89	1.24	1.14	1.03	1.15	1.11	1.69	1.54
Gd	2.81	3.77	3.62	3.38	3.94	3.75	6.45	5.76
Tb	0.39	0.48	0.49	0.45	0.56	0.55	0.92	0.81
Dy	2.27	2.60	2.69	2.48	3.25	3.18	5.23	4.51
Ho	0.45	0.49	0.52	0.48	0.67	0.65	1.07	0.89
Er	1.16	1.21	1.37	1.26	1.78	1.74	2.97	2.45
Tm	0.17	0.18	0.19	0.18	0.26	0.26	0.45	0.37
Yb	1.06	1.05	1.22	1.15	1.71	1.69	2.98	2.42
Lu	0.16	0.16	0.19	0.15	0.15	0.15	0.17	0.16

Table 3.8: Trace element and REE composition of glacial rock flours from Greenland in ppm.

	Ama1	Ama2	Ama3	Ama4	Ama5	Ama 6	Ama 7	Skj1	Skj2	Skj3
As	0.55	0.93	0.67	1.34	1.11	0.99	1.56	<0.50	<0.50	<0.50
Ba	571	535	490	644	595	536	674	1289.2	1247.5	1257.7
Be	0.94	0.99	0.92	0.98	0.99	1.00	1.07	1.15	1.28	1.22
Bi	0.05	0.05	0.06	0.07	0.07	0.06	0.08	<0.045	<0.045	<0.045
Cd	0.06	0.06	0.07	0.05	0.06	0.05	0.06	0.11	0.11	0.11
Co	8.83	9.86	7.76	15.9	14.3	10.4	16.0	16.75	10.91	11.85
Cr	51.6	63.0	57.3	76.6	74.2	61.3	76.3	29.67	27.39	29.71
Cs	0.78	0.85	0.59	1.74	1.46	0.93	1.82	0.14	0.11	0.10
Cu	18.9	25.0	17.3	38.5	38.1	26.6	39.0	38.94	13.94	15.62
Ga	18.8	18.2	17.2	21.6	20.1	18.4	22.7	23.59	21.71	22.12
Ge	0.87	0.92	0.90	0.96	0.97	0.97	1.00	1.67	1.42	1.46
Hf	4.06	4.21	5.50	2.75	2.99	3.85	3.04	5.76	6.67	7.38
In	<0.03	<0.03	<0.03	<0.03	<0.03	<0.03	<0.03	0.06	0.05	0.05
Mo	<0.50	<0.50	<0.50	<0.50	<0.50	<0.50	<0.50	1.01	<0.50	0.52
Nb	3.57	3.64	3.24	5.61	4.74	3.59	5.98	14.05	12.01	12.83
Ni	24.1	28.9	23.8	44.1	40.1	28.8	44.5	19.22	12.58	13.65
Pb	11.5	11.0	10.3	13.2	11.8	11.0	13.3	21.89	15.15	15.32
Rb	50.0	49.8	39.1	87.9	71.1	51.4	90.3	79.31	71.36	70.71
Sb	<0.06	<0.06	<0.06	<0.06	<0.06	<0.06	<0.06	<0.06	<0.06	<0.06
Sc	7.67	8.37	7.71	10.58	9.96	8.60	10.6	11.63	9.47	9.83
Sn	1.04	0.82	0.72	1.48	1.38	0.82	1.53	1.62	1.32	1.20
Sr	338	324	313	314	314	320	327	471.75	499.85	502.86
Ta	0.30	0.37	0.30	0.44	0.39	0.31	0.46	0.60	0.53	0.58
Th	3.67	4.01	3.18	7.15	6.27	4.38	7.56	2.01	1.65	1.79
U	0.53	0.54	0.53	0.69	0.62	0.53	0.74	0.28	0.22	0.25
V	43.8	48.3	43.3	71.2	62.6	49.3	71.8	57.29	43.17	45.08
W	<0.80	<0.80	<0.80	<0.80	<0.80	<0.80	<0.80	<0.80	<0.80	<0.80
Y	8.87	9.12	9.39	9.89	9.35	8.82	10.2	31.52	26.84	28.29
Zn	42.8	50.6	38.3	83.0	77.5	54.1	84.1	129.99	85.56	90.16
Zr	154	162	211	103	111	145	110	242.62	289.20	313.36
La	20.81	22.12	18.45	34.61	30.74	23.11	36.46	87.88	71.88	74.16
Ce	41.74	42.31	35.43	69.08	58.04	43.81	72.14	196.8	160.56	165.13
Pr	4.64	4.86	4.17	7.29	6.43	4.93	7.69	23.69	19.4	20.32
Nd	16.64	17.68	15.34	25.28	22.91	17.94	26.68	89.13	73.51	77.29
Sm	2.86	2.97	2.73	3.95	3.60	3.04	4.15	14.2	11.76	12.49
Eu	0.82	0.81	0.81	0.93	0.86	0.81	0.96	2.79	2.55	2.64
Gd	2.24	2.28	2.20	2.87	2.65	2.25	3.08	9.71	8.22	8.81
Tb	0.31	0.30	0.31	0.37	0.35	0.31	0.39	1.24	1.05	1.1
Dy	1.70	1.72	1.80	2.00	1.89	1.74	2.08	6.79	5.77	6.03
Ho	0.34	0.34	0.36	0.37	0.36	0.34	0.40	1.27	1.08	1.14
Er	0.89	0.89	0.91	0.96	0.93	0.87	1.03	3.18	2.73	2.87
Tm	0.12	0.13	0.14	0.14	0.13	0.13	0.14	0.43	0.37	0.39
Yb	0.85	0.82	0.89	0.87	0.83	0.82	0.93	2.6	2.18	2.34
Lu	0.16	0.19	0.17	0.13	0.13	0.12	0.13	0.38	0.33	0.34

Trace elements were analyzed by flow injection inductively coupled plasma mass spectrometry (FI-ICP-MS) after Carignan et al., (2001) at CNRS.

3.4.2.2. Sr-Nd Isotope variations

Sm and Nd are rare earth elements with Nd slightly more incompatible than Sm; and radiogenic ^{147}Sm decaying to ^{143}Nd. Assuming chondritic evolution of Earth, the deviations in initial $^{143}Nd/^{144}Nd$ ratio a given rock sample from that of the chondritic uniform reservoir (CHUR) can be used to derive the information about when the rock was separated from the mantle. The present day CHUR values are: $^{143}Nd/^{144}Nd = 0.512638$ and $^{143}Sm/^{144}Nd = 0.1966$ (Hamilton et al., 1983).The depleted mantle (DM) has $^{143}Nd/^{144}Nd = 0.51315$ and $^{143}Nd/^{144}Nd = 0.2137$ based on mid-ocean ridge basalts. The Sm-Nd model age data (Table 3.9) were reflective of the age of the surrounding rocks. The Nuuk ages are strongly biased by the ~3 Ga Nuuk gneisses. Kangerlusuaq and Amerloq are close to the general age of 2.8 Ga reworked at ~1.8 Ga with some minor new contributions at ~1.9 Ga. Igaliku is biased by the juvenile addition to that area at 1900 Ma, while Bredefjord has significant contributions from the Archean foreland to the North. Skjoldungen closely resembles the age of the region ~2.7 Ga.

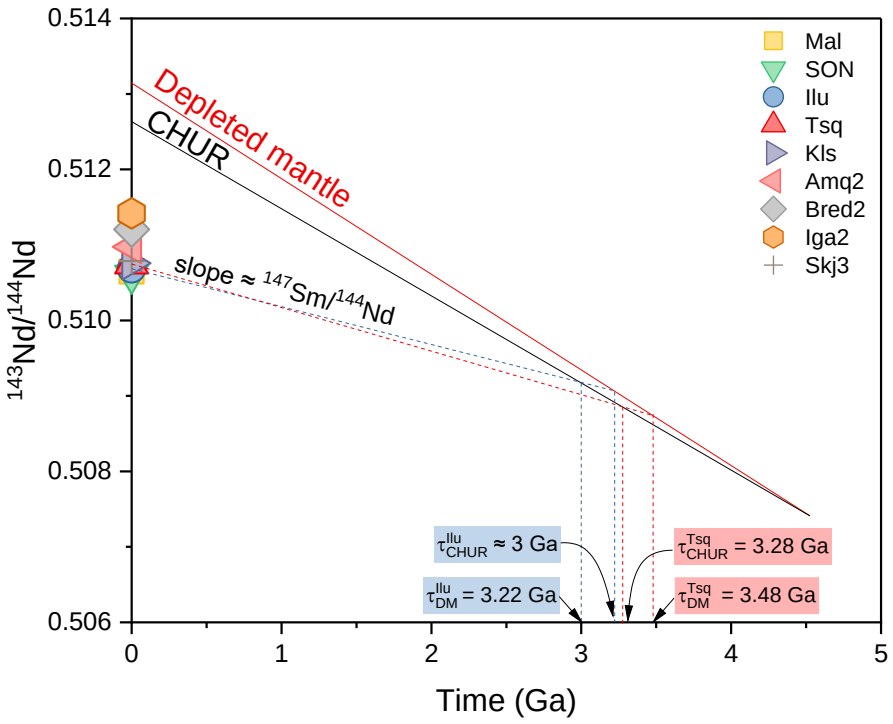


Figure 3.13: Sm-Nd model ages calculation for Ilulialik and Tasersuaq GRFs using $^{147}Sm/^{144}Nd$ and $^{143}Nd/^{144}Nd$ ratios for CHUR and depleted mantle.

Table 3.9: Sr and Nd isotope composition of glacial rock flours from Greenland.

GRF	Study area	Rb (ppm)	Sr (ppm)	$^{87}Rb/^{86}Sr$	$^{87}Sr/^{86}Sr$	Error (2σ)	Sm (ppm)	Nd (ppm)	$^{147}Sm/^{144}Nd$	$^{143}Nd/^{144}Nd$	Error (2σ)	T_{CHUR} (Ga)	T_{DM} (Ga)
MAL	Nuuk Fjord region	110.67	298.08	1.077579	0.736109	0.000006	4.17	26.10	0.096547	0.510646	0.000012	3.01435	3.23372
SON	Nuuk Fjord region	106	301	1.022188	0.737037	0.000004	3.74	23.10	0.097838	0.510682	0.000016	3.08598	3.29505
ILU	Nuuk Fjord region	171	250	1.988046	0.750708	0.000009	5.12	32.00	0.096685	0.510601	0.000015	2.99871	3.22285
TSQ	Nuuk Fjord region	85.45	291.70	0.850217	0.736156	0.000006	3.65	20.20	0.109193	0.510745	0.000016	3.27617	3.4789
KLS	Kangerlussuaq region	72.88	384.91	0.548631	0.719107	0.000008	5.22	32.65	0.096614	0.510757	0.000010	2.84984	3.09358
AMQ2	Kangerlussuaq region	68.41	365.33	0.542484	0.717259	0.000004	4.50	27.63	0.098426	0.510974	0.000019	2.56994	2.85944
BRED2	Julienhåb bugt region	68.92	339.99	0.587297	0.717873	0.000008	4.83	26.79	0.108962	0.511205	0.000009	2.47999	2.81343
IGA2	Julienhåb bugt region	127.21	533.68	0.690598	0.718027	0.000004	8.11	47.39	0.103432	0.511419	0.000018	1.98763	2.38169
SKJ3	Southeast Greenland	70.71	502.86	0.407390	0.717825	0.000005	12.49	77.29	0.097656	0.510786	0.000006	2.83556	3.08361

Rb is an alkali trace element that readily substitutes for K in K-bearing minerals such as K-feldspar and mica and is among the most incompatible elements. Sr is an alkaline earth trace element that substitutes for Ca in mineral lattices such as that of plagioclase and is less incompatible than Rb. The difference in their compatibility in melt during crystallization allows the use of Rb/Sr ratio for dating igneous rocks. The Sr isotope data for all the GRFs are presented on an isochron diagram in Figure 3.14. In Figure 3.14a Nuuk fjord GRFs show a strong linear correlation with an initial $^{87}Sr/^{86}Sr$ ratio of 0.72304 ± 0.0023 corresponding to an age of 0.98 ± 0.01 Ga. The estimated age for Nuuk fjord GRFs was much lower than that of the surrounding Archean rocks. Since the rest of the GRFs represent different geological setting it was not possible to correlate all the samples. Skjoldungen GRF Rb-Sr isotope data fits remarkably well on the 2.7 Ga reference line representing Skjoldungen igneous rocks. The difference in Rb-Sr data for the GRFs indicates that there is a differentiation of minerals taking place for the Nuuk fjord GRFs.

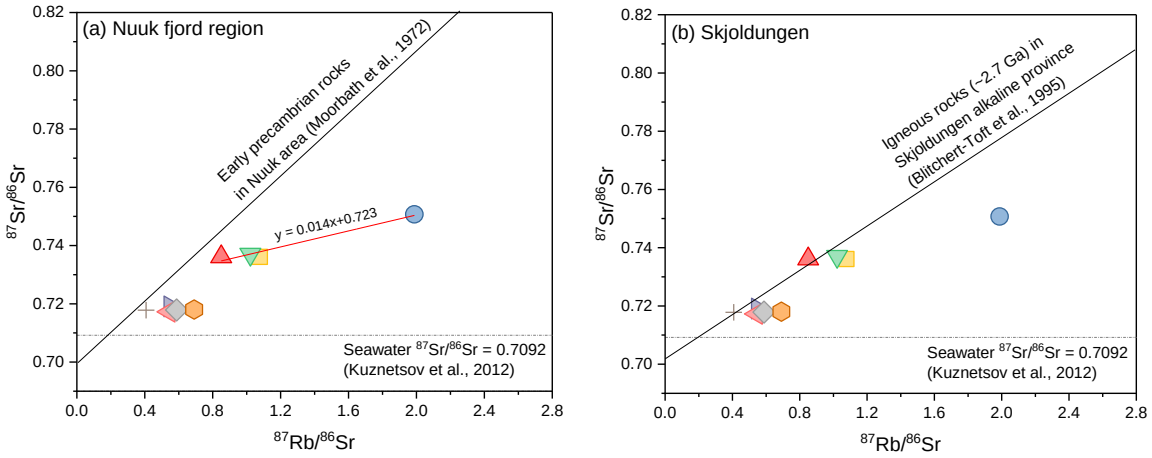


Figure 3.4.214: Rb-Sr isochron plots for Greenlandic GRFs. Reference lines for age of the surrounding rocks in (a) Nuuk gjord region and (b) Skjoldungen are plotted for reference. The horizontal line at y= 0.7092 represents the seawater ratio.

3.5. DISCUSSION

3.5.1. PROVENANCE

The GRFs are primarily derived from bedrocks surrounding their respective depositional site. CIA values in an un-weathered upper crust usually varies between 45 and 55 (Nesbitt and Young, 1982; McLennan et al., 1993) and increases with the degree of weathering. Intense chemical weathering leads to removal of alkali and alkaline earth elements that can result in CIA values to approach 100. Figure 3.15 shows CIA values between 52.88 and 61.75 indicating low degree of chemical weathering. The presence of detrital minerals in the GRFs investigated in this study physical erosion of the minerals within their respective catchment.

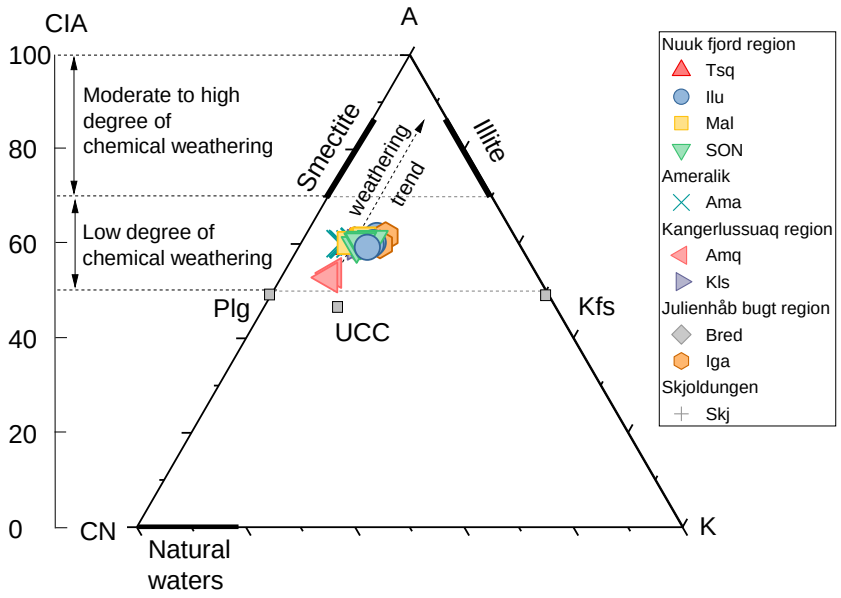


Figure 3.15: A-CN-K plot for the GRFs showing chemical index of alteration and degree of weathering among the samples. UCC =Upper continental crust; Plg= plagioclase; Kfs = K-feldspar

While majority of the GRFs were weakly peraluminous to weakly metaluminous, Amerloq shows higher metalumious character owing to a higher CaO composition. Amerloq is located in southwestern part of the central Nagssugtoqidian orogen, near the southern margin of the juvenile Paleoproterozoic (~1.92 Ga) Sisimiut charnockite suite of calc-alkaline intrusions (Kalsbeek and Nutman, 1996; Whitehouse et al., 1998). This could have contributed to a comparatively higher CaO and Na_2O content of the samples from Amerloq, which might have led to the lower CIA values. XRD analysis also reported ~2.5 % calcite in Amerloq GRF. It has

not been possible to determine if the calcite represents a marine biogenic component, a diagenetic component or a carbonate component of the subglacial catchment basement.

P and REE abundances in Amerloq were similar to those of Kangerlussuaq suggesting low contribution from the syenitic rocks present in the complex. Skjoldungen GRF exhibited an enriched REE trend in comparison to the rest of the GRFs. The raised marine deposit in Igaliku shows lower REE content at 5 m elevation than at 0.5 m elevation from the mean sea level. The enriched REE trend can be attributed to their alkaline setting and presence of P, which is likely to form complexes with REE (Blichert-Toft et al., 1995) and can be present in minerals such as apatite and monazite. Skjoldungen is an alkaline igneous province in southeast Greenland. To the inner part of the Igaliku fjord lies the alkaline Gardar igneous province (1.3-1.12 Ga), which has significant components of LILE enriched undersaturated rocks including nepheline syenites, carbonatites and lamprophyres. These could have contributed to the high REE for Bredefjord and Igaliku deposits. However, as Igaliku lies in the main agricultural area in southwest Greenland, the top surface has possibly undergone pedogenesis leading to REE loss. Amerloq and Skjoldungen show the strong influence of provenance in determining GRF composition.

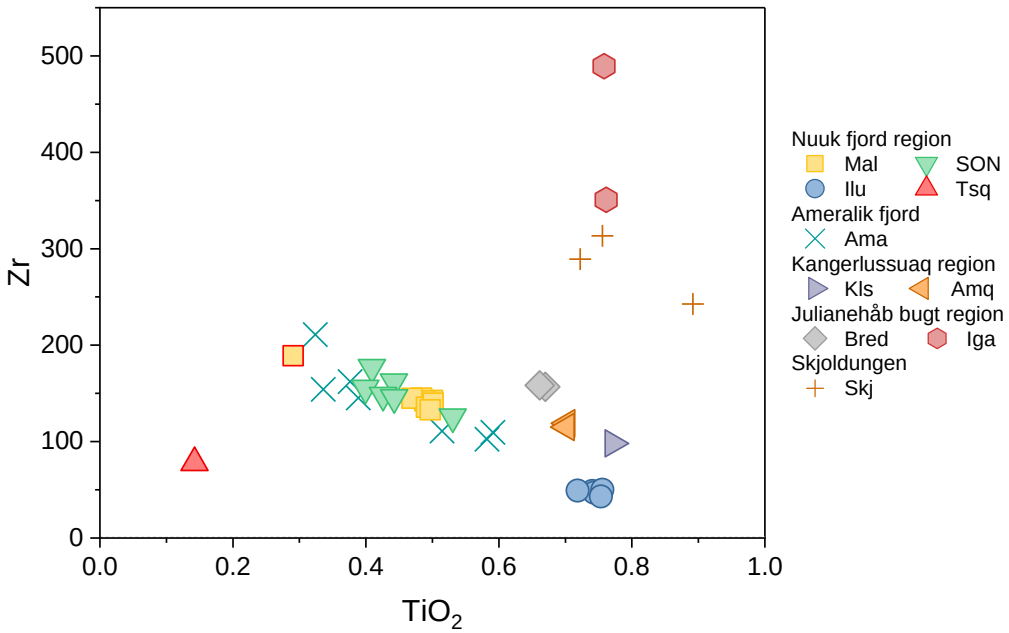


Figure 3.16: Zr versus TiO2 scatter plot showing negative correlation between the two, indicating TiO2 is not associated with HREEs. Skjoldungen and Igaliku, however, show high Zr suggesting TiO2 is associated with Zr or HREEs. Figure legend same as Figure 3.11

Heavy mineral association with sediments can be tested using scatter plots with TiO_2. TiO_2 occurs in clay minerals such as Illite or in heavy minerals such as rutile or ilmenite (Garcia et al., 1994; Ratcliffe et al., 2004). A general positive correlation between TiO_2 and Al_2O_3 for the GRFs suggests clay minerals as potential sources. TiO_2 and Zr show a weakly negative correlation for Nuuk fjord GRFs but for Skjoldungen and Igaliku GRFs, high Zr accompanied high TiO_2. This supports the HREE trends of the GRFs, where Skjoldungen and Igaliku had higher HREE content than the rest of the GRFs. XRD and SEM data coupled with chemical analysis show presence of chlorite or chloritized biotite as clay minerals in GRFs.

3.5.2. SEDIMENT SORTING

The composition of clastic sediments like glacial rock flours can be controlled by several factors, such as source rock composition, degree of chemical weathering, sediment sorting and maturity during fluvial and eolian transport and deposition, and element mobility during diagenesis and metamorphism (McLennan et al., 1980). REE, Th, Sc and HFSE have low solubility in natural waters and are generally immobile and therefore, are least affected by sedimentary processes. Consequently, these are transferred to the clastic sediments and therefore, can be used to interpret their provenance (Taylor and McLennan, 1985; McLennan, 1990; McLennan and Taylor 1991; McLennan et al., 1993). In this study, positive linear correlation between La and Th (Figure 3.17a) indicate uniform behavior between REE and Th for the GRFs.

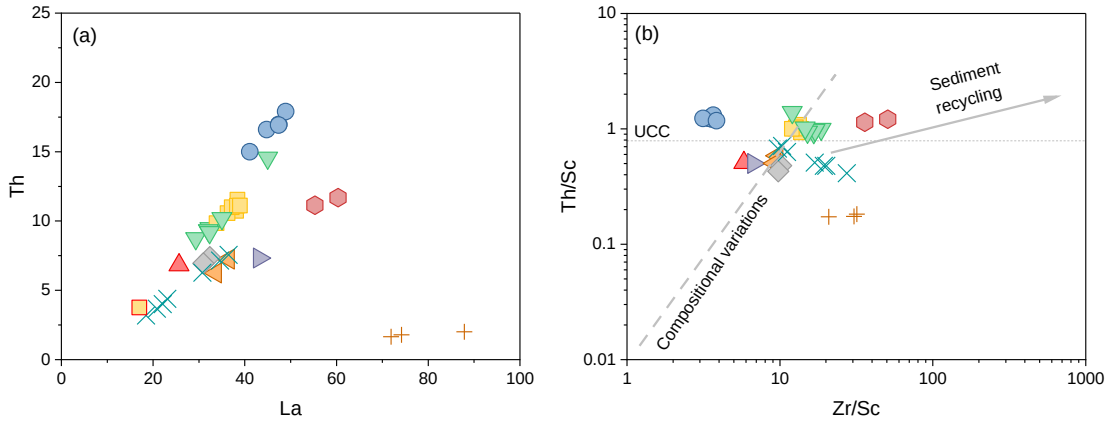


Figure 3.17: (a) Th versus La and (b) Th/Sc versus Zr/Sc ratio scatter plot for GRFs. Legend is same as Figure 3.16. Yellow filled square with red border refers to Mal-P5, which is from the soil layer at the top of the Maalutu GRF deposit.

Elements such as Th and Zr are incompatible trace elements while Sc is a compatible trace element. Therefore, ratios between such trace elements are used as geochemical parameters to constrain average provenance composition. Th/Sc ratios are sensitive to average provenance composition whereas Zr/Sc ratios are used to indicate the degree of sediment recycling (Taylor and McLennan, 1985). While majority of the GRF Th/Sc ratios plot around the upper continental crust (UCC) compositions, Skjoldungen GRF has much lower Th/Sc ratio (0.08 ± 0.005). Recycled sediments are more enriched in Zr as zircon has a strong tendency to concentrate in the coarse-grained fraction. Th/Sc versus Zr/Sc plot for Igaliku, Mal-P5 and Ameralik indicate possible effects of sediment sorting such that coarser sediments are more Zr-rich. However, low Th/Sc (average = 0.41, SD = 0.19) and low Zr/Sc (maximum = 50.8) ratios of the GRFs suggest sediment recycling is not pronounced and therefore, they are not characteristic of mature recycled sediments. The alkali content in the tidal Ameralik fjord samples decrease linearly with an increase in SiO_2. The samples with lower SiO_2 (ama4, ama5 and ama7) content were accompanied by a higher LREE content (Figure 3.12b) and a higher biotite, K-feldspar and amphibole content (Table 3.3 and 3.5). This indicates physical sorting of the material such that sites with high SiO_2 indicate quartz dilution of the bulk material.

The GRFs representing the Nuuk fjord region have originated from the granodioritic Akia terrane and therefore, have a similar source rock composition. However, they varied in their LREE composition, such that Ilulialik and Tasersuaq appeared as the two extremes for LREEs at the region while Maalutu and SON were intermediate between the two. The Ilulialik and Tasersuaq GRFs form part of an active meltwater sedimentary system in the Nuuk fjord region. Tasersuaq is a lake that receives meltwater from the Saqqap Sermersua glacier, which receives meltwater from the Greenland Ice Sheet (GrIS) by surface meltwater run-off and several outlet rivers. This means that the suspended sediment in the system may in part have interacted with the atmosphere for considerable time (years) while other parts have experienced a fast transit from sub glacial rivers to deposition the lake. Ilulialik is a tide influenced delta deposit in the Nuuk Fjord, where the water supplying suspended sediment to Ilulialik is vastly dominated by the water exiting Tasersuaq. Ilulialik also receives suspended sediment by the meltwater plume from glaciers descending into the fjord to its east and from the melting of sediment-laden icebergs. Therefore, the sediment in Ilulialik have mostly

experienced a longer transport and exposure to the atmosphere, compared to the sediment in Tasersuaq. These result in fine-grained, angular and well-sorted sediments in Ilulialik (Hopwood et al., 2016) while Lake Tasersuaq sandy sediments (Bennike et al., 2019). These indicate that the Ilulialik and Tasersuaq grain size distribution and mineral composition are likely a manifestation of sediment sorting during transit. In comparison, the poorly sorted grain size distribution in Maalutu and SON suggest that the sediments had a shorter transit time as suspended load from their origin and were deposited in a more ice-proximal setting. The sediments were deposited via meltwater discharge either directly into the sea or in a deltaic marine environment. With the onset of Holocene, the glacial retreat resulted in an isostatic uplift and exposure of the marine deposits.

In Sm-Nd model ages, Tasersuaq gives higher model age compared to Ilulialik. The old components of the basement are the 3.6 – 3.8 Ga and 3 Ga TTG gneisses, whereas granites in the area are generally 2.8 – 2.5 Ga. Biotite would be more common in the granites. Therefore, the Sm-Nd model ages are possibly closer to weighted mean model ages for the glacially eroded basement components in the sample than Rb-Sr isochron ages. The linear correlation between the Nuuk fjord GRFs indicates that the Rb-Sr alignment is a mixing line between minerals that have different closing temperatures for Rb and Sr diffusion, and are not geologically meaningful, although they show that the Sr and Rb has not been differentiated – i.e. mobilized during erosion, transport and sedimentation.

3.5.3. Environmental impact of GRF application

About 96 % of Ilulialik and 63 % of Maalutu GRF was comprised of particles finer than 20 µm. The primary mineral composition and an inherent fine grain size of the GRFs indicate applicability for enhanced weathering. Accelerating the process of natural silicate weathering by terrestrial application of crushed silicate rocks has been suggested to be advantageous alongside the intensive carbon capture technologies (Hartmann et al., 2009; Beerling et al., 2020). The CO_2 capture potential (r_{CO2}) of the GRFs was calculated based on number of moles of monovalent and divalent cations (Table 3.6). Theoretically, the maximum potential ranged from 0.13 and 0.23 t CO_2 capture t^{-1} GRF. In natural systems, however, a material's efficiency is reduced due to ocean carbonate chemistry, which is a factor of salinity, ocean water

temperature and its pCO_2. In a recent report, Beerling et al. (2020) estimate a CO_2 capture efficiency (η) of 0.86 per charge for a Representative Concentration Pathway (RCP) 8.5. Considering this efficiency value, the capture potential range from 0.1-0.2 t CO_2 t^{-1} GRF (Table 3.6). These values are much lower than for ultramafic rock (Renforth, 2012) and basalt (Beerling et al., 2020) that are preferred for enhanced weathering due to their high sequestration potential. However, the grain size and specific surface area of a material can play a vital role in reactive efficiency of the material as well as its natural availability in fine grained size would considerably reduce the cost of deployment of enhanced weathering techniques.

Moreover, the cations released due to weathering supply macronutrients essential for crop growth, which is expected to improve the soil quality. Gunnarsen et al. (2019) report a significant increase in biomass upon application of Maalutu GRF to soil. They suggest GRF as a prospective alternative to chemical fertilizers for K and Mg. These elements are potentially released from biotite upon dissolution of the material or from other K and Mg bearing mineral phases like K-feldspar, amphibole, pyroxene or chlorite. A suite of trace elements is likely to be released upon weathering but the concentration of harmful trace element is generally low in GRFs from Greenland. A suite of trace elements is likely to be released upon weathering along with alkali and alkaline earths but the concentration of harmful trace element is generally low in GRFs from Greenland. Among the GRFs investigated in this study, Amerloq showed enriched As and Mo contents exceeding the UCC concentrations. Mo content is higher than that of soil and its high concentration might be toxic to animals. Mo is likely to be present as molybdenite (MoS_2) indicated by the presence of flammable gas and ~1% total sulphur. However, chalcophile elements such as As and Cd were within the concentration range found in soil and are potentially not toxic. The slightly high U content in Amerloq GRF is also within its concentration range in soil.

Salinity in marine GRF samples as seen in Amerloq, Bredefjord and Ilulialik can pose a problem for plant growth when applied to soil but washing of Ilulialik GRF showed loss of halite with negligible changes in its chemical composition and particle size distribution. Therefore, a simple washing treatment can be implemented to reduce GRF salinity prior to their application in agricultural fields. Interestingly, halite was not detected in many of the GRFs investigated in this study. This was largely due to higher glacial freshwater concentration in

the depositional environments from where the GRFs were collected. For example, the shallow water draining the Lake Tasersuaq that enters Ilulialik via is proglacial freshwater and is low in salinity (Kjeldsen et al., 2014; Hopwood et al., 2016). Ameralik fjord is characterized by low salinity, especially in the top ~200 m, due to insolation, atmospheric heating and large inputs of meltwater discharge by the rivers near Ameragdla (Møller et al., 2006).

3.6. CONCLUSIONS

Glacial meltwater from the Greenland Ice Sheet carries range of debris particles as it travels from land to the coastal zone. The glacial milling is very intense, and a high proportion of the meltwater sediment load consists of grains in the silt-clay size fraction. The fine-grained sedimentary particles lie in suspension in the meltwater due to a low ionic strength, but upon meeting the seawater they form flocs and ultimately deposit near the shorelines. While some glacial rock flour (GRF) deposits are currently exposed along the coasts of Greenland following post-glacial isostatic uplift, many continue to form in an active sedimentary environment.

a. GRF is characterized by a high specific surface area and is predominantly silt-sized sediments with majority of them classified as light clay and clay loam textural classes in International Soil Science Society. While some GRFs display unimodal grain size distribution, some were bimodal in grain size distribution.

b. GRF consists of detrital bedrock components that were subjected to physical erosion and transport as suspended sediments in the meltwater. It is chiefly composed of plagioclase, K-feldspar, mica, quartz and amphiboles. Accessory minerals such as epidote, apatite, titanite, halite etc. constituting <1 area % of the mineral map section were determined by AQM analysis. Calcite was detected only in Amerloq GRF in minor quantities while the rest of the GRFs had negligible calcite, if present.

c. The fine-grained sediments were chemically immature and were classified as shales and wackes based on major element compositions. Microscopically, particles are irregular and in some cases, highly angular in shape. The finer sized fractions were dominated by phyllosilicates that have a tendency to aggregate with one another and often envelop the larger grain surfaces.

d. Low CIA values indicate that the degree of chemical weathering of the GRFs is low. The data suggest that sediments undergo physical sorting during transport and quartz is concentrated in the coarser-grained fraction.

e. GRFs showed strong influence of provenance in their HREE compositions. The LREE compositions of GRFs from one region varied due to sediment sorting.

f. Harmful trace element content is generally low in the GRFs from Greenland. Nonetheless, it is recommended that the presence of any harmful trace element should be critically evaluated before large-scale application.

Chapter 4

Field reports from a Glacial Rock Flour deposit in West Greenland

Abstract

Several gigatons of suspended sediments are annually transported by the meltwater to the coastal areas in Greenland. The suspended fine grained 'glacial rock flour' (GRF) form flocs upon meet the saline sea water and deposit. Maalutu is one such glacial rock flour deposit that formed ~10,000 years ago but has remained largely unweathered. The water chemistry of the streams, groundwater springs, surface ponds and pore surfaces at the Maalutu catchment are described. The groundwater springs that emerge from the base of the deposit demonstrate high solute concentrations, which then enters the stream water compositions and then is carried to the sea. The major cation concentrations are dominated by Na (3-123 mg L^{-1}) followed by Ca^{2+} (0.6-28 mg L^{-1}), Mg^{2+} (0.4-20 mg L^{-1}) and K^{+} (0.2-21 mg L^{-1}). The bivariate plots of Na-normalized molar ratios of the dissolved species (Ca, Mg and HCO_3) indicate silicate weathering for the stream and groundwater spring compositions, which represent GRF-reacted waters. The surface waters compositions have limited interaction with the GRF and the top surface of the deposit had a developed soil layer. Their solute compositions were lower than that of stream and groundwater, and mainly indicate dissolution of evaporites such as halite. The infiltration of the surface water through the deposit is possibly minimal. Therefore, as the stream water alkalinity is mainly contributed by the springs, it varies inversely with discharge during precipitation. The limited interaction of the GRF with water, post-uplift, has rendered the material largely unweathered and chemically immature.

4.1. INTRODUCTION

The melting Greenland Ice Sheet (GrIS) contributes 7-9% of the global sediment output to the seas adjacent to Greenland at present (Overeem et al., 2017). It erodes bedrock sediments, carries along the debris and transports 1.28 ± 0.51 Gt suspended sediment load to the oceans annually (Overeem et al., 2017; Syvitski and Kettner, 2011). This fine grained silicate material, referred to as glacial rock flour (GRF), provides a potential climate feedback mechanism in that its weathering may consume atmospheric CO_2. The weathering may take place either in the proglacial freshwater or marine environment, depending on the location of the deposition of the fines exported with the meltwater.

During a low discharge season, ~70% of the suspended sediments is <20 µm (Hasholt et al., 2018) and due to a large surface area it has highly charged surfaces (Kranck, 1973). Ionic strength of glacier meltwater usually ranges from 10^{-4} to 10^{-3} M and from 1 to 10 g L^{-1} for suspended sediment (Bagshaw et al., 2021). As the particles interact during transport, the colliding particles often attach to one another and form aggregates. When the meltwater meets with the seawater, which has a high ionic strength (~0.7 M), the otherwise stable fine particles become destabilized and aggregate (Gregory, 2006). It is common for the suspended meltwater particles to flocculate at the river plumes and deposit along the coastal areas (Markussen et al., 2016). Many such glacial rock flour deposits continue to form as part of an active marine sedimentary system. However, some are now exposed owing to the receding GrIS margin since the start of Holocene, which was followed by rising sea levels and an isostatic uplift of the continental landmass. A net regression thus raised marine GRF deposits, which formed in a shallow marine environment such as in Maalutu possibly ~10,000 years ago. The deposit is a poorly sorted mix of larger and finer grains and is, therefore, expected to have been ice-proximal during its deposition (Chapter 3).

A reconnaissance study and a geochemical study of the regional water bodies at Maalutu were conducted in 2017 and 2018, respectively. Here, we present our field observations and hydrochemical studies of the different water bodies at the Maalutu GRF deposit from our 10-day field investigations from 21 August 2018 to 30 August 2018. We investigated if the deposit has been subjected to significant weathering and hence, as a sink for atmospheric CO_2.

4.2. STUDY AREA

Maalutu is located in the outer Nuuk fjord system and is located 7 km north to the town of Nuuk, West Greenland. The climate is subarctic and humid with a sub-zero mean annual air temperature of -1.2°C (Karte, 1983). Mean precipitation is about 752 mm per year (Cappelen et al., 2001). Maalutu receives precipitation throughout the year but is usually covered in snow during winter months. In warm seasons (May – September), Nuuk region experiences higher rainfall while. Greenland is largely composed of Precambrian crystalline rocks which formed during a succession of Archean and early Proterozoic orogenic event and stabilized as part of the Laurentian shield ~1.6 Ga (Escher and Watt, 1976). The study area is located in the Paleo- to Mesoarchean Akia terrane at the Nuuk fjord region that forms part of the North Atlantic Craton in West Greenland. The terrane is composed of a ~3.22 Ga dioritic core with enclaves of 3.03-2.97 Ga tonalitic orthogneisses and inclusions of leucogabbro and mafic volcanic rocks and had later undergone granulite-facies metamorphism at 2.98 Ga (Garde 1997, 2007).

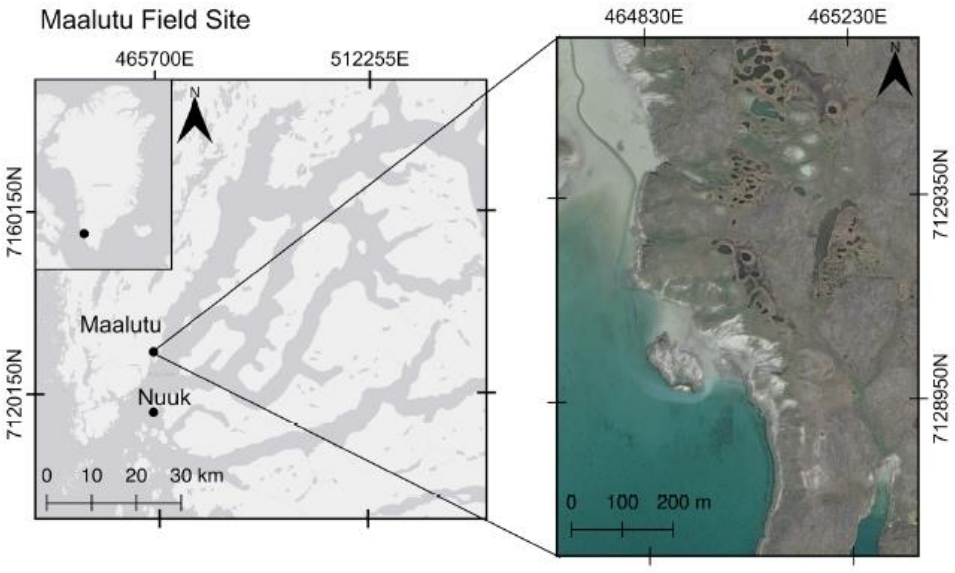


Figure 4.1: Map of the study area and sampling locations. A) Location of the Maalutu in Greenland



Figure 4.2: (a) Profile view of the glacial rock flour deposit at Maalutu. The image was taken during a low tide. (b) View of the deposit from the top showing sea level reaching till the horizontal layer marked by seaweed, pebbles and boulders as seen in (a), during high tide.

4.2.1. Field observations

Maalutu is a ~20 m high promontory (or mud terrace) with the top surface characterized by a soil layer, 60-80 cm thick; a vegetation cover of plants, such as sphagnum mosses; a hummocky structure, called earth hummocks (thúfur); and a network of ponds and lakes. Earth hummocks are the dome-shaped mounds, as seen in Figures 4.4a, b, and are common cryogenic landforms that develop due to a freeze-thaw effect (Schunke, 1977). Their occurrence indicates that the ground has been affected by sporadic permafrost. At one of the sampling sites, closer to the edge of the exposed profile, ice crystals were observed at ~60 cm depth.

The southern zone of the promontory was a steep mud cliff terrain intersected by the streams and gullies draining the surface water whereas the northern zone was a gentle terrain with soil and vegetation cover. Precipitation was accumulated on the top surface as lakes that feed the streams and gullies. Although several gullies were found draining the surface water through the deposit, their flux was trivial in comparison to one stream in the southern zone that led majority of the surface runoff to the sea. Water samples were collected from several points along this ~60 m long main stream (MS) as well as few puddles around it. The hummocky surface overlaid the glacial rock flour deposit as seen from the exposed profile of the mud terrace.

The study was continued the following year in August 2018 with a field campaign focused on sampling from the different water bodies at the study area. The previous year, MS was sampled along with three narrower springs at the field site. MS was joined by several narrow springs emerging out of the base of the deposit entered it laterally. These springs show a high electrical conductivity and pH in field measurements indicating reaction with the underlying glacial rock flour deposit. The precipitation was more sporadic in the 2018 field campaign than in the previous year and the sediments dried very quickly during daylight and become solid and stable as seen in Figure 4.4c. During low rainfall and subsequently low flux of some streams, deposition of iron oxide were observed in some parts of few gullies. The sediment around the area suggested presence of pyrite.

The UTM coordinates of the sampling sites are given in appendix A.5.



Figure 4.3: Interaction between surface runoff from the deposit and the seawater and extent of transportation of the sediments. Photo taken from the base of the deposit.

Several ellipsoidal calcite concretions were found embedded in the deposit (Figure 4.4e) with a smooth but distinct outer surface, some of which were bound to a rock surface near the streams. The observed concretions were generally <5 cm in diameter. Some of the concretions consisted of a fossil bone preserved at its center, visible with unaided eyes while most of them lacked such a visible source of organic matter. Many of the concretions were also found attached to rock surfaces.

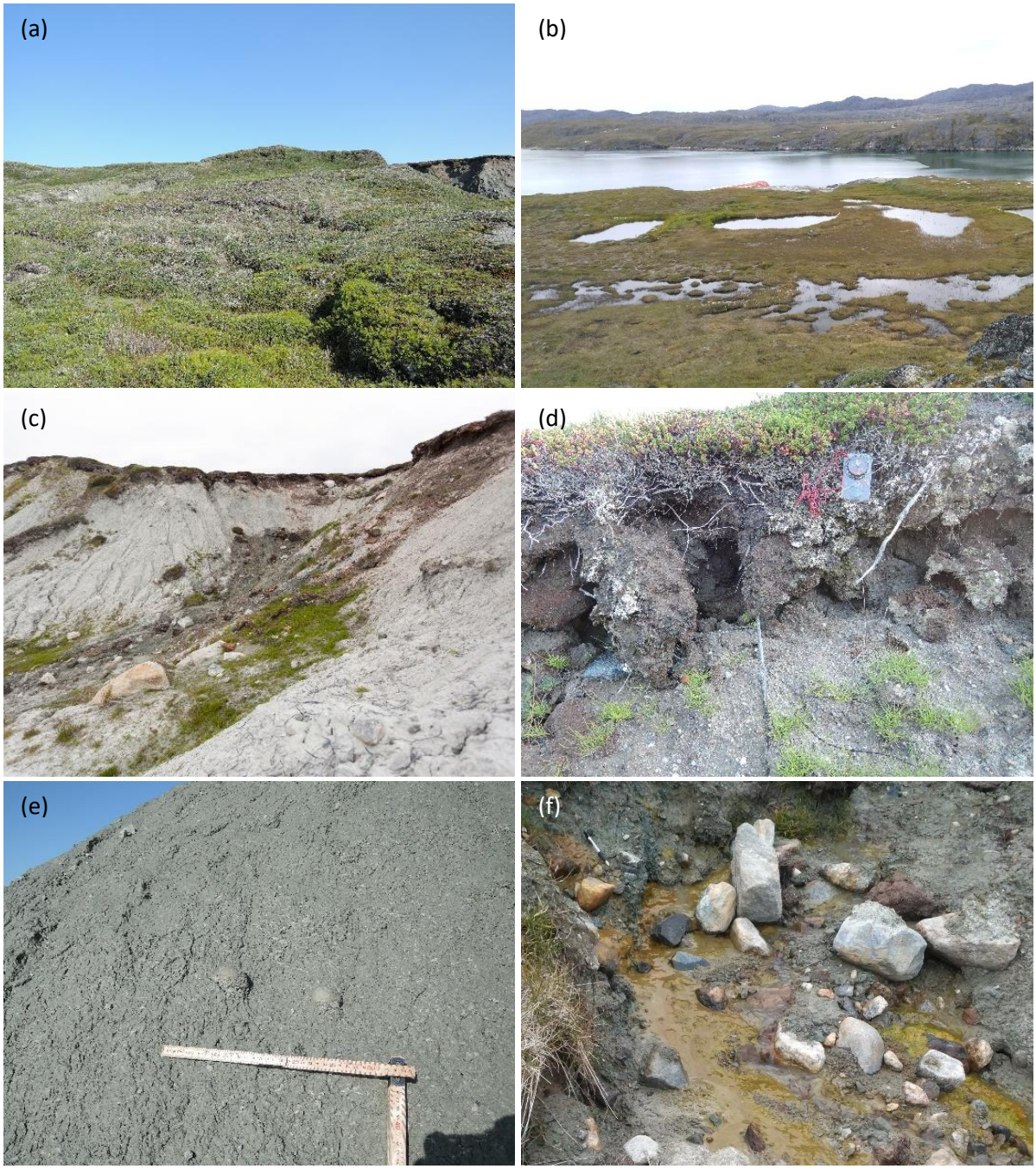


Figure 4.4: (a) Terrain at the top of Maalutu deposit showing thúfurs and ponds, (b) top view of the deposit showing surface lakes; (c) view of the deposit on a sunny day; (d) top ~10 cm surface at the study area showing soil characteristics; (e) spherical carbonate concretions ranging in few centimeters in the GRF deposit; (f) side stream during low flow (contd).



Figure 4.4: (g) main stream draining the Maalutu study area with groundwater springs entering it from the base of the deposit at the left.

4.2.2. Maalutu GRF mineralogy and composition

Glacial rock flour (GRF) is the product of abrasion and natural crushing of the bedrock by the glaciers moving along their walls resulting in fine-grained material carried by the meltwater towards the sea. Chapter 3 reports that Maalutu GRF particles are poorly sorted mix of silty clay particles and have a median size of 7.86 µm. It is composed of plagioclase (43.5 %), microcline (10.7 %), quartz (23.1 %), biotite (7.8 %), amphiboles (10.4 %), augite (1.8 %) and epidote (2.7 %). Calcite is detected by scanning electron microscopy (SEM), but is present in negligible quantities. The major element composition of the material is given in Table 4.1.

Table 4.1: Characteristics of Maalutu glacial rock flour described in Chapter 3.

Parameter	Mean	Mineral oxide	Concentration
Total CO_2	0.17 %	SiO_2	63.47 %
Organic carbon	0.03 %	Al_2O_3	15.63 %
Total sulfur	0.01 %	Fe_2O_3	5.17 %
		MnO	0.07 %
		MgO	2.62 %
BET-N_2 surface area	15 $m^2\ g^{-1}$	CaO	3.78 %
		Na_2O	3.76 %
Particle size distribution		K_2O	2.82 %
Clay (<2 µm)	30.1 %	TiO_2	0.49 %
Silt (2–20 µm)	34.9 %	P_2O_5	0.12 %

Fine sand (20–200 µm)	32.6 %	LOI	2.14 %
Coarse sand (0.2-2 mm)	2.4 %	Total	100.06

Major element (wt%), total carbon, organic carbon and total sulfur were analyzed by emission spectrometry (ICP-OES); LOI = loss on ignition at 1000 °C at *Centre de Recherches Pétrographique et Géochimiques* (CNRS), Paris.
BET-N_2 surface area was measured using Coulter SA3100 at Geological Survey of Denmark and Greenland (GEUS).
Particle size distribution was measured by wet sieving and pipette method using … at AGROLAB Agrar und Umwelt GmbH, Germany.

4.3. METHODOLOGY

4.3.1. FIELD MEASUREMENTS AND SAMPLE COLLECTION

4.3.1.1. Water sampling

Four streams were identified at the deposit, of which MS drained the highest amount of surface water to the sea. Downstream, it received lateral inputs from several springs emerging from the lowest exposed level of the deposit. The spring water was characterized by high electrical conductivity (EC) and pH (Figure 4.5). The spring waters are referred to as groundwater in this study based on their observed point of origin. Waters sampled from the network of ponds at the top of the deposit are referred to as surface water. Further, vertical porewater profiles were collected at six sites using PRENART suction cells installed at the plateau.

During first sampling at each sampling location, the site was marked with a wooden marker stick to aid replicate sampling and measurement of the temporal variation in the system. Stream water samples were collected from the four streams, at an elevation of ~3 m above mean sea level (AMSL) to estimate their overall export of dissolved matter to the sea. Groundwater samples were collected closer to their emerging point to avoid any mixing effect. The water samples were collected using a 60 mL polypropylene syringe after rinsing it several times with the sample water and were filtered into 3 sampling vials, each for cations (and Si), anions and alkalinity analysis. Samples for cations analysis were filtered directly into sampling vials with 0.1 mL 18mM HNO_3 to prevent further reaction and precipitation of cations. All samples were stored at -5°C at the field site and were sent for analysis within a few days of returning from the field. The pH and EC of the water systems were measured at

these sites using a portable WinLab data line pH- and EC meter. The pH and EC electrodes were calibrated once every day before sampling using Certipur NIST buffers.



Figure 4.5: (a) View of the main stream from the top of the deposit, carrying low EC surface water towards the sea, and downstream receiving lateral inputs from high EC groundwater springs. Their flow paths are drawn upon by a marker and the arrows indicate the direction of flow; (b) Field setup for pore water sampling showing PRENART suction sampling system.

Porewater samples were collected at six sites in the topsoil of the deposit by a suction-cup sampling system created by PRENART. PRENART suction-cup samplers were installed in 3-5 different depths at each site, and the pore water samples were extracted using a portable vacuum pump. At first, a solid cylindrical steel rod was used to create the sampling holes into the ground. The PRENART samplers were next inserted into the soil through a hollow rod similar in diameter to that of the steel rod. At all the sampling sites, the sediments were stable when the steel rod was exchanged with the sampling rods except at site P5. The sediments underneath collapsed as soon as the steel rod was removed due to an unconsolidated sandy layer. Therefore, the measured depths at P5 were 20-30 cm shallower than the initially dug depth. The overall depth from which pore samples were collected ranged from 20 to 110 cm.

4.3.1.2. Discharge measurements

Discharge at the streams and groundwater springs were measured manually using a 1" Baski cutthroat flume. Surrounding sediment at a sampling site was used to place the flume horizontally with the help of a spirit level by creating dams on either side of the flume to prevent water from flowing around the flume. The water was then allowed to flow through the flume until a free flowing condition was achieved. The discharge rate (Q) is based on different sizes of cutthroat flumes and is expressed as

$$Q = K_l \cdot W^{1.025} \cdot h_a^n \quad (4.1)$$

where Q is measured in L t^{-1}, K_l is the flume discharge constant, W is the throat width of the flume, h_a is the piezometric head and n is the discharge exponent. For the 1 inch wide and 18 inches long Baski flume, $K_l \cdot W^{1.025}$ = 225, n = 2, and Eq. 4.1 calculates Q in gallons per minute (derived from Baski Flume Flow Calculation Table).

Discharge at the four streams were measured almost daily for a period of 10 days at ~3 m elevation AMSL along with sample collection to estimate the total flux. Fewer discharge measurements for groundwater springs could be taken due to difficulty in setting up the flume, given that the springs had poorly defined origins of flow and the surface run-off from the springs was much narrower than the streams. They were taken close to the deposit from where they would emerge to complement the collected groundwater samples. Several ephemeral springs were observed at the exposed deposit profile post-precipitation making

the area extremely muddy and slippery and causing difficulty in setting up the flume. Nevertheless, samples and discharge data were obtained from four groundwater springs.

4.3.1.3. Sediment sampling

Samples were obtained from sediment profiles at nine different sites in the study area and were analyzed for inorganic and organic carbon content, and major and trace element composition. They were collected from the walls of the cylindrical steel rod used for PRENART sampling setup. The samples were stored at -5°C at the field site. After returning from the field, they were dried at 60 °C overnight and were prepared for analysis.

4.3.2. ANALYTICAL METHODS

4.3.2.1. Water composition analysis

All water samples were filtered through Frisenette 0.22 µm syringe filters into polyethylene vials and were collected for laboratory analysis of cations (Na^+, K^+, Ca^{2+}, Mg^{2+} and Si), anions (SO_4^{2-}, Cl^-, NO_3^-), alkalinity and water-stable isotopes (^2H (D) and ^{18}O). Cations were analyzed by inductively coupled plasma mass spectrometry (ICP-MS) using an Agilent 7900 at ALS Scandinavia AB. Accuracy for the cations was determined by analyzing SLRS-6 River Water - Certified Reference Material for Trace Metals, an external standard (SM1494-002) and an in-house standard. Major anions were analyzed using a Dionex Aquion Ion Chromatography (IC) system at the Department of Geosciences and Natural Resource Management (IGN), University of Copenhagen.

Water isotopes were analyzed at the University of Copenhagen on a Picarro Cavity Ring-Down Spectrometer (CRDS) L2120-I with the international standard for seawater (VSMOW) as reference. To minimize atmospheric interaction of the samples collected for alkalinity, sampling bottles were filled to the brim to avoid leaving any headspace. They were measured by Gran titration using a HACH digital titrator upon arrival to the laboratory. The precision and accuracy of the titration method was determined using 1 and 2 mM $NaHCO_3$ solutions as alkalinity standards and were within ±1 %.

4.3.2.2. Sediment major & trace element analyses

Dried sediments were crushed to <80 µm and were sent to *Centre de Recherches Pétrographique et Géochimiques* (CNRS) in Paris at *Service d'Analyse des Roches et des Minéraux* (SARM) for geochemical analysis. About 300 mg sample fused with $LiBO_2$ was dissolved in a HNO_3-H_2O_2-glycerol mixture and major elements were analyzed by emission spectrometry (ICP-OES) using a Thermo Fischer iCap6500. Trace element were analyzed by flow injection inductively coupled plasma mass spectrometry (FI-ICP-MS) using a Sciex Perkin Elmer ELAN 5000a quadrupole mass spectrometer following the techniques described in Carignan et al. (2001). The instrument was calibrated using a multi-element doped solution of the reference material BR (alkali basalt). REE contents were measured using the mass spectrometer by an automatic on-line, low pressure liquid chromatography (LC-ICPMS) sample introduction system.

4.3.2.3. Ion speciation modelling

The pCO_2 and calcite saturation indices were calculated based on the measured major cation concentrations of the water samples using the software PHREEQC 3 and WATEQ4F database (Parkhurst and Appelo, 2013).

4.4. RESULTS

4.4.1. COMPOSITION OF THE WATER AT THE DEPOSIT

The pH, electrical conductivity (EC) and temperature variations in the water samples with respect to elevation at the site are presented in Figure 4.6. From the 2018 data, the groundwater springs that enter the streams laterally show a high EC (360 – 782 µS cm^{-1}), collectively, and are higher than those found in surface (48.8 – 66 µS cm^{-1}) and stream waters (108.4 – 447 µS cm^{-1}).

The 2017 data captured a rapid increase in pH and EC downstream at ~12 m.a.s.l along MS (M2-8 to M2-1) that indicate contributions from the groundwater springs consisting of an alkaline pH (7.59 – 9.35). While the temperature for majority of the water samples ranged from 3.8 to 12 °C, porewaters display a slightly higher temperature than the surface, stream and groundwaters. Table 4.2 lists the water composition in the surface waters, pore waters, groundwater springs and stream waters in the Maalutu rock flour deposit. Among all the samples, Na was the dominant cation and varied over a wide range from 3 to 123 mg L^{-1}, while Ca^{2+} (0.6 – 28 mg L^{-1}), Mg^{2+} (0.4 – 20 mg L^{-1}) and K^{+} (0.2 – 21 mg L^{-1}) had similar relative ranges. The concentration of bicarbonate ions (HCO_3^-), measured as alkalinity, ranged from 0.9 to 215 mg L^{-1} and was the most variable among anions followed by SO_4^{2-} (0.5 – 163.4 mg L^{-1}) and Cl^- (6.2 – 32.8 mg L^{-1}). The relative abundances of major cations and anions show a characteristic distribution for the four types of water samples (Figure 4.7). While the majority of the samples were enriched in Na and K, porewaters show a slightly greater relative abundance of Si. In case of anions, pore and surface waters were dominated by Cl^- while stream and groundwater springs had a relatively higher concentration of SO_4^{2-} and HCO_3^-.

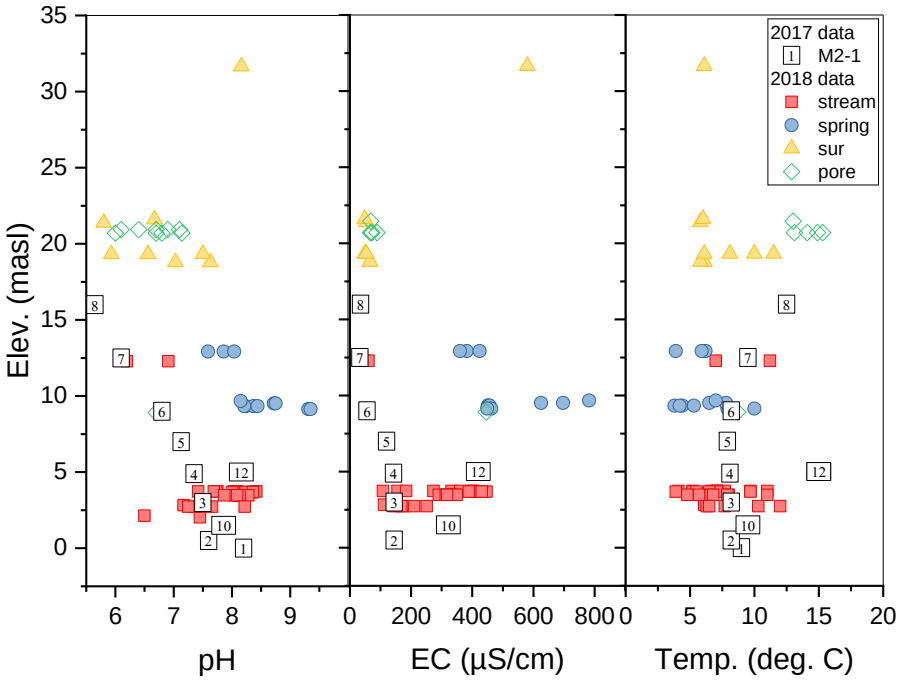


Figure 4.6: Variation in field parameters, pH, electrical conductivity (EC) and temperature of the different water samples at the field site with elevation.

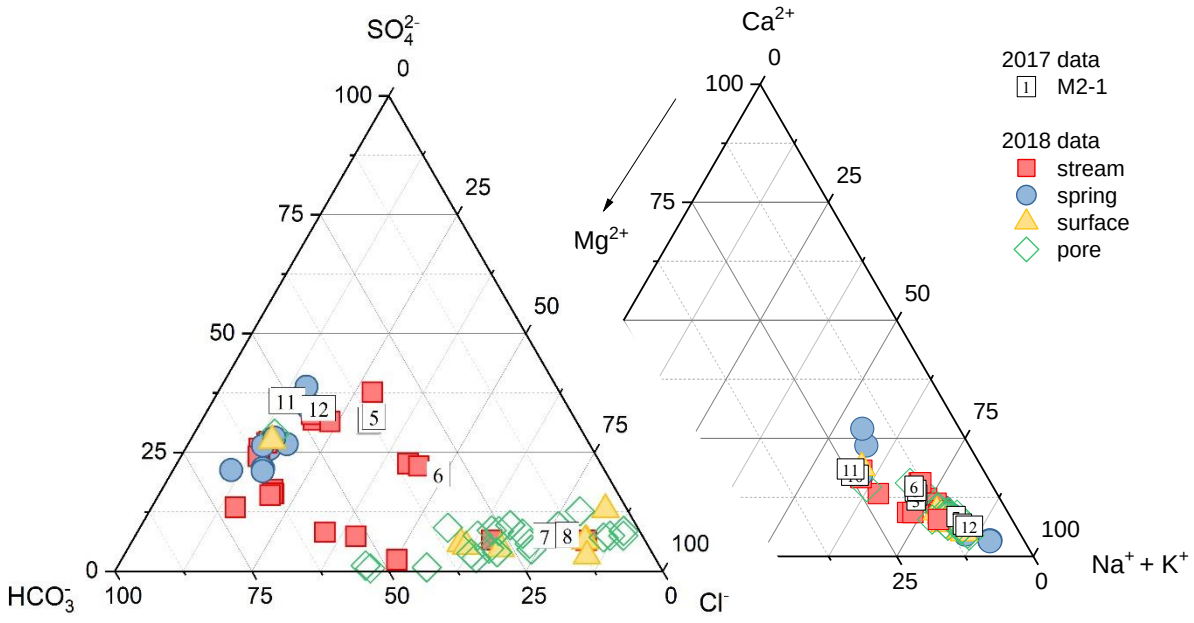


Figure 4.7: Ternary diagram showing relative molar abundances of a) major cations and b) major anions concentration in surface water, pore water, stream water and groundwater springs.

4.4.2. STREAM AND SPRING DISCHARGE

Discharges were measured at four streams and four groundwater springs at the study area. Stream discharges to the sea ranged from 0.06 × 10^{-4} m^3 s^{-1} at S10 to 9.6 × 10^{-4} m^3 s^{-1} at S1, which measured contribution via MS to the sea. MS had the highest average discharge of 4.3 × 10^{-4} m^3 s^{-1} followed by 1.4 × 10^{-4} m^3 s^{-1} at S7. The higher discharge at S1 on 23rd August 2018 can be attributed to a higher intensity of precipitation the previous day. Figure 4.8a shows the inverse relationship between discharge and EC at S1. It suggests a dilution effect of ions in stream water due to the higher supply of surface water with a lower solute concentration. The effect of precipitation was less pronounced in the other narrower streams as well as the groundwater springs investigated in this study.

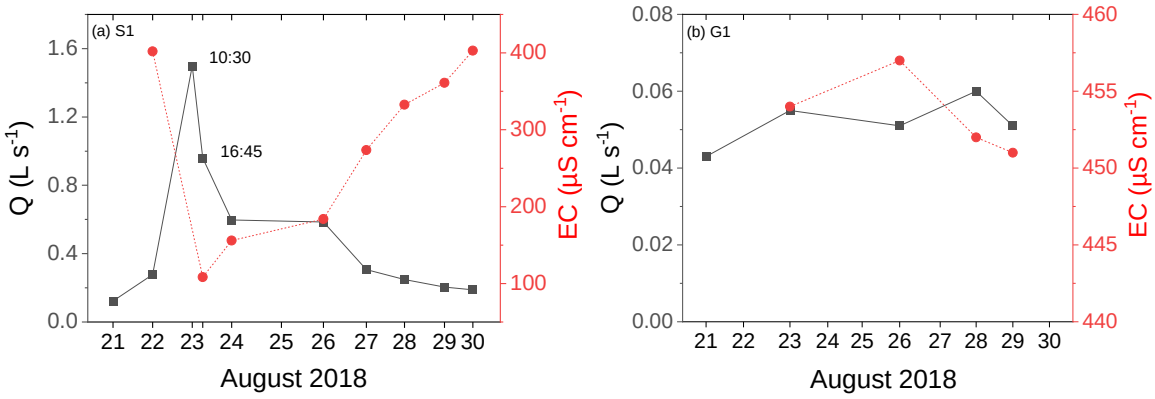


Figure 4.8: Hydrographs showing variation with respect to electrical conductivity (EC) in (a) stream water (S1) and (b) groundwater spring (G4).

The groundwater spring samples were collected before they entered the streams. The highest average discharge of 0.7 × 10^{-4} m^3 s^{-1} was recorded for the groundwater spring at G13 followed by 0.5 × 10^{-4} m^3 s^{-1} at G4. Both the streams discharging through G13 and G4 were contributing to the MS. Figure 4.8b shows negligible increase in discharge, accompanied by a decrease in EC at G4 suggesting low infiltration rate of the Maalutu glacial rock flour deposit.

Table 4.2: Detailed water sample data at Maalutu field site.

Site	Sample date and time	Elevation (m)	Depth (cm)	pH	EC (µS/cm)	Temp. (°C)	Q (L/s)	Alk. (meq/L)	Ca^{2+} (mg/L)	K^{+} (mg/L)	Mg^{2+} (mg/L)	Na^{+} (mg/L)	Si (mg/L)	SO_4^{2-} (mg/L)	NO_3^{-} (mg/L)	Cl^{-} (mg/L)	DIC (meq/L)	$\delta^{18}O$ (‰)	δD (‰)	d-excess	Sample ID
2017 Field data																					
S1-2-08				5.65	35	12.5		0.04	0.98	0.5	0.836	6.62	1.55	0.02	0.00	0.25	0.30	-13.82	-105.19	6.41	M2-08
S1-2-07				6.10	33	9.5		0.06	1.26	0.55	0.9	6.68	1.71	0.03	0.00	0.25	0.20	-13.89	-105.62	6.66	M2-07
S1-2-06				6.80	56	8.2		0.17	3.49	1.52	2.05	8.64	2.43	0.11	0.00	0.27	0.25	-13.78	-104.37	6.96	M2-06
S1-2-05				7.13	120	7.9		0.51	8.48	4.18	5.27	22.5	3.43	0.46	0.02	0.44	0.62	-13.63	-102.76	7.24	M2-05
S1-2-04				7.35	143	8.1		0.52	8.7	4.52	5.67	23.1	3.83	0.44	0.02	0.43	0.59	-13.49	-102.22	6.69	M2-04
S1-2-03				7.50	145	8.2		0.54	8.78	5.29	6.89	27.5	3.78	0.45	0.02	0.43	0.59	-13.55	-102.18	7.15	M2-03
S1-2-02				7.60	145	8.2		0.54	8.84	4.73	6.06	25.5	4.02	0.45	0.03	0.44	0.58	-13.45	-102.12	6.4	M2-02
S1-2-01				8.20	11128	9		1.07	161	144	491	3810	2.1	10.13	0.00	189.53	1.09	-10.02	-76.49	3.77	M2-01
2018 Field data																					
Stream water compositions																					
S1	21/08 11:30						0.12														n.s.
S1	22/08 11:00			7.69	402	5.2	0.28														n.s.
S1	23/08 10:30						1.50														n.s.
S1	23/08 16:45			7.42	108.4	11	0.96	0.26	3.39	2.87	2.41	13.15	2.01	15.83	0.19	10.91	265.44	-12.47	-95.98	4.46	030-QM
S1	24/08 10:00			7.75	156	6.7	0.60														n.s.
S1	26/08 16:30			7.73	184	9.7	0.59	0.54	6.62	4.69	4.36	20.2	3.3	34.46	0.25	13.50	175.78	-12.17	-93.12	4.97	057-VQ
S1	27/08 18:00			8.09	273.5	7.7	0.31	0.85	10.95	6.2	5.45	25.2	4.39	56.93	0.48	15.75	867.81	-12.37	-93.67	5.94	001-FI
S1	28/08 16:33			8.42	332.5	7.1	0.25	1.13	13.55	7.91	6.92	31	5.49	72.05	0.68	17.02	1142.30	-12.60	-94.42	6.98	004-PW
S1	29/08 16:20			8.03	361	7.1	0.20	1.27	15.6	9.66	8.55	37.6	6	84.40	0.88	18.39	1309.93	-12.70	-95.52	6.77	010-BI
S1	30/08 09:15				403	4.1	0.19														n.s.
S2	21/08 12:20						0.13														n.s.
S2	23/08 10:45						0.04														n.s.
S3	21/08 11:45						0.10														n.s.
S5	21/08 12:09						0.02														n.s.

S5	23/08 18:34	6.2	49	11.2	0.96	0.04	0.88	0.74	0.971	7.23	0.88	2.12		9.95	79.34	-12.09	-95.07	2.40	034-VB
S6	23/08 10:10	7.45				0.25	3.32	2.42	2.18	11.55	1.78	15.86	0.1	11.77	274.00	-12.69	-98.81	3.62	040-MX
S8	22/08 11:30	7.17	111.6	6.1	0.01														n.s.
S7	22/08 11:10	8	389	5.5	0.09														n.s.
S7	23/08 10:30	8.36				2.26	19.2	15	19	45	12.25	84.98	0.4	18.51	1275.75	-12.46	-93.09	7.26	036-KT
S7	24/08 10:17	8.36	447	6.5	0.07														n.s.
S7	26/08 17:00	8.33	411	9.7	0.14	1.83	19.65	13.4	14.55	28.9	10.15	82.10	2.25	16.23	896.35	-12.30	-91.42	7.41	016-KY
S7	27/08 18:24	8.24	413	7.1	0.14	1.87	20.6	14.8	17.35	33.9	10.35	82.52	2.12	16.13	906.36	-12.37	-91.24	8.07	074-MH
S7	28/08 18:16	8.32	422	5.2	0.14	1.96	20.2	14.9	16.9	32.6	10.55	80.07	1.85	15.47	961.25	-12.41	-91.56	8.20	028-EM
S7	30/08 09:22		431	3.9	0.14														n.s.
S9	22/08 11:45	7.87	349	5.7	0.09														n.s.
S9	23/08 10:55	8.03			0.05	1.79	10	9.88	8.07	42.2	9.96	47.42	0.45	20.59	891.36	-11.65	-89.43	4.24	017-DI
S9	24/08 10:17	8.09	345	6.8	0.08														n.s.
S9	26/08 17:30	8.12	332	11	0.07	1.73	9.4	10.15	8.34	41.8	10.15	31.21	0.23	13.15	963.24	-11.59	-87.26	5.82	049-OK
S9	27/08 18:40	8.28	320.4	7.9	0.05	1.67	9.06	9.97	8.08	41.3	9.58	41.64	0.28	19.47	858.44	-11.20	-86.34	3.72	058-UG
S9	28/08 18:29	8.13	313.8	6.6	0.09	1.64	8.79	9.71	8.49	42.2	9.45	39.58	0.29	18.64	867.52	-11.05	-87.05	1.67	070-SL
S9	29/08 17:52	8.19	291	8	0.07	1.63	8.98	8.54	6.87	36.5	8.7	40.67	0.3	19.23	878.06	-11.30	-87.05	3.71	015-DU
S9	30/08 09:30		318	4.8	0.06														n.s.
S10	22/08 12:00	7.25	142.5	6.3	0.08														n.s.
S10	23/08 11:14	7.38			0.04	0.56	3.71	4.06	4.22	14.45	6.98	7.55		15.43	448.51	-13.29	-98.54	8.43	055-QP
S10	24/08 10:33	7.44	168.3	7.7	0.03														n.s.
S10	26/08 18:00	7.66	175.2	12	0.01	5.22	5.89	6.25	19.85	7.54	5.22	11.78		18.20	648.11	-12.75	-94.23	8.28	027-VW
S10	27/08 19:05	8.22	210	10.3	0.00														n.s.
S10	28/08 18:43				0.00														n.s.
S10	30/08 09:45		251	6.5	0.00														n.s.
S11	23/08 12:04	6.5			0.00	0.11	1.06	0.57	1.035	7.59	1.66	2.44		9.03	240.07	-12.48	-95.80	5.19	063-VA
Groundwater spring compositions																			
G4 (S1)	21/08 11:59				0.04														n.s.
G4 (S1)	23/08 17:43	8.37	454	5.3	0.06	1.52	14.7	12.6	10.85	59.5	7.36	63.65	0.78	14.05	769.40	-13.04	-97.10	7.82	032-BT
G4 (S1)	26/08 16:00	8.21	457	4.2	0.05	1.51	14.3	11.8	10.35	57.6	7.38	107.16	1.38	21.00	835.13	-13.58	-97.17	11.92	051-JU
G4 (S1)	28/08 17:01	8.44	452	3.8	0.06	1.52	14.1	11.2	9.8	55.1	6.94	45.53	0.64	8.40	624.14	-13.17	-97.16	8.83	041-NB
G4 (S1)	29/08 16:30	8.24	451	4.4	0.05	1.53	14.55	11.4	9.58	55.2	7.4	106.66	1.7	20.54	800.93	-13.30	-97.27	9.67	013-VS

G12 (S1)	23/08 17:25		9.35	449	10	0.01	1.54	13.95	12.55	10.45	63.8	7.11	71.84	0.35	17.86	1075.52	-13.12	-96.58	8.91	031-ZI
G12 (S1)	28/08 16:46		9.31	462	7.9	0.01	1.57	13.35	11.65	9.78	62.8	6.74	112.44	0.79	22.72	871.36	-13.00	-95.70	8.87	024-AR
G13 (S1)	23/08 18:18		7.86	382.2	6.2	0.02	1.21	25.4	11.95	12.35	28.8	8.99	98.55	0.44	14.56	758.47	-13.04	-97.08	7.86	033-DP
G13 (S1)	29/08 16:42						1.33	25.3	10.05	10.1	23.7	7.56	93.02	0.61	14.81	1375.39	-13.07	-96.83	8.40	009-XU
G13 (S1)	29/08 17:28		8.04	424	5.9	0.12	1.98	20.5	14.25	16.25	32	10.05	84.25	1.65	16.27	1049.16	-12.45	-91.59	8.43	054-CX
G15 (S9)	26/08 18:30		8.62	687	8.9	0.01	3.51	7.88	15.7	9.49	119	6.96	113.49	0.93	32.77	1147.65	-12.40	-92.39	7.11	071-JI
G15 (S9)	27/08 19:42		8.15	782	7	0.00	3.44	12.75	21	17	123	5.99	163.43	1.1	32.42	979.59	-12.17	-94.08	4.31	066-FW
G15 (S9)	28/08 18:45		8.72	625	6.5	0.00	3.52	8.24	15.55	9.09	117.5	6.9	117.75	1.14	32.83	1248.35	-12.49	-92.27	8.05	012-OA
G15 (S9)	29/08 18:33		8.75	697	7.8	0.01	3.53	8.26	15.8	9.45	117.5	6.88	117.75	1.17	32.53	1472.66	-12.23	-92.08	6.29	043-JF
Surface Water compositions																				
L14	23/08 19:03		5.93	49.1	11.5	0.63	0.04	0.82	0.71	0.987	7.03	0.68	2.05		9.96	133.44	-11.99	-95.08	1.83	035-KT
L14	28/08 17:31		6.56	52	10	0.00	0.04	0.87	0.58	1.015	7.28	0.64	2.26		10.59	62.18	-11.35	-89.55	1.83	026-LD
L16	28/08 19:11		7.03	66	5.8	0.00	0.17	1.69	1.36	1.475	7.95	3.86	2.53		11.00	232.39	-9.78	-80.12	-1.45	044-CB
L16	29/08 19:48		7.63	65.8	6.1	0.02	0.18	1.81	1.39	1.52	7.77	3.72	3.06		11.64	205.34	-10.12	-81.49	-0.09	037-AU
"E1"	29/08 19:13		8.24	784	8	0.14	0.31	1.75	1.34	1.83	9.34	2.31	1.51		11.79	274.14	-11.77	-91.10	3.64	011-CI
	26/08 19:00		7.69	62.6	7.3	0.02	0.13	1.44	1.2	1.235	7.6	3.72	2.15		11.41	137.51	-9.16	-77.93	-4.29	047-FL
L1	22/08		5.8	54.5	5.8		0.01	1.12	0.48	1.26	7.19	1.24	4.61		10.84	56.78	-13.66	-104.36	5.82	053-SX
L2	22/08		6.67	48.8	6		0.04	0.78	0.47	0.973	7.4	0.39	1.08		10.70	71.80	-11.47	-92.07	0.15	069-IU
WP	28/08 19:44		8.16	580	6.1		2.00	28.1	14.35	20	42.4	7.41	91.76		18.44	902.26	-13.22	-95.19	11.03	021-CE
Porewater compositions																				
P1	24/08 09:20	25	7.67	446	8.7		1.91	19	15.8	18.15	36.8	10.45	93.96		17.65	2130.53	-12.57	-93.20	8.15	061-MS
P2	24/08 10:40	45	6	71.8	13.1		0.02	3.39	1.34	2.38	13.45	6.65	3.51	1.49	15.43	48427.8	-12.67	-92.15	9.86	064-ZG
P2	24/08 10:40	26.5	7.14	67.4	14.1		0.02	0.88	0.15	1.16	9.76	5.76	2.11	0.17	9.06	46893.6	-12.58	-91.55	9.53	060-QA
P2	24/08 10:40	35	6.7	89	15.3		0.02	1.39	0.54	1.58	11.7	6.99	5.17	1.17	19.87	45151.4	-12.92	-92.73	11.00	045-TY
P2	24/08 10:40	56.5	6.8	69.6	14.9		0.03	0.96	0.21	1.16	9.65	5.58	3.25	0.33	14.46	45738.7	-12.66	-91.59	10.00	046-HW
P3	27/08 11:00	42	6.7				0.05	1.1	0.33	0.81	5.26	2.28	1.33	0.3	6.22	77626.1	-11.44	-87.36	4.68	039-PU
P3	27/08 11:00	20	7.1				0.09	1.69	0.69	1.27	7.03	2.93	1.84	0	10.91	90.67	-11.72	-86.06	8.04	038-JK
P3	27/08 11:00	58	6.4				0.12	1.05	0.51	0.85	5.79	2.11	1.87	0.11	9.57	310.48	-12.18	-89.88	7.96	007-OT
P3	27/08 11:00	85	6.9				0.13	1.34	0.38	1.09	6.92	2.81	3.07	0.08	9.48	160.84	-12.41	-91.41	8.24	052-MG
P3	27/08 11:00	110	6.1				0.15	1.4	0.77	1.08	8.68	3.9	3.85	0.08	8.72	706.42	-11.96	-90.16	5.84	068-IK
P4	29/08 14:10	70		68.3	13		0.07	1.04	0.66	1.17	8.52	5.29	4.40	0	13.04	86.32	-14.50	-103.76	12.88	019-XM

P4	29/08 14:10	20				0.14	1.8	0.92	1.38	8.21	3.22	1.83	0	11.47	164.89	-12.44	-93.09	7.01	059-WG
P4	29/08 14:10	50				0.14	1.27	0.48	1.47	8.81	6.34	4.34	0.08	12.53	191.92	-13.78	-99.70	11.17	020-FU
P4	29/08 14:10	40				0.15	1.4	0.35	1.55	9.13	7.13	4.45	0	12.36	204.19	-13.49	-97.96	10.53	022-DS
P4	29/08 14:10	30				0.17	1.61	0.47	1.82	8.88	4.73	1.42	0	12.16	208.89	-11.80	-89.03	5.80	029-OL
P5	30/08 09:00	36	6.63	46.3	8.5	0.03	0.9	0.46	0.88	6.34	3.12	3.58	0	8.23	56552.1	-12.85	-91.88	11.26	050-KS
P5	30/08 09:00	47	5.93	50.5	7.9	0.08	1.04	0.65	0.78	5.17	2.6	3.25	0	8.34	356.94	-12.92	-93.76	10.08	003-EA
P5	30/08 09:00	61	6.19	61	7.8	0.10	1.24	0.55	1.04	7.68	3.44	3.50	0	11.48	320.05	-13.01	-94.86	9.71	014-YQ
P6	30/08 09:15	20				0.17	0.68	0.41	0.45	3.37	1.02	1.80	0	11.24	234.40	-12.06	-90.74	6.25	005-CK
P6	30/08 09:15	30	6.24	79.4	9.3	0.27	2.26	0.45	1.57	10.75	4.04	0.51	0	12.90	762.00	-12.67	-92.67	9.06	072-HP
P6	30/08 09:15	75				0.29						3.17	0	15.00		-13.95	-100.42	11.74	075-GD
P6	30/08 09:15	40	5.74	111.7	9	0.51	4.43	0.83	2.53	12.4	7.67	0.57	0	15.87	3553.97	-13.04	-96.28	8.45	067-DA
P6	30/08 09:15	50	5.69	129.8	9.1	0.61	5.2	1.4	3.01	12.55	8.26	1.33	0	18.31	4769.09	-13.27	-98.71	8.56	065-WG
	30/08 20:00		7.05	180	6.2	1.06	8.37	5.73	6.13	16.15	9.2	13.72	0	15.83	1043.60	-10.77	-85.17	1.52	042-HP
						0.05	0.62	1.74	1.1	6.97	0.39	0.80	0	10.91	59.99	-9.34	-80.16	-4.99	073-CD
					6.1	1.07	12.95	9.49	8.57	35.6	5.7	72.95	0.46	18.39	1188.10	-13.07	-95.57	9.64	056-DY
						1.53	17.95	11.65	11.55	48.6	7.22	106.24	0.49	20.06	1589.02	-13.44	-96.42	11.56	048-IP

n.s. = no sample; - = no data

DIC = $[CO_{2\,(aq)}] + [HCO_3^-] + [CO_3^{2-}]$. Since carbonates are negligible in Maalutu GRF, $[CO_3^{2-}]$ was assumed zero in this calculation.
$[CO_{2\,(aq)}] = K_o \times pCO_2$, where K_o is the solubility coefficient such that K_o = -60.2409 + 93.4517 (100/T) + 23.3585 ln (T/100) for non-saline waters (T in Kelvin; Weiss, 1974).

Cations were analyzed by inductively coupled plasma mass spectrometry (ICP-MS) using an Agilent 7900 at ALS Scandinavia AB. Major anions were analyzed using a Dionex Aquion Ion Chromatography (IC) system at the Department of Geosciences and Natural Resource Management (IGN), University of Copenhagen. Water isotopes were analyzed by a Picarro Cavity Ring-Down Spectrometer (CRDS) L2120-I at IGN and alkalinity was measured using Hach-digital titrator at the Globe institute.

The stream water to which each groundwater spring water contributes to is referred to in brackets after the site name.

4.4.3. ALKALINITY AND pCO_2

The alkalinity in stream water was primarily contributed by the groundwater springs that enter the stream én route to the sea. The water samples had a distinct alkalinity versus pH distribution (Figure 4.9). The groundwater and stream water samples exhibit a positive correlation between alkalinity and pH while surface and pore waters appear uncorrelated. Unlike the majority of the pore water samples, P1 plots higher clustering with the groundwater spring samples suggesting its groundwater source.

Averaging the product of stream water alkalinities and their corresponding discharge estimates, indicates an overall 0.158 mmoles s^{-1} alkalinity flux to the sea. If the measured alkalinity flux is assumed representative for the year, it results 5.25×10^3 moles yr^{-1} total annual alkalinity flux. Therefore, the specific alkalinity flux for the given area is 1.91×10^5 moles km^{-2} yr^{-1}.

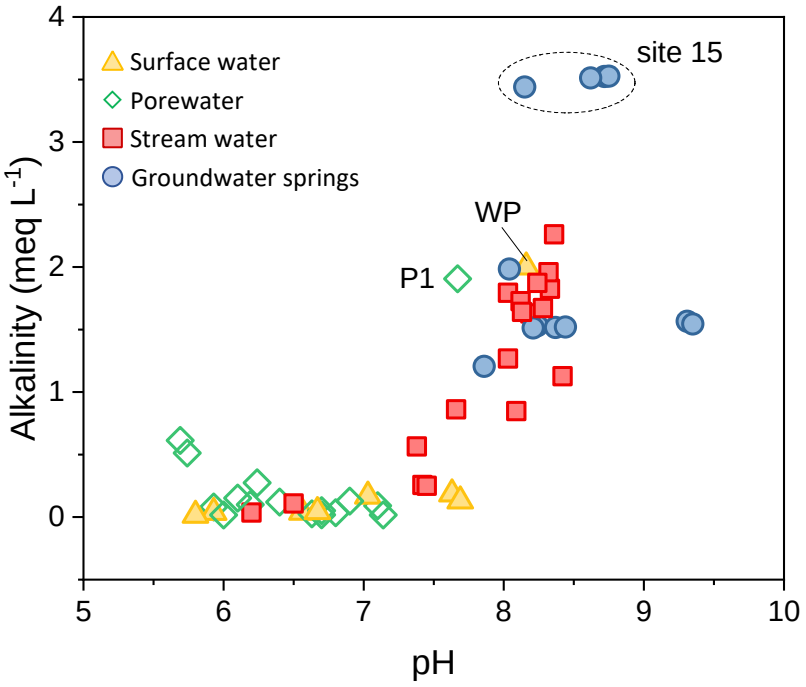


Figure 4.9:Cross plot for alkalinity versus pH in surface water, pore water, stream water and groundwater springs at Maalutu.

For every mole of alkalinity produced during silicate weathering, a single mole of atmospheric CO_2 is sequestered. Therefore, the average annual alkalinity flux indicates that an average 5.25×10^3 moles of CO_2 is consumed due to surface runoff at Maalutu annually. Over a timescale of 10,000 years since the material has been deposited, assuming that the drainage

pattern has remained unchanged, 0.23 t CO_2 has been sequestered due to silicate weathering annually.

The partial pressure of CO_2 (pCO_2) of the water samples was estimated by the ion speciation program PHREEQC from WATEQ4F database, using their pH values and major ion concentrations. In general, majority of water samples illustrate a high pCO_2 with respect to the atmosphere pCO_2, reflecting a CO_2-enriched composition (Figure 4.10). The solubility of CO_2 in water decreases with temperature. Therefore, atmospheric pCO_2 has a lower saturation state in cold water, dominating in high latitude regions. The lower limit for all the water systems were very close to the atmospheric pCO_2. The few samples that ranged below this limit, as seen especially in surface waters, indicate their undersaturation with respect to dissolved CO_2.

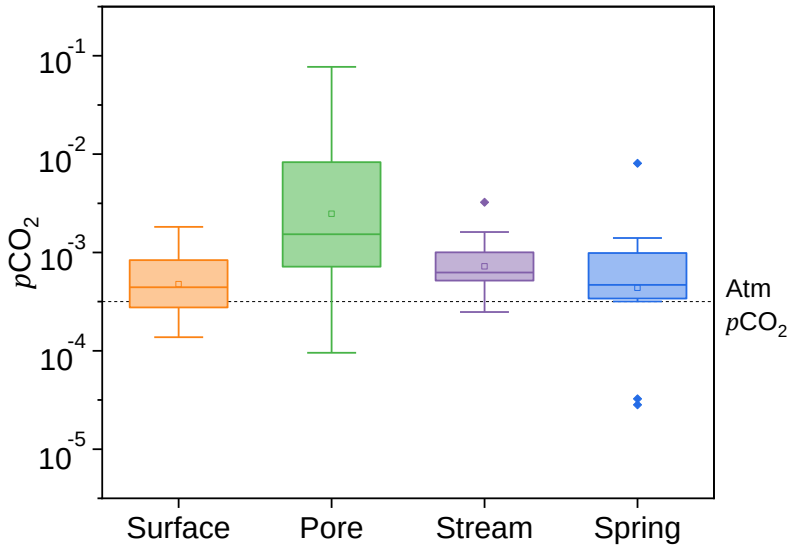


Figure 4.10: Distribution of pCO2 in surface water, porewater, stream water and groundwater springs at Maalutu; with the horizontal line representing the atmospheric pCO_2.

The variation in the stream waters and groundwater springs pCO_2 was small and these waters showed negligible response to higher discharge following the event of heavy rain. The pCO_2 for pore water samples were higher than the atmospheric pCO_2, except for two samples, and had a wide range from $10^{-3.32}$ to $10^{-1.11}$.

4.4.4. STABLE ISOTOPIC COMPOSITION

Figure 4.11 shows the dual isotope plot for all samples from streams, groundwater springs, surface lakes as well as pore water collected during field campaigns in August 2017 and 2018, plotted relative to the global meteoric water line (GMWL) defined by $\delta D = 8\ \delta^{18}O + 10$ (Craig, 1961), for comparison.

In the 2018 field campaign, surface water samples (n = 8) collected from the lakes and ponds at the top of the field site had $\delta^{18}O$ values ranged from -13.66 to -9.16 ‰ (mean = -11.34 ‰) and δD values ranged from -104.36 to -77.93 ‰ (mean = -89.48 ‰). The stream water samples (n = 19) were characterized by $\delta^{18}O$ values ranging from -13.29 to -11.05 ‰ (mean = -12.22) and had δD values ranging from -98.81 to -86.34 ‰ (mean = -92.58 ‰). The groundwater samples (n = 12) showed $\delta^{18}O$ values ranging from -13.58 to -12.17 ‰ (mean = -12.85 ‰) and δD values ranging from -97.27 to -91.59 ‰ (mean = -95.15 ‰). The 22 porewater samples ranged from -14.50 to -11.44 ‰ (mean = -12.73 ‰) for $\delta^{18}O$ and -103.76 to -86.06 ‰ (mean = -93.42 ‰) for δD.

With the exception of a few samples, the majority of the water samples of all types plot to the right of (or below) the GMWL suggesting substantial evaporation has occurred, especially in the surface water samples. Groundwater spring samples appear in two groups of which samples from G4 and G12 plot closer to GMWL, suggesting possible reaction with GRF. In comparison, G13 and G15 plot farther from GMWL, suggesting they were dominated by meteoric water. Both G4 and G12 were sampled closer to the emerging point of their respective springs from the base of the deposit, supporting the previous observation.

Surface waters exhibit a much wider range of $\delta^{18}O$ and δD values compared to groundwater springs, stream waters and porewaters. They become heavier downstream indicating the effect of mixing with the GRF-reacted waters from the groundwater springs.

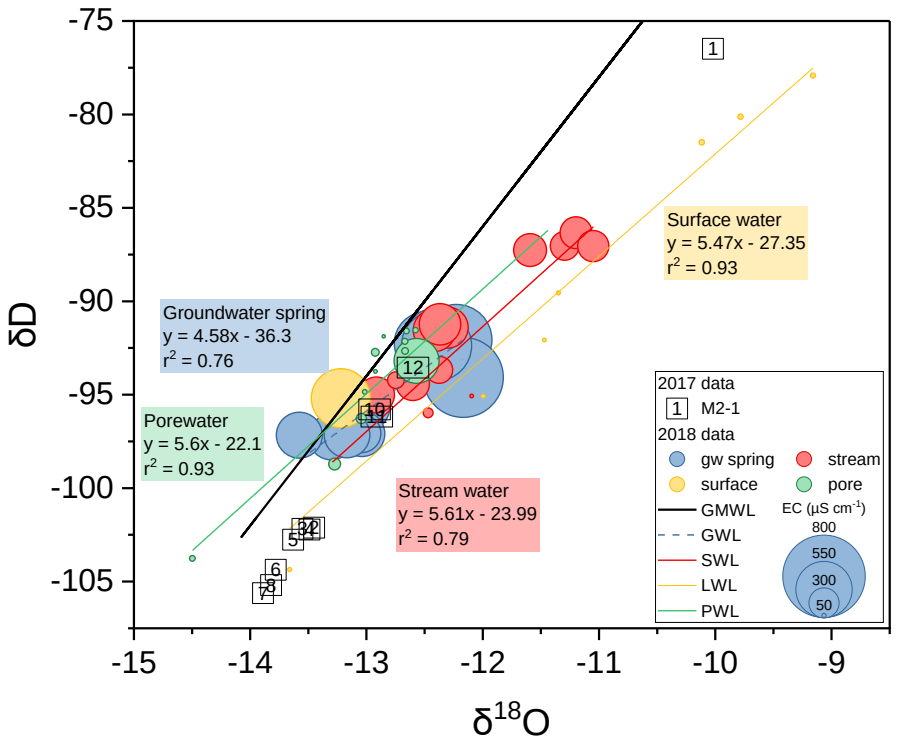


Figure 4.11: Dual isotope plot of δD-$δ_{18}$O for different water samples collected from Maalutu field site. Linear fit lines for the sample categories and bubble scale for the level of electrical conductivity (EC) refer to the 2018 water samples. GMWL = global meteoric water line; PWL =porewater line; GWL = groundwater line; SWL = stream water line; LWL = surface (lake) water line.

The water sample data from 2017 field campaign are presented by numeric symbols in Figure 4.11, where the numbers represent the sample ID. The M2-1 sample was taken from the mouth of the MS further from the high-tide sea level and possibly represents a mix of stream water and seawater. The samples from M2-2 to M2-8 were from the MS profile whereas the samples from M10 to M12 were derived from groundwater springs or puddles near the MS, where the water had reacted with the GRF. Although a variation can be observed in the stream water data from the two years, the GRF-reacted waters appear uniform.

The 2017 field sampling followed several days of heavy rain in comparison to relatively sporadic events of rainfall in 2018 field duration. Therefore, the higher concentration of meteoric water is more notable in the 2017 stream water samples. Moreover, the samples plot in an almost numerical sequence such that the stream water becomes heavier downstream as it mixes with the GRF-reacted waters from the groundwater springs.

4.5. DISCUSSIONS

4.5.1. SOURCE OF CATIONS AND ANIONS

Glacial meltwaters acquire solute during transport via carbonate and silicate mineral weathering of the GRFs. Base cations are released during exchange with aqueous protons sourced from dissolved CO_2 and/or oxidation of sulfides (e.g. pyrite). Protons may also be derived from sulfuric acid scavenged from the atmosphere during precipitation (Tranter et al., 1993; Ryu and Jacobson, 2012).

Mineral weathering by carbonic acid

$$(Na, K)\,AlSi_3O_8 + CO_2(aq) + H_2O \rightarrow (Na^+, K^+) + Al(OH)_3 + 3\,SiO_2(aq) + 2\,HCO_3^- \quad (2)$$

$$(Ca, Mg)\,Al_2Si_2O_8 + CO_2(aq) + H_2O \rightarrow (Ca^{2+}, Mg^{2+}) + Al(OH)_3 + 3\,SiO_2(aq) + 2\,HCO_3^- \quad (3)$$

$$(Ca, Mg)\,CO_3 + CO_2(aq) + H_2O \rightleftharpoons (Ca^{2+}, Mg^{2+}) + 2\,HCO_3^- \quad (4)$$

Mineral weathering by sulfuric acid

$$(Na, K)\,AlSi_3O_8 + H_2SO_4 + H_2O \rightarrow (Na^+, K^+) + Al(OH)_3 + 3\,SiO_2(aq) + SO_4^{2-} \quad (5)$$

$$(Ca, Mg)\,Al_2Si_2O_8 + H_2SO_4 + H_2O \rightarrow (Ca^{2+}, Mg^{2+}) + Al(OH)_3 + 3\,SiO_2(aq) + SO_4^{2-} \quad (6)$$

$$(Ca, Mg)\,CO_3 + H_2SO_4 \rightleftharpoons (Ca^{2+}, Mg^{2+}) + SO_4^{2-} + 2\,HCO_3^- \quad (7)$$

Pyrite oxidation

$$FeS_2 + 15O_2(aq) + H_2O \rightleftharpoons 16H^+(aq) + 4Fe(OH)_3(s) + 8SO_4^{2-} \quad (8)$$

The major base cation in the GRF-reacted waters is Na^+, which reflects the dissolution of Na-containing silicate minerals in the GRF. The major anions in the GRF-reacted waters is HCO_3^- and SO_4^{2-} reflecting mineral weathering reactions involving both carbonic acid and sulfuric acid. A relatively long residence time of the meltwater is likely to enable the reaction to progress as seen in the groundwater springs. The contribution of various ions and their possible sources is investigated using cross-plots as shown in Figure 4.12. The total major ion content in surface water samples was <1 mmol L^{-1}, in general, but sample WP had a significantly high ionic concentration and alkalinity (2 meq L^{-1}). WP was a small pond at the surface of the deposit and far from the exposed profile. This could have been a result of

seepage of the GRF-reacted water. This, however, could not be ascertained from the collected data.

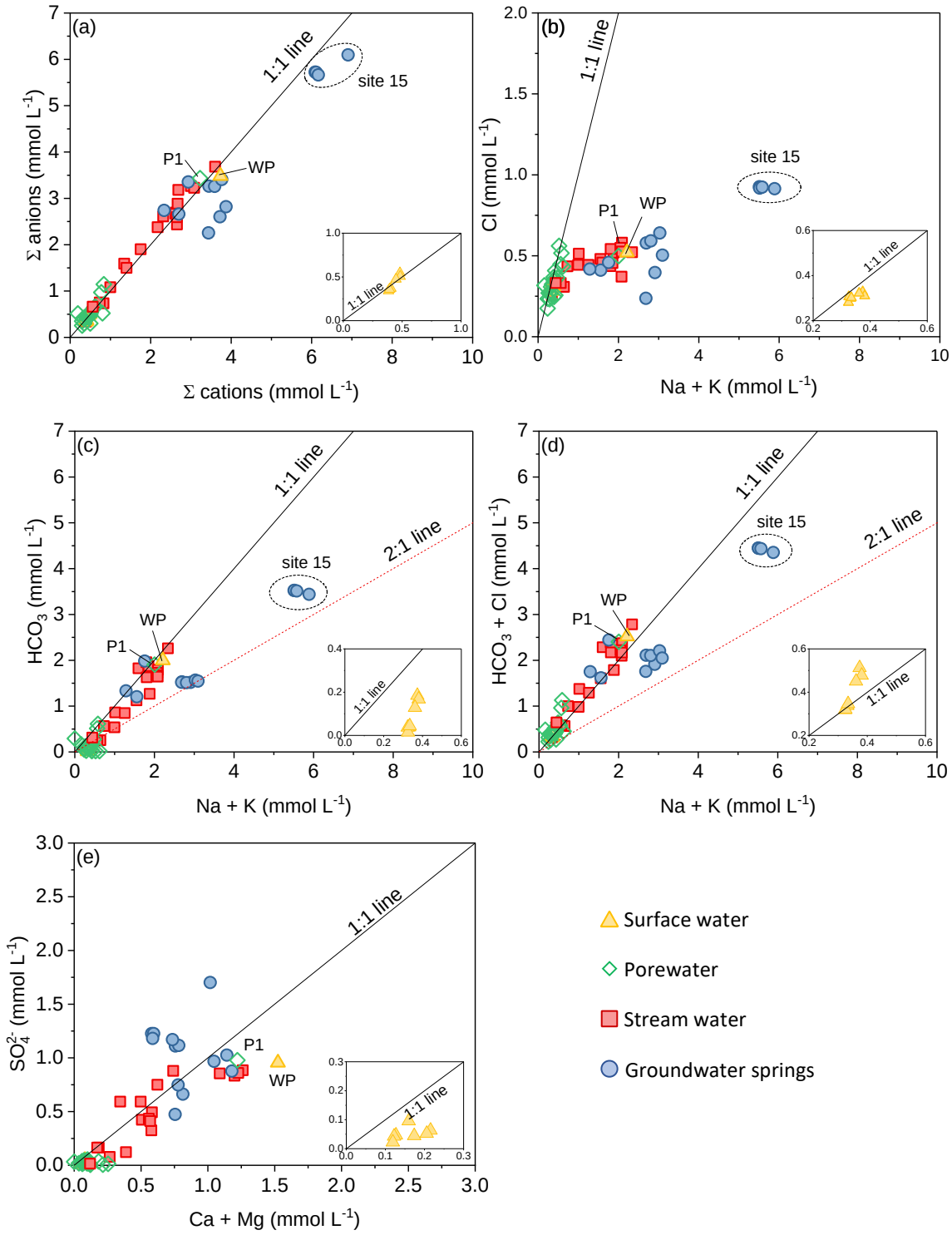


Figure 4.12: Bivariate plot showing total major anion versus total major cation concentrations in surface water, pore water, stream water and groundwater springs. Inset plot shows the zoomed area for surface water compositions.

The plot of Cl versus Na+K (Figure 4.12b) shows that most of the surface and pore water samples follow a 1:1 line. This indicates that the major ions in surface and pore waters are primarily introduced due to dissolution of halites. As the site is coastal deposit, atmospheric input of sea-salt aerosols. The pore water sample that deviates towards the right from the 1:1 line due to a higher solute concentration was obtained from site P1. This site was near the MS at an elevation of ~9 m and the sample was collected from 25 cm depth. Considering its location, it possibly represents the water flowing through the deposit, referred to as groundwater in this study. Both groundwater and stream water compositions deviate from this trend of halide stoichiometric ratios.

The four groundwater spring samples that cluster together with the highest total anions and cations (Figure 4.12a) were from site 15 and form part of the stream represented by site 9. The lowest stream discharge was found at site 9, with a discharge of 0.06 L s^{-1}. Its average alkalinity was 1.7 meq L^{-1}, comparable to the average alkalinity of the groundwater. The groundwater contribution to the stream, measured at site 15 (~10 m.a.s.l.), contributed highest alkalinity (~3.5 meq L^{-1}) in the investigated area.

In the plot of HCO_3 versus Na+K (Figure 4.12c), stream water samples cluster around the 1:1 line while groundwater springs show a clustering around 2:1 HCO_3 versus Na+K line. This suggests that majority of the solute release is due to mineral weathering by carbonic acid. The deviation towards higher Na+K suggests they were due to mineral weathering by sulfuric acid. However, this was primarily observed in groundwater springs that were exposed to the atmosphere for a relatively shorter time than the surface water. This would indicate oxidation of pyrites supplying the protons for the reaction to occur. Water samples show enrichment in Ca^{2+} and Mg^{2+} ions that correlate with SO_4^{2-} as seen in Figure 4.12e. The presence of sulfate in our water analysis data are in accord with our field observation of pyrite at the site observation. Its presence in negligible quantities might have resulted in non-detection under X-ray diffraction analysis and scanning electron microscopy. These cross plots for mass balance do not suggest all Na^+ and K^+ ions were balanced by HCO_3^- and all Ca^{2+} and Mg^{2+} ions were balanced by SO_4^{2-}, but are employed to study the difference in trends of the four water bodies investigated in this study.

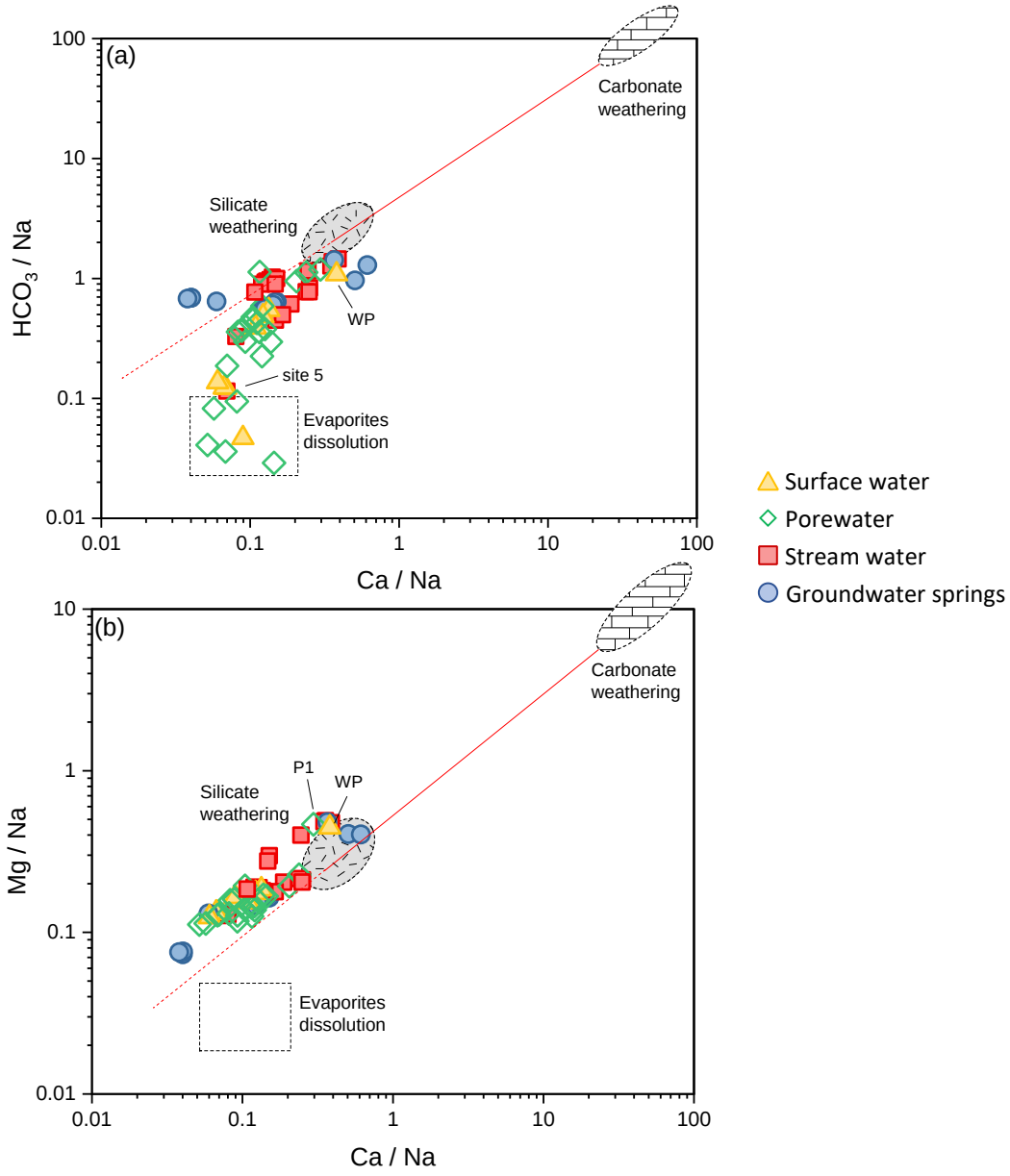


Figure 4.13: Bivariate plots of molar ratios (a) Na-normalized Ca and HCO_3 and (b) Na-normalized Ca and Mg. The shaded oval domains represent the ranges of approximate compositions of the silicate and carbonate end members, and the dashed box represents the evaporite end member (after Gaillardet et al., 1999).

While mineral weathering to be the dominant process contributing groundwater springs, Figure 4.12d indicates that stream water chemical composition is a result of both mineral weathering and dissolution of halites. This is ascertained with the aid of bivariate mixing plot model of Na-normalized molar ratios of the dissolved species (Ca, Mg and HCO_3) proposed by Gaillardet et al., (1999). In this model, silicate end-member refers to the water draining

silicates and has Ca/Na = 0.35 ± 0.15, Mg/Na = 0.24 ± 0.12 and HCO_3/Na = 2 ± 1. Similarly, carbonate end-member refers to the water draining carbonates, which is dominated by Ca- and Mg-dominated reservoirs and has Ca/Na close to 50, Mg/Na close to 10 and HCO_3/Na close to 120. The evaporite end-member composition is difficult to constrain due to diversity in salt rock types. However, it is characterized by a depleted HCO_3 with respect to Mg and Ca.

The bivariate mixing diagram for Na-normalized HCO_3 and Mg versus Ca show a clustering of our data near the global average domain for silicate weathering (Figure 4.13). A low discharge for the sampled data with respect to large riverine data that the model employs, overall contributes to a lower cationic weathering. High precipitation can also contribute to a lower value due to dilution. The pore water and surface water data in Na-normalized HCO_3 versus Ca veer downward from the silicate-carbonate line illustrating a strong influence of evaporation (Figure 4.13a). This deviation for the stream water and groundwater springs was minimal to non-existent. The stream water sample from site 5 has a low HCO_3/Na value and plots closer to the evaporites domain. This sample was collected from the MS at an elevation of ~12 m, flowing sub-vertically, before addition of any groundwater springs were observed. The downward deviation was absent in the plot of Na-normalized Mg versus Ca but again, samples were observed to cluster close to the domain indicating silicate weathering (Figure 4.13b).

The Al concentrations in the water samples ranged from 0.0003 to 0.038 mmol L^{-1} while Fe concentrations ranged from below detection limit (0.0001 mmol L^{-1}) to 0.072 mmol L^{-1} (Appendix, A.4). Porewater samples were similar to surface water in their cation concentration. However, they had a relatively higher variation in Al concentration than samples from groundwater and surface water. The Al and Si concentrations in the porewater samples varied spatially as well as at different depths (20-110 cm) in a given site. This variation is most likely resulting from the heterogeneity in the sediment layers and their respective interaction with the ambient water. The pH in porewater ranged between 5.69 and 7.14. The top layer of the plateau was a soil layer and had a lower Al at all porewater sampling sites possibly due to Al-organic matter complexes (Takahashi and Dahlgren, 2016). The soil layer is rich in humic substances, which can form complexes with cations such as Al^{3+} and Fe^{3+}. The low Al concentration in groundwater, however, might also be attributed to the higher pH that reduces Al solubility and promotes its precipitation as Al-hydroxides.

4.5.2. DISCHARGE RATE AND SOLUTE CONCENTRATION

Samples from four streams were collected at the deposit. On our third field day at Maalutu there was a heavy discharge of surface waters to the streams due to heavy rain the night before. Thus, the higher supply of surface water with a lower solute concentration diluted the stream water resulting in a decline in EC. The dilution effect, as inferred from EC, was more evident in the MS (site 1; Figure 4.8a). It received contributions from both a network of ponds at the top surface as well as several groundwater springs emerging out of the deposit. As the discharge rate slowly decreased to attain its previous value, EC measured in the stream water also increased. The average discharge for stream water was 0.180 L s^{-1} whereas for groundwater was 0.039 L s^{-1}. Based on a 27, 461 m^2 drainage area of the Maalutu GRF deposit (Grønbæk, 2019), an average drainage (or specific discharge) of 206.63 mm yr^{-1} was estimated for the streams. Table 4.3 lists the average drainage, pH and alkalinity for the streams and the groundwater springs.

Table 4.3: Average drainage and alkalinity at Maalutu

	Average drainage mm yr^{-1}	Average alkalinity mmoles L^{-1}	pH
Stream water	206.63	1.365	7.84
Groundwater spring	45.25	2.132	8.51

The event of heavy rainfall increased the discharge rate at the site 4 groundwater spring negligibly. The EC also correlated with the higher discharge but the change appeared largely insignificant (Figure 4.8b). In the other groundwater springs, discharge was higher during our second sampling (Appendix, A.4). These suggest that surface water have possibly infiltrated through the top layers of the soil profile and contributed to the groundwater discharge. However, the average alkalinity flux to the sea via the four streams investigated at the deposit were comparable.

4.5.3. CO_2 CONSUMPTION AND ALKALINITY

Figure 4.14 shows the pCO_2 in MS water as it carries surface water downstream to the sea. In the 2017 data, the surface water is supersaturated with CO_2 but it rapidly loses CO_2 to reach an equilibrium with the atmospheric pCO_2. At ~7-12 m distance from the margin of the promontory, it is joined by the GRF-reacted waters via the groundwater springs, after which it continues to lose CO_2 until an equilibrium with the atmospheric pCO_2 was reached. This also

contributed to a drop in the dissolved inorganic carbon (DIC) of the stream water in the first ~5 m downstream transport. In Akuliarusiarsuup Kuua River (AKR; also called Watson river) draining the Isunnguata and Russell Glaciers near Kangerlussuaq, for example, Ryu and Jacobson (2012) report that ~25 % of the excess CO_2 evades to the atmosphere during downstream flow. They note that although the glacial rivers show decrease in dissolved CO_2, the weathering reactions in Greenland minimize CO_2 evasion to the atmosphere. Unlike the 2017 data, however, the 2017 data does not show CO_2 supersaturation in the surface water indicating the dissolved CO_2 was already in equilibrium with the atmosphere.

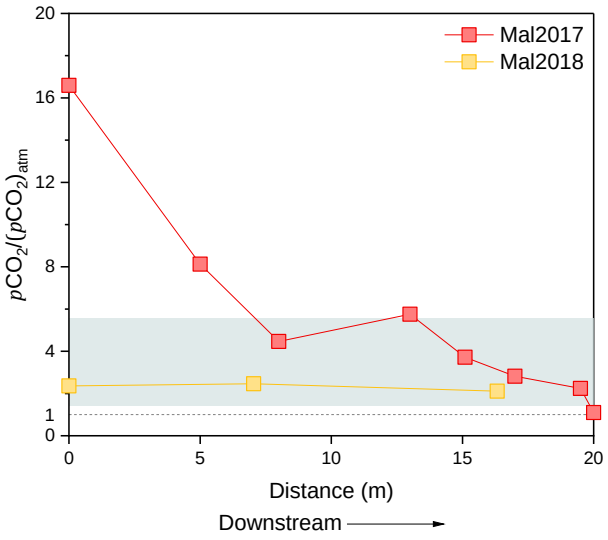


Figure 4.14: pCO_2/ $pCO_{2(atm)}$ ratio of Maalutu main stream (MS) from 2017 and 2018 field campaigns. The shaded region shows mean ± standard deviation ratio for Akuliarusiarsuup Kuua River (AKR) from Ryu and Jacobson (2012).

As the GRF is a silicate mineral composite, the dominant weathering process is silicate weathering. The CO_2 transport in MS is associated with a change in the dominant phase of speciation from dissolved CO_2 to HCO_3^- as the stream water pH increases from acidic (~5) to weakly basic (~8) when the groundwater springs enter the stream laterally. The groundwater springs carrying the GRF-reacted water were high in alkalinity. In comparison, the increase in alkalinity in AKR is more gradual and a significant rise can be observed from ~10 km from the glacial margin. This shows that the GRF at the Kangerlussuaq fjord region is reacting with the river water. The alkalinity contribution at Maalutu is ~10 times higher in a much smaller transit as the groundwater has possibly had a much longer residence time thereby allowing more reaction to take place between the GRF and the water. However, despite the high potential

in Maalutu GRF to consume CO_2, it contribution as an atmospheric CO_2 sink is insignificant. The amount of CO_2 sequestration from Greenlandic Rivers and streams is trivial with respect to the global carbon evasion flux to influence the present atmospheric CO_2 levels.

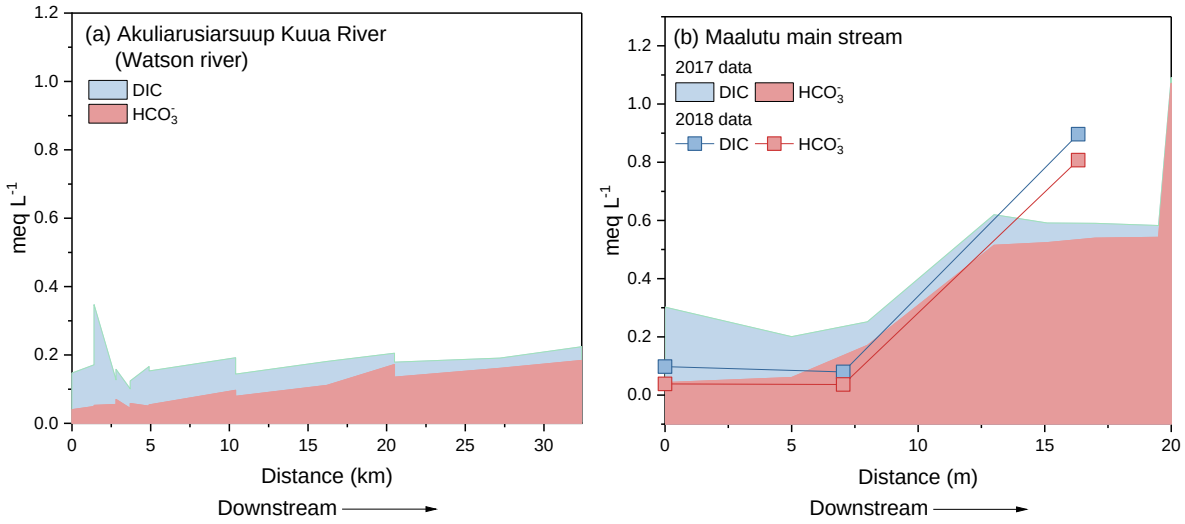


Figure 4.15: Dissolved inorganic carbon (DIC) and bicarbonate alkalinity contributions from Maalutu main stream (MS) compared with Akuliarusiarsuup Kuua River (AKR). AKR data from Ru and Jacobson (2012).

Low infiltration rate of the precipitated water at Maalutu limits the detrital sediments from weathering. Several such raised marine GRF deposit were discovered near Nuuk during our reconnaissance field campaign in 2017. However, glaciation and low temperature is likely to limit silicate weathering to chiefly comminution of the bedrock.

4.6. CONCLUSIONS

Maalutu GRF deposit is a ~20 m high promonitory that has been uplifted post Holocene and has been exposed ~10 ka. It is overlain by a soil layer few centimeters thick and displays common features as a subarctic landform. It is fed by precipitation and is also affected by sporadic permafrost. However, the infiltration rate of the deposit is low which limits the deposit sediments from reacting with the surrounding water. The fine-grained size and characterisitc primary mineral composition of the GRF enables it to react with the water traversing through the deposit, releasing solutes into the water and producing high alkalinity.

Maalutu GRF deposit is composed of detrital minerals but negligible mineral weathering has left the chemically immature material unweathered since its deposition. Its drainage setting prevents it from performing as an atmospheric CO_2-sink.

Chapter 5

Acid and alkaline leach of Glacial Rock Flour and its dissolution reaction in ambient and elevated pCO_2 conditions

Abstract

Maalutu glacial rock flour deposit is an uplifted marine deposit near Nuuk, West Greenland that was deposited ~10 ka. It remains mostly unreacted *in situ,* but field data from the site suggest that it is highly reactive upon interaction with the water flowing through the deposit. In this study, the chemical reactivity of glacial rock flour was investigated using acid and alkaline leaching tests as well as batch reactor experiments. The leaching tests are performed with another glacial rock flour representing an active marine environment. The two rock flours are different in their textural and mineralogical composition as well. Both the rock flours show that surface area of the reacting material plays a critical role in their dissolution kinetics.

The reactor experiments are conducted in ambient air and with an increased pCO_2 of 0.05 atm and in two parts. In the first part, the dissolution kinetics experiments were performed at room temperature, using deionized water in equilibrium with the two pCO_2 conditions. For the second part, the resulting suspensions were divided into two, and each half was amended with either additional material or additional deionized water. Sampled aliquots from the continuously-stirred suspensions were filtered and concentrations of Si, Na, Ca, Mg, K, Al and Fe were determined. All cation-release curves reached a plateau except for Si, which continued to increase. Al and Fe in the solution maintained low concentrations, indicating scavenging by secondary minerals. Both the solutions were supersaturated with respect to quartz, kaolinite and gibbsite but was subsaturated with albite and amorphous SiO_2. K-feldspar was near equilibrium.

5.1. INTRODUCTION

Natural weathering of silicate minerals consumes atmospheric CO_2 and releases cations and bicarbonate ions. Accelerating this process by the application of crushed silicate rocks can speed up the process to occur at timescales comparable with those of human activity. However, grinding large amounts of rocks to produce such fine-grained materials will incur a vast capital cost. Renforth (2012) estimate that rock comminution can potentially cost 4.45-53.2 US$ t^{-1} material. Meanwhile, gigatons of freshly eroded and bedrock fragments pulverized naturally by the moving glaciers are being deposited along the shorelines of Greenland annually (Overeem et al., 2017; Hawkings et al., 2017). These fragments range from boulders to fine-grained silt particles in size.

The fine-grained 'glacial rock flour' (GRF) has been reported to supply macronutrients in marine environments (Meire et al., 2016) and to increase biomass significantly in nutrient-deficit agricultural systems (Gunnarsen et al., 2019). It has a 2-11 µm median particle size and a specific surface area ranging between 4.5-19.6 m^2 g^{-1} (ref. Chapter 3). Derived from a granitic gneiss basement, the GRFs are mainly composed of primary minerals that have been subjected to an intense mechanical crushing. The mineral assemblage constitutes quartz, plagioclase, K-feldspar, biotite, chlorite, amphibole and augite, in varying proportions at different depositional sites, based on their provenance and degree of sorting (Chapter 3). Based on their physical properties, GRFs can be of two types – poorly sorted GRFs with a bimodal particle size distribution (PSD) and relatively well-sorted GRFs with a unimodal PSD. In this study, dissolution experiments were performed using Maalutu and Ilulalik GRFs representing bimodal and unimodal PSD, respectively. These two GRFs are also representative of two different type of the environmental setting of GRF deposits. While several GRF deposits, such as in Ilulialik, continue to form in an active sedimentary environment, some of the deposits currently lie exposed following the isostatic rebound after glacial retreat, such as in Maalutu. Both the GRF deposits are part of the Nuuk fjord region but are different in their PSD and present environmental setting. Field studies from the deposit suggest that the material has undergone negligible weathering, and due to its composition and particle size, it is chemically immature (ref. Chapter 4). Therefore, it is a material of interest in determining whether and if so, how.

Here, we present experimental data from three sets of laboratory dissolution experiments: 1) acid leaching of Ilulialik and Maalutu GRF; 2) alkaline leaching of Ilulialik and Maalutu GRF; 3) reactor experiments at two partial pressures of CO_2 (pCO_2) using Maalutu GRF with deionized (DI) water at room temperature to study the dissolution of the material. The first two experiments help us study the influence of pH on the two GRFs and determine whether GRF dissolution is a bulk dissolution method or biased towards one mineral over another. The third experiment was performed using Maalutu GRF to complement the field trials conducted using the material as a potential fertilizer in Brazil and Africa (e.g. Gunnarsen et al., 2019; Gunnarsen, 2020). While ambient pCO_2 condition was selected to simulate the reaction at the GRF deposit, an elevated pCO_2 condition was selected to simulate its possible reaction in a soil environment. Soil CO_2 are mainly controlled by biological activities and can range from ~2-3 % but often ~10% depending on the plant-growing season (Richter and Markewitz, 1995; Oh et al., 2005). An elevated pCO_2 of 5 % CO_2 (0.05 atm) was used in this study to represent a realistic soil pCO_2.

5.2. Background of reaction kinetics

In general, dissolution reactions take the form

$$\mathrm{A}_{\nu_A}\,\mathrm{B}_{\nu_B(\mathrm{s})} \underset{r_-}{\overset{r_+}{\rightleftarrows}} \nu_{\mathrm{A}}\,\mathrm{A}^{q_{\mathrm{A}}}_{(\mathrm{aq})} + \nu_{\mathrm{B}}\,\mathrm{B}^{q_{\mathrm{B}}}_{(\mathrm{aq})} \tag{5.1}$$

where ν_i is the stoichiometric coefficient of the reaction, q_i is the charge of the aqueous species and r_+ and r_- denote the rates of forward and backward reactions, respectively. Feldspars are expected to undergo the following reactions in the presence of dissolved carbon dioxide:

$$KAlSi_3O_8 + CO_{2\,(aq)} + 2\,H_2O \rightleftarrows K^+ + Al(OH)_3 + 3\,SiO_{2(aq)} + HCO_3^- \tag{5.2a}$$

$$NaAlSi_3O_8 + CO_{2\,(aq)} + 2\,H_2O \rightleftarrows Na^+ + Al(OH)_3 + 3\,SiO_{2(aq)} + HCO_3^- \tag{5.2b}$$

$$CaAl_2Si_2O_8 + 2\,CO_{2\,(aq)} + 4\,H_2O \rightleftarrows Ca^{2+} + 2\,Al(OH)_3 + 2\,SiO_{2(aq)} + 2\,HCO_3^- \tag{5.2c}$$

In geologic systems, the reactions can easily proceed at conditions close to equilibrium, where both forward and backward reactions can occur simultaneously, such that

$$r_{net} = r_+ - r_- \quad (5.3)$$

However, neither r_+ nor r_- can be measured individually. Additionally, if Si-containing secondary phase(s) precipitate, its rate of precipitation (r_{sec}) would further reduce the net rate. In this case, one would measure an effective net reaction rate ($\tilde{r}_{net}$) rather than the actual net rate (r_{net}), such that

$$\tilde{r}_{net} = r_+ - r_- - r_{sec} \quad (5.4)$$

Therefore, dissolution experiments rates are usually determined at far-from-equilibrium conditions, where r_- is negligible and $r_{net} \approx r_+$. Mineral dissolution rates are usually normalized to the surface area of the material and are expressed as moles of a given component per unit surface area per unit time (Brantley, 2008) and by convention, feldspar dissolution rates are based on Si flux, such that

$$r_{net} = \frac{V_o}{\nu_{Si} S_A m} \frac{d[Si]}{dt} \quad (5.5)$$

where V_o is the volume of solution, S_A is the specific surface area of the mineral, m is the mass of the mineral and ν_{Si} is the stoichiometric coefficient of Si in the silicate mineral of interest.

5.3. Experimental method

5.3.1. Starting material

The glacial rock flour used in this study were collected from Maalutu, a raised marine GRF deposit and Ilulialik, an active marine GRF deposit in the Nuuk fjord region in West Greenland. Chapters 3 and 4 in this thesis, detail the origin and regional geology of the study areas. Maalutu and Ilulialik represent two different types of GRF based on grain size distribution. Maalutu is a poorly sorted GRF with a bimodal grain distribution whereas Ilulialik is a relatively well-sorted GRF with a unimodal grain distribution. The GRFs consist of quartz, plagioclase, K-feldspar, biotite, amphibole, epidote and augite and their detailed chemical composition and characteristics are given in Table 5.1. The plagioclase is dominated by oligoclase with around 20 % anorthite component while K-feldspar is dominated by microcline. Due to high salinity

in Ilulialik GRF, a washed Ilulialik GRF sample was used following the steps given in Chapter 3 (Box 3.1). Both GRFs were dried overnight at 60 °C to remove any residual moisture, were gently crushed in a mortar to loosen aggregates in the material and were sieved through a 100 micron mesh. No material was discarded in the process.

Table 5.1: Characteristics of Maalutu and Ilulialik GRFs (ref. Chapter 3)

	Maalutu	Ilulialik (unwashed)	Ilulialik (washed)
Mineral oxide			
SiO_2	63.47 %	52.05 %	54.45 %
Al_2O_3	15.63 %	15.62 %	16.47 %
Fe_2O_3	5.17 %	8.14 %	8.49 %
MnO	0.07 %	0.11 %	0.12 %
MgO	2.62 %	4.78 %	4.93 %
CaO	3.78 %	3.56 %	3.66 %
Na_2O	3.76 %	4.22 %	3.43 %
K_2O	2.82 %	3.32 %	3.51 %
TiO_2	0.49 %	0.67 %	0.71 %
P_2O_5	0.12 %	0.11 %	0.12 %
LOI	2.14 %	7.34 %	3.15 %
Total	100.06	99.91	99.04
Total CO_2	0.17 %	0.47 %	0.58 %
Organic carbon	0.03 %	-	0.07 %
Total sulfur	0.01 %	0.08 %	0.01 %
Particle size distribution			
Clay (<2 µm)	30.1 %	67.4 %	-
Silt (2–20 µm)	34.9 %	27.7 %	-
Fine sand (20–200 µm)	32.6 %	4.2 %	-
Coarse sand (0.2-2 mm)	2.4 %	0.5 %	-
BET-N_2 surface area	15 $m^2 g^{-1}$	19.6 $m^2 g^{-1}$	-

Major element (wt%), total carbon, organic carbon and total sulfur were analyzed by emission spectrometry (ICP-OES); LOI = loss on ignition at 1000 °C at *Centre de Recherches Pétrographique et Géochimiques* (CNRS), Paris.
BET-N_2 surface area was measured using a Coulter SA3100 at Geological Survey of Denmark and Greenland (GEUS).
Particle size distribution was measured by wet sieving and pipette method at AGROLAB Agrar und Umwelt GmbH, Germany.

5.3.2. EXPERIMENTAL SETUP

5.3.2.1. Acid-extractable Si leaching experiment

About 25 and 50 mg GRFs were weighed and added to 50 mL 15 mM HNO_3 solutions (pH≈2) pre-heated to 60 °C in 50 mL centrifuge tubes, which were then placed in a water bath set to 60 °C and continuously agitated at 100 rpm. Time was noted upon adding the GRFs. At the required time intervals, the centrifuge tubes were removed from the water bath and were put into cold water to cease the reaction. After about 6 minutes, the samples were centrifuges at 8700 rpm for 1 hour. The supernatant solution from the centrifuged sample was carefully extracted using a pipette without disturbing the pellet at the base of the tube and filtered through Frisenette 0.22 µm syringe filters. Approximately 1-2 mL solution was left and the pellet was dislodged by vigorous shaking the tube. In case of any material sticking to the walls of the tube, it was put into ultrasonic bath for few minutes. For the next measurement, fresh ~40 mL HNO_3 solution was quickly added to the tube and then the lower meniscus of the solution was adjusted to 50 mL. The filtered supernatant was measured for Si concentration with a WINLAB dataline photometer using the molybdate blue method (ASTM D859-16). The accuracy and precision of the method was determined by preparing in-house Si standards using Sigma Aldrich Silicon Standard for ICP.

5.3.2.2. Alkali-extractable Si leaching experiment

GRF samples were leached in 200 mL 0.1 M Na_2CO_3 solution (pH=11.2) in an HDPE Erlenmeyer flask preheated to 85 °C. The flasks were kept in a water bath and were shaken continuously at 100 rpm. The saturation state of the leaching solutions for each GRF were varied by allowing 25 mg and 50 mg solid masses to react until they reached a steady-state concentration. Time was noted when the samples were added to the leaching solutions and 10 mL aliquots were taken out from the flask using a polypropylene syringe at regular time intervals. The aliquots were filtered through Frisenette 0.22 µm syringe filters into centrifuge tubes and were neutralized immediately with 0.2 M HNO_3 in a 1:1 ratio to prepare for colorimetric blue analysis. Silica concentrations were measured with a WINLAB dataline photometer using the molybdate blue method similar to acid-leach method (ASTM D859-16).

Alkaline leaching using a weak base are commonly used to determine amorphous silica and the steps were followed as outlined by Hawkings et al., 2017.

5.3.2.3. GRF dissolution at two pCO_2 conditions

The dissolution experiments were performed for Maalutu GRF in two parts at two pCO_2 conditions each (Table 5.3 and 5.4). They were set up in glass bottles containing 2 L deionized water and 50 g GRF at room temperature (22 ± 2 °C). All the reaction vessels were kept on a shaker table and agitated continuously during the experiment to keep the solid phase in suspension. For one reaction vessel, ambient air (experimental phase denoted M-1) was bubbled through the suspension and for the other vessel, 0.05 atm CO_2 was introduced from a cylinder (experimental phase C-1). The gas pressure was maintained in a way that air bubbles could be seen on the solution surface.

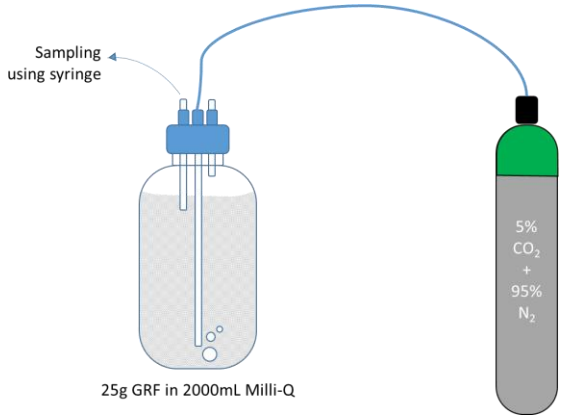


Figure 5.1: Experimental setup for the GRF dissolution experiment at two pCO_2 conditions.

The experiment was performed in two parts for each pCO_2 condition. In the initial experiment, the inlet gas was bubbled through a glass dispersion tube into the reaction container for both setups. In all experiments 50 g Maalutu GRF was introduced into the reaction vessel containing 2 L deionized water. The second part involved dividing the end solution from the initial experiment into two halves and followed by treatment of each half with either fresh GRF (MG for ambient air; CG for elevated pCO_2) or fresh DI water (MW for ambient air; CW for elevated pCO_2). The added fresh DI water was pre-equilibrated with the respective gas before treatment.

The solutions were measured for changes in electrical conductivity (EC) and pH at regular intervals. EC was measured directly from the reaction vessel. During such measurement, the flow rate of the 0.05 atm pCO_2 was increased to minimize influx of ambient air. The EC electrode was also calibrated prior to each sampling using 85 and 147 µS cm^{-1} VWR NIST standards. Approximately 3 mL aliquot was obtained to measure pH with a Mettler Toledo SevenCompact Duo. The sample size was kept at a minimum to avoid altering the solution chemistry of the reacting solution. The pH electrode was calibrated with Certipur NIST buffer solutions at pH 4.01, 6.86 and 9.18 prior to sampling. For each sampling event, approximately 35 mL aliquots were withdrawn from the reaction vessel using a 60 mL polypropylene syringe, and the samples were filtered using 0.2 µm Frisenette polycarbonate membrane filters. The filtrate was divided into three parts, for measurement of alkalinity, cation and anion concentrations. Alkalinity was measured using a Hach digital titrator by Gran function plot method. Samples for determination of cation concentration were acidified immediately after filtration with 0.2 mL 6M HNO_3 and were sent to ALS Scandinavia AB for inductively coupled plasma mass spectrometry (ICP-MS) analysis. SLRS-6 River Water - Certified Reference Material for Trace Metals, an external standard (SM1494-002) and an in-house standard were analyzed for determining the precision and accuracy for the cations. Anions were analyzed using a Dionex Aquion Ion Chromatography (IC) system at the University of Copenhagen.

5.3.3. CALCULATION OF MINERAL SATURATION INDICES

Saturation indices were calculated for the reacting mineral phases i.e. albite, anorthite, K-feldspar, quartz as well as possible secondary phases (e.g. Illite, kaolinite, gibbsite, amorphous $Al(OH)_3$, amorphous $Fe(OH)_3$ and amorphous SiO_2) based on the measured major cation concentrations and pH using the software PHREEQC 3 and WATEQ4F database (Parkhurst and Appelo, 2013).

5.3.4. REPRODUCIBILITY

The aqueous solutions were measured at regular intervals and release curve patterns from the dissolution reactions were similar to that in the literature for various media (for eg.

Holdren and Berner, 1979; Busenberg and Clemency, 1976). The accuracy and precision of the data for various analyses was within 5 % and any inconsistencies were easily discernible, as seen in Tables 5.4 and 5.5. While some of the data were replicated at least twice, most of the results were based on single point data. The low standard deviation from the initial data, albeit few, prompted the author to explore the possible scenarios that GRF can be subjected to, in order to address the objective of the study.

5.4. RESULTS

The reactiveness of Maalutu and Ilulialik GRFs were investigated by comparing the Si concentrations in acidic and alkaline solutions. A third set of experiments were conducted for Maalutu GRF in pure water equilibrated with ambient and elevated pCO_2 conditions, comparing the effectiveness of elevated pCO_2 levels in promoting mineral dissolution. In all the experiments, the general shape of the release curves with respect to time followed a trend similar to those reported in the literature for freshly ground silicate minerals in batch dissolution experiments (for eg. Holdren and Berner, 1979; Petrovich, 1981; Chou and Wollast, 1984; Busenberg and Clemency, 1976). GRF is a heterogeneous silicate mineral composite and different and the dissolution rates for different minerals may vary with respect to the dissolution of other mineral species. Here, Si concentration in the leaching solutions was used as an indicator for mass of GRF dissolution in different media. The amounts of Na, K, Ca and Mg released from dissolving GRF were also compared for the pCO_2 experiments.

5.4.1. GRF DISSOLUTION IN ACIDIC PH

Maalutu and Ilulialik GRFs were leached in HNO_3 solution to compare their reactivity in an acidic medium (pH≈2). Figure 5.2 (a) shows that, at the end of the experiment, the amount of Si released was higher in the solution where higher mass of GRF was added. This would be an expected observation due to availability of a larger surface area and indicates that silica saturation was not reached. In the batch experiment, the reacted solution was extracted at each sampling and fresh leaching solution was added to the reacted material. The introduction of fresh leaching solution to the reacted GRF at each sampling point allowed the

reaction to occur far from equilibrium. The Si releases were proportional to the mass of starting material for both types of GRF, such that the Si release for 50 mg GRF was ca. twice that for 25 mg GRFs. Differences in Si releases from the two GRF localities, i.e. Maalutu and Ilulialik, suggest a dependence on their material characteristics. Ilulialik GRFs showed higher Si release than Maalutu GRFs for their respective starting amounts.

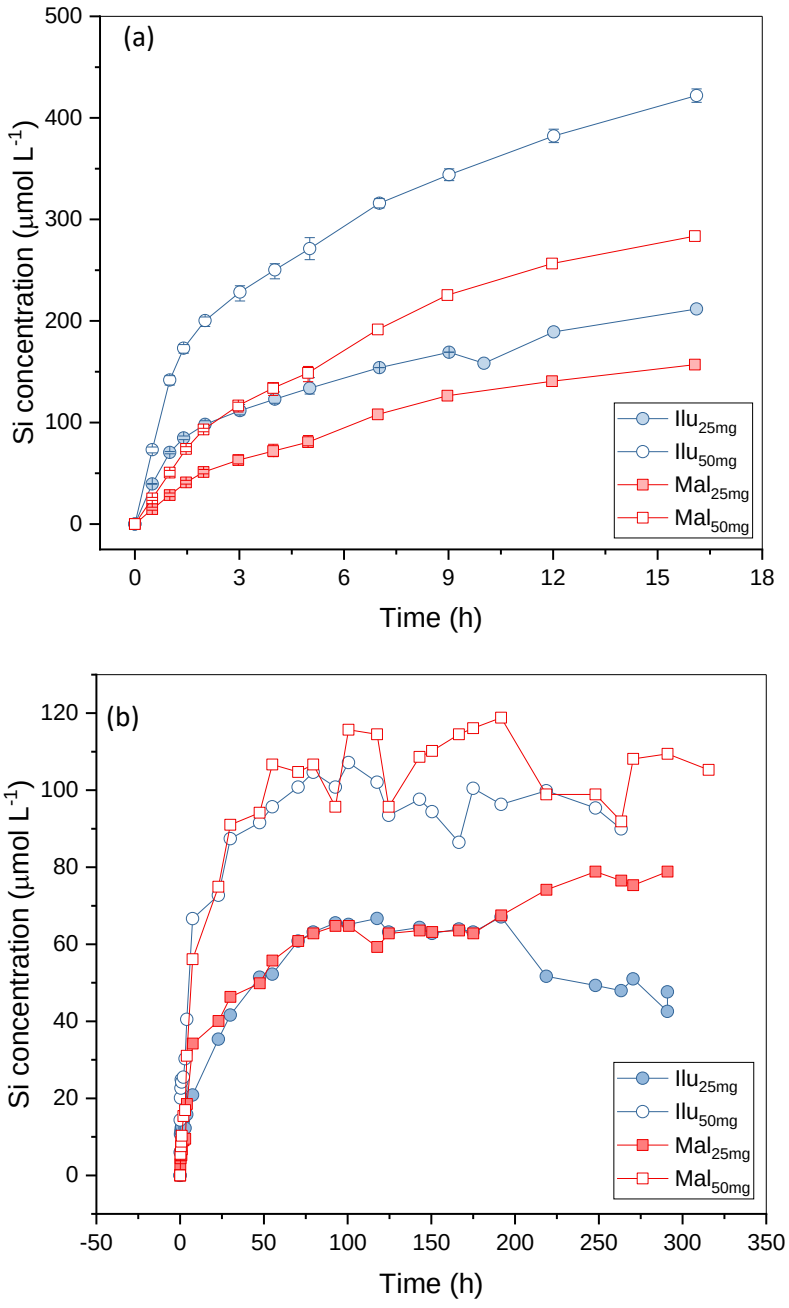


Figure 5.2: Evolution of Si concentration with time in GRF dissolution experiments at (a) 60 °C and pH≈2 15 and (b) 85 °C and pH=11.2. Majority of the points denote average between 2-3 replicate leaches and the bars show the maximum and minimum values obtained.

Table 5.2:(a) Si concentration in acid leaching solution using Maalutu GRF

	Maalutu-50 mg				Maalutu-25 mg		
Sample	Time (h)	Si (ppm)	Si (µmol L^{-1})	Sample	Time (h)	Si (ppm)	Si (µmol L^{-1})
Start	0.00	1.579	26.289	Start	0.00	0.00	0.000
M2-1-1	0.50	3.175	52.854	M1-1-1	0.50	0.841	13.999
M2-1-2	1.00	2.993	49.823	M1-1-2	1.00	0.821	27.667
M2-1-3	1.47	2.487	41.391	M1-1-3	1.47	0.704	25.386
M2-1-4	1.97	2.624	43.682	M1-1-4	1.97	0.599	21.688
M2-1-5	2.97	2.526	6.215	M1-1-5	2.97	0.596	19.890
M2-1-6	3.97	1.898	31.591	M1-1-6	3.97	0.428	17.044
M2-1-7	4.97	1.648	27.430	M1-1-7	4.97	0.640	17.776
M2-1-8	9.97	1.579	26.289	M1-1-8	9.97	0.903	25.682
Start	0.00	0.000	0.000	Start	0.00	0.000	0.000
M2-2-1	0.50	1.401	23.313	M1-2-1	0.50	0.815	13.558
M2-2-2	1.00	2.828	47.067	M1-2-2	1.00	0.808	27.006
M2-2-3	1.47	2.877	47.889	M1-2-3	1.47	0.808	26.896
M2-2-4	1.97	2.632	43.808	M1-2-4	1.97	0.596	23.368
M2-2-5	2.97	2.350	39.115	M1-2-5	2.97	0.694	21.472
M2-2-6	3.97	2.151	35.802	M1-2-6	3.97	0.515	20.123
M2-2-7	4.97	1.792	29.827	M1-2-7	4.97	0.436	15.829
Start	0.00	0.000	0.000	Start	0.00	0.000	0.000
M2-3-1	0.50	1.559	25.949	M1-3-1	0.50	0.998	16.611
M2-3-2	1.00	3.109	51.748	M1-3-2	1.00	0.839	30.576
M2-3-3	1.47	2.921	48.619	M1-3-3	1.47	0.751	26.465
M2-3-4	1.97	2.546	42.377	M1-3-4	1.97	0.641	23.169
M2-3-5	2.97	2.732	45.473	M1-3-5	2.97	0.847	24.767
M2-3-6	3.97	2.683	44.657	M1-3-6	3.97	0.639	24.734
M2-3-7	4.97	2.108	35.087	M1-3-7	4.97	0.525	19.374
M2-3-8	6.97	3.170	52.763	M1-3-8	6.97	1.243	29.427
M2-3-9	8.97	4.230	70.406	M1-3-9	8.97	1.112	39.198
M2-3-10	11.97	3.901	64.930	M1-3-10	11.97	0.851	32.673
M2-3-11	16.07	3.483	57.973	M1-3-11	16.07	0.987	30.593

Table 5.2: (b) Si concentration in acid leaching solution using Ilulialik GRF

Ilulialik-50 mg				Ilulialik-25 mg			
Sample	Time (h)	Si (ppm)	Si (µmol L^{-1})	Sample	Time (h)	Si (ppm)	Si (µmol L^{-1})
Start	0.00	0.000	0.00	Start	0.00	0.000	0.000
I2-1-1	0.50	4.436	4.30	I1-1-1	0.50	2.362	39.320
I2-1-2	1.00	4.121	7.87	I1-1-2	1.00	1.924	71.348
I2-1-3	1.40	1.922	9.33	I1-1-3	1.40	0.923	47.391
I2-1-4	2.02	1.701	10.80	I1-1-4	2.02	0.901	30.363
I2-1-5	3.02	1.922	12.50	I1-1-5	3.02	0.961	30.996
I2-1-6	4.02	1.298	13.57	I1-1-6	4.02	0.741	28.329
I2-1-7	5.02	1.545	14.94	I1-1-7	5.02	0.854	26.548
I2-1-8	10.02	1.857	23.98	I1-1-8	10.02	0.847	28.312
I2-1-9	15.09	0.796	27.23				
I2-1-10	20.09	0.544	29.48	Start	0.00	0.000	0.000
				I1-2-1	0.50	2.351	39.139
Start	1.00	0.000	69.220	I1-2-2	1.00	4.159	69.220
I2-2-1	1.40	4.556	43.949	I1-2-3	1.40	2.640	43.949
I2-2-2	2.02	4.224	26.106	I1-2-4	2.02	1.568	26.106
I2-2-3	3.02	1.843	24.388	I1-2-5	3.02	1.465	24.388
I2-2-4	4.02	1.630	23.668	I1-2-6	4.02	1.422	23.668
I2-2-5	5.02	1.606	20.539	I1-2-7	5.02	1.234	20.539
I2-2-6	7.02	1.328	34.970	I1-2-8	7.02	2.101	34.970
I2-2-7	9.02	1.108	41.079	I1-2-9	9.02	2.468	41.079
I2-2-8	12.02	2.966	35.203	I1-2-10	12.02	2.115	35.203
I2-2-9	16.12	1.755	42.676	I1-2-11	16.12	2.564	42.676
				Start	0.000	0.00	0.000
Start	2.395	4.62	39.863	I1-3-1	2.395	4.62	39.863
I1-3-2	4.257	7.76	70.850	I1-3-2	4.257	7.76	70.850
I1-3-3	2.695	9.00	44.855	I1-3-3	2.695	9.00	44.855
I1-3-4	1.585	10.29	26.377	I1-3-4	1.585	10.29	26.377
I1-3-5	1.498	11.59	24.928	I1-3-5	1.498	11.59	24.928
I1-3-6	1.356	12.62	22.572	I1-3-6	1.356	12.62	22.572
I1-3-7	1.163	13.57	19.358	I1-3-7	1.163	13.57	19.358
I1-3-8	2.067	16.39	34.404	I1-3-8	2.067	16.39	34.404
I1-3-9	2.423	17.85	40.330	I1-3-9	2.423	17.85	40.330

Table 5.3:(a) Si concentration in alkaline leaching solution using Maalutu GRF

	Maalutu-50 mg				Maalutu-25 mg		
Sample	Time (h)	Si (ppm)	Si (µmol L^{-1})	Sample	Time (h)	Si (ppm)	Si (µmol L^{-1})
Start	0.00	0.00	0.00	Start	0.00	0.00	0.000
M2_1	0.08	0.000	0.00	M1_1	0.08	0.000	0.000
M2_2	0.25	0.336	5.59	M1_2	0.17	0.171	2.845
M2_3	0.50	0.45	7.55	M1_3	0.33	0.27	4.412
M2_4	0.75	0.52	8.72	M1_4	0.58	0.31	5.196
M2_5	1.00	0.62	10.29	M1_5	0.83	0.31	5.196
M2_6	2.00	0.92	15.38	M1_6	1.08	0.41	6.763
M2_7	3.00	1.02	16.95	M1_7	2.08	0.55	9.114
M2_8	4.00	1.87	31.06	M1_8	3.08	0.57	9.506
M2_9	7.50	3.37	56.13	M1_9	4.08	1.11	18.518
M2_10	22.83	4.50	74.94	M1_10	7.58	2.05	34.192
M2_11	30.00	5.47	91.01	M1_11	22.92	2.41	40.069
M2_12	47.50	5.66	94.14	M1_12	30.08	2.78	46.339
M2_13	55.08	6.41	106.68	M1_13	47.58	3.00	49.865
M2_14	70.50	6.29	104.72	M1_14	55.17	3.35	55.743
M2_15	79.50	6.409	106.68	M1_15	70.58	3.655	60.837
M2_16	92.75	5.750	95.71	M1_16	79.58	3.773	62.796
M2_17	100.58	6.95	115.69	M1_17	92.83	3.89	64.755
M2_18	117.67	6.88	114.52	M1_18	100.75	3.89	64.755
M2_19	124.55	5.75	95.71	M1_19	117.75	3.56	59.269
M2_20	143.00	6.53	108.64	M1_20	124.63	3.77	62.796
M2_21	150.50	6.62	110.21	M1_21	143.08	3.82	63.579
M2_22	166.50	6.88	114.52	M1_22	150.58	3.80	63.188
M2_23	175.00	6.97	116.09	M1_23	166.58	3.82	63.579
M2_24	191.67	7.14	118.83	M1_24	175.08	3.77	62.796
M2_25	218.67	5.94	98.90	M1_25	191.75	4.06	67.498
M2_26	248.00	5.94	98.90	M1_26	218.75	4.46	74.159
M2_27	263.42	5.52	91.88	M1_27	248.08	4.74	78.861
M2_28	270.58	6.50	108.15	M1_28	263.42	4.60	76.510
M2_29	291.10	6.57	109.42	M1_29	270.58	4.53	75.334
M2_30	315.58	6.32	105.28	M1_30	291.10	4.74	78.861

Table 5.3: (b) Si concentration in alkaline leaching solution using Ilulialik GRF

Ilulialik-50 mg				Ilulialik-25 mg			
Sample	Time (h)	Si (ppm)	Si (µmol L^{-1})	Sample	Time (h)	Si (ppm)	Si (µmol L^{-1})
Start	0.00	0.00	0.000	Start	0.00	0.00	0.000
I2_1	0.08	0.862	14.346	I1_1	0.08	0.359	5.979
I2_2	0.25	1.207	20.089	I1_2	0.25	0.642	10.681
I2_3	0.50	1.36	22.641	I1_3	0.50	0.69	11.465
I2_4	0.75	1.49	24.875	I1_4	0.75	0.74	12.249
I2_5	1.00	1.46	24.236	I1_5	1.00	0.76	12.641
I2_6	2.00	1.53	25.513	I1_6	2.00	0.85	14.208
I2_7	3.00	1.82	30.299	I1_7	3.00	0.74	12.249
I2_8	4.00	2.43	40.508	I1_8	4.00	0.95	15.775
I2_9	7.50	4.01	66.671	I1_9	7.50	1.25	20.869
I2_10	22.83	4.37	72.733	I1_10	22.83	2.12	35.367
I2_11	30.00	5.25	87.409	I1_11	30.00	2.50	41.637
I2_12	47.50	5.50	91.557	I1_12	47.50	3.09	51.432
I2_13	55.08	5.75	95.705	I1_13	55.08	3.14	52.216
I2_14	70.50	6.06	100.809	I1_14	70.50	3.66	60.837
I2_15	79.50	6.287	104.638	I1_15	79.50	3.796	63.188
I2_16	92.75	6.057	100.809	I1_16	92.75	3.938	65.539
I2_17	100.58	6.44	107.191	I1_17	100.58	3.91	65.147
I2_18	117.67	6.13	102.086	I1_18	117.67	4.01	66.714
I2_19	124.55	5.62	93.471	I1_19	124.55	3.80	63.188
I2_20	143.00	5.86	97.619	I1_20	143.00	3.87	64.363
I2_21	150.50	5.67	94.428	I1_21	150.50	3.77	62.796
I2_22	166.50	5.19	86.452	I1_22	166.50	3.84	63.971
I2_23	175.00	6.04	100.490	I1_23	175.00	3.80	63.188
I2_24	191.67	5.79	96.343	I1_24	191.67	4.03	67.106
I2_25	218.67	6.00	99.852	I1_25	218.67	3.10	51.675
I2_26	248.00	5.73	95.386	I1_26	248.00	2.96	49.319
I2_27	263.33	5.40	89.962	I1_27	263.33	2.88	47.973
				I1_28	270.50	3.06	51.002
				I1_29	291.02	2.56	42.588
				I1_30	291.02	2.86	47.637

5.4.2. GRF DISSOLUTION IN ALKALINE pH

Figure 5.2 (b) shows the temporal evolution of Si released in the alkaline leaching solutions of Maalutu and Ilulialik. The experiments were conducted for a longer period in comparison to acid-leach experiments for the solution to reach a steady-state concentration. For both GRFs, higher amount of solid mass generated higher Si release and were fairly proportional, indicating the reactions occur far from equilibrium. Unlike the acid-leach releases, Maalutu and Ilulialik GRFs follow a similar trend for their respective amounts of solid masses. The Si concentrations were lower in alkaline-leached solutions than in acid-leached solutions.

5.4.3. GRF DISSOLUTION AT TWO pCO_2 CONDITIONS

Two lines of dissolution experiments were conducted using Maalutu GRF at ambient and 0.05 atm pCO_2 and in two parts. In first part of the experiments, GRF was reacted with DI water, after which the end solutions were divided into two equal halves. For both lines of the experiments, one half was then amended with additional DI water, while the other was amended with additional GRF, to test if the steady concentration level represented exhaustion of a reactive component of the GRF, saturation with respect to a primary or secondary phase, or changing reaction rates with change in solution chemistry. The temporal changes in solute concentration are illustrated in Figures 5.3 and 5.4 for ambient and 0.05 atm pCO_2. The evolution of chemical compositions in the aqueous solutions with respect to time are given in Tables 5.4 and 5.5.

For the first part of both lines of the experiments, the rapid release of cations in the initial stage was coincident with the increase in pH, which suggests that the reaction consumed protons, possibly by ion exchange at the silicate mineral surfaces. The dissolution of ultrafine particles, which is present in high abundance in the GRF (Section 3.3.2), could also result in a high initial release (Holdren and Berner, 1979). Na concentrations were the highest among all cations for both pCO_2 conditions. The concentrations of divalent cations were comparatively lower and lacked any systematic trend during the ambient conditions but at 0.05 atm pCO_2, the overall cation release was higher and followed a non-linear trend similar to the

monovalent ions. At the end of the first part of the experiment, the Ca and Mg concentrations were 4.8 and 5.5 times higher than their ambient pCO_2 counterparts, respectively, while K concentration was almost double in the 0.05 atm pCO_2 experiment, relative to ambient air. Although the initial Na release rate was approximately 1.5 times higher at the elevated pCO_2, the overall rise in its concentration was less pronounced compared to that of Ca, Mg and K. the steady increase in Si release at both pCO_2 conditions show that although concentrations of these cations remained nearly constant, the GRF was continuously dissolving.

Sampling of aliquots from the aqueous solutions in the first part of the experiments, led to less than 1 L starting solution for the second part of the experiments. Due to a difference in amount of additional GRF in the second part for ambient and elevated pCO_2 experiments, their solid to water ratio were dissimilar (Tables 5.4 and 5.5). Upon adding 1 L DI water, the major cation concentrations were reduced by approximately their respective dilution factor in both ambient and elevated pCO_2 experiments. Addition of fresh GRF, however, produced different concentration curves for the two pCO_2 experiments. In the elevated pCO_2, all major cation concentrations experienced a rapid increase within the first 10 minutes of adding GRF, similar to first part of the experiment. In the ambient pCO_2, only Na concentration increased, whereas K and Si concentrations were halved. Si concentration of the aqueous solution continued to rise but the increase in K concentration was minimal. By the end of the second part of the experiment, Na concentration had almost doubled from the initial value.

Throughout all the experiments, Al and Fe concentrations in both pCO_2 conditions remained relatively negligible, suggesting they did not enter into solution or likely precipitated as secondary phases. In the first part of the experiments, all the aqueous solutions were subsaturated with respect to the albite but reached saturation and were supersaturated with respect to quartz, gibbsite, illite and kaolinite. K-feldspar reached near saturation at both pCO_2 conditions. Saturation indices for selected minerals are shown in Figure 5.4. No secondary phases were determined by XRD on the reacted material after the first part of the experiments. This does not indicate absence of secondary phase but rather that the proportion of precipitated material might have been too low for XRD detection. GRF reacted in ambient pCO_2 was found to contain 5 % amorphous or undetermined clay content while at the 0.05 atm pCO_2, it did not show any content of unknown phases in the analysis. Since there is likelihood of precipitation of secondary phases due to non-stoichiometric release in Si and

Al, the reaction rates calculated from Eq. 5.5, were apparent reaction rates and are shown in Figure 5.6.

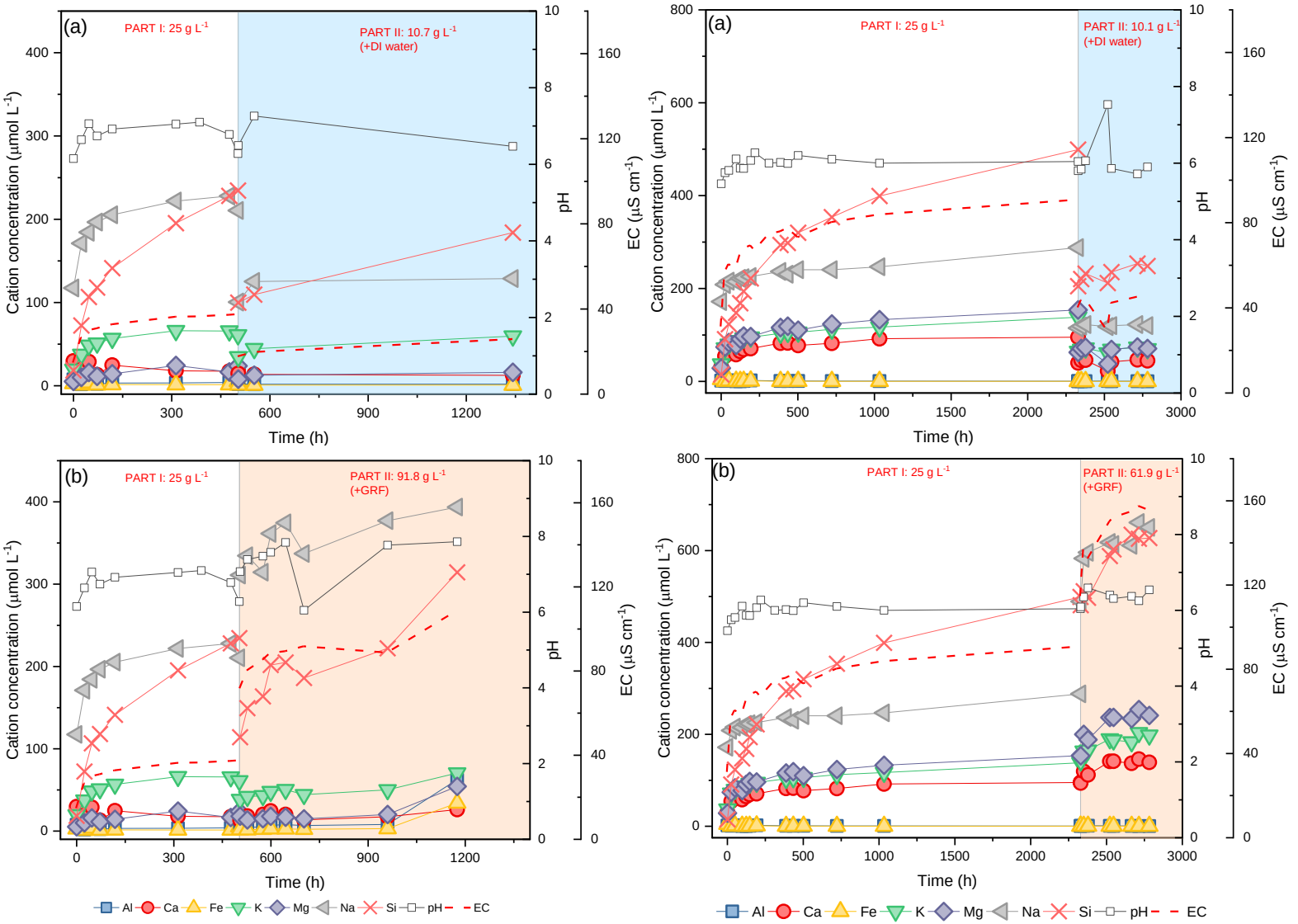


Figure 5.4.3.3: Temporal evolution of cation concentrations during the first and second part of experiments at (a) and (b) ambient pCO_2, and (c) and (d) 0.05 atm pCO_2. The first part is common in (a) and (b), and in (c) and (d). Full page view for each plot is given in Appendix: A.7- A.10.

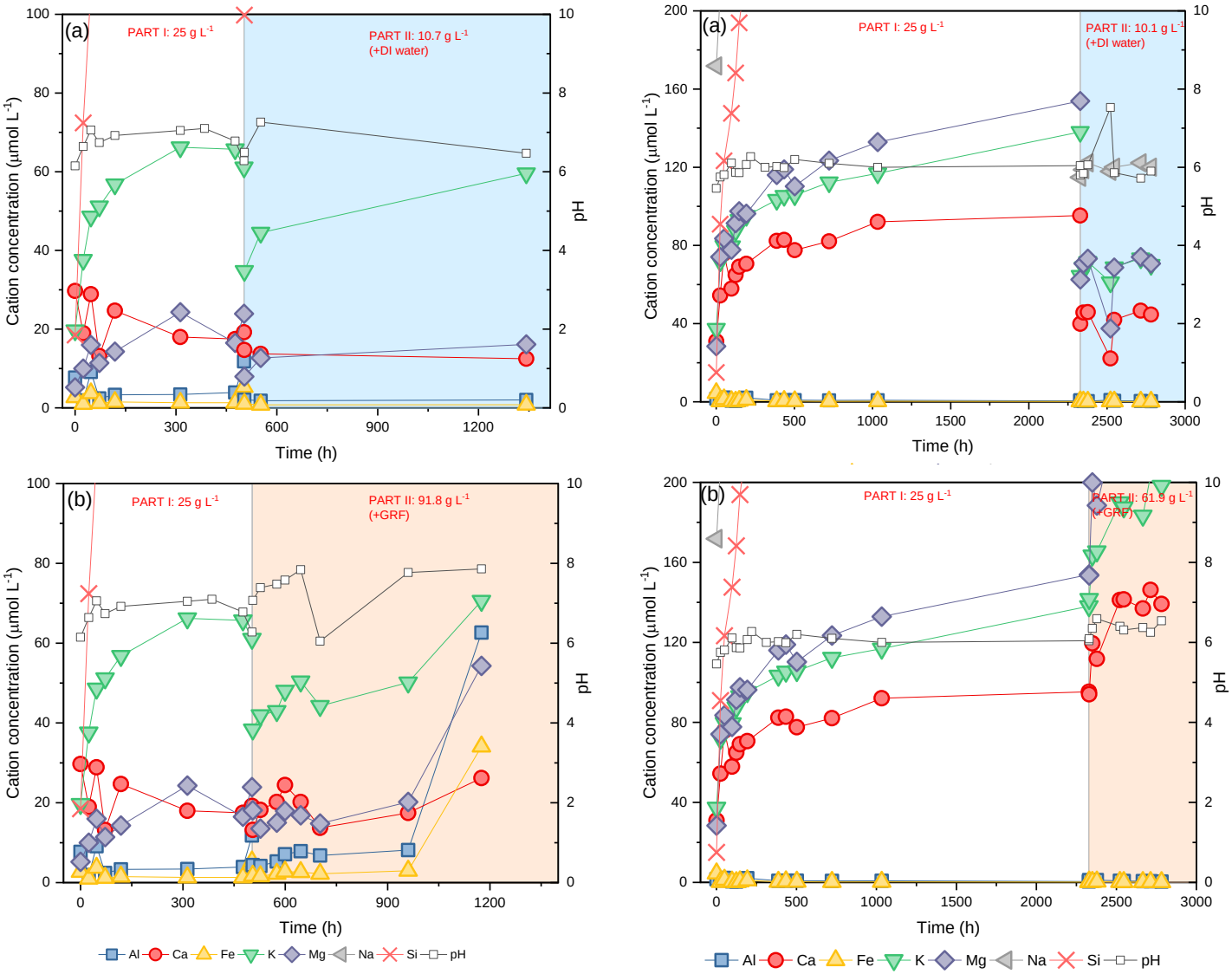


Figure 5.4.34: Zoomed in view for plots from Figure 5.3 to show the temporal variation in the first and second part of experiments at (a) and (b) ambient pCO_2, and (c) and (d) 0.05 atm pCO_2. The first part is common in (a) and (b), and in (c) and (d).

Table 5.4: Solution composition during the first and second part of experiments at ambient pCO_2.

	Time h	pH	EC µS cm^{-1}	Al mmol L^{-1}	Ca mmol L^{-1}	Fe mmol L^{-1}	K mmol L^{-1}	Mg mmol L^{-1}	Na mmol L^{-1}	Si mmol L^{-1}	Alkalinity mEqv L^{-1}	Cl mmol L^{-1}	SO_4 mmol L^{-1}	NO_3 mmol L^{-1}
PART I: GRF (50 g) + DI water (2 L), 25 g L^{-1}														
200108-M-1	0.08	6.15	14.82	0.008	0.030	0.003	0.020	0.005	0.117	0.019	0.032	0.050	0.016	0.018
200108-M-2	24.08	6.64	26.6	0.002	0.019	0.001	0.038	0.010	0.171	0.072	0.123	0.048	0.014	0.016
200108-M-3	46.92	7.06	30.03	0.009	0.029	0.004	0.049	0.016	0.184	0.107	0.159	0.047	0.020	0.016
200108-M-4	71.92	6.74	30.92	0.002	0.013	0.001	0.051	0.011	0.197	0.118	0.186	0.054	0.017	0.015
200108-M-5	118.25	6.92	32.78	0.003	0.025	0.002	0.057	0.014	0.205	0.141	0.187	0.053	0.022	0.021
200108-M-6	313	7.05	36.39	0.003	0.018	0.001	0.066	0.024	0.222	0.195	0.237	0.054	0.028	0.023
200108-M-7	385.17	7.1	36.56	0.004	0.026	0.001	0.075	0.057	0.594	0.209	0.239	0.194	0.024	0.011
200108-M-8	475.97	6.78	37.28	0.004	0.018	0.001	0.066	0.017	0.228	0.228	0.238	0.054	0.017	0.011
200108-M-9	502.33	6.28	37.57	0.012	0.019	0.005	0.061	0.024	0.211	0.235	0.243	0.056	0.021	0.011
PART II: End solution from I (0.749 L) + DI water (1 L), 10.7 g L^{-1}														
200108-M1-1	503.42	6.49	17.79	0.002	0.015	0.001	0.035	0.008	0.100	0.100	0.090	0.022	0.011	0.010
200108-M1-3	552.08	7.26	19.82	0.002	0.014	0.001	0.045	0.013	0.125	0.109	0.139	0.192	0.020	0.014
200108-M1-5	1342.08	6.47	25.86	0.002	0.012	0.001	0.060	0.016	0.129	0.184	0.188	0.025	0.011	0.007
PART II: End solution from I (0.749 L) + GRF (50 g), 91.8 g L^{-1}														
200108-M2-1	528.58	7.07	71.83	0.004	0.013	0.002	0.038	0.018	0.311	0.114	0.289	0.062	0.011	0.012
200108-M2-2	551.33	7.39	80.34	0.004	0.018	0.002	0.042	0.014	0.334	0.149	0.155	0.119	0.035	0.032
200108-M2-3	599.00	7.48	85.3	0.005	0.020	0.002	0.043	0.015	0.314	0.164	0.363	0.106	0.034	0.031
200108-M2-4	623.42	7.58	88.66	0.007	0.024	0.003	0.048	0.018	0.361	0.202	0.388	0.116	0.038	0.035
200108-M2-5	669.25	7.84	89.46	0.008	0.020	0.003	0.050	0.017	0.375	0.205	0.389	0.120	0.039	0.034
200108-M2-6	726.08	6.05	91.76	0.007	0.014	0.002	0.044	0.015	0.337	0.186	0.392	0.105	0.035	0.028
200108-M2-7	984.17	7.77	88.77	0.008	0.017	0.003	0.050	0.020	0.377	0.222	0.459	0.119	0.041	0.032
200108-M2-8	1199.33	7.86	108.7	0.063	0.026	0.034	0.071	0.054	0.394	0.314	0.516	0.122	0.048	0.039

There was an abrupt elevation in elemental concentrations at 385 h for the ambient pCO_2, which were not accompanied by a comparable change in pH, EC or the alkalinity of the solution. It was possibly due to presence of solid particles in the filtered sample and was part of an experimental artifact. They were excluded from the plots (Figures 5.3-5.4) to aid in visual interpretation.

Table 5.5: Solution composition during the first and second part of experiments at 0.05 atm pCO_2.

	Time h	pH	EC µS cm^{-1}	Al mmol L^{-1}	Ca mmol L^{-1}	Fe mmol L^{-1}	K mmol L^{-1}	Mg mmol L^{-1}	Na mmol L^{-1}	Si mmol L^{-1}	Alkalinity mEqv L^{-1}	Cl mmol L^{-1}	SO_4 mmol L^{-1}	NO_3 mmol L^{-1}
PART I: GRF (50 g) + DI water (2 L), 25 g L^{-1}														
200115-C-1	0.08	5.46	31.26	0.002	0.031	0.004	0.037	0.028	0.172	0.015	0.215	0.048	0.015	0.014
200115-C-3	25	5.75	56.79	0.001	0.054	0.000	0.072	0.074	0.208	0.091	-	0.047	0.018	0.014
200115-C-4	49.92	5.81	60.57	0.002	0.076	0.001	0.080	0.084	0.216	0.123	0.487	0.046	0.019	0.014
200115-C-5	97.25	6.11	58.73	0.000	0.058	0.000	0.080	0.078	0.215	0.148	0.465	0.045	0.019	0.012
200115-C-6	124.16	5.87	65.17	0.000	0.065	0.000	0.087	0.091	0.222	0.168	0.515	0.047	0.022	0.013
200115-C-7	146.5	5.86	67.9	0.001	0.069	0.000	0.093	0.098	0.223	0.194	0.547	0.051	0.027	0.017
200115-C-8	192.58	6.07	69.36	0.002	0.071	0.001	0.095	0.096	0.226	0.222	0.553	0.051	0.027	0.017
200115-C-9	220.33	6.27	67.13	0.001	0.085	0.000	0.130	0.166	0.796	0.219	0.541	0.106	0.028	0.013
200115-C-10	311.75	6	74.7	0.001	0.079	0.000	0.108	0.125	0.370	0.271	0.610	0.061	0.029	0.013
200115-C-11	386.92	6.02	75.93	0.001	0.082	0.000	0.103	0.116	0.237	0.294	0.610	0.071	0.025	0.017
200115-C-12	434.25	5.99	77.55	0.001	0.083	0.000	0.105	0.119	0.231	0.298	0.628	0.053	0.023	0.016
200115-C-13	502.33	6.2	73.23	0.001	0.078	0.000	0.106	0.110	0.241	0.320	0.611	0.047	0.023	0.016
200115-C-14	722	6.1	80.3	0.001	0.082	0.000	0.112	0.123	0.241	0.354	0.652	0.048	0.024	0.016
200115-C-15	1032.67	6	83.91	0.001	0.092	0.000	0.117	0.133	0.247	0.399	0.702	0.048	0.025	0.016
200115-C2-0	2328.33	6.04	90.85	0.000	0.095	0.000	0.138	0.154	0.288	0.499	0.751	0.049	0.032	0.016
PART II: End solution from I (0.677 L) + DI water (1 L), 10.1 g L^{-1}														
200115-C1-1	2329	5.8	40.24	0.001	0.040	0.000	0.064	0.063	0.115	0.205	0.306	0.019	0.014	0.008
200115-C1-2	2349.28	5.84	43.59	0.000	0.046	0.000	0.069	0.071	0.119	0.220	0.349	0.020	0.015	0.007
200115-C1-3	2377.42	6.06	44.19	0.000	0.046	0.000	0.072	0.073	0.122	0.232	0.348	0.019	0.014	0.007
200115-C1-4	2522	7.53	29.37	0.001	0.022	0.000	0.061	0.038	0.118	0.212	0.231	0.019	0.015	0.008
200115-C1-5	2546.5	5.86	42.36	0.001	0.042	0.000	0.069	0.069	0.120	0.235	0.332	0.018	0.015	0.007
200115-C1-6	2715.87	5.72	45.23	0.000	0.047	0.000	0.073	0.074	0.122	0.254	0.361	0.019	0.014	0.010
200115-C1-7	2781.75	5.9	43.81	0.000	0.045	0.000	0.070	0.071	0.120	0.248	0.356	0.019	0.015	0.006
PART II: End solution from I (0.677 L) + GRF (25 g), 61.9 g L^{-1}														
200115-C2-1	2329.65	6.09	114.8	0.001	0.094	0.000	0.142	0.153	0.489	0.481	0.835	0.120	0.049	0.038
200115-C2-2	2349.75	6.35	137.1	0.001	0.120	0.000	0.163	0.200	0.583	0.511	1.073	0.123	0.054	0.012
200115-C2-3	2377.92	6.59	132.6	0.001	0.112	0.000	0.165	0.188	0.596	0.497	1.019	0.126	0.056	0.018
200115-C2-4	2522.5	6.4	150.2	0.001	0.141	0.000	0.190	0.237	0.618	0.588	1.227	0.126	0.058	0.009

200115-C2-5	2546.5	6.31	152.1	0.001	0.141	0.000	0.187	0.237	0.613	0.602	1.240	0.126	0.058	0.009
200115-C2-6	2665.8	6.37	155	0.001	0.137	0.000	0.183	0.234	0.611	0.634	1.143	0.118	0.056	0.008
200115-C2-7	2713.8	6.25	157.6	0.001	0.146	0.000	0.204	0.254	0.661	0.626	1.269	0.132	0.062	0.009
200115-C2-8	2782.42	6.54	155.6	0.000	0.139	0.000	0.198	0.241	0.650	0.627	1.200	0.137	0.063	0.041

There was an abrupt elevation in elemental concentrations at 220 h and 311 h for the elevated pCO_2 which were not accompanied by a comparable change in pH, EC or the alkalinity of the solution. It was possibly due to presence of solid particles in the filtered sample and was part of an experimental artifact. They were excluded from the plots (Figures 5.3-5.4) to aid in visual interpretation.

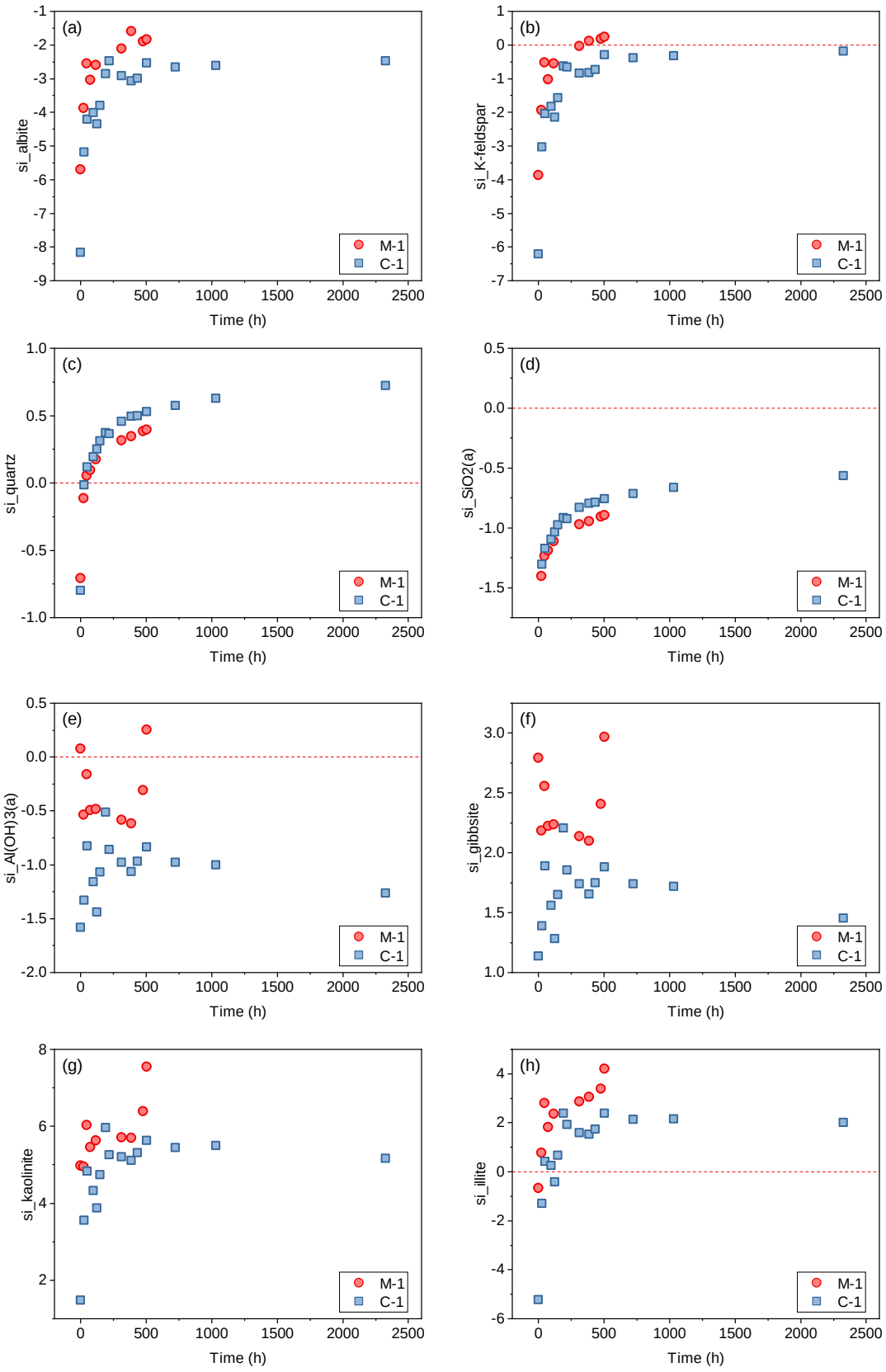


Figure 5.4.35: Temporal evolution of saturation indices of (a) albite, (b) K-feldspar, (c) quartz, (d) amorphous SiO_2, (e) amorphous $Al(OH)_3$, (f) gibbsite, (g) kaolinite, and (h) illite, during the first part of the experiment at ambient pCO_2 (M-1) and 0.05 atm pCO_2 (C-1).

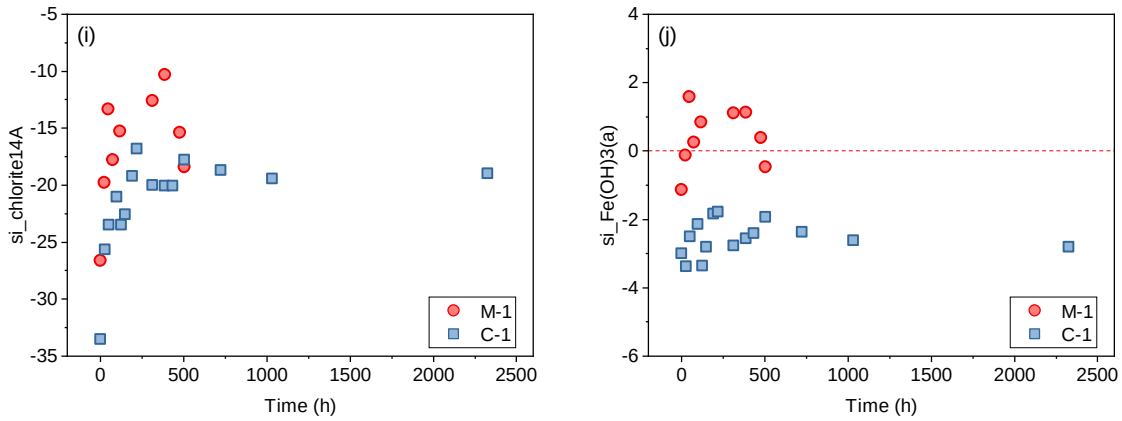


Figure 5.4.35: Temporal evolution of saturation indices of (i) chlorite and (j) amorphous $Fe(OH)_3$, during the first part of the experiment at ambient pCO_2 (M-1) and 0.05 atm pCO_2 (C-1). (contd.)

Throughout all the experiments, Al and Fe concentrations in both pCO_2 conditions remained relatively negligible, suggesting they did not enter into solution or likely precipitated as secondary phases. All the aqueous solutions were supersaturated with respect to quartz, gibbsite, illite and kaolinite. Saturation indices for selected minerals are shown in Figure 5.5.

No secondary phases were determined by XRD in the reacting material after the first part of the experiments. The precipitated material may also be too small in quantity for XRD detection. GRF reacted in ambient pCO_2 was found to contain 5 % amorphous or undetermined clay content while at the 0.05 atm pCO_2, it did not show any content of unknown phases in the analysis. Since there is likelihood of precipitation of secondary phases due to non-stoichiometric release in Si and Al, the reaction rates calculated from Eq. 5.5, were apparent reaction rates and are shown in Figure 5.6.

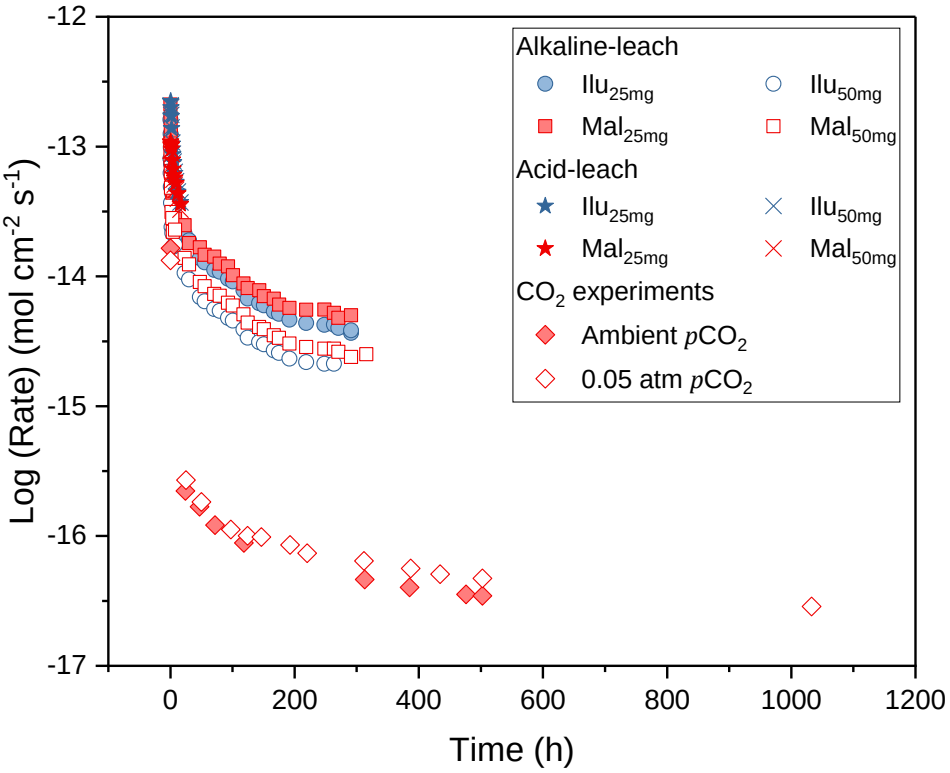


Figure 5.6: Log dissolution rate of Maalutu and Ilulialik GRFs in mol/cm2/in acidic and alkaline media, and at ambient at elevated (0.05 atm) pCO2 conditions

Table 5.5: XRD data for Maalutu before and after pCO_2 experiments in wt. %

	MAL	M-1 final	C-15 final
plagioclase	43.5(4)	38.3(5)	42.0(4)
microcline	10.7(3)	11.7(3)	11.2(3)
quartz	23.1(2)	11.4(2)	16.9(2)
biotite	7.8(3)	19.0(6)	14.5(6)
chlorite		2.6(2)	1.3(9)
amphibole	10.4(3)	9.1(3)	9.9(3)
augite	1.8(2)	1.1(2)	2.1(3)
epidote	2.7(3)	1.9(3)	2.1(3)

XRD analysis were performed using a Bruker-AXS D8 Advance diffractometer equipped with a Cu X-ray tube at Department of Geosciences and Nature Resource Management (IGN), University of Copenhagen. The values in bracket indicates the standard error in measurement. MAL data is from Chapter 3.

5.5. Discussions

Maalutu and Ilulialik GRFs represent two types of GRFs based on their particle size distribution (PSD). While Maalutu is a poorly sorted GRF with a bimodal PSD, Ilulialik is a relatively well sorted and has a unimodal PSD. The constituent mineralogy, however, does not vary much except the higher concentration of mica and lower concentration of quartz in Ilulialik than in Maalutu, owing to the accumulation of mica in the finer-sized grains. The dissolution curves can be identified as three stages in each of the experimental results – an initial rapid increase in concentration, followed by a region of continuously decreasing rate, which approaches a steady metastable state of equilibrium.

5.5.1. Acid and Alkaline leach

In acid leaching of the GRFs, Maalutu has a lower initial release than Ilulialik, however, they follow a curve parallel to one another after the first stage of the reaction. The high initial release is likely associated with the exchange of cations and the dissolution of ultrafine particles (Holdren and Berner, 1979), which is more abundant in Ilulialik GRF. The finer grains are predominantly mica, which is present in ~3 times higher quantities in Ilulialik than in Maalutu. Biotite dissolution is faster at lower pH due to availability of higher H^+ ions that can interact with the interlayer K^+ ions in biotite (Acker and Bricker, 1992). During alkaline leach, however, both Ilulialik and Maalutu GRF dissolution followed the same Si release curve pattern for the same mass of starting material. This indicates that mineral specific dissolution is low in an alkaline pH suggesting GRF acts as a bulk material.

Dissolution of silicate minerals advance by exchange of protons and diffusion of alkalis and alkaline earths out of the mineral surface into the solution. For feldspars, the rapid depletion in cations and Si and/or Al retention in the mineral surface thus forms a silica and alumina rich residual layer. At the initial stages of alteration of this layer, diffusion is likely to be fast due to a high concentration gradient at the interface of mineral surface and solution. However, as the thickness of such an altered layer increases with time, it acts as a diffusion barrier lowering the solute transfer rate thereby decreasing the overall dissolution rate (Chou and Wollast, 1984; Lasaga, 1984). This preferential leaching of cations might contribute to the non-stoichiometry of solute concentration of the aqueous solutions at the initial stages of the

reaction. Wollast and Chou (1985), for example, report that albite dissolution proceeds through a rapid initial Na release with proportions of silica and alumina retained in the residual layer varying with pH. In general, this altered layer grows thicker at lower pH and can range from tens to many hundreds of angstroms (Chou and Wollast, 1984; Muir and Nesbitt, 1991). At lower pH, Al extraction is higher than Si such that the residual layer of Si is thicker than that of Al. However, at pH> 5, Al extractions from the mineral surface is the same as Si maintaining the Al/Si ratio of the residual layer same as that of the initial feldspar.

As the reaction proceeds over a period of time, the rate of diffusion of cations from the mineral surface through the altered layer slows to match the release rate of Si from the exterior of the layer so that a steady state, stoichiometric release rate is reached. The retention of Si in the residual layer at lower pH prevents dissolution of larger particles beyond a significant exchange of cations with the solution protons leaving a layer of almost pure silica. Therefore, the Si release in acid leaching of the GRFs show that the differences in their PSD influence their dissolution mechanism and dissolution of ultrafine particles was primarily the reason for the disparity between the two GRF releases of same starting amount.

In alkaline leach of the GRFs, however, the difference in mineral composition does not appear to affect GRF dissolution. Both Maalutu and Ilulialik GRF follow similar Si release curve pattern for majority of the experiment. The variations were likely part of an experimental artifact as despite the differences, they follow similar pattern. The almost overlapping release curves for the two GRFs suggest that the dissolution is a bulk dissolution of the material. The proportionality between Si release and the amount of the reacting material GRFs indicate that the available surface area is a primary factor determining the extent of reaction. The specific surface area for Maalutu and Ilulialik GRF is 15 and 19.6 $m^2\ g^{-1}$ (Chapter 3). Although Ilulialik has ~25 % higher specific surface area, the difference was seemingly negligible in influencing their Si release significantly.

5.5.2. ELEMENT-TO-MINERAL ATTRIBUTION

Dissolution experiments using GRF were performed using DI water at room temperature at two pCO_2 conditions. Similar to the Si release at acid and alkaline leach experiments, the Si release was higher at lower pH resulting from elevated pCO_2 condition than at near neutral

pH conditions. The analysis of water chemistry of the aqueous solutions allows us to explore mineral specific contribution.

Mineral heterogeneity of GRF and the possible formation of secondary phases greatly complicate the element-to-mineral attribution, especially for Si and Al. Na is the only element that can be primarily assigned to a specific mineral, plagioclase. Based on the mineral composition of Maalutu GRF and simplifying assumptions, K release can be attributed mainly to the dissolution of K-feldspar and/or biotite, Mg to that of biotite and/or amphibole, and Ca to that of plagioclase and/or amphibole. Based on Eq. 5.2a, Na^+ released from albite, should be balanced by formation of HCO_3^-. This allowed us to use Na^+ ions in the solution as markers for bicarbonate contribution from plagioclase. Similarly, Ca^{2+} and K^+ were used as markers for bicarbonate contribution from anorthite and K-feldspar dissolution.

Al and Fe continued to maintain an overall low concentration in the aqueous solutions, under both ambient and 0.05 atm pCO_2 conditions. Al and Fe releases are highly dependent on pH and generally precipitate as $Al(OH)_3$ and $Fe(OH)_3$, respectively, near the sub-neutral pH conditions. As the precipitation of secondary phases cannot be discounted from the water chemistry data, the apportion was primarily to compare the results from the two pCO_2 conditions. Carbonates are present in negligible quantities (e.g. calcite <0.02 wt. %) in Maalutu GRF, so their contribution to solute release in the aqueous solutions is most likely insignificant. Since the experiments take place in near-neutral pH, total alkalinity can be approximated to the bicarbonate concentration.

Figure 5.7 illustrates the area curves for the sum of two or more cations representing a maximum possible alkalinity contribution due to their respective mineral dissolution. These were then compared with the expected alkalinity, calculated by equating the conservative ions concentration, and the observed alkalinity data. In both ambient and elevated pCO_2 experiments, the expected alkalinity overlapped with the observed alkalinity for majority of the data. However, they were ~0.1 mEqv L^{-1} lower than the area curves of the total major cation concentrations and followed their trends in parallel, in both the lines of experiments. The disparity can be attributed to dissolution of salts in the aqueous solutions at the initial stages of the experiments, which thereafter maintained a constant difference with respect to the contribution from dissolution of minerals. The dissolution of salts contributed to ~15 % and ~30 % of the total major cations concentration in the first part of the ambient pCO_2 and

elevated pCO_2 experiments, respectively. For the purpose of simplicity, composition of the aqueous solution under ambient pCO_2 can be explained by plagioclase dissolution alone; whereas, in the elevated pCO_2, it exceeded the expected area curve for feldspars and involved dissolution of more than one mineral, possibly biotite and/or amphibole.

In general, feldspar dissolution rates are reported to increase as pH is lowered in the acidic range. Monovalent ions are more easily dissociated than divalent ions due to a higher anion affinity. A lower pH has higher H^+ concentration, which can promote interaction between these species, thereby, releasing higher K^+ in the aqueous solution. Garrels and Howard, (1959) note that the interaction between K-feldspar and hydrogen ions structurally disrupts the mineral surface and H^+-K^+ exchange depletes the surface in K, leaving a transition zone that develops into a diffusional barrier slowing the reaction. In plagioclase dissolution, although the initial rate of Na^+ release was higher in the elevated pCO_2, Na concentrations were comparable in both pCO_2 experiments (Figures 5.3 and 5.4). Chou and Wollast, (1984) showed that when albite is reacted with water in the acidic range of pH, increase in Na release is significant only at pH < 2. This could explain the negligible difference in Na concentration of the solution in the two lines of experiments as pH of the experiments in this study ranged between 5 and 8.

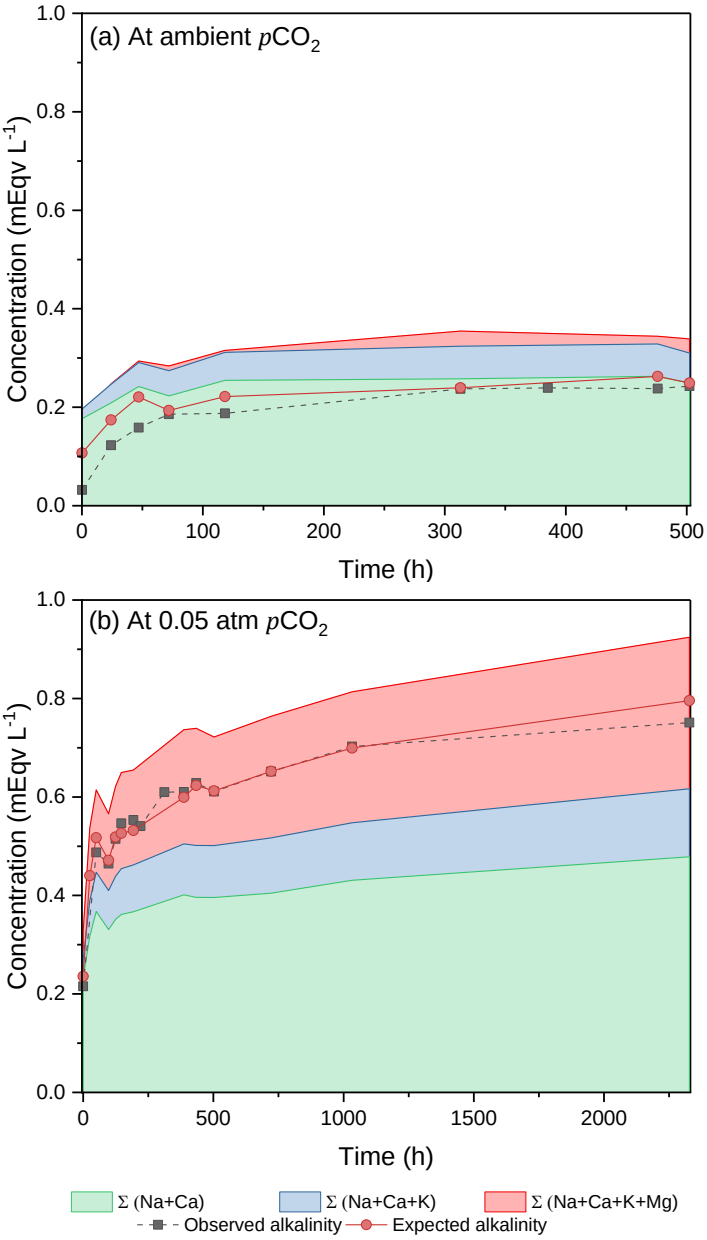


Figure 5.7: Area curves showing major cation concentration in the aqueous solutions for first part of the experiment at ambient and 0.05 atm pCO_2. Expected alkalinity was obtained by equating the conservative ions concentration, and the observed alkalinity data.

K-feldspar, biotite and amphibole were the next in terms of abundance in Maalutu GRF after plagioclase and quartz. Since K-feldspar and biotite weight percentages are comparable, K^+ in the aqueous solution could be derived from either or both of the minerals. To assess the relative contributions of biotite and K-feldspar to K^+ release in the aqueous solutions, K concentration was plotted with respect to that of Mg (Figure 5.8). Bulk stoichiometric ratio for biotite in Maalutu GRF was calculated using assigned composition data from Automated Quantitative Mineralogy using SEM (Section 3.3.3).

Biotite dissolution occurs by interaction between the mineral's non-hydrated interlayer K and the H^+ ions in the solution. K^+ release from biotite is expected to occur faster due to its comparatively weaker bond with the silica sheet. Therefore, the K/Mg trend under ambient conditions suggest a higher rate of release of K compared to Mg, which could be due to significant K-feldspar dissolution in addition to biotite dissolution, and/or an incongruent, selective K-leaching from biotite.

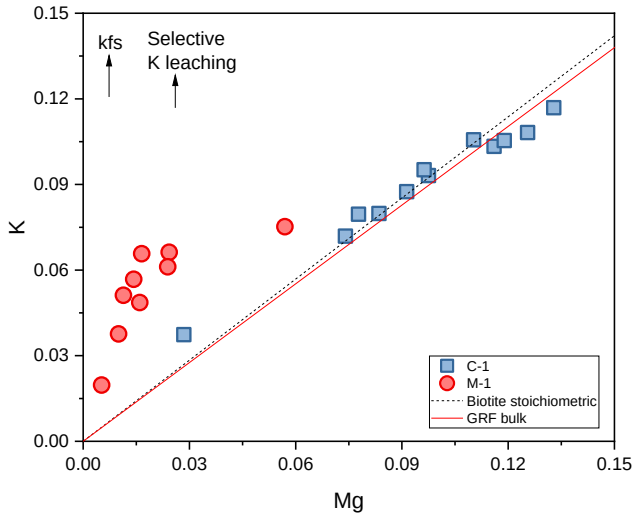


Figure 5.5.28: Cross-plot of K versus Mg comparing contribution from biotite and/or K-feldspar (kfs) during experiments M-1 and C-1. Since K/Mg for kfs is negligible, arrows indicate a kfs dissolution or a selective K leaching.

At elevated pCO_2, the K/Mg ratio followed a trend, which was similar to the stoichiometric K/Mg ratio of Maalutu biotite. However, this ratio was also similar to the molar K/Mg ratio in bulk GRF. Therefore, it is not straightforward to allocate K^+ and Mg^{2+} in the solution to specific minerals in the GRF. It is also possible that the dissolution rates for K and Mg bearing phases were effectively similar in the fine-grained material due to the large exposed surface area. This would imply that bias for dissolution of any particular major phase was insignificant and that all minerals were represented by their modal proportions in the bulk dissolution rate of the GRF.

5.5.3. DISSOLUTION MECHANISMS CONTROLLING THE APPARENT STEADY STATE RELEASE

In dissolution experiments, the shape of the release curves can be controlled by several factors, such as (i) reactants approaching equilibrium, (ii) precipitation of secondary phases, (iii) change in reactant abundance, (iv) change in reactant surface area, or (v) depletion of high-energy components. The set of three sets of GRF dissolution experiments were performed to help us identify if there is a preferential dissolution of one mineral phase over another. The aqueous solutions in the first part of both ambient and 0.05 atm pCO_2 experiments reached apparent steady state release of cations towards the end of the experiment. As no fresh GRF was added in the first part of the pCO_2 experiments and solid to water ratio was kept constant during the experiment, the stabilization of release rates of cations could be due to (i), (ii) or (v).

If the aqueous solution were saturated with respect to one or more primary minerals, the dissolution would no longer be occurring far from equilibrium and the rate of backward reaction would become significant. Therefore, the net reaction would be a resultant of both forward and backward reactions (Eq. 5.3). Moreover, it can be further affected by the precipitation of secondary phases that are likely to have formed from reaction products of the dissolution of primary minerals (Eq. 5.4). An exchange of ions might also be continuously occur during the non-stoichiometric dissolution of minerals. In such cases, unless additional DI water changes the pH of the aqueous solution considerably from the first part of the experiment, it would result in minimal to negligible increase in cation concentration. If, however, the reactions were limited due to slowing of the release rate of cations, adding fresh GRF would provide new reactive surface area with which the solution species canfigure 5.5 interact. In case the aqueous solution was not already saturated with the mineral components, additional GRF can lead to a substantial release of cations due to ion exchange and mineral dissolution.

In both ambient and 0.05 atm pCO_2 experiments, additional DI water decreased the solute concentration of the end solutions from the first experiment, approximately by the factor of dilution. PHREEQC modelled data suggests that K-feldspar reached near-equilibrium and quartz was supersaturated, whereas albite and anorthite were undersaturated in the both

the pCO_2 experiments. This indicates that while dissolution of K-feldspar was limited by its saturation, plagioclase dissolution was possibly limited by the development of cation-depleted surface rich in Al and/or Si, which slows further release of cations. Since pH of the aqueous solutions remains stable to the up to 0.3 units, this does not affect the equilibrium of the system in the reaction vessels.

Addition of GRF in the ambient pCO_2 condition resulted in an instantaneous release of Na at an approximately same rate as the first part of the experiment. Similar to the first part, the rapid initial release suggest cation exchange process with H^+ in the aqueous solution. As PHREEQC modelled data suggests that the aqueous solution was undersaturated with respect to albite (Figure 5.3c), it indicates further plagioclase dissolution may also occur. The drop in K and Si concentrations could be due to precipitation of secondary phases containing K and Si, such as illite (Figure 5.5h). Berger et al. (1995) propose a model where the conversion of kaolinite to end-member illite is promoted when the high K^+/H^+ activity ratio of the aqueous environment overcomes the kinetic barrier to illite crystallization and growth. In this study, this can be prompted by both K-feldspar and biotite as the source for K^+. In simple terms, the reactions may be shown as:

$$\underset{\text{Albite}}{NaAlSi_3O_8} + 2\ Al(OH)_3 + K^+ \rightarrow \underset{\text{Illite}}{KAl_3Si_3O_{10}(OH)_2} + Na^+ + H_2O \qquad (6)$$

However, a definitive reason cannot be concluded for this observation. In the elevated pCO_2 condition, all major cations were instantaneously released at an approximately same rate as the initial experiment indicating cation exchange. Although K feldspar was near equilibrium in the first part of the experiment based on the PHRREQC data, other K-bearing phases, such as biotite, can contribute to K concentration in the solution, in case mineral dissolution occurs. These suggest that if the GRF is reacting in a far from equilibrium condition, higher solute release can be obtained. In an application perspective, this would suggest that the continuous extraction of solutes from the soil by plants will facilitate higher cation release from the GRF, without adding more fresh GRF.

5.5.4. EFFECT OF GRAIN SIZE AND SURFACE AREA

The rapid solute release at the initial stage of silicate mineral dissolution can be attributed to dissolution of the fine particles and reaction at the sites of high surface free energy (Holdren and Berner, 1979). As silicate mineral dissolution occurs at the interface of the mineral surface and water, the surface area of GRF plays a vital role in controlling its overall dissolution rate. Maalutu GRF has a 7 µm median grain size based on laser diffraction and 15 $m^2 g^{-1}$ BET surface area. It has 63% of particles in the silt and clay size fraction (<20 µm; Section 3.3.2).

GRF has undergone a process of intense crushing in the glacial environment resulting in a fine-grained material. Quartz remains more resistant to diminution during the glacial erosion and constitutes ~25 % of the bulk Maalutu GRF. However, due to a relatively larger volume of the quartz grains, they skew the volume-based distribution towards the larger grain size. This contributes to the bimodality of the material's volume-based distribution. Steffensen (2020) compare the volume-based size distribution of Maalutu GRF at three different size fractions and illustrate predominance of quartz in larger grains. He notes that while feldspar is predominant in all size fractions, the finest grain size fraction is enriched in mica and amphiboles while quartz is more enriched in the coarser size fractions, which could have contributed to high cation release rates in the initial stage of the dissolution reactions.

For feldspar dissolution, previous studies (Holdren and Speyer, 1985a, 1985b, 1987) report a decrease in mineral reactivity at the size range 37–75 µm. They suggest that laboratory grinding and crushing the material to a finer size does not necessarily expose additional reactive sites but instead might destroy them physically. However, for feldspars with grain size less than 37 µm they report an increase in reaction rates, which they attribute to its high surface energy. It is possible that the bulk dissolution rate of the material is independent of a particular mineral phase and is representative of the modal proportions in the bulk material. However, acid leaching of Maalutu and Ilulialik GRFs suggests that higher cation release in the acidic media could be due to higher biotite content. Biotite dissolution rate depends on its edge/basal surfaces ratio such that the edge of biotite particles are more reactive than the basal planes. Acker and Bricker (1992) note that a low pH operates by cracking the biotite surface during K-exchange, exposing more octahedral Mg to the solution, thereby facilitating their release.

5.6. CONCLUSIONS

The leaching experiments show that surface area available for reaction is a critical factor in the extent of GRF dissolution and solute release. The mineral composition of a GRF becomes an important feature in its dissolution kinetics at lower pH. This is likely due to H^+ ions facilitating the release of interlayer K from biotite. At a higher pH release of cations into the solution is low and the GRF behaves as a bulk material. This was also observed in the first part of the pCO_2 experiments where weakly acidic solution resulting from elevated CO_2, led to higher cation release into the solution.

Part two of the pCO_2 experiments show that GRF dissolution is limited by its minerals reaching a state of equilibrium with respect to the aqueous solution. However, addition of DI water to the reacted solution shows that the minerals instantaneously release cations to reach a state of equilibrium in the new solution.

Chapter 6

Conclusions and Perspectives

Glacial rock flour is produced by glacial abrasion of the bedrock pulverizing the detrital sediments to clay to silt-sized particles and carried by the meltwater from their source to the sea. In Chapter 3, the physical and chemical characteristics of GRFs from 10 sites in Greenland show that the material is essentially a heterogeneous silicate mineral composite. The low infiltration rate together with low temperature has possibly rendered the material chemically immature. Physical sorting of the GRF particles and differentiation of minerals occurs as seen in Tasersuaq and Ilulialik. However, REE and trace element compositions strongly reflect their surrounding rocks compositions and provenance. Their Sm-Nd isotope model ages closely resemble the age of the surrounding region. Owing to this, despite the similarity in their fine-grained size and mineral composition, GRF is not a generic material and each GRF geochemical characteristics is a subject to its provenance and transit history.

The field reports from Maalutu GRF deposit in West Greenland show how GRF interacts with water in its natural environment. The observations from the collected data attest to the inferences made from the geochemical characterization in the previous chapter that the GRF is highly reactive. The GRF-reacted waters show high solute concentration and high alkalinity, which consequently contribute to the sea. A low rate of infiltration, however, limits the extent of reaction. The cold Arctic climate may also intercept the process of reaction. These have rendered the ~10 ka deposit largely unweathered.

The weathering processes are further investigated in controlled laboratory setting using sets of dissolution experiments, where GRF was subjected to various media. The two GRFs selected for the leaching tests represent different textural and mineral composition as well as are derived from two different environmental setting at present. While acid leaching of the two GRFs suggest that its dissolution is a factor of its mineral composition, alkaline leach of the GRFs indicate that GRF dissolution is a bulk dissolution of the material. Both the leaching tests, however, agree that GRF dissolution is a factor of surface area available for reaction.

The reactor experiments at ambient and elevated pCO_2 conditions show that the GRF minerals are more reactive in an elevated pCO_2 condition, releasing higher cation content and alkalinity. Moreover, they show that the steady state of dissolution reached by the solution cations is in response to a state of equilibrium of the reacting minerals. Therefore, extraction of solutes, such as by plants in an agricultural field, will facilitate more solute release.

Future perspectives

A closer study of the surficial features and reaction processes using atomic force microscopy, for example, might be helpful in studying the GRF dissolution characteristics.

Dissolution experiments of GRF performed in a far from equilibrium condition can elucidate on how much solute can be extracted from the material.

Similar dissolution experiments at ambient and elevated pCO_2 conditions using other glacial rock flours, such as Skjoldungen, which is also composed of detrital minerals but has higher specific surface area, may also be helpful.

Appendix

A.1. AQM-SEM data for GRFs from Greenland

	Mal		Ilu		SON		Tsq		Bred		Skj	
	Ar%	Wt%	Ar%	Wt%	Ar%	Wt%	Ar%	Wt%	Ar%	Wt%	Ar%	Wt%
Oligoclase/ Andesine	29.25	31.58	16.09	17.46	29.77	32.18	30.93	33.29	23.27	26.22	29.77	32.18
Anorthite	10.35	11.77	13.25	15.15	8.62	9.82	5.52	6.26	6.93	8.23	8.62	9.82
K-feldspar	6.84	7.21	1.88	1.99	7.45	7.87	5.94	6.24	6.90	7.59	7.45	7.87
Quartz	16.65	18.18	5.31	5.83	22.73	24.85	16.21	17.65	14.59	16.63	22.73	24.85
Biotite	12.20	15.09	28.29	35.15	8.94	11.06	10.08	12.43	7.26	9.37	8.94	11.06
Muscovite	1.53	3.05	1.03	2.05	1.27	2.52	1.68	3.33	1.64	3.40	1.27	2.52
Chloritised biotite	2.86	3.54	9.27	11.53	2.03	2.52	2.77	3.41	7.79	10.05	2.03	2.52
Amphibole	6.13	7.63	7.17	8.97	5.74	7.16	11.32	14.04	7.48	9.72	5.74	7.16
Epidote	0.45	0.63	0.08	0.12	0.55	0.78	0.49	0.69	0.60	0.88	0.55	0.78
Clinochlore	0.19	0.23	0.51	0.63	0.17	0.21	0.74	0.91	1.75	2.26	0.17	0.21
Chamosite	0.11	0.13	0.13	0.16	0.08	0.10	0.24	0.29	1.49	1.92	0.08	0.10
Apatite	0.05	0.07	0.03	0.04	0.04	0.05	0.13	0.17	0.14	0.19	0.04	0.05
Fe-Oxide/ Hydroxide	0.76	0.31	0.98	0.41	0.67	0.28	1.12	0.46	3.06	1.32	0.67	0.28
Ferrogedrite	0.11	0.13	0.26	0.32	0.08	0.10	0.14	0.17	0.76	0.98	0.08	0.10
Fe metal	0.01	0.01	0.00	0.00	0.12	0.05	2.00		0.01	0.01	0.12	0.05
Titanite	0.15	0.22	0.07	0.10	0.14	0.20	0.27	0.38	0.38	0.57	0.14	0.20
Ilmenite	0.03	0.07	0.01	0.01	0.02	0.04	0.03	0.06	0.07	0.14	0.02	0.04
Smectite	0.06	0.04	0.06	0.04	0.06	0.04	0.03	0.02	0.06	0.05	0.06	0.04
Enstatite	0.03	0.04	0.00	0.00	0.06	0.09	0.04	0.05	0.02	0.02	0.06	0.09
Calcite	0.02	0.02	0.00	0.00	0.02	0.02	0.02	0.02	0.21	0.24	0.02	0.02
Illite	0.012	0.013	0.01	0.01	0.01	0.01	0.01	0.01	0.01	0.01	0.01	0.01
Zircon	0.005	0.010	0.00	0.00	0.01	0.02	0.00	0.01	0.01	0.02	0.01	0.02
Kaolinite	0.009	0.009	0.01	0.01	0.01	0.01	0.03	0.03	0.03	0.03	0.01	0.01
Rutile	0.005	0.008	0.00	0.00	0.00	0.00	0.00	0.01	0.04	0.08	0.00	0.00
Ferrosilite	0.006	0.008	0.00	0.00	0.02	0.02	0.02	0.03	0.01	0.02	0.02	0.02
Halite	0.013	0.005	0.00	0.00	0.00	0.00	0.01	0.01	0.00	0.00	0.00	0.00
Gedrite	0.004	0.004	0.00	0.00	0.00	0.01	0.01	0.02	0.02	0.03	0.00	0.01
Tourmaline	0.003	0.004	0.00	0.00	0.00	0.00	0.00	0.01	0.00	0.00	0.00	0.00
Monazite	0.003	0.001	0.00	0.00	0.00	0.00	0.00	0.00	0.01	0.00	0.00	0.00

A.2. Detailed data from AQM-SEM

A.2.1. ILU-W_2005580_2detail (washed)

	Area %	Weight %	Assigned Composition
Biotite	20.34	23.99	O 38.27; Si 25.99; Fe 12.04; Al 9.88; Mg 6.31; K 6.29; Na 1.21;
Oligoclase /Andesine	18.59	19.15	O 39.94; Si 35.07; Al 11.66; Na 6.43; Ca 2.76; Fe 2.08; Mg 1.14; K 0.91;
Chloritised biotite	10.22	12.06	O 38.3; Si 25.82; Fe 16.02; Al 9.34; Mg 5.79; K 2.98; Na 1.76;
Amphibole	10.18	12.08	O 40.16; Si 27.98; Fe 11.91; Al 7.23; Ca 6.48; Mg 6.25;
Quartz	9.53	9.93	Si 43.37; O 42.74; Al 4.71; Fe 2.73; Mg 2.36; Na 1.77; K 1.43; Ca 0.88;
Anorthite	8.96	9.72	O 41.17; Si 30.12; Al 10.51; Fe 4.89; Ca 4.26; Mg 3.68; Na 2.86; K 2.51;
K-feldspar	3.29	3.31	O 39.34; Si 35.04; K 11.01; Al 9.88; Fe 1.96; Na 1.06; Mg 1.04; Ca 0.68;
Clinochlore	2.20	2.59	O 44.1; Si 22.72; Mg 10.84; Al 10.31; Fe 9.66; K 2.37;
Fe-Oxide/Hydroxide	2.00	0.78	O 61.03; Fe 38.97;
Chamosite	1.69	1.99	O 33.46; Fe 28.95; Si 21; Al 8.36; Mg 5.3; K 2.93;
Muscovite	1.66	3.15	O 42.96; Si 30.89; Al 13.83; K 7.14; Mg 3.36; Fe 1.83;
Ferrogedrite	0.51	0.60	O 39.28; Si 25.99; Fe 18.35; Al 10.29; Mg 4.08; K 2;
Apatite	0.12	0.14	Ca 44.21; O 44.03; P 11.76;
Titanite	0.11	0.16	O 41.68; Si 20.26; Ti 20.26; Ca 17.79;
Epidote	0.10	0.13	O 36.18; Si 21.32; Ca 16.74; Al 12.71; Fe 12.26; Mg 0.77;
Smectite	0.04	0.03	O 53.69; Si 24.24; Al 14.9; Mg 3.2; Fe 2.51; Ca 1.47;
Enstatite	0.04	0.06	O 41.37; Si 32.54; Mg 17.57; Fe 6.15; Al 0.79; Na 0.62; Ca 0.55; K 0.41;
Calcite	0.02	0.03	Ca 85.85; Si 4.37; Fe 3.84; Mn 3.48; P 1.26; Mg 1.19;
Ferrosilite	0.02	0.03	O 42.21; Si 33.37; Fe 13.06; Mg 8.12; Al 1.25; Ca 0.8; K 0.61; Na 0.57;
Illite	0.02	0.02	O 43.96; Si 27.74; Al 11.55; K 6.91; Fe 6.38; Mg 3.04; Ti 0.42;
Gedrite	0.01	0.01	O 41.86; Si 20.09; Al 14.26; Mg 14.08; Fe 8.49; K 1.22;
Kaolinite	0.01	0.01	O 42.9; Al 30.8; Si 24.21; Mg 0.65; Fe 0.62; Na 0.53; Ca 0.3;
Ilmenite	0.01	0.02	O 36.47; Fe 34.68; Ti 28.84;

A.2.2. MAL-detail-bulk

	Ar %	Wt %	Assigned Composition
Oligoclase/Andesine	27.95	29.74	O 39.73; Si 35.34; Al 12.15; Na 5.97; Ca 2.86; Fe 2.06; Mg 0.96; K 0.93;
Quartz	19.25	20.71	Si 48.32; O 43.69; Al 2.76; Fe 1.99; Mg 0.99; Na 0.82; K 0.82; Ca 0.6;
Anorthite	10.18	11.41	O 40.97; Si 30.99; Al 10.96; Ca 4.9; Fe 4.47; Mg 2.98; Na 2.37; K 2.36;
Biotite	8.32	10.14	O 37.02; Si 31.88; Al 10.31; Fe 9.26; K 6.12; Mg 3.9; Na 1.52;
Amphibole	7.32	8.97	O 38.96; Si 29.5; Fe 12.03; Al 7.4; Ca 6.73; Mg 5.38;
K-feldspar	6.35	6.61	O 38.73; Si 36.03; K 11.12; Al 10.2; Fe 1.76; Na 0.86; Mg 0.69; Ca 0.61;
Chloritised biotite	4.19	5.10	O 37.86; Si 27.79; Fe 15.31; Al 9.76; Mg 5; K 2.51; Na 1.77;
Fe-Oxide/Hydroxide	2.11	0.86	O 58.77; Fe 41.23;
Muscovite	1.85	3.62	O 42.54; Si 32.58; Al 13.64; K 6.79; Mg 2.77; Fe 1.67;
Chamosite	0.83	1.01	O 32.75; Fe 28.93; Si 23.35; Al 8.77; Mg 3.98; K 2.22;
Clinochlore	0.49	0.60	O 44.33; Si 20.84; Mg 11.41; Fe 11.32; Al 10.98; K 1.11;
Ferrogedrite	0.36	0.44	O 39.48; Si 26.42; Fe 18.77; Al 10.13; Mg 3.23; K 1.97;
Epidote	0.18	0.25	O 34.2; Si 22.07; Ca 17.64; Al 13.21; Fe 12.53; Mg 0.36;
Titanite	0.15	0.22	O 37.82; Ti 22.16; Si 20.39; Ca 19.63;
Enstatite	0.07	0.09	O 41.73; Si 32.51; Mg 17.71; Fe 5.55; Al 0.97; Ca 0.86; Na 0.39; K 0.28;
Smectite	0.06	0.04	O 55.99; Si 23; Al 14.86; Mg 2.79; Fe 1.92; Ca 1.44;
Apatite	0.06	0.07	Ca 45.49; O 42.51; P 12;
Ferrosilite	0.02	0.02	O 41.44; Si 32.2; Fe 12.32; Mg 11.29; Al 1.09; Ca 0.76; Na 0.48; K 0.41;
Gedrite	0.01	0.02	O 42.17; Si 19.16; Mg 14.67; Al 14.3; Fe 9.35; K 0.36;
Kaolinite	0.01	0.01	Si 40.4; O 38.63; Al 15.26; Na 2.15; Mg 1.85; Ca 1.16; Fe 0.55;
Illite	0.01	0.01	O 45.55; Si 28.59; Al 10.75; K 6.37; Fe 5.48; Mg 2.73; Ti 0.53;
Ilmenite	0.01	0.02	O 35.16; Fe 35.08; Ti 29.75;
Fe metal	0.01	0.00	Fe 100;
Zircon	0.01	0.01	Zr 43.43; O 34.27; Si 22.3;
Calcite	0.01	0.01	Ca 88.74; Si 3.58; Fe 3.25; Mn 2.09; Mg 1.98; P 0.36;

A.2.3. MAL-2_2005582overview

	Ar %	Wt %	Assigned Composition
Oligoclase/Andesine	29.25	31.58	O 35.86; Si 35.4; Al 13.84; Na 6.2; Ca 3.7; Fe 2.62; K 1.31; Mg 1.07;

Quartz	16.65	18.18	Si 52.66; O 39.59; Al 2.7; Fe 2.06; K 0.82; Mg 0.77; Ca 0.73; Na 0.67;
Biotite	12.20	15.09	Si 33.22; O 32.36; Al 11.86; Fe 10.69; K 6.08; Mg 3.88; Na 1.91;
Anorthite	10.35	11.77	O 35.77; Si 30.67; Al 12.68; Fe 6.61; Ca 5.51; Mg 3.02; K 2.93; Na 2.8;
K-feldspar	6.84	7.21	Si 35.6; O 34.72; K 12.95; Al 11.63; Fe 2.19; Na 1.1; Ca 0.95; Mg 0.86;
Amphibole	6.13	7.63	O 35.23; Si 29.49; Fe 13.33; Al 8.06; Ca 7.91; Mg 5.99;
Chloritised biotite	2.86	3.54	O 34.37; Si 29.6; Fe 13.83; Al 11.83; Mg 5.17; K 3; Na 2.2;
Muscovite	1.53	3.05	O 38.74; Si 32.72; Al 15.01; K 7.67; Fe 3.4; Mg 2.46;
Fe-Oxide/Hydroxide	0.76	0.31	O 57.27; Fe 42.73;
Epidote	0.45	0.63	O 31.94; Si 21.51; Ca 20.61; Al 15.52; Fe 10.01; Mg 0.41;
Clinochlore	0.19	0.23	O 37.7; Si 24.06; Fe 13.5; Mg 11.49; Al 11.42; K 1.83;
Titanite	0.15	0.22	O 36.06; Ti 22.61; Ca 20.91; Si 20.42;
Chamosite	0.11	0.13	O 31.6; Fe 28.97; Si 22.19; Al 11.35; Mg 4.28; K 1.61;
Ferrogedrite	0.11	0.13	O 38.69; Si 25.83; Fe 17.3; Al 12.24; Mg 3.96; K 1.98;
Smectite	0.06	0.04	O 47.8; Si 27.08; Al 15.22; Fe 4.02; Mg 3.69; Ca 2.19;
Apatite	0.05	0.07	Ca 51.74; O 37.56; P 10.71;
Ilmenite	0.03	0.07	Fe 37.85; Ti 34.25; O 27.9;
Enstatite	0.03	0.04	O 36.69; Si 31.79; Mg 20.16; Fe 9.41; Al 0.87; Ca 0.69; Na 0.29; K 0.1;
Calcite	0.02	0.02	Ca 88.78; P 6.88; Fe 2.32; Si 0.96; Mn 0.7; Mg 0.36;
Natriumchloride	0.01	0.01	Na 100;
Fe metal	0.01	0.01	Fe 100;
Illite	0.01	0.01	O 44.43; Si 28.05; Al 12.12; K 6.32; Fe 6.06; Mg 2.83; Ti 0.19;
Kaolinite	0.01	0.01	O 54.96; Si 26.81; Al 16.7; Mg 0.75; Na 0.62; Ca 0.1; Fe 0.06;
Ferrosilite	0.01	0.01	O 42.31; Si 31.37; Fe 13.83; Mg 9.02; Al 1.04; Na 1.02; Ca 0.99; K 0.43;
Zircon	0.01	0.01	Zr 43.73; O 32.61; Si 23.66;

A.2.4. SKJbulk

	Ar %	Wt %	Assigned Composition
Oligoclase/Andesine	40.82	42.56	O 38.97; Si 34.14; Al 14.28; Na 7.41; Ca 3.69; Fe 0.86; K 0.39; Mg 0.27;
K-feldspar	21.93	22.34	O 37.15; Si 35.08; K 13.73; Al 11.45; Na 1.16; Fe 0.82; Ca 0.39; Mg 0.22;

Quartz	13.69	14.44	Si 54.67; O 42.59; Fe 0.92; Al 0.67; Ca 0.34; K 0.32; Na 0.26; Mg 0.22;
Amphibole	6.79	8.16	O 36.07; Si 24.76; Fe 16.14; Ca 10.53; Mg 6.63; Al 5.87;
Fe-Oxide/Hydroxide	3.64	1.45	Fe 56.28; O 43.72;
Biotite	2.60	3.10	O 35.4; Si 27.8; Fe 13.31; Al 10.3; K 7.24; Mg 4.94; Na 1;
Muscovite	1.03	1.98	O 44.2; Si 30.28; Al 14.8; K 8.42; Fe 1.57; Mg 0.73;
Anorthite	0.99	1.09	O 40.51; Si 27.72; Al 12.66; Ca 8.46; Fe 5.32; Na 2.37; K 1.57; Mg 1.39;
Chloritised biotite	0.97	1.16	O 37.3; Si 23.28; Fe 19.84; Al 10.17; Mg 6.22; K 2; Na 1.19;
Apatite	0.89	1.11	Ca 50.58; O 34.79; P 14.63;
Chamosite	0.71	0.85	O 34.37; Fe 29.12; Si 19.38; Al 10.36; Mg 5.37; K 1.4;
Ilmenite	0.35	0.68	Fe 38.23; Ti 34.5; O 27.28;
Clinochlore	0.35	0.42	O 40.03; Si 19.97; Fe 17.37; Mg 11.05; Al 10.59; K 0.98;
Epidote	0.19	0.26	O 33.63; Si 20.87; Ca 19.42; Al 13.78; Fe 11.99; Mg 0.31;
Ferrogedrite	0.13	0.16	O 39.32; Si 24.91; Fe 18.82; Al 11.78; Mg 3.69; K 1.48;
Titanite	0.05	0.07	O 36.87; Ti 22.2; Ca 22.04; Si 18.88;
Ferrosilite	0.03	0.04	O 41.87; Si 32.2; Fe 13.49; Mg 10.34; Al 0.76; Ca 0.51; K 0.42; Na 0.4;
Fe metal	0.03	0.01	Fe 100;
Enstatite	0.02	0.03	O 40.62; Si 30.76; Mg 17.17; Fe 9.63; Al 0.82; Ca 0.37; Na 0.34; K 0.29;
Monazite	0.02	0.01	O 60.92; P 35.89; Si 3.19;
Zircon	0.01	0.02	Zr 48.96; O 31.27; Si 19.77;
Smectite	0.01	0.01	O 51.31; Si 24.48; Al 15.9; Fe 4.11; Mg 2.31; Ca 1.89;
Kaolinite	0.01	0.01	O 46.97; Si 33.92; Al 16.04; Na 1.4; Ca 0.66; Fe 0.56; Mg 0.46;
Rutile	0.01	0.01	Ti 56.71; O 43.29;
Illite	0.01	0.01	O 46.04; Si 26.29; Al 11.71; K 7.76; Fe 5.85; Mg 2.01; Ti 0.34;
Natriumchloride	0.01	0.00	Na 100;

A.2.5. BRED2_2005581overview

	Ar %	Wt %	Assigned Composition
Oligoclase/Andesine	23.27	26.22	O 36.84; Si 35.92; Al 13.61; Na 7.18; Ca 2.74; Fe 2.15; K 0.78; Mg 0.78;

Quartz	14.59	16.63	Si 52.76; O 40.05; Al 2.42; Fe 2.24; Mg 0.77; K 0.59; Na 0.59; Ca 0.58;
Chloritised biotite	7.79	10.05	O 34.45; Si 27.08; Fe 16.6; Al 11.79; Mg 6; K 2.2; Na 1.88;
Amphibole	7.48	9.72	O 35.59; Si 28.12; Fe 13.43; Ca 9.41; Mg 7; Al 6.45;
Biotite	7.26	9.37	O 32.9; Si 31.04; Al 12.45; Fe 11.77; K 6.32; Mg 4.05; Na 1.46;
Anorthite	6.93	8.23	O 38.06; Si 29.09; Al 13.1; Ca 7.15; Fe 5.66; Na 2.54; Mg 2.52; K 1.88;
K-feldspar	6.90	7.59	Si 35.39; O 35.2; K 13.63; Al 11.66; Fe 1.95; Na 0.87; Mg 0.66; Ca 0.64;
Fe-Oxide/Hydroxide	3.06	1.32	O 54.44; Fe 45.56;
Clinochlore	1.75	2.26	O 36.85; Si 20.97; Fe 18.64; Al 11.37; Mg 11.07; K 1.1;
Muscovite	1.64	3.40	O 39.66; Si 30.58; Al 16.87; K 8.36; Fe 2.68; Mg 1.85;
Chamosite	1.49	1.92	O 31.76; Fe 28.47; Si 20.95; Al 10.87; Mg 6.59; K 1.36;
Ferrogedrite	0.76	0.98	O 37.64; Si 25.56; Fe 18.11; Al 12.13; Mg 4.85; K 1.72;
Epidote	0.60	0.88	O 32.74; Si 22.32; Ca 20.93; Al 14.19; Fe 9.25; Mg 0.57;
Titanite	0.38	0.57	O 37.05; Ti 22.48; Ca 21.07; Si 19.4;
Calcite	0.21	0.24	Ca 92.56; Fe 3.1; P 1.68; Si 1.44; Mn 0.88; Mg 0.35;
Apatite	0.14	0.19	Ca 50.73; O 37.75; P 11.51;
Ilmenite	0.07	0.14	Fe 39.32; Ti 33.27; O 27.42;
Smectite	0.06	0.05	O 47.86; Si 26.42; Al 15.82; Fe 4.83; Mg 3.38; Ca 1.69;
Rutile	0.04	0.08	Ti 58.43; O 41.57;
Kaolinite	0.03	0.03	O 49.64; Si 32.34; Al 15.31; Na 1.18; Mg 0.72; Ca 0.42; Fe 0.4;
Gedrite	0.02	0.03	O 39.19; Si 20.52; Al 14.29; Mg 13.96; Fe 11.45; K 0.59;
Enstatite	0.02	0.02	O 38.99; Si 32.82; Mg 19.54; Fe 7.14; Al 0.68; Ca 0.41; Na 0.32; K 0.09;
Ankerite	0.02	0.02	O 45.95; Ca 29.55; Mg 13.42; Fe 8.67; Si 1.78; Al 0.62;
Fe metal	0.01	0.01	Fe 100;
Illite	0.01	0.01	O 45.36; Si 26.22; Al 12.33; Fe 6.48; K 6.43; Mg 2.63; Ti 0.56;

A.2.6. SON_2005583_2detail

	Ar %	Wt %	Assigned Composition
Oligoclase/Andesine	43.56	44.85	O 39.33; Si 36.22; Al 11.97; Na 6.64; Ca 2.7; Fe 1.75; Mg 0.7; K 0.69;
Quartz	16.57	17.25	Si 49; O 43.06; Al 2.64; Fe 2.07; Mg 0.97; Na 0.85; K 0.81; Ca 0.6;
Anorthite	7.92	8.59	O 39.12; Si 31.06; Al 10.95; Fe 5.65; Ca 5; Mg 3.14; K 2.59; Na 2.47;
Biotite	7.08	8.35	O 36.91; Si 31.83; Al 10.09; Fe 9.8; K 5.78; Mg 3.91; Na 1.69;
Amphibole	6.33	7.51	O 38.17; Si 29.7; Fe 12.37; Al 7.32; Ca 6.8; Mg 5.64;
K-feldspar	5.46	5.49	O 38.18; Si 36.56; K 11.09; Al 10.21; Fe 1.76; Na 0.91; Mg 0.73; Ca 0.57;
Chloritised biotite	3.15	3.71	O 36.79; Si 29.16; Fe 14.59; Al 9.71; Mg 4.84; K 2.9; Na 2;
Muscovite	1.27	2.41	O 41.95; Si 33.03; Al 13.42; K 6.62; Mg 2.79; Fe 2.19;
Fe-Oxide/Hydroxide	1.00	0.39	O 62.43; Fe 37.57;
Epidote	0.33	0.44	O 35.09; Si 21.68; Ca 17.45; Al 12.84; Fe 12.68; Mg 0.25;
Chamosite	0.32	0.37	O 32.37; Fe 28.17; Si 24.11; Al 8.61; Mg 4.12; K 2.62;
Clinochlore	0.20	0.23	O 45.24; Si 23.61; Al 10.43; Mg 10.25; Fe 8.84; K 1.63;
Apatite	0.11	0.14	Ca 47.42; O 38.94; P 13.63;
Ferrogedrite	0.11	0.13	O 38.71; Si 26.61; Fe 18.88; Al 10.4; Mg 3.24; K 2.17;
Smectite	0.06	0.04	O 55.05; Si 23.99; Al 14.64; Mg 2.99; Fe 1.96; Ca 1.37;
Titanite	0.05	0.07	O 40.62; Si 23.03; Ti 19.53; Ca 16.82;
Calcite	0.01	0.01	Ca 90.56; Fe 4.12; Si 2.81; Mn 1.91; Mg 0.48; P 0.12;

A.2.7. TSQ_2005579detail

	Area %	Weight %	Assigned Composition
Oligoclase/Andesine	32.80	33.30	O 40.04; Si 35.65; Al 11.96; Na 6.86; Ca 2.94; Fe 1.56; Mg 0.5; K 0.49;
Quartz	16.34	16.78	Si 49.4; O 43.92; Al 2.04; Fe 1.72; Na 0.87; Mg 0.81; Ca 0.66; K 0.59;
Amphibole	12.57	14.71	O 39.68; Si 27.87; Fe 11.76; Ca 7.9; Mg 6.66; Al 6.13;
Biotite	8.83	10.27	O 38.52; Si 26.52; Fe 11.86; Al 9.98; K 6.45; Mg 5.63; Na 1.03;
K-feldspar	6.30	6.25	O 39.07; Si 35.93; K 11.68; Al 9.98; Fe 1.55; Na 0.76; Ca 0.55; Mg 0.47;

Anorthite	5.64	6.03	O 40.96; Si 28.95; Al 11.43; Ca 7.72; Fe 4.42; Mg 2.62; Na 2.19; K 1.72;
Chloritised biotite	4.05	4.71	O 38.51; Si 25.23; Fe 16.92; Al 9.26; Mg 5.81; K 2.82; Na 1.45;
Fe-Oxide/Hydroxide	1.74	0.67	O 59.13; Fe 40.87;
Muscovite	1.71	3.20	O 42.74; Si 29.96; Al 15.73; K 7.86; Mg 2.14; Fe 1.58;
Clinochlore	1.06	1.23	O 44.41; Si 22.6; Mg 11.27; Al 10.27; Fe 9.79; K 1.66;
Chamosite	0.90	1.05	O 34.11; Fe 29.27; Si 20.65; Al 8.43; Mg 5.02; K 2.51;
Epidote	0.33	0.43	O 35.15; Si 21.46; Ca 17.81; Al 13.06; Fe 12.18; Mg 0.34;
Titanite	0.30	0.41	O 38.79; Ti 22.03; Ca 19.74; Si 19.44;
Ferrogedrite	0.21	0.24	O 39.2; Si 25.98; Fe 18.71; Al 10.54; Mg 3.67; K 1.9;
Apatite	0.18	0.22	Ca 46.95; O 40.12; P 12.93;
Enstatite	0.18	0.23	O 42.98; Si 31.69; Mg 17.76; Fe 5.46; Al 0.78; Ca 0.55; Na 0.44; K 0.33;
Ferrosilite	0.06	0.08	O 41.58; Si 32.33; Fe 12.49; Mg 10.97; Al 0.87; Ca 0.83; Na 0.49; K 0.44;
Ilmenite	0.05	0.09	Fe 35.74; O 33.25; Ti 31;
Smectite	0.04	0.03	O 57.18; Si 22.15; Al 15; Mg 2.09; Fe 2.03; Ca 1.56;
Kaolinite	0.01	0.01	O 44.06; Si 30.91; Al 22.26; Na 1.21; Fe 0.56; Mg 0.56; Ca 0.45;
Tourmaline	0.01	0.01	O 50.93; Si 21.57; Al 19; Mg 3.43; Fe 3.14; Na 1.62; Ca 0.31;
Calcite	0.01	0.01	Ca 88.42; Si 4.65; Mg 2.43; Fe 2.26; Mn 1.36; P 0.88;
Gedrite	0.01	0.01	O 41.58; Si 18.88; Mg 14.91; Al 14.33; Fe 9.7; K 0.6;
Illite	0.01	0.01	O 44.81; Si 27.65; Al 11.1; K 6.77; Fe 6.37; Mg 2.87; Ti 0.43;

A.2.8. MAL-detail-bulk

	Ar %	Wt %	Assigned Composition
Oligoclase/Andesine	27.95	29.74	O 39.73; Si 35.34; Al 12.15; Na 5.97; Ca 2.86; Fe 2.06; Mg 0.96; K 0.93;
Quartz	19.25	20.71	Si 48.32; O 43.69; Al 2.76; Fe 1.99; Mg 0.99; Na 0.82; K 0.82; Ca 0.6;
Anorthite	10.18	11.41	O 40.97; Si 30.99; Al 10.96; Ca 4.9; Fe 4.47; Mg 2.98; Na 2.37; K 2.36;
Biotite	8.32	10.14	O 37.02; Si 31.88; Al 10.31; Fe 9.26; K 6.12; Mg 3.9; Na 1.52;
Amphibole	7.32	8.97	O 38.96; Si 29.5; Fe 12.03; Al 7.4; Ca 6.73; Mg 5.38;
K-feldspar	6.35	6.61	O 38.73; Si 36.03; K 11.12; Al 10.2; Fe 1.76; Na 0.86; Mg 0.69; Ca 0.61;
Chloritised biotite	4.19	5.10	O 37.86; Si 27.79; Fe 15.31; Al 9.76; Mg 5; K 2.51; Na 1.77;
Fe-Oxide/Hydroxide	2.11	0.86	O 58.77; Fe 41.23;
Muscovite	1.85	3.62	O 42.54; Si 32.58; Al 13.64; K 6.79; Mg 2.77; Fe 1.67;
Chamosite	0.83	1.01	O 32.75; Fe 28.93; Si 23.35; Al 8.77; Mg 3.98; K 2.22;
Clinochlore	0.49	0.60	O 44.33; Si 20.84; Mg 11.41; Fe 11.32; Al 10.98; K 1.11;
Ferrogedrite	0.36	0.44	O 39.48; Si 26.42; Fe 18.77; Al 10.13; Mg 3.23; K 1.97;
Epidote	0.18	0.25	O 34.2; Si 22.07; Ca 17.64; Al 13.21; Fe 12.53; Mg 0.36;
Titanite	0.15	0.22	O 37.82; Ti 22.16; Si 20.39; Ca 19.63;
Enstatite	0.07	0.09	O 41.73; Si 32.51; Mg 17.71; Fe 5.55; Al 0.97; Ca 0.86; Na 0.39; K 0.28;
Smectite	0.06	0.04	O 55.99; Si 23; Al 14.86; Mg 2.79; Fe 1.92; Ca 1.44;
Apatite	0.06	0.07	Ca 45.49; O 42.51; P 12;
Ferrosilite	0.02	0.02	O 41.44; Si 32.2; Fe 12.32; Mg 11.29; Al 1.09; Ca 0.76; Na 0.48; K 0.41;
Gedrite	0.01	0.02	O 42.17; Si 19.16; Mg 14.67; Al 14.3; Fe 9.35; K 0.36;
Kaolinite	0.01	0.01	Si 40.4; O 38.63; Al 15.26; Na 2.15; Mg 1.85; Ca 1.16; Fe 0.55;
Illite	0.01	0.01	O 45.55; Si 28.59; Al 10.75; K 6.37; Fe 5.48; Mg 2.73; Ti 0.53;
Ilmenite	0.01	0.02	O 35.16; Fe 35.08; Ti 29.75;
Fe metal	0.01	0.00	Fe 100;
Zircon	0.01	0.01	Zr 43.43; O 34.27; Si 22.3;
Calcite	0.01	0.01	Ca 88.74; Si 3.58; Fe 3.25; Mn 2.09; Mg 1.98; P 0.36;

A.2.9. MAL-detail-bulk

	Ar %	Wt %	Assigned Composition
Oligoclase/Andesine	27.95	29.74	O 39.73; Si 35.34; Al 12.15; Na 5.97; Ca 2.86; Fe 2.06; Mg 0.96; K 0.93;
Quartz	19.25	20.71	Si 48.32; O 43.69; Al 2.76; Fe 1.99; Mg 0.99; Na 0.82; K 0.82; Ca 0.6;
Anorthite	10.18	11.41	O 40.97; Si 30.99; Al 10.96; Ca 4.9; Fe 4.47; Mg 2.98; Na 2.37; K 2.36;
Biotite	8.32	10.14	O 37.02; Si 31.88; Al 10.31; Fe 9.26; K 6.12; Mg 3.9; Na 1.52;
Amphibole	7.32	8.97	O 38.96; Si 29.5; Fe 12.03; Al 7.4; Ca 6.73; Mg 5.38;
K-feldspar	6.35	6.61	O 38.73; Si 36.03; K 11.12; Al 10.2; Fe 1.76; Na 0.86; Mg 0.69; Ca 0.61;
Chloritised biotite	4.19	5.10	O 37.86; Si 27.79; Fe 15.31; Al 9.76; Mg 5; K 2.51; Na 1.77;
Fe-Oxide/Hydroxide	2.11	0.86	O 58.77; Fe 41.23;
Muscovite	1.85	3.62	O 42.54; Si 32.58; Al 13.64; K 6.79; Mg 2.77; Fe 1.67;
Chamosite	0.83	1.01	O 32.75; Fe 28.93; Si 23.35; Al 8.77; Mg 3.98; K 2.22;
Clinochlore	0.49	0.60	O 44.33; Si 20.84; Mg 11.41; Fe 11.32; Al 10.98; K 1.11;
Ferrogedrite	0.36	0.44	O 39.48; Si 26.42; Fe 18.77; Al 10.13; Mg 3.23; K 1.97;
Epidote	0.18	0.25	O 34.2; Si 22.07; Ca 17.64; Al 13.21; Fe 12.53; Mg 0.36;
Titanite	0.15	0.22	O 37.82; Ti 22.16; Si 20.39; Ca 19.63;
Enstatite	0.07	0.09	O 41.73; Si 32.51; Mg 17.71; Fe 5.55; Al 0.97; Ca 0.86; Na 0.39; K 0.28;
Smectite	0.06	0.04	O 55.99; Si 23; Al 14.86; Mg 2.79; Fe 1.92; Ca 1.44;
Apatite	0.06	0.07	Ca 45.49; O 42.51; P 12;
Ferrosilite	0.02	0.02	O 41.44; Si 32.2; Fe 12.32; Mg 11.29; Al 1.09; Ca 0.76; Na 0.48; K 0.41;
Gedrite	0.01	0.02	O 42.17; Si 19.16; Mg 14.67; Al 14.3; Fe 9.35; K 0.36;
Kaolinite	0.01	0.01	Si 40.4; O 38.63; Al 15.26; Na 2.15; Mg 1.85; Ca 1.16; Fe 0.55;
Illite	0.01	0.01	O 45.55; Si 28.59; Al 10.75; K 6.37; Fe 5.48; Mg 2.73; Ti 0.53;
Ilmenite	0.01	0.02	O 35.16; Fe 35.08; Ti 29.75;
Fe metal	0.01	0.00	Fe 100;
Zircon	0.01	0.01	Zr 43.43; O 34.27; Si 22.3;
Calcite	0.01	0.01	Ca 88.74; Si 3.58; Fe 3.25; Mn 2.09; Mg 1.98; P 0.36;

A.5. Field Site Locations for Chapter 4

Sample site	Type	UTM(x)	UTM(y)	Sample site	Type	UTM(x)	UTM(y)
1	stream	7129015	465040.9	15	spring	7129088	464991.7
4	spring	7129013	465069.5	16	surface	7129116	465005
5	stream	7129014	465082.2	E1	stream	64.28895	51.72536
6	stream	7129015	465033.7	L1	surface	7129093	465102.3
7	stream	7129028	465036.6	L2	surface	7129110	465077.1
9	stream	7129065	464969	P1	pore	7129019	465068.3
10	stream	7129135	464920.8	P2	pore	7129067	465076.1
11	stream	7128830	465287.3	P3	pore	7129067	465121.8
12	spring	7129009	465064.5	P4	pore	7129141	465074.2
13	spring	7129012	465086.1	WP	surface	7129276	465463
14	surface	7129026	465098				

A.6. PHREEQC Script for Chapter 5

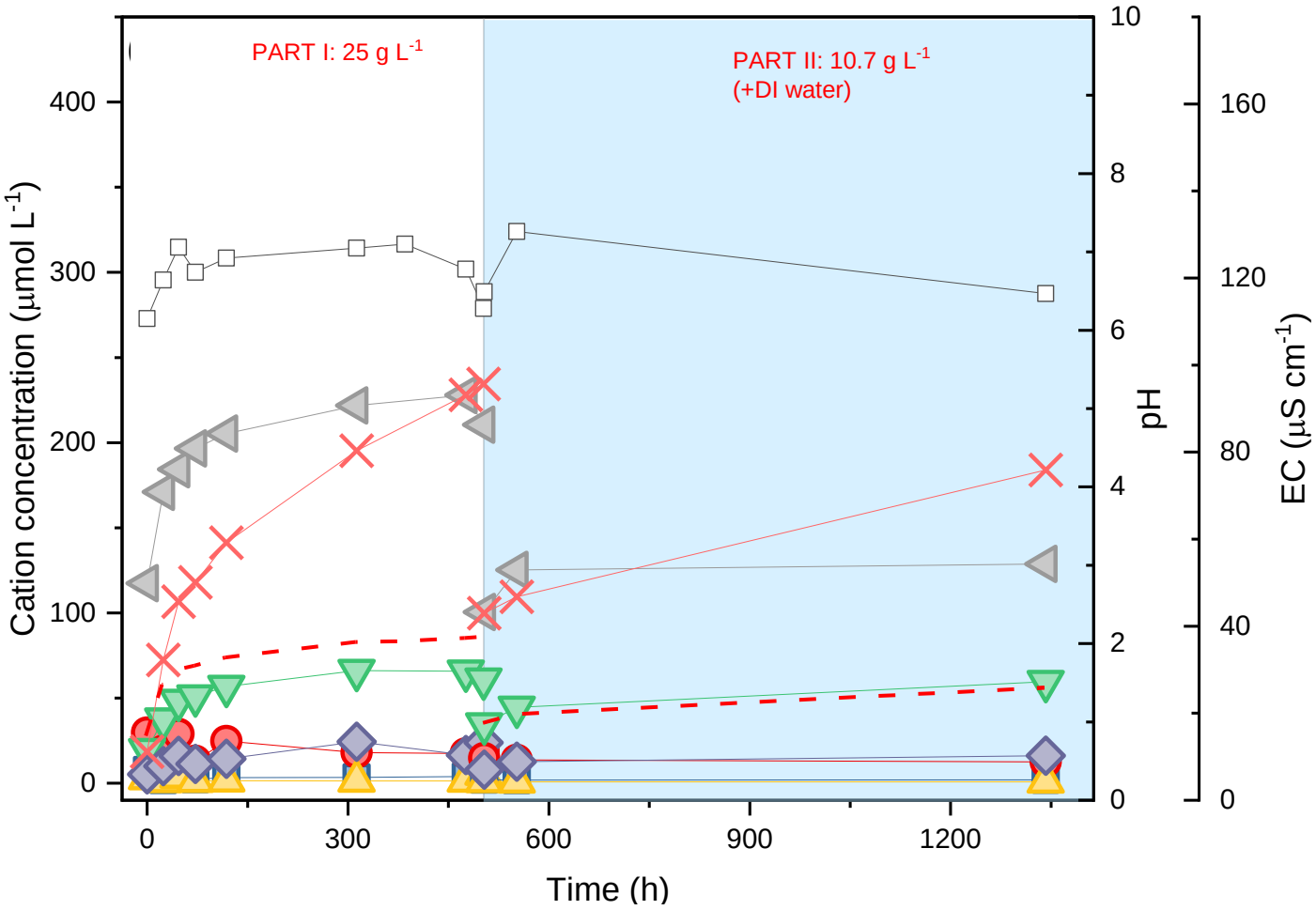
```
DATABASE c:\phreeqc\database\WATEQ4F.DAT
SOLUTION_SPREAD
-units mmol/L
-temp 22

PHASES
K-feldspar
        KAlSi3O8 + 8 H2O = K+ + Al(OH)4- + 3 H4SiO4
        -log_k     -20.573
        -delta_h 30.820    kcal
        -Vm 108.15
-file field_data_major_minerals.xlsx
USER_PUNCH
-headings si_Allophane(A) si_Allophane(P) PCO2_atm Err%
-start
10 punch 10^(SI("CO2(g)"))
20 punch PERCENT_ERROR
-end

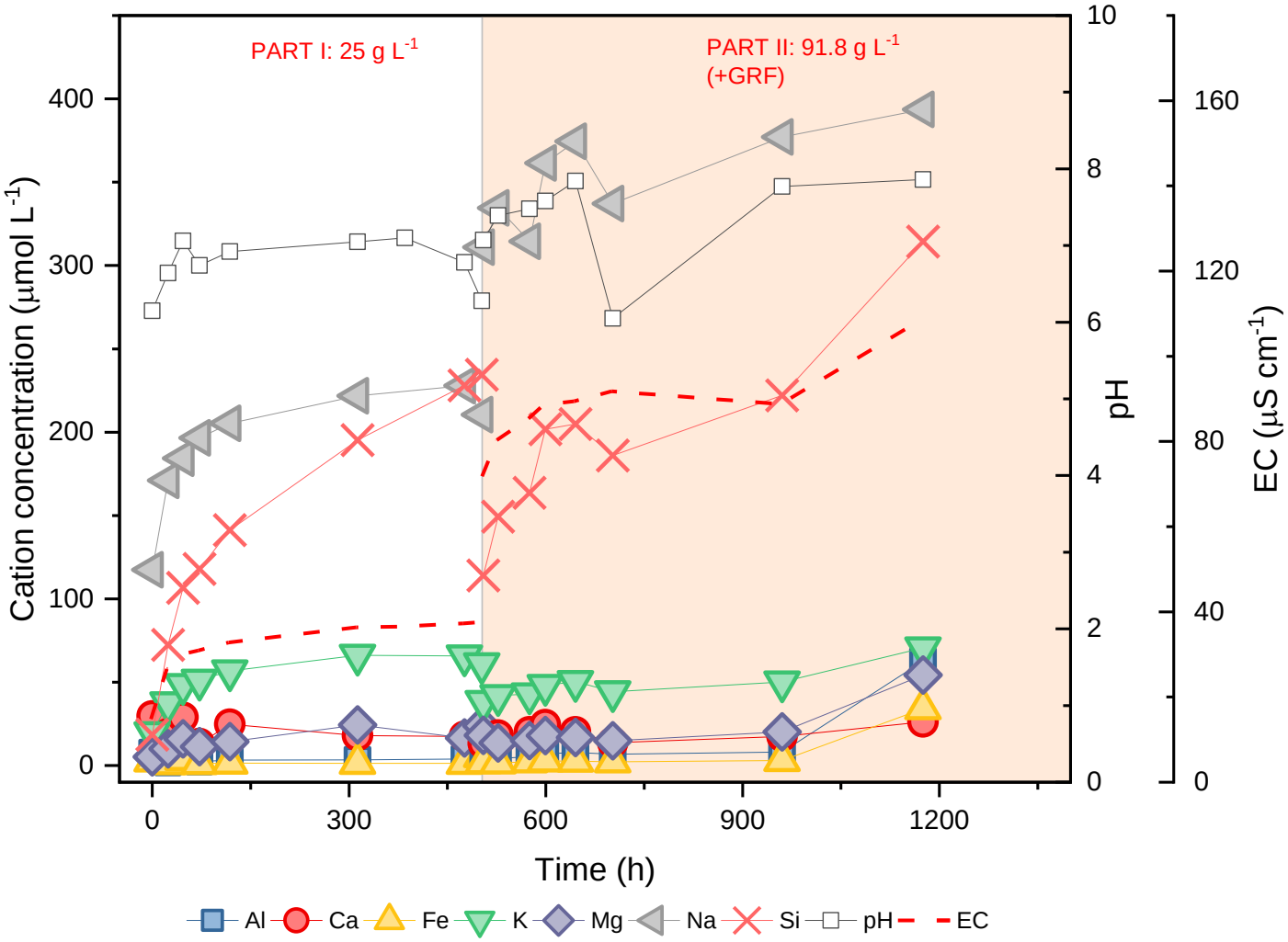
SELECTED_OUTPUT
-file expt-speciation.xls
-saturation_indices calcite co2(g) albite anorthite K-feldspar chlorite14A quartz SiO2(a) chalcedony epidote gibbsite Al(OH)3(a) gypsum Fe(OH)3(a) Ferryhydrite illite kaolinite tremolite

END
```

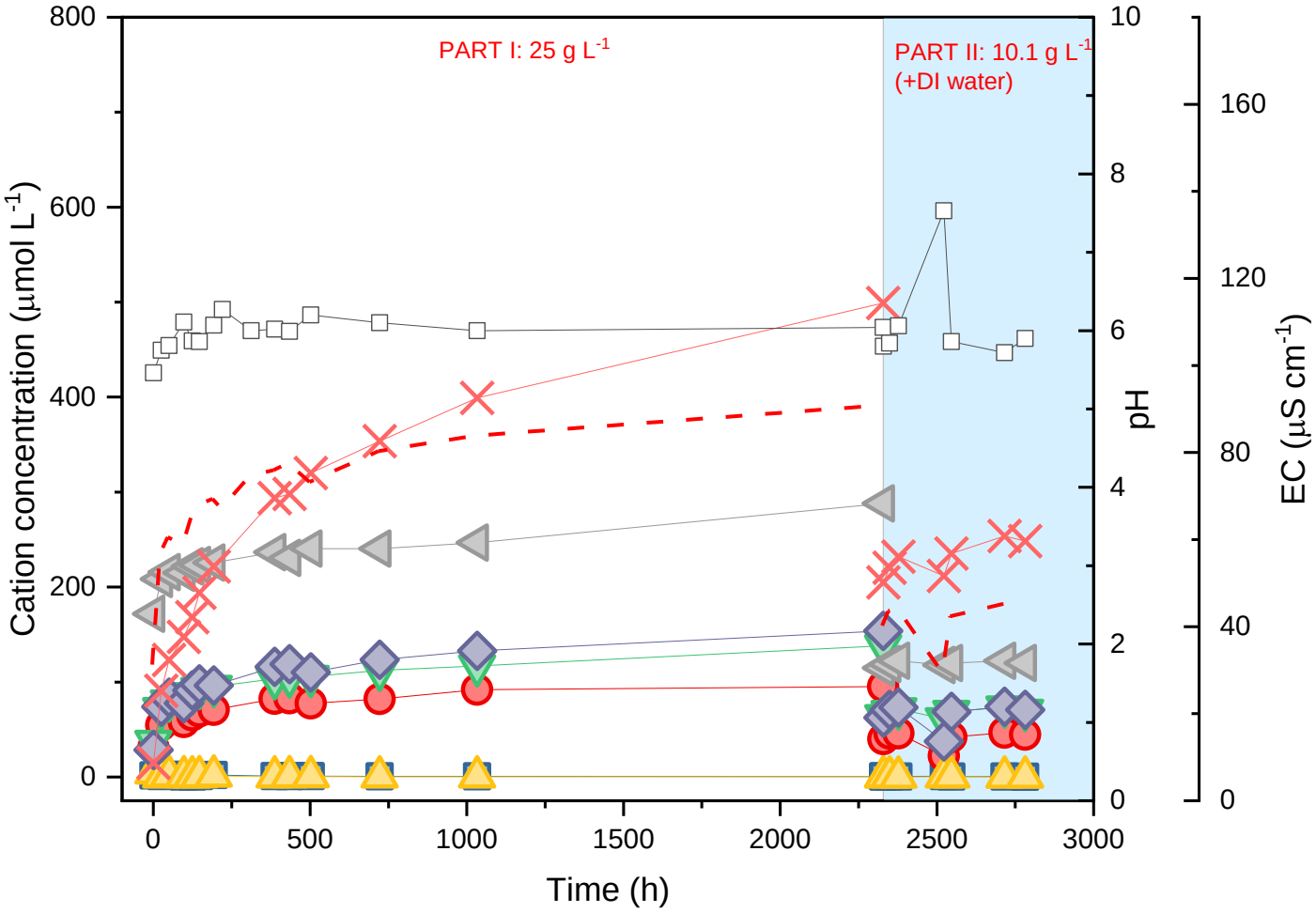
A.7. Temporal evolution of cation concentrations during the first and second part of experiments at ambient pCO_2. The first part is common in both A.7 and A.8.(Chapter 5)



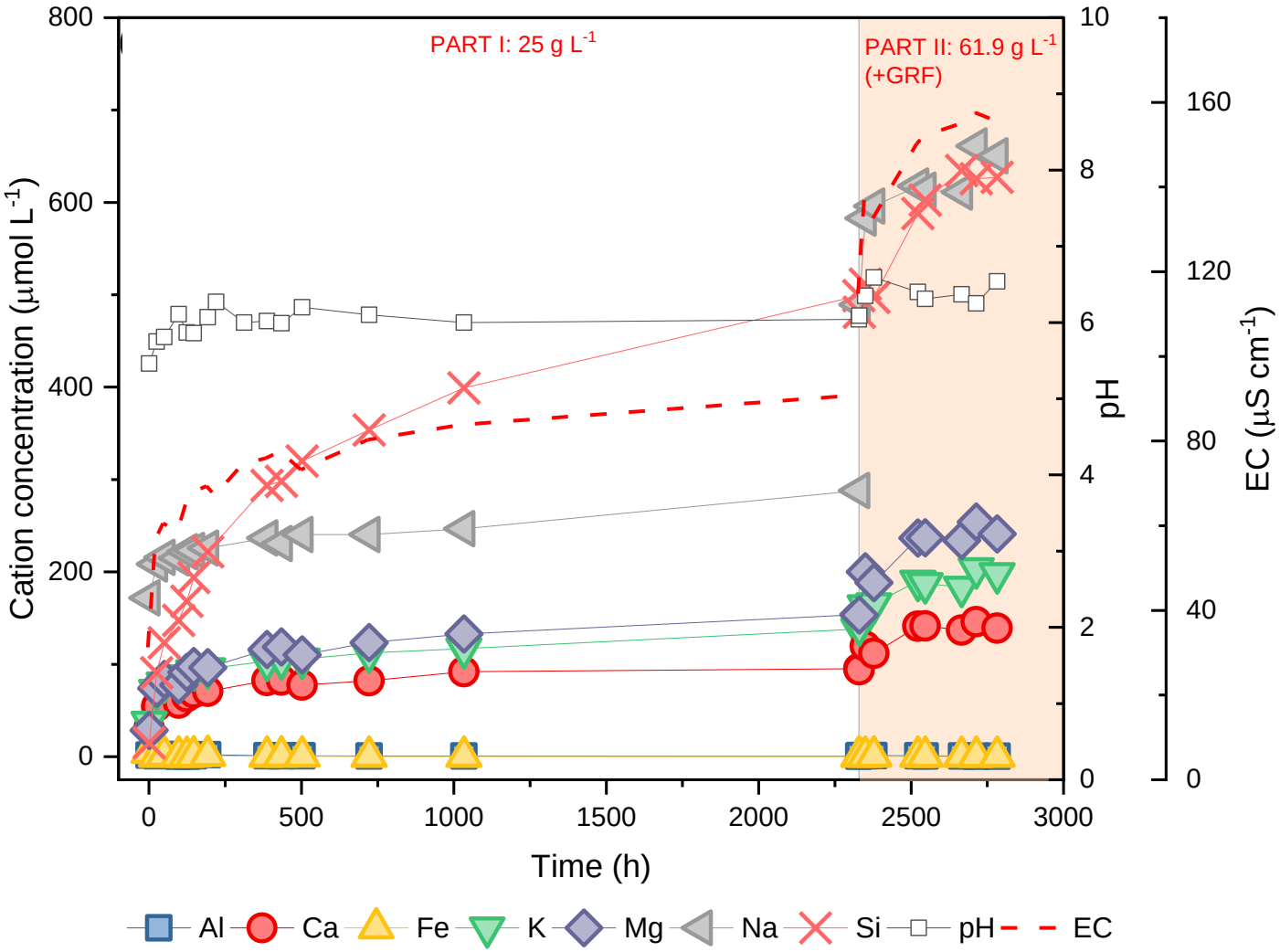
A.8. Temporal evolution of cation concentrations during the first and second part of experiments at ambient pCO_2. The first part is common in A.7 and A.8. (Chapter 5)



A.9. Temporal evolution of cation concentrations during the first and second part of experiments at 0.05 atm pCO_2. The first part is common in A.9 and A.10. (Chapter 5)



A.10. Temporal evolution of cation concentrations during the first and second part of experiments at 0.05 atm pCO_2. The first part is common in A.9 and A.10. (Chapter 5)



References

1. Acker, J. G., & Bricker, O. P. (1992). The influence of pH on biotite dissolution and alteration kinetics at low temperature. *Geochimica et Cosmochimica Acta*, *56*(8), 3073-3092.

2. Allaway, W. H. (1968). Agronomic controls over the environmental cycling of trace elements. In *Advances in agronomy* (Vol. 20, pp. 235-274). Academic Press.

3. Bagshaw, E. A., Wadham, J. L., Tranter, M., Beaton, A. D., Hawkings, J. R., Lamarche-Gagnon, G., & Mowlem, M. C. (2021). Measuring pH in low ionic strength glacial meltwaters using ion selective field effect transistor (ISFET) technology. *Limnology and Oceanography: Methods*, *19*(3), 222-233.

4. Barker, F. (1979). Trondhjemite: definition, environment and hypotheses of origin. In *Developments in petrology* (Vol. 6, pp. 1-12). Elsevier.

5. Beerling, D. J., Kantzas, E. P., Lomas, M. R., Wade, P., Eufrasio, R. M., Renforth, P., Sarkar, B., Andrews, M.G., James, R.H., Pearce, C.R. and Mercure, J.F., et al. (2020). Potential for large-scale CO 2 removal via enhanced rock weathering with croplands. *Nature*, *583*(7815), 242-248.

6. Bendixen, M., Iversen, L. L., Bjørk, A. A., Elberling, B., Westergaard-Nielsen, A., Overeem, I., Barnhart, K.R., Khan, S.A., Box, J.E., Abermann, J., Langley, K.& Kroon, A. (2017). Delta progradation in Greenland driven by increasing glacial mass loss. *Nature*, *550*(7674), 101-104.

7. Bendixen, M., Overeem, I., Rosing, M. T., Bjørk, A. A., Kjær, K. H., Kroon, A., Zeitz, G. and Iversen, L. L. (2019). Promises and perils of sand exploitation in Greenland. *Nature sustainability*, *2*(2), 98-104.

8. Bennike, O., Jensen, J. B., Sukstorf, F. N., & Rosing, M. T. (2019). Mapping glacial rock flour deposits in Tasersuaq, southern West Greenland. *Geological Survey of Denmark and Greenland Bulletin*, *43*, 10-34194.

9. Biemans, H., Siderius, C., Lutz, A. F., Nepal, S., Ahmad, B., Hassan, T., von Bloh, W., Wijngaard, R.R., Wester, P., Shrestha, A.B. and Immerzeel, W.W. (2019). Importance of snow and glacier meltwater for agriculture on the Indo-Gangetic Plain. *Nature Sustainability*, *2*(7), 594-601.

10. Binney, H., Edwards, M., Macias-Fauria, M., Lozhkin, A., Anderson, P., Kaplan, J. O., Andreev, A., Bezrukova, E., Blyakharchuk, T., Jankovska, V. and Khazina, I. (2017). Vegetation of Eurasia from the last glacial maximum to present: Key biogeographic patterns. *Quaternary Science Reviews*, *157*, 80-97.

11. Blichert-Toft, J., Rosing, M. T., Lesher, C. E., & Chauvel, C. (1995). Geochemical constraints on the origin of the late Archean Skjoldungen alkaline igneous province, SE Greenland. *Journal of Petrology*, *36*(2), 515-561.

12. Bowen, H. J. M. (1966). Trace elements in biochemistry. *Trace elements in biochemistry.*

13. Brantley, S. L. (2008). Kinetics of mineral dissolution. In *Kinetics of water-rock interaction* (pp. 151-210). Springer, New York, NY.

14. Busenberg, E., & Clemency, C. V. (1976). The dissolution kinetics of feldspars at 25 C and 1 atm CO2 partial pressure. *Geochimica et Cosmochimica Acta*, *40*(1), 41-49.

15. Carignan, J., Hild, P., Mevelle, G., Morel, J., & Yeghicheyan, D. (2001). Routine analyses of trace elements in geological samples using flow injection and low pressure on-line liquid

chromatography coupled to ICP-MS: A study of geochemical reference materials BR, DR-N, UB-N, AN-G and GH. *Geostandards Newsletter*, *25*(2-3), 187-198.

16. Chadwick, B., & Garde, A. A. (1996). Palaeoproterozoic oblique plate convergence in South Greenland: a reappraisal of the Ketilidian Orogen. *Geological Society, London, Special Publications*, *112*(1), 179-196.

17. Chou, L., & Wollast, R. (1984). Study of the weathering of albite at room temperature and pressure with a fluidized bed reactor. *Geochimica et Cosmochimica Acta*, *48*(11), 2205-2217.

18. Colbourn, G., Ridgwell, A., & Lenton, T. M. (2015). The time scale of the silicate weathering negative feedback on atmospheric CO2. *Global Biogeochemical Cycles*, *29*(5), 583-596.

19. Drewry, D. J. (1986). *Glacial geologic processes*. E. Arnold.

20. Edwards, D. P., Lim, F., James, R. H., Pearce, C. R., Scholes, J., Freckleton, R. P., & Beerling, D. J. (2017). Climate change mitigation: potential benefits and pitfalls of enhanced rock weathering in tropical agriculture. *Biology letters*, *13*(4), 20160715.

21. Eisma, D. (1986). Flocculation and de-flocculation of suspended matter in estuaries. *Netherlands Journal of sea research*, *20*(2-3), 183-199.

22. Escher, A., & Watt, W. S. (1976). *Geology of Greenland* (Vol. 603). Copenhagen: Geological Survey of Greenland.

23. Evans, D. J., Twigg, D. R., Rea, B. R., & Shand, M. (2007). Surficial geology and geomorphology of the Brúarjökull surging glacier landsystem. *Journal of Maps*, *3*(1), 349-367.

24. FIZ (2020) Inorganic Crystal Structure Database. Leibniz Institute for Information Infrastructure, Karlsruhe.

25. Fournelle, J., Cathey, H., Pinard, P. T., & Richter, S. (2016). Low voltage EPMA: experiments on a new frontier in microanalysis-analytical lateral resolution. In *IOP Conference Series: Materials Science and Engineering* (Vol. 109, No. 1, p. 012003). IOP Publishing.

26. Frederiksen, L. M. Remineralisation Potential of Glacier Rock Flour, (2018) Master's Thesis, University of Copenhagen

27. Fridahl, M., & Lehtveer, M. (2018). Bioenergy with carbon capture and storage (BECCS): Global potential, investment preferences, and deployment barriers. *Energy Research & Social Science*, *42*, 155-165.

28. Friend, C. R., & Nutman, A. P. (2005). New pieces to the Archaean terrane jigsaw puzzle in the Nuuk region, southern West Greenland: steps in transforming a simple insight into a complex regional tectonothermal model. *Journal of the Geological Society*, *162*(1), 147-162.

29. Gaillardet, J., Dupré, B., Louvat, P., & Allegre, C. J. (1999). Global silicate weathering and CO2 consumption rates deduced from the chemistry of large rivers. *Chemical geology*, *159*(1-4), 3-30.

30. Garde, A. A. (1997). Accretion and evolution of an Archaean high-grade grey gneiss–amphibolite complex: the Fiskefjord area, southern West Greenland. *GEUS Bulletin*, 1-115.

31. Garde, A. A. (2007). A mid-Archaean island arc complex in the eastern Akia terrane, Godthåbsfjord, southern West Greenland. *Journal of the Geological Society*, *164*(3), 565-579.

32. Garrels, R. M., & Howard, P. (1957). Reactions of feldspar and mica with water at low temperature and pressure. *Clays and clay minerals*, *6*(1), 68-88.

33. Goldich, S. S. (1938). A study in rock-weathering. *The Journal of Geology*, *46*(1), 17-58.

34. Gornall, J., Betts, R., Burke, E., Clark, R., Camp, J., Willett, K., & Wiltshire, A. (2010). Implications of climate change for agricultural productivity in the early twenty-first century. *Philosophical Transactions of the Royal Society B: Biological Sciences*, *365*(1554), 2973-2989.

35. Graham, S., & Keulen, N. (2019). Nanoscale Automated Quantitative Mineralogy: A 200-nm Quantitative Mineralogy Assessment of Fault Gouge Using Mineralogic. *Minerals*, *9*(11), 665.

36. Griffin, W. L., McGregor, V. R., Nutman, A., Taylor, P. N., & Bridgwater, D. (1980). Early Archaean granulite-facies metamorphism south of Ameralik, West Greenland. *Earth and Planetary Science Letters*, *50*(1), 59-74.

37. Grønbæk, N. T. Detailed geochemical and hydrogeological study of the Maalutu glacial rock flour, Nuuk, Greenland. (2019) Master's Thesis, University of Copenhagen

38. Gunnarsen, K. C. Plant nutritional value of Greenlandic glacial rock flour – an amendment to improve weathered and nutrient poor soils. (2020) PhD Thesis, University of Copenhagen

39. Gunnarsen, K. C., Jensen, L. S., Gómez-Muñoz, B., Rosing, M. T., & de Neergaard, A. (2019). Glacially abraded rock flour from Greenland: Potential for macronutrient supply to plants. *Journal of Plant Nutrition and Soil Science*, *182*(5), 846-856.

40. Hamilton, P. J., O'nions, R. K., Bridgwater, D., & Nutman, A. (1983). Sm-Nd studies of Archaean metasediments and metavolcanics from West Greenland and their implications for the Earth's early history. *Earth and Planetary Science Letters*, *62*(2), 263-272.

41. Harnois, L. (1988). The CIW index: a new chemical index of weathering. *SedG*, *55*(3), 319-322.

42. Hartmann, J., West, A. J., Renforth, P., Köhler, P., De La Rocha, C. L., Wolf-Gladrow, D.A., Dürr, H.H. and Scheffran, J. (2013). Enhanced chemical weathering as a geoengineering strategy to reduce atmospheric carbon dioxide, supply nutrients, and mitigate ocean acidification. *Reviews of Geophysics*, *51*(2), 113-149.

43. Hasholt, B., Bobrovitskaya, N., Bogen, J., McNamara, J., Mernild, S. H., Milburn, D., & Walling, D. E. (2006). Sediment transport to the Arctic Ocean and adjoining cold oceans. *Hydrology Research*, *37*(4-5), 413-432.

44. Hasholt, B., Mikkelsen, A. B., Nielsen, M. H., & Larsen, M. A. D. (2013). Observations of runoff and sediment and dissolved loads from the Greenland ice sheet at Kangerlussuaq, West Greenland, 2007 to 2010. *Z. Geomorphol*, *57*(2), 3-27.

45. Hasholt, B., van As, D., Mikkelsen, A. B., Mernild, S. H., & Yde, J. C. (2018). Observed sediment and solute transport from the Kangerlussuaq sector of the Greenland Ice Sheet (2006–2016). *Arctic, Antarctic, and Alpine Research*, *50*(1), S100009.

46. Hawkings, J. R., Wadham, J. L., Benning, L. G., Hendry, K. R., Tranter, M., Tedstone, A., Nienow, P. and Raiswell, R. (2017). Ice sheets as a missing source of silica to the polar oceans. *Nature communications*, *8*(1), 1-10.

47. Hawkings, J. R., Wadham, J. L., Tranter, M., Lawson, E., Sole, A., Cowton, T., Tedstone, A.J., Bartholomew, I., Nienow, P., Chandler, D. and Telling, J. (2015). The effect of warming climate on nutrient and solute export from the Greenland Ice Sheet. *Geochem. Perspect. Lett*, *1*, 94-104.

48. Hawkings, J. R., Wadham, J. L., Tranter, M., Raiswell, R., Benning, L. G., Statham, P.J., Tedstone, A., Nienow, P., Lee, K. and Telling, J. (2014). Ice sheets as a significant source of highly reactive nanoparticulate iron to the oceans. *Nature communications*, *5*(1), 1-8.

49. Hawkings, J., Wadham, J., Tranter, M., Telling, J., Bagshaw, E., Beaton, A., Simmons, S.L., Chandler, D., Tedstone, A. and Nienow, P. (2016). The Greenland Ice Sheet as a hot spot of phosphorus weathering and export in the Arctic. *Global Biogeochemical Cycles*, *30*(2), 191-210.

50. Herron, M. M. (1988). Geochemical classification of terrigenous sands and shales from core or log data. *Journal of Sedimentary Research*, *58*(5), 820-829.

51. Holdren Jr, G. R., & Berner, R. A. (1979). Mechanism of feldspar weathering—I. Experimental studies. *Geochimica et Cosmochimica Acta*, *43*(8), 1161-1171.

52. Holdren Jr, G. R., & Speyer, P. M. (1985a). Reaction rate-surface area relationships during the early stages of weathering—I. Initial observations. *Geochimica et Cosmochimica Acta*, *49*(3), 675-681.

53. Holdren Jr, G. R., & Speyer, P. M. (1985b). pH dependent changes in the rates and stoichiometry of dissolution of an alkali feldspar at room temperature. *American Journal of Science, 285*(10), 994-1026.

54. Holdren Jr, G. R., & Speyer, P. M. (1987). Reaction rate-surface area relationships during the early stages of weathering. II. Data on eight additional feldspars. *Geochimica et Cosmochimica Acta*, *51*(9), 2311-2318.

55. Hombourger, C., & Outrequin, M. (2013). Quantitative analysis and high-resolution X-ray mapping with a field emission electron microprobe. *Microscopy Today*, *21*(3), 10-15.

56. Hopwood, M. J., Connelly, D. P., Arendt, K. E., Juul-Pedersen, T., Stinchcombe, M. C., Meire, L., Esposito, M. and Krishna, R. (2016). Seasonal changes in Fe along a glaciated Greenlandic fjord. *Frontiers in Earth Science*, *4*, 15.

57. Huh, Y. (2003). Chemical weathering and climate—a global experiment: a review. *Geosciences Journal*, *7*(3), 277-288.

58. Hunter, K. A., & Liss, P. S. (1979). The surface charge of suspended particles in estuarine and coastal waters. *Nature*, *282*(5741), 823-825.

59. Hunter, K. A., & Liss, P. S. (1979). The surface charge of suspended particles in estuarine and coastal waters. *Nature*, *282*(5741), 823-825.

60. Kalsbeek, F., & Nutman, A. P. (1996). Anatomy of the Early Proterozoic Nagssugtoqidian orogen, West Greenland, explored by reconnaissance SHRIMP U-Pb zircon dating. *Geology*, *24*(6), 515-518.

61. Karte, J. (1983). Periglacial phenomena and their significance as climatic and edaphic indicators. *GeoJournal*, *7*(4), 329-340.

62. Keller, W. D., & Reesman, A. L. (1963). Glacial milks and their laboratory-simulated counterparts. *Geological Society of America Bulletin*, *74*(1), 61-76.

63. Kjeldsen, K. K., Mortensen, J., Bendtsen, J., Petersen, D., Lennert, K., & Rysgaard, S. (2014). Ice-dammed lake drainage cools and raises surface salinities in a tidewater outlet glacier fjord, west Greenland. *Journal of Geophysical Research: Earth Surface*, *119*(6), 1310-1321.

64. Kranck, K. (1973). Flocculation of suspended sediment in the sea. *Nature*, *246*(5432), 348-350.

65. Kuznetsov, A. B., Semikhatov, M. A., & Gorokhov, I. M. (2012). The Sr isotope composition of the world ocean, marginal and inland seas: Implications for the Sr isotope stratigraphy. *Stratigraphy and Geological Correlation*, *20*(6), 501-515.

66. Lasaga, A. C. (1984). Chemical kinetics of water-rock interactions. *Journal of geophysical research: solid earth*, *89*(B6), 4009-4025.

67. Maggi, F. (2005). *Flocculation Dynamics of Cohesive Sediment. Delft, The Netherlands: Delft University of Technology* (Doctoral dissertation, Ph. D. dissertation, 965p.

68. Markussen, T. N., Elberling, B., Winter, C., & Andersen, T. J. (2016). Flocculated meltwater particles control Arctic land-sea fluxes of labile iron. *Scientific reports*, *6*(1), 1-8.

69. McDonough, W. F., & Sun, S. S. (1995). The composition of the Earth. *Chemical geology*, *120*(3-4), 223-253.

70. McGregor, V. R. (1973). A Discussion on the evolution of the Precambrian crust-The early Precambrian gneisses of the Godthåb district, West Greenland. *Philosophical Transactions of the Royal Society of London. Series A, Mathematical and Physical Sciences*, *273*(1235), 343-358.

71. McGregor, V. R., & Mason, B. (1977). Petrogenesis and geochemistry of metabasaltic and metasedimentary enclaves in the Amitsoq gneisses, West Greenland. *American Mineralogist*, *62*(9-10), 887-904.

72. McLennan, S. M., & Taylor, S. R. (1991). Sedimentary rocks and crustal evolution: tectonic setting and secular trends. *The Journal of Geology*, *99*(1), 1-21.

73. McLennan, S. M., Hemming, S., McDaniel, D. K., & Hanson, G. N. (1993). Geochemical approaches to sedimentation, provenance, and tectonics. *Special Papers-Geological Society of America*, 21-21.

74. McSwiggen, P. (2014, March). Characterisation of sub-micrometre features with the FE-EPMA. In *IOP Conference Series: Materials Science and Engineering* (Vol. 55, No. 1, p. 012009). IOP Publishing.

75. Medford, A. K., Hall, B. L., Lowell, T. V., Kelly, M. A., Levy, L. B., Wilcox, P. S., & Axford, Y. (2021). Holocene glacial history of Renland Ice Cap, East Greenland, reconstructed from lake sediments. *Quaternary Science Reviews*, *258*, 106883.

76. Meire, L., Meire, P., Struyf, E., Krawczyk, D. W., Arendt, K. E., Yde, J.C., Juul Pedersen, T., Hopwood, M.J., Rysgaard, S. and Meysman, F.J.R. (2016). High export of dissolved silica from the Greenland Ice Sheet. *Geophysical Research Letters*, *43*(17), 9173-9182.

77. Mietta, F., Chassagne, C., Manning, A. J., & Winterwerp, J. C. (2009). Influence of shear rate, organic matter content, pH and salinity on mud flocculation. *Ocean Dynamics*, *59*(5), 751-763.

78. Mikkelsen N., Bennike O., Larsen B., Nørgaard-Pedersen N., Poulsen M.D., Simonsen A., Arqe E. (2006) Cruise report: the Galathea 3 expedition to Greenland 2006. Holocene fjord and shelf processes in West Greenland: a record of environmental and climatic change Geological Survey of Denmark and Greenland Report 2006, 25 pp

79. Moorbath, S., O'nions, R. K., Pankhurst, R. J., Gale, N. H., & McGregor, V. R. (1972). Further rubidium-strontium age determinations on the very early Precambrian rocks of the Godthaab district, West Greenland. *Nature Physical Science*, *240*(100), 78-82.

80. Muir, I. J., & Nesbitt, H. W. (1991). Effects of aqueous cations on the dissolution of labradorite feldspar. *Geochimica et Cosmochimica Acta*, *55*(11), 3181-3189.

81. Møller, H. S., Jensen, K. G., Kuijpers, A., Aagaard-Sørensen, S., Seidenkrantz, M. S., Prins M, Endler R, Mikkelsen N. (2006). Late-Holocene environment and climatic changes in Ameralik Fjord, southwest Greenland: evidence from the sedimentary record. *The Holocene*, *16*(5), 685-695.

82. Nesbitt, H., & Young, G. M. (1982). Early Proterozoic climates and plate motions inferred from major element chemistry of lutites. *Nature*, *299*(5885), 715-717.

83. Nielsen, T. F., & Rosing, M. T. (1990). The Archaean Skjoldungen alkaline province, South-East Greenland.

84. Nutman, A. P., & Friend, C. R. (2007). Adjacent terranes with ca. 2715 and 2650 Ma high-pressure metamorphic assemblages in the Nuuk region of the North Atlantic Craton, southern West Greenland: Complexities of Neoarchaean collisional orogeny. *Precambrian Research*, *155*(3-4), 159-203.

85. Nutman, A. P., & Rosing, M. T. (1994). SHRIMP U-Pb zircon geochronology of the late Archaean Ruinnæsset syenite, Skjoldungen alkaline province, southeast Greenland. *Geochimica et Cosmochimica Acta*, *58*(16), 3515-3518.

86. Nutman, A. P., Friend, C. R., Barker, S. L., & McGregor, V. R. (2004). Inventory and assessment of Palaeoarchaean gneiss terrains and detrital zircons in southern West Greenland. *Precambrian Research*, *135*(4), 281-314.

87. Nutman, A. P., Friend, C. R., Baadsgaard, H., & McGregor, V. R. (1989). Evolution and assembly of Archean gneiss terranes in the Godthåbsfjord region, southern West Greenland: structural, metamorphic, and isotopic evidence. *Tectonics*, *8*(3), 573-589.

88. Nutman, A. P., Kalsbeek, F., & Friend, C. R. (2008). The Nagssugtoqidian orogen in South-East Greenland: Evidence for Paleoproterozoic collision and plate assembly. *American Journal of Science*, *308*(4), 529-572.

89. Nørgaard-Pedersen, N., & Mikkelsen, N. (2009). 8000 year marine record of climate variability and fjord dynamics from Southern Greenland. *Marine Geology*, *264*(3-4), 177-189.

90. Odler, I. (2003). The BET-specific surface area of hydrated Portland cement and related materials. *Cement and Concrete Research*, *33*(12), 2049-2056.

91. Oelkers, E. H., Gislason, S. R., & Matter, J. (2008). Mineral carbonation of CO2. *Elements*, *4*(5), 333-337.

92. Oh, N. H., Kim, H. S., & Richter Jr, D. D. (2005). What regulates soil CO2 concentrations? A modeling approach to CO2 diffusion in deep soil profiles. *Environmental Engineering Science*, *22*(1), 38-45.

93. Overeem, I., Hudson, B. D., Syvitski, J. P., Mikkelsen, A. B., Hasholt, B., Van Den Broeke, M.R., Noël, B.P.Y. and Morlighem, M. (2017). Substantial export of suspended sediment to the global oceans from glacial erosion in Greenland. *Nature Geoscience*, *10*(11), 859-863.

94. Palandri, J. L., & Kharaka, Y. K. (2004). *A compilation of rate parameters of water-mineral interaction kinetics for application to geochemical modeling*. Geological Survey Menlo Park CA.

95. Parkhurst, D. L., & Appelo, C. A. J. (2013). Description of input and examples for PHREEQC version 3: a computer program for speciation, batch-reaction, one-dimensional transport, and inverse geochemical calculations (No. 6-A43). US Geological Survey.

96. Peccerillo, A., & Taylor, S. R. (1976). Geochemistry of Eocene calc-alkaline volcanic rocks from the Kastamonu area, northern Turkey. *Contributions to mineralogy and petrology*, *58*(1), 63-81.

97. Peters, G. P., Aamaas, B., Berntsen, T., & Fuglestvedt, J. S. (2011). The integrated global temperature change potential (iGTP) and relationships between emission metrics. *Environmental Research Letters*, *6*(4), 044021.

98. Petrovich, R. (1981). Kinetics of dissolution of mechanically comminuted rock-forming oxides and silicates—I. Deformation and dissolution of quartz under laboratory conditions. *Geochimica et Cosmochimica Acta*, *45*(10), 1665-1674.

99. Pettijohn, F. J. (1943). Archean sedimentation. *Bulletin of the Geological Society of America*, *54*(7), 925-972.

100. Pin, C., & Zalduegui, J. S. (1997). Sequential separation of light rare-earth elements, thorium and uranium by miniaturized extraction chromatography: application to isotopic analyses of silicate rocks. *Analytica Chimica Acta*, *339*(1-2), 79-89.

101. Renforth, P. (2012). The potential of enhanced weathering in the UK. *International Journal of Greenhouse Gas Control*, *10*, 229-243.

102. Richter, D. D., & Markewitz, D. (1995). How deep is soil?. *BioScience*, *45*(9), 600-609.

103. Rickwood, P. C. (1989). Boundary lines within petrologic diagrams which use oxides of major and minor elements. *Lithos*, *22*(4), 247-263.

104. Rietveld, H. M. (1969). A profile refinement method for nuclear and magnetic structures. *Journal of applied Crystallography*, *2*(2), 65-71

105. Rosing, M. T., Nielsen, T. F. D., & Vasudev, V. N. (1988). An alkaline igneous province in the Skjoldungen area, Southeast Greenland. In *The Archaean Terrains in South-East Greenland; Open file rept. GGU* (pp. 55-66).

106. Ryu, J. S., & Jacobson, A. D. (2012). CO2 evasion from the Greenland Ice Sheet: A new carbon-climate feedback. *Chemical Geology*, *320*, 80-95.

107. Sanz-Perez, E. S., Murdock, C. R., Didas, S. A., & Jones, C. W. (2016). Direct capture of CO2 from ambient air. *Chemical reviews*, *116*(19), 11840-11876.

108. Schunke, E. (1977). Zur Okologie der Thufur Islands= The ecology of thufurs in Iceland.

109. Shand, S.J. (1943). Eruptive Rocks; Their Genesis, Composition, Classification, and Their Relation to Ore Deposits, with a Chapter on Meteorites (Revised Second Edition). Hafner Publishing Co., New York.

110. Steffensen, T. The Mineralogy and Modelled Dissolution of Maalutu Glacial Rock Flour in relation to Enhanced Weathering (2020) Master's Thesis, University of Copenhagen

111. Stolzenbach, K. D., & Elimelech, M. (1994). The effect of particle density on collisions between sinking particles: implications for particle aggregation in the ocean. *Deep Sea Research Part I: Oceanographic Research Papers*, *41*(3), 469-483.

112. Streckeisen, A. (1974). Classification and nomenclature of plutonic rocks recommendations of the IUGS subcommission on the systematics of igneous rocks. *Geologische Rundschau*, *63*(2), 773-786.

113. Strefler, J., Amann, T., Bauer, N., Kriegler, E., & Hartmann, J. (2018). Potential and costs of carbon dioxide removal by enhanced weathering of rocks. *Environmental Research Letters*, *13*(3), 034010.

114. Sukstorf, F. N., Bennike, O., & Elberling, B. (2020). Glacial Rock Flour as Soil Amendment in Subarctic Farming in South Greenland. *Land*, *9*(6), 198.

115. Syvitski, J. P., & Kettner, A. (2011). Sediment flux and the Anthropocene. *Philosophical Transactions of the Royal Society A: Mathematical, Physical and Engineering Sciences*, *369*(1938), 957-975.

116. Taylor, S. R., & McLennan, S. M. (1985). The continental crust: its composition and evolution.

117. van Gool, J. A., Connelly, J. N., Marker, M., & Mengel, F. C. (2002). The Nagssugtoqidian Orogen of West Greenland: tectonic evolution and regional correlations from a West Greenland perspective. *Canadian Journal of Earth Sciences*, *39*(5), 665-686.

118. Vester-Ebbesen, A. Silicate weathering and carbon dioxide reactivity of glacial rock flour from Maalutu, Greenland. (2020) Master's Thesis, University of Copenhagen

119. Wang, S., Miller, A., Llamazos, E., Fonseca, F., & Baxter, L. (2008). Biomass fly ash in concrete: Mixture proportioning and mechanical properties. *Fuel*, *87*(3), 365-371.

120. White, A. F., & Blum, A. E. (1995). Effects of climate on chemical_ weathering in watersheds. *Geochimica et Cosmochimica Acta*, *59*(9), 1729-1747.

121. Whitehouse, M. J., Kalsbeek, F., & Nutman, A. P. (1998). Crustal growth and crustal recycling in the Nagssugtoqidian orogen of West Greenland:: Constraints from radiogenic isotope systematics and U–Pb zircon geochronology. *Precambrian Research*, *91*(3-4), 365-381.

122. Windley, B. F. (1991). Early Proterozoic collision tectonics, and rapakivi granites as intrusions in an extensional thrust-thickened crust: the Ketilidian orogen, South Greenland. *Tectonophysics*, *195*(1), 1-10.

123. Windley, B. F., & Garde, A. A. (2009). Arc-generated blocks with crustal sections in the North Atlantic craton of West Greenland: crustal growth in the Archean with modern analogues. *Earth-Science Reviews*, *93*(1-2), 1-30.

124. Windley, B. F., & Garde, A. A. (2009). Arc-generated blocks with crustal sections in the North Atlantic craton of West Greenland: crustal growth in the Archean with modern analogues. *Earth-Science Reviews*, *93*(1-2), 1-30.

125. Winterwerp, J. C. (2002). On the flocculation and settling velocity of estuarine mud. *Continental shelf research*, *22*(9), 1339-1360.

126. Wollast, R., & Chou, L. (1985). Kinetic study of the dissolution of albite with a continuous flow-through fluidized bed reactor. In *The chemistry of weathering* (pp. 75-96). Springer, Dordrecht.

127. Young, R. A. (Ed.). (1993). *The rietveld method* (Vol. 6). Oxford: Oxford university press.



Astrid and I taking samples in the field using field setup in Maalutu, West Greenland in August 2018.
© Søren Jessen

2021

FACULTY OF SCIENCE

KØBENHAVNS UNIVERSITET